PENINSULA TECHNIKON

Department of Electrical Engineering

Faculty of Engineering

MINITIATURISED DEDICATED APPLICATION OPTO-ELECTRONIC SENSORS IN THE EVOLUTION OF SMART SYSTEMS

by

Mohamed Tariq Ekeramodien Kahn

Submitted in fulfillment of the requirement for the degree

Doctor of technology (D.Tech): Electrical Engineering

Under the supervision of

Professor Raynitcka Tzoneva

DECEMBER 2002

ACKNOWLEDGMENTS

The initial impetus for this research started with Dr Mark Davis, originally with the EDRC (Energy Development and Research Centre) of the University of Cape Town (and now in England), who suggested the continuation of my research work in optical fibre sensors to topics involving new technology in energy research. From there I developed an initial proposal with Professor Yong Hua Song of the University of Brunel, and subsequently revised the proposal and registered under Professor Raynitchka Tzoneva of Peninsula Technikon for the research towards this degree. To these three I owe my first acknowledgement of thanks.

Having embarked on this avenue the research was then supported by a research grant GUN 2040624 from the National Research Foundation (NRF) and instrumentation, laboratory equipment and software from Peninsula Technikon, Fiber Optic Systems, Nebuweb and the Brunel Institute of Power Systems (BIPS)department of the University of Brunel.

The author hereby wishes to extend thanks to Mr Alexander Carberry of BIPS, whose assistance with software, and whose software platforms was used in this research, made aspects of this task possible, and without whom certain relevant deadlines would not have been achievable.

Appreciation is extended to the Dean of the Faculty of Engineering, Dr Oswald Franks, and the Head of Department of Electrical Engineering, as well as the Vice Rector Academic , Professor Anthony Staak, whose encouragement always gave me the necessary motivation to complete this task.

PENINSULA TECHNIKON

Abstract

MINITIATURISED DEDICATED APPLICATION OPTO-ELECTRONIC SENSORS IN THE EVOLUTION OF SMART SYSTEMS

by MTE KAHN

In the last decade, the South African Electricity Supply Commission would have had their ability to serve an ever demanding public severely tested. With the dilemma of providing electricity supply through hazardous environmental conditions, and with prospects of supplying power even beyond South African borders, the need for a comprehensive damage and power delivery assessment strategy becomes all the more relevant. The rapid growth being made in the evolution of so called "intelligent" structures, with inherent sensor, actuator and control mechanisms built in can have direct influence on a power distribution network. At least in the foreseeable future, the impact of photonic sensors with inherent miniaturization, a foremost candidate in Smart System technology, can play a vital role in damage assessment of a potentially large network such as that found in the supply of electricity.

Smart systems are nonliving systems that integrate the functions of sensing, actuation, logic and control, to respond adaptively to changes in their condition or environment to which they are exposed, in a useful and usually repetitive manner. Sensors are a fundamental part of the evolution of such systems and form the basis for the topic of this dissertation. The use of optical fiber sensors is increasing widely mainly due to their (a) miniature size, (b) remote signal processing ability, and (c) multiplexing capabilities. Because of the above features a variety of optical fiber sensing techniques has evolved over the years having potential for a myriad of applications.

In this work a systems model and equations was developed for modeling the propagation of light in a optical waveguide, in order to study a Fabry Perrot sensor topology for application as a miniaturised sensor in a new type of smart structure, namely a smart electrical power system. A unique model and equations for a wideband extrinsic Fabry-Perot interferometric (EFPI) optical fiber current sensor, with necessary software to implement a stand-alone system, was also developed. To implement a miniaturized point sensor system with the design and development of all the signal processing models along with the necessary hardware specifications and software satisfying real-time signal processing requirements was challenging.

The importance of multiplexing the sensors can also not be overstated. To say that much of the current economic and technological progress worldwide is due in part to mixed-signal communications systems would not be incorrect. Along the vein of advancing the state-of-the-art, this research project addresses a new area of multiplexing by taking a novel approach to network different types of miniaturized sensors , constructing the appropriate models with signal processing, and verifying the results. Two different sensor types were selected, a Fabry Perrot fiber optic sensor and a simulated digital output sensor, and were networked using code division multiplexing. The experimentation showed that the interconnection of these sensors using code division multiplexing was feasible and that the mixed signal demultiplexing system, allowed the disparate signals to be identified. An analysis of an expanded system was performed, with the results showing that the ultimate number of sensors that could be multiplexed with this technique ranges from the hundreds into the millions, depending on the specific design parameters used. This technique is unique in a power system application and significantly contributed to this field a networked optical fibre based sensor scenario that was not previously reported. The primary objective of this research, i.e. to investigate, develop, analyse and model sensor deployment and electronic signal processing in optical fibre sensors suitable for intelligent or smart power system applications, was achieved.

TABLE OF CONTENTS

LIST OF FIGURES

GLOSSARY

AJ: Anti-Jam, designed to resist interference or jamming.

Absorption. The process whereby light is lost. It is caused by the presence of residual impurities, including OH^-(hydroxyl) ions.

Actuator A device, in this case electromechanical, to correct or otherwise influence the outcome of a process or event.

ADXL A type micro electro mechanical acceleration sensor used in vibration measurement applications.

Analogue signal. A signal in which variations in intensity are used to transmit information. An analogue signal varies continuously with time.

Bandwidth. This is typically 100 000MHz km for singlemode and 500 MHz km for multimode fibre at 1300nm.

Baudot Related to data rate and also known as the Baud rate

BPSK Binary Phase Shift Keying, a digital DSB suppressed carrier modulation.

CDMA Code Division Multiple Access -- a way to increase channel capacity.

Chip The time it takes to transmit a bit or single symbol of a PN code.

CT Current transformer. Specifically used in current measurement applications.

Code A digital bit stream with noise-like characteristics.

Correlator The receiver component that demodulates a Spread Spectrum signal.

Composite cables Cables which contain both optical fibre and copper pairs. The latter often being used to transmit electrical power.

Cut-off wavelength. The wavelength of light at which single mode fibre starts to propagate one mode only. This is typically at greater than 1150nm.

Connector A device which couples the fibre to the source or detector

Coupler A device which splits or joins lightwaves in two or more optical fibres

Coupling loss Occurs at the point where the fibre and receiver or detector connects

Crosstalk It occurs due to the presence of one channel's signal in an adjacent channel

De-spreading The process used by a correlator to recover narrow band information from a spread spectrum signal.

Directional coupler Routes the optical power to a specific port depending on the direction of propagation

Dispersion is a measure of the spreading of an injected light pulse

Distributed Reference to sensors, controllers and actuators widely dispersed through a system.

Distributed-feedback laser A type of laser diode with spectral width of <0.01 nm

DSP digital signal processing, a technique distinct from analogue signal processing

EFPI External Fabry Perrot interferometer, where forward and reflected waves from a fully and partially reflective surface in a cavity external to optical fibre create and interference pattern which is detectable as an intensity variation of light.

EMI Electro magnetic interference, a common source of induced noise

Fabry-Perot Interferometric method used to detect phase and convert the signal into an amplitude variation

Fabry-perot laser Laser based on a the optical resonance in a cavity, the centre wavelength which has a typical tolerance of +/-3 nm

Fabry-perot resonator This is a bandpass optical filter that transmits a narrow band of wavelengths and reflects others

FBG Fibre Bragg grating, a type of optical fibre interference pattern that is laser written in the fibre, causing changes in the refractive index

FPI Fabry Perrot interferometer, created by an interferometric cavity in which forward and reflected waves from a fully and partially reflective surface in the cavity create interference which is detectable.

FIR Finite impulse response filter. An technique used in DSP applications.

FOG Fibre-optic gyroscope. A technique used to detect rotation, i.e. Sagnac interferometer method.

Frequency division multiplexing Data in channels of bandwidth(BW) are upconverted in a mixer/modulator by carrier frequencies(f) to form a single transmission channel. The combined channels and the resultant composite waveform is transmitted over the fibre link

HV High voltage, generally above 11kV in power system applications, but definition may vary.

ILED Infrared light emitting diode, emits light above the visible spectrum

IFPI Intrinsic Fabry perrot interferometer, created by splicing the interferometric cavity in line with the fibre.

Intelligent structure A structure that have both sensory elements, actuators and controllers highly distributed throughout it that can enable it to respond to changes in conditions automatically.

Interferometry Technique used to determine the refractive index profiles of optical fibres, i.e. phase detection

IIR Infinite impulse response filter, as opposed to a finite response filter in digital signal processing

Jitter This is defined as short-term timing or phase variations in a received regenerated signal pulse from that of the ideal

Laminate Reference to layered construction method envisioned in the manufacture of intelligent systems.

LPG Long period grating, a type of optical fibre interference pattern that is laser written in the fibre, causing changes in the refractive index

LD Laser diode, a monochromatic coherent light source generated with semiconductors

LED light emitting diode, a incoherent semiconductor based light source

Mach-Zender interferometer A method based on transmitted light interferometry

Macrobending Light lost from the optical core due to macroscopic effects such as tight bends being induces in the fibre itself

MDP Minimum detected power. This is the received power less any coupling losses between detector and any coupling device

Michelson method Reflected light based interferometer

Microbending Light lost from the optical core due to microscopic effects resulting from deformation and damage to the core-cladding interface.

Modal noise Noise caused due to different time delays which in turn is caused by dispersion

MOEMS micro opto electro mechanical systems, a miniaturised structure in silicon.

Monolithic *Uniform throughout. The antithesis of laminated.*

Multimode fibre Fabricated from either multicomponent glass compounds

Multiplexing This function combines multiple channels into a composite signal for transmission.

Numerical aperture *Refers to the relationship between the core, air, cladding and the* acceptance angle of an optical fibre interface.

Operating wavelength It is the wavelength at which the optical source transmits light.

Optical aperture Area onto which light falls

Optical receiver It contains a photodetector, amplification section, and signal-recovery circuitry. It converts the received optical power signal to a voltage signal

Optical transmitter This contains the drive electronics and optical source. It converts the transmitted signal voltage to optical power

PCN Personal Communication Network. PCNs are usually short range (hundreds of feet to 1 mile or so) and involve cellular radio type architecture. Services include digital voice, FAX, mobile data and national/international data communications.

PCS Personal Communication System. PCSs are usually associated with cordless telephone type devices. Service is typically digital voice only.

PN Pseudo Noise - a digital signal with noise-like properties.

Photocurrent It is the current generated when optical power is absorbed by the detector

Polarimetric sensor Used to detect changes in the polarization state of the light caused by an external disturbance, i.e. used for pressure measurement

Receiver dynamic range It is the range of wavelengths that the receiver can detect

Responsivity It is the ratio of the photocurrent generated for a unit of optical power

Rx Receiver of optical signals

RF Radio Frequency - generally a frequency from around 50 kHz to around 3 GHz. RF is usually referred to whenever a signal is radiated through the air.

Sagnac Name of a ring laser type of interferometer

Singlemode fibre Fabricated from a single narrow strand of doped silica in order to reduce attenuation. It allows only one lightwave mode to propagate with no multiple reflections within the fibre.

SLED Superluminescent diode. A wideband optical source.

SOT Selective observability transducer, where sensor information are polled.

Splice A point where two fibres are permanently joined

Star-coupler It couples power from one of N fibre input ports to all N output ports

SS Spread Spectrum, a wideband modulation which imparts noise-like characteristics to a signal.

T-coupler It splits power in one direction from one fibre to two

TDM Time division multiplexing. Interleaves multiple lower-speed digital data channels for transmission over one higher speed channel

Transducer A device that transform energy from one type to another, usually with reference to sensory elements. Typically the transformation of kinetic energy to electrical energy.

Tx Transmitter. An optical source or otherwise, used to send data over a link.

Waveguide It refers here mostly to a fibre optic cable although RF waveguides are more common.

Wavelength coupler Couples power from multiple sources, operating at different wavelengths, onto a single fibre

WDM Wavelength division multiplexing. Individual transmission channels are carried on separate optical wavelengths and combined in a single fibre at the optical link

Wireless LAN Wireless Local Area Network - a 400m or less range computer-to-computer data communications network.

Wireless UAN Wireless Universal Area Network - a collection of wireless MANs or WANs that link together an entire nation or the world. UANs use very small aperture (VSAT) earth station gateway technology.

LIST OF SYMBOLS

A	amplitude
δ	phase difference
$\mathbf{E}$	electric induction field
$\mathbf{B}$	magnetic induction fields
$\mathbf{D}$	electric displacement field
$\mathbf{H}$	magnetic field
K	Kerr constant
k	constant : used and explained in context in text.
$\mathbf{k}$	propagation vector
$\mathbf{e}$	complex polarization vector
Re	real
Im	imaginary
$\mathbf{S}$	stokes vector
$\mathbf{J}$	jones vector
I	intensity
I_{ph}	photo current
I_p	electric field power
T_I	transmitted intensity
F	contrast
n	refractive index
r	reflectivity

N	number of turns
n	refractive index
k_0	wave number in a vacuum
Φ	rotating phase polarization
l	length
λ	wavelength
V	verdet constant
V	voltage
g	resonator gap length
ϕ	phase change
E_x	electric field x component
E_y	electric field y component
T_I	transmitted light intensity

Chapter 1

OPTICAL FIBRE SENSORS AND SENSOR TECHNOLOGY FOR INTELLIGENT POWER SYSTEMS: AN INTRODUCTION AND LITERATURE SURVEY

1.1 Background to the problem

1.1.1 Smart or "intelligent" systems

Smart systems are nonliving systems that integrate the functions of sensing, actuation, logic and control, to respond adaptively to changes in their condition or environment to which they are exposed, in a useful and usually repetitive manner (Udd, 1995). Smart materials possess both sensing and actuation capability. Smart structures are the result of a design philosophy that emphasises a predictive, adaptive and repetitive system response (Udd, 1995; Crawley, 1994). Defence and aerospace are prime developers of as well as markets for smart technology (Crawley, 1994). Most military uses are classified, however opto-electronic and photonic sensor and data link information from many unclassified and declassified systems are nowadays available in the literature (Culshaw, 1995;Udd, 1995). In recent years there has been an increasing interest in integrated opto-electronic circuits. Applications for micro-machined opto-electromechanical systems (MOEMS) and integrated optics (photonics) in future markets for smart systems are anticipated to be enormous (Gialorenzi, 1982 & Kim et al 1996).

1.1.2 Optical Fiber Sensors as a viable technology in "intelligent" systems

With the reduction in the cost of micro-electronics and optical fibre technology, the development of smart systems has become more and more popular (Culshaw, 1995). The past two decades have seen a rapidly growing interest in the field of fiber-optic sensors (Udd, 1995). This growth in interest has been brought into effect mainly by the advances made in the related fields like opto-electronics and optical signal processing. Some of the principal reasons for the popularity of optical fiber based sensor systems are (Gialorenzi, 1982) small size, light weight, immunity to electromagnetic interference (EMI), passive (all dielectric) composition, high

temperature performance, large bandwidth, higher sensitivity as compared to existing techniques, and multiplexing capabilities. Moreover, the widespread use of optical fiber communication devices in the telecommunication industry has resulted in a substantial reduction in optical fiber sensor cost (Udd E, 1991). As a result, optical fiber sensors have been developed for a variety of applications in industry, medicine, defense and technology research. Some of these applications include gyroscopes for automotive navigation systems (Quist et al, 1996), strain sensors for smart structures (Fuhr, 1995 & Kahn, 1997) and for the measurement of various physical and electrical parameters like temperature, pressure, liquid level, acceleration, voltage and current in process control applications (Udd, 1991). Information about the measurand is primarily conveyed in all optical fiber sensors by a change in either polarization, phase, frequency, intensity or a combination of the above.

Optical fiber sensors can be broadly classified on the basis of their operating principle as intensity based or interferometric type (Udd, 1991). Intensity based sensors are inherently simple and require simple electronic support. However, sensitivity is often traded off to realize these advantages. Interferometric sensors on the other hand require relatively complicated signal processing techniques but have extremely high sensitivity. Optical fiber sensors are further classified as intrinsic or extrinsic. In intrinsic type of sensors, the fiber functions as both the transmission and sensing element. Thus the parameters to be measured change the light guiding properties of the fiber, which can be detected and demodulated to obtain information about the parameter. Whereas in extrinsic fiber sensors, the fiber merely acts as the transmission medium, bringing light to and from the sensing medium. Mach-Zehnder interferometer, Michelson interferometer and Fabry-Perot interferometer are some of the fiber optic interferometers in use today. New applications for optical fibre sensors are still evolving today (Culshaw, 1995).

1.1.3 Sensor applications to date

Some of the major applications which have been implemented, demonstrated, or proposed for optical fiber sensors are presented below.

1.1.3.1 Measurement of strain:

Optical fiber sensors have been shown to measure strain in a multitude of ways (Flavin et al, 1995; Sirkis et al, 1995; Zimmerman et al, 1989). Strain measurement has also been implemented with distributed and multiplexed sensors (Horiguchi. et al,1995). Due to lightweight, minute size, and remote interrogation capabilities of optical fiber sensors strain measurements of structures with imbedded sensors have also been implemented (Habel, 1995).

1.1.3.2 Measurement of temperature:

Optical fiber sensors for the measurement of temperature have been widely demonstrated, implemented, and commercialized (Dills,1983), with a wide variety of applications including the measurement of temperature in nuclear reactors (Gottlieb,1981). Measurement of temperature in high electro-magnetic field or in high radiation is possible with optical fiber sensors (Fuhr, 1995). Temperature can also be measured with distributed or multiplexed fiber sensors.

1.1.3.3 Measurement of pressure:

Fiber optic sensors can be used for measurements of pressure(Wang A. 1992). Measurement of pressure in boilers, chemical process reactors, combustion engines, airplane wings, and human body can be implemented with optical fiber sensors (Udd,1991).

1.1.3.4 Measurement of acoustic signals:

Optical fiber sensors have been demonstrated to detect weak acoustic signals (Buccaro,1977; Cole,1997). It has been used as a "point", "gradient", or "directional" sensing device for the purpose of designing

hydrophone (Culshaw,1988). It has also been used to detect signals of surface acoustics.

1.1.3.5 Measurement of vibration:

One of the uses of optical fiber sensor is the vibration measurements (Murphy, 1992; Yu et al, 1995). This has also been the subject of the Masters Degree in technology dissertation (Kahn,1998) presented at Peninsula Technikon. Other research have also shown that vibration in the range of 1.1.4 Hz to 85 kHz has been demonstrated to be accurately measured by optical fiber sensor techniques (Limanova,1996). Optical fiber sensors have been proposed to measure the high temperature seismic events of the deep boreholes and the volcanic regions of the earth surface (Limanova,1996).

1.1.3.6 Measurement of displacement:

Optical fiber sensors has been demonstrated and used as high precision displacement sensors, specially, for applications where micrometer or nanometer resolutions are required over short dynamic ranges (Wang, 1995; Wang et al, 1992). Optical fiber sensors has been proposed for the accurate measurement of the relative drift of the floors of the multistoried buildings when they undergo wind or earthquake loading.

1.1.3.7 Measurement of chemical material:

Due to its inert and non-electrical nature and remote sensing abilities optical fiber sensors are commercially being used for sensing various chemical materials. Fiber optic sensors can be used for detection or measurement of the concentration of various toxic or explosive gases such as CO, CH_4, C_2H_6, N_2O, and SO_2 (Jeffers,1985; Hordrik,1983; Chan et al, 1984). Optical fiber sensors have also been demonstrated to be used for in-situ composite cure monitoring (Luo,1996; Druy,1988). Fiber optic sensors can be used for food processing, photographic and similar chemical processing, hazardous waste analysis, groundwater monitoring, and stack gas analysis (Milanovich,1983; Udd, 1991).

1.1.3.8 Measurement of Biomedical processes:

One of the most significant applications of optical fiber sensors is in biomedical engineering (Migani,1995). Optical fiber sensors have been demonstrated to measure or detect pH (hydrogen ion concentration) for both clinical or non-clinical purposes (Markle,1981; Petersen,1984; Michie,1995; Deboux, 1995). A fiber optic sensor has been demonstrated to accurately measure the concentration of glucose (Mansauri,1984). Optical fiber sensors can be used to measure the velocity of blood flow of vessels (Tanaka & Benedick,. 1975), or the temperature or pressure of any part of the human body, by guiding the sensor fiber within a catheter tube.

1.1.3.9 Embedded sensors for smart materials and smart structures:

Optical fiber sensors are considered to be one of the prime candidates for smart materials and smart structures (Measures,1992; Urruti, 1998; Wood,1989). Due to their light weight, miniature size, multiplexing capabilities, and remote interrogation abilities fiber optic sensors have aptly been imbedded in building beams or bridge columns for nondestructive evaluation of these structures (Nellen et al,1996). Large networks such as electricity supply networks are also prime candidates for being considered intelligent networks if appropriate sensor and control mechanisms are included in its structure.

1.2. Overview of Optical Fiber Sensing Techniques

In an optical fiber sensor system the change of the measurand alters one or more optical properties of the sensor creating a variation in electrical measurables like voltage or current by optical-to-electrical conversion using photodetectors, and thus enable any measurements to be performed through the medium of optics(Udd, 1995). As the optical wavelengths are measured in the units of nanometers and the responsivity of photodetectors are very high, very precise measurement of the measurand is possible through fiber optic sensors(Udd, 1995). Techniques of implementations of optical fiber sensors are very wide and broad(Crawley, 1994). Some of the major sensing techniques of optical fiber sensors are discussed here. Note that many of these techniques have a

displacement resolution reported in the order of nanometers or even in picometers (Grattan,1995; Murphy,1992).

1.2.1 Intensity based sensors technique:

The basic concept of intensity based sensors is very simple, either the reflective or the transmissive intensity of light is modulated by the measurand (Lagakos,1981;Lawson,1983;Bert et al,1987). The major limitation of any intensity based sensor is the lack of any suitable reference intensity signal. Any intensity fluctuations in the output not associated with the measurand produce erroneous results (Udd,1991).

1.2.2 Fabry-Perot interferometric technique:

In Fabry-Perot interferometric sensor there are two reflective surfaces enclosing a Fabry-Perot (FP) cavity of an optically transparent medium (Born,1975). The reference signal and the sensing signal reflects from these two interfaces, and the interfered signal is monitored. Any change of measurand changes the length and/or any other optical properties of the FP cavity, causing a change in the interfered signal. Depending on the type of the cavity, the sensor can be termed either as intrinsic FP interferometric (IFPI) sensor, or extrinsic FP interferometric (EFPI) sensor. For the case of EFPI sensor the FP cavity is formed outside the optical fiber (Khan,1997). This will be elaborated upon in Chapter 3

1.2.3 Mach-Zehnder interferometric technique:

In a Mach-Zehnder interferometric sensor the coherent light source is launched into a single-mode fiber, which is then split into two arms, using a fiber optic coupler, the sensing arm and the reference arm (Udd,1991; Marshall,1996). These two arms are then recombined using a second fiber optic coupler known as recombiner. The recombined, or the interfered, signal is detected by a photodetector Any change of measurand changes the phase of the coherent signal of the sensing arm, causing an appropriate change in the detected signal.

1.2.4 Michelson interferometric technique:

The main difference of a Michelson interferometric sensor compared to a Mach-Zehnder one is that light is reflected back by mirror from both the reference arm and the sensing arm and then recombined by the same coupler which split them. So there is only one 2x2 coupler for a Michelson interferometer, in one side of the coupler is the sensing arm and the reference arm(both having mirrors at the ends), and on the other side of the coupler is the optical source and the detector. The detector detects the interfered (or recombined) signal which changes with the change of measurand on the sensing arm.

1.2.5 Sagnac Interferometric technique:

In Sagnac interferometric sensors beams of light propagate in clockwise and counterclockwise directions inside an optical fiber ring. When the ring of fiber rotates in the clockwise direction, the optical beam propagating in the clockwise direction traverses a light path longer than the light path traversed by the counterclockwise beam (which is known as Sagnac effect). Any change of speed of rotation of the fiber ring changes the difference of the optical paths between these two counter-propagating beams (Udd,1991; Marshall,1996).

1.2.6 White light interferometric techique:

When the system light source, in interferometric sensor systems discussed above, is of wide band, rather than of a single coherent frequency, it is termed a white light interferometric sensor system. In white light interferometric systems the sensor is interrogated over a wide band of optical frequencies (or wavelengths) and the signal response is acquired and processed for the entire band. The white light interferometric systems have several inherent advantages, though their signal processing techniques are more complex than that of single frequency systems. Among the advantages are the precise and accurate measurements, the self calibrating capabilities, and the wide unambiguous dynamic range of operations (Culshaw,1995).

1.2.7 Absorption spectroscopic technique:

In absorption spectroscopic sensors the measurand causes some of the spectrum of the wide band light source transmitted through an optical fiber to be absorbed or attenuated (Grattan,1995). These types of techniques are widely used in chemical sensors.

1.2.8 Fiber Bragg grating (FBG) technique:

Bragg gratings are periodic refractive index variations written into the core of an optical fiber by exposure to an intense UV interference pattern (Meltz,1996). For an FBG sensor, changes of measurand are encoded as changes in the periodicity or refractive index of the grating and thereby shifting the wavelength of the reflected wave. The measurements of the measurand is achieved by detecting the wavelength of the reflected wave.

1.2.9 Long period grating (LPG) technique:

One of the newest techniques in the optical fiber sensor technology is the LPG sensor (Vengsarkar,1996). While in an FBG sensor, coupling of energy occurs from the forward propagating fundamental mode to the reverse propagating fundamental mode, coupling of energy in an LPG sensor occurs from the forward propagating fundamental mode to the forward propagating cladding modes, which attenuate very rapidly due to the lossy cladding-coating interface. The measurements of the measurand is thus achieved by detecting the attenuated wavelength in the transmission spectrum.

1.2.10 Wavelength modulation technique:

In a wavelength modulated optical fiber sensor usually a wide band source is employed. A change in measurand of such a system causes wavelength dependent intensity variations over the spectrum of the source (Claus, 1997). By using diffraction gratings and charged coupled device elements, a graph of wavelength versus intensity of the optical output can be achieved for the whole spectrum of the source. The measurements of the measurand can be achieved by processing the measurand-induced wavelength dependent intensity modulated signals, i.e. by processing the wavelength versus output intensity graph. Note that, any system using white light interferometric sensors, absorption

spectroscopic sensors, FBG sensors, or LPG sensors can be generalized as a system of wavelength modulated optical fiber sensor (Udd, 1995; Claus, 1997). There are some distinct advantages of wavelength modulated optical fiber sensor systems over other types of sensor systems like intensity modulated systems or single frequency interferometric sensor systems (Udd, 1995) (Grattan & Meggit, 1995).

Among the advantages of wavelength modulated techniques are:

- Accuracy of measurements are independent of small intensity variations of the source of the system.
- The unambiguous range of the movement of the sensing fiber is not limited to only quarter of a wavelength of a single frequency source, rather a wide dynamic range is achieved.
- The sensitivity of the sensor is independent of the variations of the measurand.
- Since the information about the measurand is inscribed over a wide band rather than over a single frequency, a higher measuring precision and accuracy is achieved.
- A single low cost wide band source like LED is required rather than expensive quadrature phase-shifted coherent laser sources (Murphy,1991).
- Direct measurement and self calibrating qualities are achieved for Fabry-Perot interferometric type sensors.

1.3 Motivation for the research

In the last decade, the South African Electricity Supply Commission has had its ability to serve an ever demanding public severely tested (Dooly,1998). With the dilemma of providing electricity supply through hazardous environmental conditions, and with prospects of supplying power even beyond South African borders, the need for a comprehensive damage assessment strategy becomes all the more relevant (Davis, 1998). The rapid growth being made in the evolution of so called "intelligent" structures, with inherent sensor, actuator and control mechanisms built in can have direct influence on a power distribution network (Davis, 1998). At least in the foreseeable future, the impact of photonic sensors, a

foremost candidate in Smart Structure technology, can play a vital role in damage assessment of a potentially large network such as that found in the supply of electricity.

Photonic sensors, generally characterised by point and distributed sensor techniques using fibre-optic cables, are ideally suited for long haul sensor requirements in a HV supply network(Udd, 1995). This research will focus primarily on the applicability of fibre-optic sensors to measure electrical parameters and/or damage assessment in electricity supply and power system networks. There are four areas of immediate potential photonic sensor development and applications (Culshaw,1995) namely:

- Damage assessment to power lines
- Damage assessment to substations, transformers and generators
- Transformerless current, and
- Voltage transducers

The advantages of integrated opto-electronic sensor technology, cost, and ease of data transmission and processing will need to be looked at, as well as the techniques for non invasive sensor development that would not require interruption in electricity supply in the deployment of sensor networks even on a nation-wide level.

1.3.1 Overview of optical fibre sensors for electrical measurands

Optical fiber sensors have been reported to measure current, magnetic field, and voltage (Culshaw,1995, Bucholtz et al,1995). Vectorial measurement of magnetic field has been proposed using optical fiber sensors (Annovaci-Lodi et al,1992). Voltage measurement using liquid-core optical fiber sensor has also been attempted (Kuribara,1983).

Measuring current of high voltage power lines was achieved optically using the Mach-Zender inteferometer technique (Gialorenzi,1982; Arditty et al,1981; Rogers,1997, Swart,1997). This current must be measured accurately as it is distributed to the customer who is charged for the amount of electricity consumed. The current is also used for proper control of the grid network and for rapid indication of fault conditions to allow for corrective action. Conventional current

transformers, using primary and secondary induction windings, are fairly widespread for this measurement purpose but they require costly high voltage insulation between the two windings. Current transformers have two different functions that consist of metering and protection. The metering coil must have high accuracy, up to 120% of full load, and saturation may then commence which relieves the metering equipment of heavy overloads during faults. The protection coils must have a low accuracy up to full load, but higher accuracy must be maintained at ten times the full load current. The other factor contributing the shortcomings of the current transformer is the saturation effects owing to the ferromagnetic hysteresis and from relatively low bandwidth owing to the large winding inductance.

Magnetic field measurement has become an essential procedure in many industrial, scientific and defense projects today. Weather satellites routinely map the earth's magnetic field for scientific information. Airplanes and ships use the earth's magnetic field to compute direction as well as altitude, in case of airplanes. Measuring magnetic field is one of the primary methods of estimating high voltages and currents in industrial environments. Magnetic field detection is of much interest to defense scientists, particularly in the area of minefield and submarine detection. All the above reasons have made the development of reliable, rugged, extremely sensitive magnetic field sensors, highly essential. Small, fiber optic-based magnetic field sensors could be used for many applications which are inaccessible to electrical based sensors. A variety of optic fiber based magnetic field sensors have already been developed (Udd,1991). But these, in general, are relatively large or have low sensitivity when compared to small electrical based semiconductor Hall effect sensors or magnetoresistive sensors commonly in use (Lenz,1990). Measurement of low level magnetic fields in particular, is the topic of research in many defense and weather related areas these days. Extensive research has been conducted to investigate fiber-based schemes to measure magnetic fields with a higher sensitivity. Some of the fiber and non-fiber based methods presently being studied for low-level magnetic field measurement are presented below. Oliver et al report the use of a thin magnetic film, which is "read" using the magneto-optic Kerr effect (Oliver et al,1993).

1.3.2 Overview of sensor networking and multiplexing.

Multiplexing is defined as simultaneously communicating two or more messages on the same channel. One has only to look at the communications technology that surrounds us to realize that multiplexing is everywhere. The car radio carries several different signals at once as does the television and the Internet. Combining signals onto one media has resulted in a new society, one where the participants can communicate effectively and easily. The first person to implement multiplexing was Emile Baudot in 1874 (Feher,1981). His system enabled telegraphers to send 6 signals simultaneously over one line. Later, Marconi developed a means for sending signals over the airwaves by using a spark gap transmitter operating on a specific frequency. This paved the way for other transmitters and receivers to be used simultaneously, each operating on its own frequency. In effect, the modern broadcast world uses multiplexing to allow many stations to broadcast over the same media, the airwaves.

Multiplexing is a key ingredient in internetworking, which is described as collection of individual networks, connected by intermediate networking devices, that functions as a single large network (Keiser,1991). Three common forms of multiplexing are:

- Frequency Division Multiplexing (FDM), sometimes called Wavelength Division Multiplexing (WDM),
- Time Division Multiplexing (TDM) and
- Code Division Multiplexing (CDM).

With FDM, different signals are separated by frequency. AM broadcasting is an example of FDM, where one hears a station at 810 kHz, another at 820 kHz another at 830 kHz and so on. With TDM the signals are transmitted at different times rather than different frequencies (Baudot's code mentioned above was a form of TDM), and with CDM, each signal possesses a different code and the detector (receiver) is trained to look for that particular code. Each form of

multiplexing has its own advantages and disadvantages and lends itself to a particular application. FDM is used for analog cellular communications as well as for optical fiber communications.

TDM is used for digitial cellular communications and for both optical fiber and electronic communications of a digital nature. CDM is used for Personal Communications Systems (PCS) and is perhaps the fastest growing form of multiplexing. Originally devised during World War II for use in RADAR, it saw limited use until the development of PCS. It provides for a good signal to noise ratio and increased security (Feher,1981). As computing power has increased over the years, so has the use of computers and software to achieve multiplexing goals. For example today, the CISCO router uses both hardware and software to achieve the multiplexing required for the Internet. Additionally, CDM makes use of the increased processing power to form its long codes and algorithms. The aforementioned examples of multiplexing use identical information sources; that is voice is multiplexed with voice, digital data with digital data and so forth. However, the current challenge to connecting various systems is to support communication between disparate technologies and recently effort has been made to multiplex different signals together. This is the primary concept involved with the highly successful CISCO Company and their mixed signal routers (Green, 1993) Multiplexing different types of signals is one reason the Internet has expanded and continues to bring new possibilities of communications to the consumer. In fact, the high speed multiple access communication systems now form the basis of much of the current economic and technical progress world wide.

Taking this concept one step further is the combining of signals from different sources, such as different types of sensors. To do this on a large scale would allow a further expansion of communications. However, this is one area of multiplexing where little if anything has been done (Mlodzianowski & Culshaw, 1988) (Street & Edwards,1995) (Whitesel et al, 1997). This area of research is just as fundamental as multiplexing communications signals, but may be more difficult to envision because the number of possible sensor devices is large.

1.4 Objectives of the research

1.4.1 Preamble

In recent years power system networks have grown in complexity in order to extend the supply of electricity to wider networked areas (Gordean et al, 1991). Energy control centers must therefore retain highly skilled operators to provide power system control and proper analysis of power system phenomena (Rudolph, 1998). The evolution of an "intelligent"or smart power system to detect incipient abnormal system conditions and to take pre-determined counter actions, other than the isolation of faulted items is envisaged through this research endeavour.

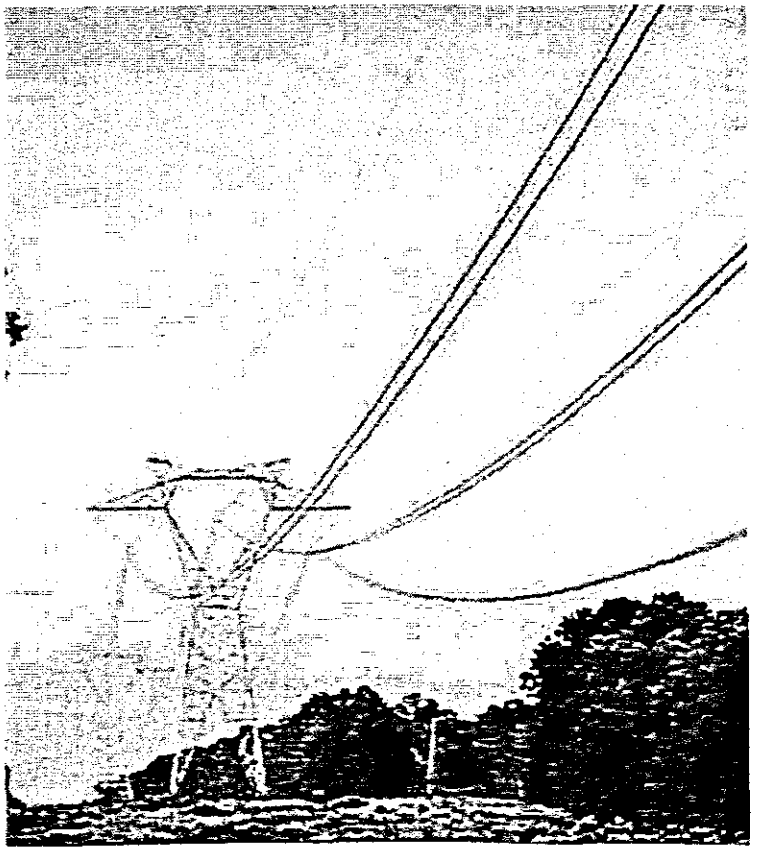

Figure 1.1 Electrical reticulation with embedded optical fibre

1.4.2 Context

In the late 1970's, the Electric Power Research Institute (USA) (Rhyne, 1982) supported research in three areas namely:

- The ABB Compuguard Project – An attempt to use power line carriers to implement two way communications between remote units and a central computer.

- The Westinghouse Project – An attempt to use dedicated land lines to implement communications between a central computer and substations.
- The Lilco Project – An attempt to use UHF radio to implement two way communications

All these attempts claimed limited success under certain conditions (Rhyne, 1982). With the deployment of fibre optic HV cable , Figure 1.1, a new possibility of not only communication, but also the relaying of sensor information emerged (Bucholtz et al,1995). This was particularly so because optical fibre sensors advanced tremendously during the nineties.(Culshaw,1995, Bucholtz et al,1995).

1.4.3 Approach to the study

From the above it was found reasonable to determine if opto electonic sensors for electrical parameter and damage assessment in large scale networks, such as an electricity supply and power system network, were applicable. These sensors were miniature by nature and much smaller than conventional current transformers. Since motivation existed for miniature opto electronic sensors applications (Gialorenzi,1982; Arditty et al,1981; Rogers,1997, Swart,1997), it was therefore feasible to develop topologies for fibre-optic sensor deployment in power system applications as well as an implementation of such sensors with reliable multiplexing technology in a large network. The wide area protection that is envisaged herewith is offered as a solution for the critical problems faced by power utilities with regard to power system transients (Abel et al,1993). Such a sensor configuration should at the present moment be unique (Culshaw, 1995), and should add a new dimension to reliable national and international energy supply implementation (Marks, 1999).

1.4.4 Formulation of particular objectives

1.4.4.1 Objective 1

Although optical fibre sensors for electrical measurements has emerged in developments in the past decade, it has not been applied in a large networked application such as a power system (Measures, 1992) (Marks, 1999). The focus would be on developing an optical fibre sensor, as a class of miniaturised sensors (Udd, 1995), with novel application areas such as voltage and current measurement in real time, and to network such sensors for a large-scale application like the national grid.

Because of the advantages that optical fiber sensor systems offer, as stated earlier, a great amount of recent work in fiber optic sensor technology has focused on the utilization of interferometric sensing techniques, or on other types of wavelength modulated techniques such as FBG or LPG sensing techniques (Marshall, 1996). Most of the literature dealing with optical fibre sensors for electrical measurands were using distributed sensing approaches based on Mach Zehnder interferometry (Gialorenzi,1982; Arditty et al,1981; Rogers,1997, Swart,1997). None have so far reported applications using the Fabry Perrot technique in such an application. The Fabry Perrot technique is a type of point sensor (Udd, 1995), and would therefore be the smallest possible configuration for sensor topology.

- The primary objective of this research was therefore to develop, model and analyse sensor deployment and electronic signal processing in optical fiber based sensors that would be suitable for use in a large networked applications.

This would be crucial in the evolution of an intelligent or smart structure (Udd, 1995) (Marks, 1999), which in this case is a power system.

Figure1.2 Typical substation where sensors are deployed.

The following sub problems was solved:

1.4.4.2 Objective 2

A review of technology (section 1.1.2 , 1.1.3 and 1.2 above) suggests that the four different interferometric sensor configurations, namely the Michealson, Mach Zehnder, Sagnac and Fabry-Perot interferometers, have been most popular in fibre-optic sensor development. Since the Fabry Perrot technique have not been applied to this application it was seen as a viable research objective to develop a sensor head based on this technique. Since electrical parameters were the intended measurands, such a sensor would have to be wideband (Murphy,1991), and for ruggedness, an EFPI instead of an IFPI (Kahn,1999;Claus, 1997). This leads to the following objective i.e.

- the development of a complete model of a wide-band extrinsic Fabry-Perot interferometric (EFPI) sensor system, along with the development of all the associated equations.

This would serve as the generic main sensor element in line with the first objective.

The model had to provide an insight into the modulation of signal responses and appropriate demodulation techniques. Certain hardware and software may then be specified that was required to implement a system that was capable of processing the EFPI sensor signals over the spectrum of a wideband source. If this was achieved it was then also possible to specify and develop the interfaces and the associated software necessary to interconnect the optical fiber sensor system to a network of sensors, which may include sensors having digital outputs also.

1.4.4.3 Objective 3

Having achieved the development of a complete model of a wide-band extrinsic Fabry-Perot interferometric (EFPI) sensor system, it would then be possible to

- derive parameters for the development of real time optical fibre sensors for the measurement of current and voltage in high voltage applications.

1.4.4.4 Objective 4

The design and modeling results thus obtained from objectives 2 and 3 forms part of a larger vision of alternative methods for the characterization of power measurements in a distribution network as stated in 1.3.2 and 1.3.3 previously. This prompted as part of this research a requirement to

- analyse, model and develop techniques to multiplex and network the sensors.

It was foreseen that the technical barriers analyzed in this project would be similar to that of multiplexed communications systems (Arditty & Puech, 1981). The primary limit that would need careful assessment was the number of sensors one can multiplex on an optical fibre network (Feher 1981). It was envisaged herewith that a large-scale sensor network would be created that could be interfaced to standard control algorithms.

1.4.4.5 Delineation

The research does not deal with the control algorithms and the actuation part of the newly proposed network.

1.5 Organization of the Dissertation

This dissertation was organized in the following chapters.
Chapter 2 deals with optical electromagnetic principles pertaining to this study. In order for us to fully appreciate the development of optical electromagnetics for sensors or light waves for sensors, dissertation start with Maxwell's equations and derive pertinent relationships from that.

In Chapter 3 the dissertation analyses the theoretical basis of the Fabry Perot etalon and use this as the basis to develop a model for a generic real time sensor for HV applications later on.

Chapter 4 builds on the principles out lined in chapters 2 and 3. The optical wave is confined to an optical fibre and what follows is a development of a novel light beam propagation model, which can be numerically implemented for designing the sensors. In the design of sensors for a large system such as the national grid, the modelling of the waveguide structure for developing generic sensor deployment and sensor data telemetry become important. This play a role in shaping the assumptions for multiplexing techniques, as well as the Fabry Perrot sensor heads that make use of electro-optic effects for voltage and current measurements, which is an essential consideration in this research.

In Chapter 5 the signal response, and the signal processing techniques for the non-monochromatic lightwave extrinsic Fabry-Perot interferometric (EFPI) sensor system is presented. Equations are derived to model the behavior of the non-monochromatic lightwave EFPI sensor system, which provide an insight into the modulation of the signal responses and their demodulation techniques, applicable for digital signal processing to be applied to the sensor. With this absolute value of the EFPI gap measurable, it is proved that the digital data capture is possible and may be algorithmically implemented by means of digital signal processing techniques. The EFPI sensor developed in this application is for the measurement of current in high voltage applications.

It was a challenge to find out the value of the External Fabry Perot Interferometer air gap length g, from the complex signal response of the non-monochromatic lightwave EFPI sensor system proposed for the generic current sensor. This is largely the topic of concern in Chaper 6. It is known that due to the Gaussian profile of a broadband optical source, the shape of the signal response is somewhat Gaussian, but modulated with the fringe pattern, including peaks and troughs. With the increase of the EFPI gap, the number of fringe peaks within the same wavelength range, of the signal response, gets increased, decreasing the distance (in terms of wavelength) between adjacent fringe peaks. Also, the non-monochromatic lightwave EFPI sensor system has a signal response where the frequency of occurrence of fringe peaks decreases gradually towards the higher end of the wavelength values, i.e., there is a chirp in the frequency of the fringe pattern, distancing any two adjacent fringe peaks further for larger values of wavelengths. In

this chapter there are presented several methods in to process this complicated signal response of the non-monochromatic lightwave EFPI sensor system, to find the EFPI gap length *g*, and as such any measurand (in this case current) that relates to that.

The previous development resulted in a rudimentary but new real time optical current sensor. In chapter 7 the characteristics of optical current sensors, specifically for relaying applications where measurement of fault-level currents may be required are discussed.

Chapter 8 introduces sensor telemetry for intelligent systems using the code division multiplexing techniques commonly employed in cellular telephone networks . In this chapter, this code division multiplexing is explored with the idea of expanding it to a more desirable large scale sensor network using optical fibre for applications in electrical energy distribution systems.

In order to network many sensors as discussed in Chapter 8, the study is taken further in Chapter 9 with an exploration of successful multiplexing methods and multiplexing algorithms that have been used on same-signal devices. Code division multiplexing has been used to multiplex same-signal communications devices for some time. Closely related research has resulted in the multiplexing of fiber optic sensors onto the same network. Given the enormity of the work that has in the process of this research transpired, this makes sense. In this chapter, this same-signal multiplexing work is explored with the idea of expanding it to a more desirable mixed-signal network, for the optical fiber sensor design for large networks which is part of the objectives of this dissertation.

Chapter 10 follows as a logical continuation of chapter 9. One of the prime aims of this thesis was to model the multiplexing of different optical fiber and other electrical sensor signal sources using a software and signal processing approach in a large (smart) network. An analysis was performed to determine the issues involved in multiplexing the different sensor signal sources, and how those issues could be resolved using good software design. The systems analysis also determined the correct operating parameters.

Chapter 11 discuss the experimental development. The proof of this networked sensor system is, of course, with the experimental effort to see what results can be obtained when bread boarded hardware and software were combined together and tested. In performing the experimentation, two distinct sensors were placed in the optical fibre communications system in such a way that they had their respective signals sent to the same fibre. The codes were generated using standard flip flop registers and the signals received at the detector were analysed with Nebuweb software specifically designed to receive the different sensor signals.

When considering the evolution of a smart system of the sort described in this dissertation, one must consider the results when the system is expanded. This is the topic of chapter 12. The primary limit is the number of sensors, and if the system is expanded beyond what was demonstrated, i.e. the two fiber optic and one digital interface sensors, other limitations come into play. Previously the desire is to have a large system of optical fiber and mixed signal sensors in the system was expressed. These limitations include bit error rate limitation on sensor resolution, time jitter, number of codes, physical device limitation, response time, and system topology and is discussed in this chapter, which essentially forms an analysis of results.

Chapter 13 details the conclusions of the dissertation, namely how the objectives was achieved, and indicates future applications and enhancements.

The appendices provide some of the firmware and software that was developed using Nebuweb's platforms, for acquiring data and processing signals for the system. Also included are the Matlab simulation codes for the system models and data analysis.

Chapter 2

OPTICAL ELECTROMAGNETIC PRINCIPLES PERTAINING TO THIS STUDY

2.1 Introduction

To fully appreciate the development of optical electromagnetics for sensors, or lightwaves for sensors, we start with the work and contribution of James Clark Maxwell, who theorised in 1864 that light waves are electromagnetic in nature (Culshaw,1995). In a vacuum, electromagnetic waves are a combination of an oscillating electric field E and magnetic induction field B(Lorrain & Corson, 1979). The dynamics of these fields are governed by what is known as Maxwell's equations.

2.2 The Helmholtz equation

When the field is excited by an alternating source, a special case in electromagnetic theory occurs to waves in a confined waveguide (Born & Wolfe, 1975). In fact this sort of analysis is useful for periodic fields, through resolution to frequency components by Fourier analysis (Yevick, 1994). Working from Maxwell's equations for linear, isotropic non-dispersive materials the chapter start the derivations from first principles. When electromagnetic waves propagate in a medium, the electric (E) and magnetic induction fields (B) interact with the molecules. The result is that these fields are modified and also known as the electric displacement field D and the magnetic field H. It is a well known technique in electrical engineering derivations to use E instead of D (Lorrain & Corson, 1979), and this will be adhered to in this dissertation.

$$\frac{\partial \overline{H}}{\partial t} = -\frac{1}{\mu} \nabla \times \overline{E} \qquad (2.1)$$

$$\frac{\partial \overline{E}}{\partial t} = -\frac{1}{\varepsilon}\nabla \times \overline{H} - \frac{\sigma}{\varepsilon}\overline{E} \tag{2.2}$$

$$\nabla \cdot \overline{H} = 0 \tag{2.3}$$

$$\nabla \cdot \overline{E} = \frac{\rho}{\varepsilon} \tag{2.4}$$

All the quantities are assumed to be sinusoidal. Every quantity can be expressed in terms of its magnitude and relative phase. A complex or phasor quantity is used to represent each quantity in this way. For example a quantity A, which may be a function of space and time, is written as $Ae^{j\omega t}$. A is now a complex quantity that is not now a function of time but represents a sinusoidal variation with time. It signifies a magnitude (its modulus) and phase delay (its argument).

Substituting the sinusoidal terms into the equations above results in the following

$$j\omega\overline{H} = -\frac{1}{\mu}\nabla \times \overline{E} \tag{2.5}$$

$$j\omega\overline{E} = -\frac{1}{\varepsilon}\nabla \times \overline{H} - \frac{\sigma}{\varepsilon}\overline{E} \tag{2.6}$$

$$\nabla \cdot \overline{H} = 0 \tag{2.7}$$

$$\nabla \cdot \overline{E} = \frac{\rho}{\varepsilon} \tag{2.8}$$

Further simplifications can be made by regarding equations (2.5) and (2.6) as simultaneous equations. Taking the curl of both sides of equation (2.5) gives

$$j\omega\nabla\times\overline{H}=-\frac{1}{\mu}\nabla\times\nabla\times\overline{E} \tag{2.9}$$

Substituting $\nabla\times E$ from equation (2.6) gives

$$j\omega(j\omega\varepsilon\overline{E}+\sigma\overline{E})=\frac{1}{\mu}\nabla\times\nabla\times\overline{E} \tag{2.10}$$

or

$$\sigma\mu\overline{E}-\omega^2\varepsilon\mu\overline{E}=\nabla\times\nabla\times\overline{E} \tag{2.11}$$

Using the general identity

$$\nabla\times\nabla\times\overline{A}=\nabla(\nabla\cdot\overline{A})-\nabla^2\overline{A}$$

We have

$$\nabla\times\nabla\times\overline{E}=\nabla(\nabla\cdot\overline{E})-\nabla^2\overline{E}$$

[Note that $\nabla^2\,\mathbf{A}=\nabla(\nabla.\,\mathbf{A})$.]

Substituting the result of equation (2.8) gives

$$\nabla\times\nabla\times\overline{E}=\nabla\frac{\rho}{\varepsilon}-\nabla^2\overline{E}$$

which, when substituted into equation (2.11) gives the following

$$\sigma\mu\overline{E}-\omega^2\varepsilon\mu\overline{E}=\nabla\frac{\rho}{\varepsilon}-\nabla^2\overline{E} \tag{2.12}$$

A similar development, working from equation (2.6) gives

$$-\omega^2\mu\varepsilon\overline{H} = \nabla^2\overline{H} + j\omega\mu\sigma\overline{H} \tag{2.13}$$

In a source-free region, equations (2.12) and (2.13) become

$$\nabla^2\overline{E} + \omega^2\mu\varepsilon\overline{E} = 0 \tag{2.14}$$

and

$$\nabla^2\overline{H} + \omega^2\mu\varepsilon\overline{H} = 0 \tag{2.15}$$

By putting $k = \omega\sqrt{\mu\varepsilon}$ the equation become

$$\nabla^2\overline{H} + k^2\overline{H} = 0 \tag{2.16}$$

and

$$\nabla^2\overline{E} + k^2\overline{E} = 0 \tag{2.17}$$

the components of **E** and **H** all satisfy what is known as the Helmholtz equation. We will look at more detail in the solution of these equations in the next section.

2.3 Boundary Conditions

Maxwell's equations can be further restated (Guenther, 1990) as follows in order to facilitate the development of a model for a generic sensor for applications in a sensor network.

$$\nabla \times \overline{B} - \varepsilon_0 \mu_0 \frac{\partial \overline{E}}{\partial t} = \mu_0 J_m \qquad (2.18)$$

$$\nabla \times \overline{E} = -\frac{\partial \overline{B}}{\partial t} \qquad (2.19)$$

$$\nabla \cdot \overline{E} = \frac{\rho_+ + \rho_b}{\varepsilon_0} \qquad (2.20)$$

$$\nabla \cdot \overline{B} = 0 \qquad (2.21)$$

Time harmonic fields in which all field vectors have a time dependence expressed as $e^{j\omega t}$ are now assumed for the rest of this chapter. In linear isotropic media the electric field vector, E, and the electric displacement vector, D, are connected by the simple linear relationship

$$\overline{D} = \varepsilon \overline{E}, \ldots\ldots \varepsilon = \varepsilon_0 \varepsilon_r \qquad (2.22)$$

where ε_0. is the permittivity of a vacuum and ε_r is the relative permittivity.

In optics the dielectric properties of a material are conventionally characterized in terms of its refractive index,

$$n = \sqrt{\varepsilon_r}$$

The relation between the magnetic field, H, and the flux density, B, is similarly given by

$$\overline{B} = \mu \overline{H}, \ldots \mu = \mu_0 \mu_r \qquad (2.23)$$

and was seen before .

Here μ_0 is the permeability of free space and μ_r is the relative permeability.Maxwell's equations must often be solved in situations where discontinuities of permittivity are encountered. This is particularly true in waveguide problems where Maxwell's equations are not solved in free space (Lorrain & Corson,1979).

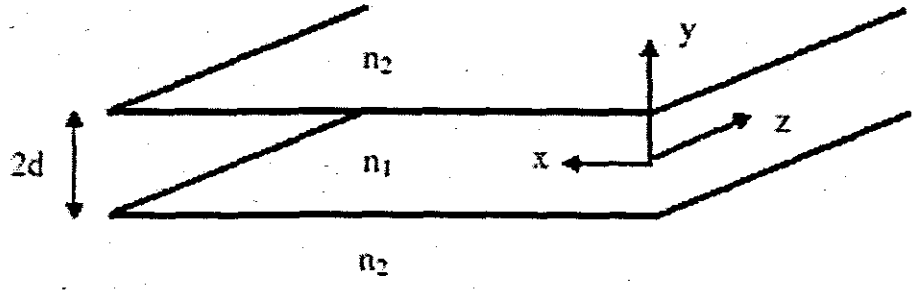

Figure 2.1 Boundaries between different indices of refraction

At a boundary between two media distinguished by the indices 1 and 2, the conditions on the electric field components parallel (t) and normal (n) to the dielectric interface are

$$E_{1t} = E_{2t}$$
$$\varepsilon_1 E_{1n} = \varepsilon_2 E_{2n} \qquad (2.24)$$

Similarly, in non magnetic materials, the boundary conditions on the magnetic field components parallel and normal to the surface are

$$H_{1t} = H_{2t}$$
$$H_{1n} = H_{2n} \qquad (2.25)$$

From Maxwell's equations, a single equation for the electric field in a general dielectric waveguide structure with a refractive index distribution $n=n(x,y,z)$

can be derived by eliminating H between equations (2.18) and (2.19). Replacing all time derivatives by $j\omega$. this gives

$$\nabla\times\nabla\times\overline{E}=\omega^2\varepsilon\mu\overline{E}=k^2\overline{E} \tag{2.26}$$

where

$$k(x,y,z)=\omega\sqrt{\varepsilon\mu}=\frac{2\pi n(x,y,z)}{\lambda} \tag{2.27}$$

and λ is the free-space wavelength. By taking the divergence of the extreme left and right hand sides of equation (2.9), it is found that

$$\nabla\bullet\overline{E}=\frac{\overline{E}\nabla k^2}{k^2} \tag{2.28}$$

Using the identity $\nabla\times\nabla\times\equiv\nabla\nabla-\nabla^2$ and substituting equation (2.11) into equation (2.9) reduces the vector wave equation for the electric field to

$$\nabla^2\overline{E}+\nabla\left(\frac{\overline{E}\cdot\nabla\varepsilon}{\varepsilon}\right)+k^2\overline{E}=0 \tag{2.29}$$

Similarly, a wave equation for the magnetic field may be derived by eliminating E from equations (2.3) and (2.4) to give

$$\nabla^2\overline{H}-k^2\nabla\left(\frac{1}{k^2}\right)\times\left(\nabla\times\overline{H}\right)+k^2\overline{H}=0 \tag{2.30}$$

2.4 Plane Electromagnetic Waves in Optical Fibre

Considering how the wave propagation in an isotropic medium occurs (Yevick, 1994), and thus eliminating H and D from Maxwell's two "curl" equations, it is found that

$$\nabla\times\overline{B}=\varepsilon\mu\frac{\partial\overline{E}}{\partial t} \tag{2.31}$$

$$\nabla\times\overline{E}=-\frac{\partial\overline{B}}{\partial t} \tag{2.32}$$

Combining the above two equations,

$$\nabla\times\nabla\times\overline{E}=-\frac{\partial}{\partial t}\nabla\times\overline{B}=-\varepsilon\mu\frac{\partial^2\overline{E}}{\partial t^2} \tag{2.33}$$

$$\nabla\times\nabla\times\overline{E}=\nabla(\nabla\bullet\overline{E})-\nabla^2\overline{E}=-\nabla^2\overline{E} \tag{2.34}$$

$$\nabla^2\overline{E}=\varepsilon\mu\frac{\partial^2\overline{E}}{\partial t^2}=\frac{\varepsilon_r\mu_r}{c^2}\frac{\partial^2\overline{E}}{\partial t^2}=\frac{1}{v^2}\frac{\partial^2\overline{E}}{\partial t^2} \tag{2.35}$$

where $1/c^2 = \varepsilon\mu$ and c is the speed of light in a vacuum and v is the speed of light in the medium. The refractive index is defined as

$$n\equiv\sqrt{\varepsilon_r\mu_r}$$

and so

$$v = \frac{c}{\sqrt{\varepsilon_r \mu_r}} \tag{2.36}$$

Consider the wave equation in Cartesian coordinates,

$$\frac{\partial^2 \overline{E}}{\partial x^2} = \frac{1}{v^2}\frac{\partial^2 \overline{E}}{\partial t^2} \tag{2.37}$$

In one dimension, the wave equation has solutions of which the simplest example is a plane wave in an unbounded medium,

$$\overline{E}(\overline{r}, t) = \mathrm{Re}\, E_0 \overline{e}_1 e^{j(\overline{k}\bullet\overline{r}-\omega t)} \tag{2.38}$$

Here **k** is the propagation vector (real), E_0 is the amplitude (which can be complex) and $\mathbf{e}_1$ is the complex polarization vector normalized by

$$\overline{e}_1 \bullet \overline{e}_1^* = 1 \tag{2.39}$$

so that

$$\nabla \bullet \overline{E} = 0 = Re\, E_0 (j\overline{k} \bullet \overline{e}_1) e^{j(\overline{k}\bullet\overline{r}-\omega t)} \tag{2.40}$$

We will often omit "Re", leaving it implicit.

Therefore

$$\overline{k} \bullet \overline{e}_1 = 0 \tag{2.41}$$

$$\nabla \times \overline{E} = \frac{\partial \overline{B}}{\partial t} \text{ or } \frac{\partial \overline{B}}{\partial t} = -Re\, E_0 (j\overline{k} \times \overline{e}_1) e^{j(\overline{k}\bullet\overline{r}-\omega t)} \tag{2.42}$$

Integrating with respect to time,

$$\overline{B} = \mathrm{Re}\, E_0 \frac{\overline{k} \times \overline{e}_1}{\omega} e^{j(k \cdot r - \omega t)} \tag{2.43}$$

Let us define $\mathbf{k_u} = \mathbf{k} \div |\mathbf{k}|$ (unit vector)

$\mathbf{e_2} = \mathbf{k_u} \times \mathbf{e_1}$ (which can be complex) (2.44)

Evidently, for a complex orthonormal triad.

$$\mathbf{k_u}\, \mathbf{e_1} = \mathbf{k_u}\, \mathbf{e_2} = \mathbf{e_1}\, \mathbf{e_2} = 0 \tag{2.45}$$

We can write , $\overline{B}(r,t) = -\mathrm{Re}\, B_0 \overline{e}_2 e^{j(\overline{k} \cdot \overline{r} - \omega t)}$ (2.46)

Where

$$B_0 = \frac{kE_0}{\omega} \tag{2.47}$$

From Maxwell's equation (2.31) we have

$$B_0 j\overline{k} \times e_2 = \varepsilon\mu(-j\omega) E_0 \overline{e}_1, \tag{2.48}$$

of magnitude

$$B_0 = \frac{\omega \varepsilon E_0}{k}$$

We have two equations relating $\frac{B_0}{E_0}$

Hence,

$$\omega^2 = \frac{k^2}{\varepsilon\mu} = \frac{c^2 k^2}{\varepsilon_r \mu_r} = k^2 v^2 \tag{2.49}$$

The velocity of light decreases as it passes into a denser medium because of the above relationship.

2.5 Jones and Stokes Vectors

2.5.1 Jones Vector

We will assume the direction of propagation is in the *z*-direction

$$E_x(z,t) = \mathrm{Re}\, E_0 a e^{j(\bar{k}\bullet\bar{r}-\omega t)} \tag{2.50}$$

$$E_y(z,t) = \mathrm{Re}\, E_0 b e^{j(\bar{k}\bullet\bar{r}-\omega t)} \tag{2.51}$$

The electric vector thus has the following form (Haus, 1984) when propagating through an isotropic medium,

$$\bar{E} = \begin{pmatrix} A_x e^{j\delta_x} \\ A_y e^{j\delta_y} \end{pmatrix} e^{j(\bar{k}\bullet\bar{r}-\omega t)} \tag{2.52}$$

Here A and δ are the amplitude and phase respectively for each of the x and y components and are real. The x and y components will in general have different phases to admit the possibility of a previous interaction with anisotropic media. This is the Jones vector representation of the electric field. In this simple description of light, it is assumed to be monochromatic, coherent and perfectly polarized. As the electric vector propagates in space, it will rotate in space according to the difference in phases. Plotting the electric vector parametrically as a function of time, results in various possibilities for the polarization depending on the phase difference and amplitude ratio. If E_x and E_y will have the same phase, and the wave will be linearly polarized.

In Figure 2.1 several possibilities of this polarization is shown

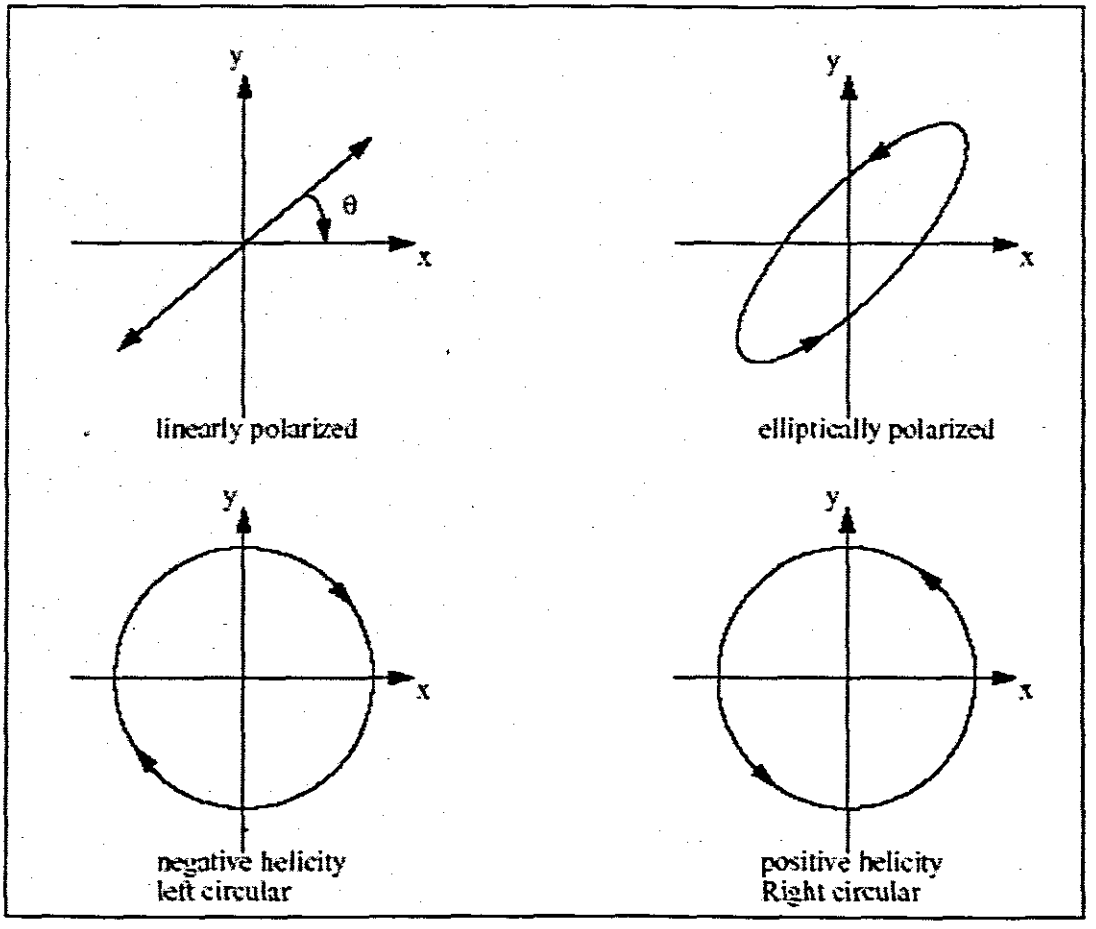

Figure 2.1 Polarization of lightwaves confined to optical fibre.

2.5.2 Unpolarized Light

When light is unpolarized, the radiation is a random mixture of two independent components with equal amplitudes,

$$|E_x|^2 = |E_y|^2 \tag{2.53}$$

This is true for whatever two orthonormal basis vectors are chosen.

2.5.3 Stokes Vector

In addition to the Jones representation for the phase and magnitude of the electric vector, an alternative representation (Haus, H. A., 1984) is the Stokes vector,

$$\overline{S} = \begin{pmatrix} S_0 \\ S_1 \\ S_2 \\ S_3 \end{pmatrix} = \begin{pmatrix} \left\langle |E_x|^2 + |E_y|^2 \right\rangle \\ \left\langle |E_x|^2 - |E_y|^2 \right\rangle \\ \left\langle 2\,\mathrm{Re}(E_x \cdot E_y) \right\rangle \\ \left\langle 2\,\mathrm{Im}(E_x \cdot E_y) \right\rangle \end{pmatrix} = \begin{pmatrix} \left\langle A_x^2 + A_y^2 \right\rangle \\ \left\langle A_x^2 - A_y^2 \right\rangle \\ \left\langle 2A_x A_y \cos(\delta_y - \delta_x) \right\rangle \\ \left\langle 2A_x A_y \sin(\delta_y - \delta_x) \right\rangle \end{pmatrix} \tag{2.57}$$

This representation in practice is often more useful than the Jones representation even though it looks more complicated. For monochromatic, perfectly polarized light, the components are related by,

$$S_0^2 = S_1^2 + S_2^2 + S_3^2 \tag{2.58}$$

Equation (2.58) is true only for perfectly polarized, monochromatic light. In practice, there will be some dispersion over a range of frequency or the light will be depolarized or randomly polarized. For all these cases, the amplitude and phase will be functions of time. The components of the Stokes vector thus represent time averaged (eg. $\langle ... \rangle = \frac{1}{T}\int_0^T ...dt$) quantities over a time T long enough to give constant values,

For example, if the intensity is defined as,

$$I = S_0 + \left\langle |A_x|^2 + |A_y|^2 \right\rangle \tag{2.59}$$

The consequence of dispersion is that the polarization properties of the electric vector will fluctuate randomly in time. The parametric mapping of the electric vector will produce blurred contours and the light will be partially or randomly polarized. If the light shows no preference to a particular polarization state, it is unpolarized. An example is natural or sunlight. For this case the Stokes vector is

$$\overline{S} = (S_0, 0, 0, 0) \tag{2.60}$$

The Stokes vector describing quasi-monochromatic light has elements that are time averaged quantities and the equality of Equation (2.58) must be replaced by

$$S_0^2 \geq S_1^2 + S_2^2 + S_3^2 \tag{2.61}$$

It should be noted that in many experimental situations, depolarization can readily occur and care must be taken to either account for it or minimize it (Kim & Ryu, 1996)(Li et al,1998). The most common source of depolarization in optical measurement is multiple scattering by such systems as dense suspensions or liquid crystals.

2.6 Numerical Solution

Clearly the key to finding sinusoidal (or periodic) solutions to electromagnetic problems is through the solution of the Helmholtz equation. The Helmholtz equation can be solved analytically only for simple domains. In general it is necessary to find a numerical solution to assist with modeling and development of specific elements in the optical fibre sensor.

The finite element method , and finite difference method are traditional methods of solution. In these methods the mesh of the electromagnetic domain is required. In subsequent chapters, development of a model for light beam propagation and a solution to the Helmholtz equation in optical fibres for applications in novel voltage and current transducers are shown by using a different technique.

Chapter 3

ANALYSIS OF FABRY PERROT ETALON INTERFEROMETRY AND ELECTRO-OPTIC EFFECTS SPECIFIC TO THE SENSOR DEVELOPMENT.

3.1 Introduction

This chapter presents an analysis of Fabry Perrot etalon interferometry and electro-optic effects that are specific to voltage and current sensor development. The Fabry-Perot interferometer was devised by Charles Fabry (1867-1945) and Alfred Perot (1863-1925) and was used originally to measure wavelengths with high precision and to study the fine structure of spectral lines. A Fabry-Perot interferometer consists essentially of two optically flat, partially reflecting plates of glass or quartz with their reflecting surfaces held accurately parallel. If the plate spacing can be mechanically varied, the device is called an interferometer, whereas if the plates are held fixed by spacers, it is called an etalon.

The Fabry-Perot Interferometer employs multiple beam interference to produce a sharp interference pattern of very high resolution (of the order of nanometres). The apparatus, invented in 1896, has played considerable role in high-resolution spectroscopy, and the majority of investigations of hyperfine structure have been made by means of the Fabry-Perot etalon and the photographic method. For a long time the apparatus was very little developed and its use was limited to this kind of investigation. It was not realised until the early 1950's that it could be used with success outside the photographic region, and over a large range of resolutions; considerable progress, both theoretical and practical have been made.

The decade thereafter saw the birth of the first laser. The idea of such an optical amplifier was first theorised by Einstein in 1916. He first predicted the existence of a new radiative process called *stimulated emission*. However, it was not until 1954 that his theory was tested, when C.H. Townes and co-workers developed a microwave amplifier based on stimulated emission of radiation (maser). This was adopted to the visible region and in 1960 T. H. Maiman built the first laser (light amplification by the stimulated emission of radiation) using a ruby crystal as an amplifying medium. Very shortly after, Javan and associates developed the first He-Ne laser which emits light in the visible and infrared regions. Several other lasers were created following this, also using a gas as a medium, emitting light from various parts of the visible spectrum. For a greater part of the 1960's the laser was considered "a solution in search of a problem" as it had no great practical use at the time. This can be compared to the discovery of Bose-Einstein condensates lately. Yet in the 1970's and 80's it became a unique source of intense, coherent light. Great developments ensued as CD-players and other optical devices became mainstream. The laser based on the Fabry Perot resonator, has revolutionised optics and the photonics industry, and given new life to an old science. This chapter will analyze the theoretical basis of the Fabry Perot etalon which is used in the development of a model for a generic real time sensor for high voltage applications in subsequent chapters.

3.2 Theory of Multiple-Beam Interference

The analysis of open resonators consisting of two parallel orthogonal parallelepiped conductors has been among the first to be carried out by computer techniques, approximately 40 years ago (Fox &Li,1961). The semi-open nature of the parallel plate resonator eliminates large number of possible modes, which would be rapidly damped by the radiation from the open sides (Schawlow & Townes, 1958), keeping only longitudinal resonances. This fact has played an essential role in the development of laser systems at optical frequencies and the construction of active quantum electronic devices. The system of parallel plate reflectors has been used for very long in the classical Fabry-Perot interferometer (Jenkins & White, 1957) and this is why it is

usually referred to as Fabry-Perot resonator. Indeed, Fabry-Perot interferometers of a metal-dielectric-metal configuration have been widely used as bandpass optical filters and laser resonators (Wait, 1962) (Born & Wolf, 1980)(Haus,1984). Recently, there has been a continuously increasing interest of using Fabry-Perot structures as a wavemeter at microwave and millimetre wavelength frequencies (McCleary et al, 1994) (Sanagi et al,1996) (Dryagin et al, 1996) (Fuji et al, 1996), as well as to determine the material properties of high temperature superconductors (De Melo et al, 1995.) (Mourachkine & Barel, 1995) (Gevorgian et al, 1996) (Feng et al, 1996) (Farber E et al,1996) (Roan & Zaki, 1997). Similar open type structures are proposed to be used at sub-millimetre wavelengths where, contrary to the optical wavelengths, the resonator dimensions are comparable to the operation wavelengths. In this case, it is required to compute the resonance properties of low order modes in the Fabry-Perot type structures. The same statements are valid for optical microresonators where, again, low order modes are employed. The following paragraphs proceed to discuss this theory in order to derive a Fabry Perot model for real time applications in a sensor scenario.

The simplest Fabry-Perot Interferometer consists of two parallel partially reflective plates as shown in figure 3.1. When light is incident on these plates, some of the light is reflected and some is transmitted through the surface.

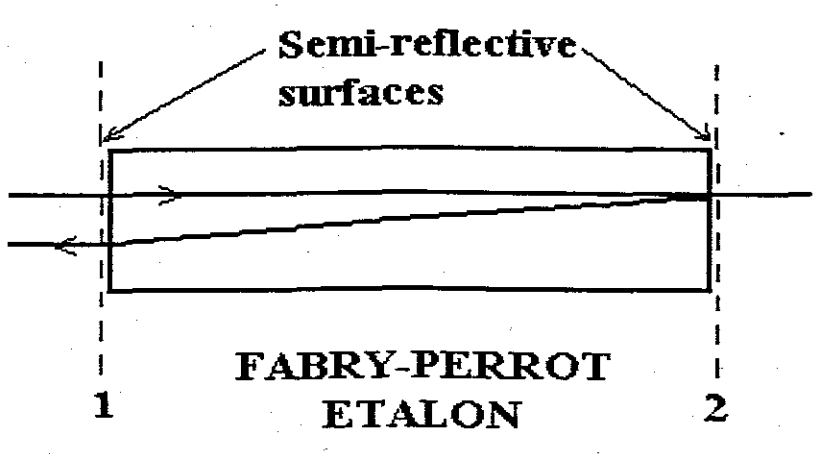

Figure 3.1 The Fabry Perrot etalon

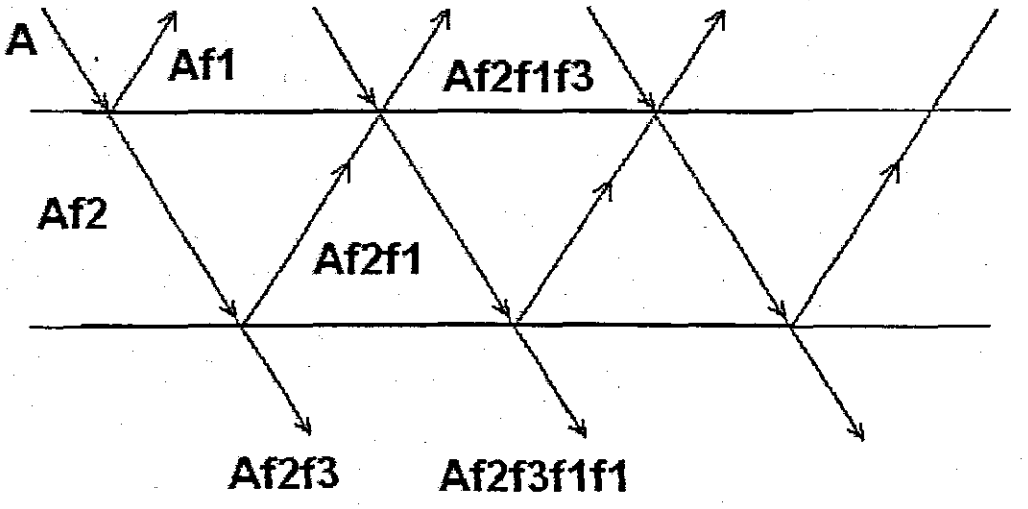

Figure 3.2 Fabry Perrot parallel plate resonator

Consider a narrow monochromatic beam from a source S of amplitude A, with an incident angle θ, as in figure 3.2

Multiple reflection occurs between the plates. The phase difference δ , given by successive reflected beams is

$$\delta = 2n_2 kg \cos\theta \qquad (3.1)$$

where $k = 2\pi/\lambda$, (Guenther (1990))

and n is the refractive index with g as the resonator gap length.

The reflection coefficient of the dielectric layer is defined as $r = f_1$ and the reflectivity of the layer is defined as r_2.

The transmitted amplitudes E of the various reflected waves form a geometric progression in terms of reflectivity.

$$E; Er^2; Er^4; Er^6 .... \qquad (3.2)$$

Each transmitted wave will have a constant phase difference relative to its neighbour, given by

$$\delta = (4\pi g n_2 \cos\theta t)/\lambda \qquad (3.3)$$

The nth transmitted wave is of the form $Er^2 ne^{j\delta n} = r^2 nAf_2 f_3 e^{j\omega t + n\delta}$.

To obtain the resultant amplitudes, E_R ,we sum over all the waves

$$E_R = E\,(1+r^2e^{j\delta}+r^4e^{j2\delta}+r^6e^{j3\delta}) \tag{3.4}$$

$$= E\,(1+r^2\cos\delta+r^4\cos 2\delta+\ldots) \tag{3.5}$$

$$+jE\,(r^2\sin\delta+r^4\sin 2\delta+r^6\sin 3\delta+\ldots) \tag{3.6}$$

Now for $-1 < x < 1$

$$\frac{1}{1-x} = 1+x^2+x^4\ldots.. \tag{3.7}$$

rewriting the left hand side:

$$\Rightarrow \frac{1}{1-r^2e^{j\delta}} = 1+r^2e^{j\delta}+r^4e^{j2\delta}+\ldots \tag{3.8}$$

$$\frac{1}{1-r^2e^{j\delta}} = \frac{1}{1-r^2e^{j\delta}}\frac{1-r^2e^{-j\delta}}{1-r^2e^{-j\delta}} \tag{3.9}$$

$$= \frac{1-r^2e^{-j\delta}}{1-r^2(e^{j\delta}+e^{-j\delta})+r^4} \tag{3.10}$$

But $e^{\pm j\delta} = \cos\delta \pm j\sin\delta$

$$= \frac{1-r^2\cos\delta + jr^2\sin\delta}{1-2r^2\cos\delta+r^4} \tag{3.11}$$

Equating real and imaginary parts,

Real:

$$\frac{1-r^2\cos\delta}{1-2r^2\cos\delta+r^4} = 1+r^2\cos\delta+r^4\cos 2\delta+\ldots \tag{3.12}$$

Imaginary:

$$\frac{r^2 \sin\delta}{1-2r^2\cos\delta+r^4} = r^2\sin\delta + r^4\sin 2\delta + r^6 \sin 3\delta... \tag{3.13}$$

The intensity of the transmitted light is

$$T_I = |E_R| = E_R E_R^* \tag{3.14}$$

which is the sum of the squares of the real and imaginary terms we have just calculated.

$$T_I \propto \frac{E[1-r^2\cos\delta + jr^2\sin\delta]}{[1-2r^2\cos\delta+r^4]^2} = \frac{E^2}{[1-2r^2\cos\delta+r^4]^2} \tag{3.15}$$

Rearranging,

$$(1+r^4-2r^2\cos\delta)^2 = (1-r^2)^2 + 4r^2\sin^2\frac{\delta}{2} \tag{3.16}$$

$$\Rightarrow T_I \propto \frac{E^2}{(1-r^2)^2 + 4r^2\sin^2\frac{\delta}{2}} \tag{3.17}$$

The intensity is a maximum when $\delta = 0;2\pi;4\pi...$

$$T_{max} \propto \frac{E^2}{(1-r^2)^2} \tag{3.18}$$

and the intensity is a mimimum when $\delta = \pi;3\pi;5\pi...$

$$T_{min} \propto \frac{E^2}{(1+r^2)^2} \tag{3.19}$$

We can write the intensity transmitted through the dielectric layer in terms of I_{max}.

$$T_I = \frac{T_{\max}}{1 + F\sin^2\frac{\delta}{2}} \tag{3.20}$$

where F is known as the *contrast,*

$$F = \frac{4r^2}{(1-r^2)^2} \tag{3.21}$$

The relative transmission of the dielectric layer can be expressed in a format called the *Airy Function.*

$$\frac{T_I}{T_{\max}} = \frac{1}{1 + F\sin^2\frac{\delta}{2}} \tag{3.22}$$

3.3 Electro-optical high voltage and current measurement techniques

3.3.1 Analysis of a possible technique of using optical fibre sensors to measure current.

A common application technique for single mode optical fiber would be that fibre is coiled in a large number of turns around a high voltage conductor that is carrying a large current. The current flowing through the conductor gives rise to a magnetic field. Consequently the field lines around such a current are cylindrical in form and they lie parallel with the fiber axis as it coils around the bar. Laser light is then launched into the fiber coil and whilst propagating through the coil of fiber the light comes under the influence of the magnetic field. In order to maintain accuracy, the laser light has to be linearly polarized. Polarized light can be defined as optical radiation with its electrical field vibrating in a specific regular mode (Rogers, 1997). The linearly polarized light comes under the action of the longitudinal magnetic field as it propagates and thus experiences the Faraday magneto optic effect. This effect rotates the direction of polarization by an amount proportional to the magnetic field and to the path length along which the field acts. The rotation caused by the

magnetic field will result in an action known as circular birefringence. Circular birefringence can be described as light that is right-hand circular polarized and will travel faster down the axis of a matching right-hand spiraled crystal structure than left hand circularly polarized light (Rogers, 1997). Hence the two circular polarization components propagate without a change of form, but are at different velocities. If these two components of light travel at different velocities, a phase difference is inserted between them and as a result of this, when recombined, they again form a resultant that is linearly polarized but rotated with respect to the original direction.

Optical fibres and some garnets are susceptible to the Faraday effect due to the large Verdet constant of it. The Verdet constant relates to the line integral of H, the magnetic field strength, to the rotation of Φ of the polarisation plane of a linearly polarised wave propagating along the line L:

$$\Phi = V\oint Hdl \qquad \textit{for one turn} \qquad (3.21)$$

$$\Phi = NV\oint Hdl \qquad \textit{for N turns} \qquad (3.22)$$

Where N = number of turns wrapped around the conductor;

V = Verdet constant of the glass fiber;

H = magnetic field strength;

l = the path length;

Φ = rotating polarisation plane;

The Verdet constant is approximately inversely proportional to the operating wavelength squared.

$$V \propto \frac{1}{\lambda^2} \qquad (3.23)$$

If the light is guided in a path that encloses a conductor, then according to Ampere's circuital law and the loop integration equation above, the rotation is due only to the number of turns of light around the conductor, N, and the total current inside the loop.

Hence:

$$\Phi = VNI \qquad (3.24)$$

where I is the current flowing through the conductor and Φ is the value to be measured by the light wave detector electronics.

3.3.2 Analysis of Magnetic Field Measurement as an indirect current sensor.

Optic fiber based sensors can be used in a number of different configurations to measure low-level magnetic fields. Sensors using the Faraday effect in optic fiber have been common for a number of years. These sensors depend on the Faraday rotation induced in fibers carrying linearly polarized light in the presence of external magnetic field. The induced Faraday rotation can be determined polarimetrically by placing the fiber coil between polarizes and measuring the optical transmission through the system (Day, 1994). The Faraday rotation can also be measured interferometrically using a Sagnac interferometer (Arditty et al, 1981). Sensitivity of Faraday-effect sensors can be increased by increasing the length of the fiber exposed to the external magnetic field. The sensors are thus bulky for ultra-low-level magnetic fields. Another commonly followed approach is to use interferometric fiber sensors to measure the strain produced in a magnetostrictive material in the presence of an external magnetic field. The principal advantage of these sensors is the much improved sensitivity, obtained without increasing the size of the sensor. A Mach-Zehnder type interferometric arrangement can be used with the magnetostrictive material geometrically coupled to the sensing arm as either a ribbon, cylinder sandwich or sputter-coated sheath (Picon et al, 1994).

Conventional means of measuring high voltages and currents rely on the measurement consuming a (hopefully) small amount of the power from the system. For instance, a resistive divider does draw some small amount of current. In power engineering, this small power is called the "burden".

Instead of directly measuring the quantity of interest, you can measure the changes in properties of some material as a result of the surrounding electrical or magnetic field. The power required for making the measurement is provided by the measuring equipment itself. One family of these techniques relies on the changes in optical properties of certain materials in electrical and magnetic fields: the Kerr effect, the Pockels effect, and the Faraday effect.

All of these techniques rely on various mechanisms by which a material rotates the polarization of light passing through. The amount of rotation depends on the electric or magnetic field. The performance is determined largely by how well it is possible to measure the change in polarization of the light. High quality polarizing film has a transmission ratio of 1000:1 between aligned and crossed.

If one wanted to measure the E field around an operating Tesla coil, as well as the waveforms, the electro-optic sensor could be mounted on a long insulated rod with fiber optic cables to send the light to and from the measuring cell. An alternate scheme could be to use a laser and appropriate prisms or mirrors to send the light out to the cell along the support and to return it to a detector. In the latter case, the sensor itself could be mounted to the high voltage terminal, with the laser and detector mounted at some distance away.

3.3.4 Kerr Cells

Birefringenge (DiDomenico, 1972) is the division of light into two components (an "ordinary" and an "extraordinary ray"), and is found in materials which have two different indices of refraction in different directions (i.e., when light entering certain transparent materials, such as calcite, splits into two beams which travel at different

speeds). Birefringence is also known as double refraction. The quantity known as birefringence is defined as

$$\Delta n \equiv n_e - n_w \tag{3.25}$$

Crystals possessing birefringence include hexagonal (such as calcite), tetragonal, and trigonal crystal classes exhibit birefringence, and are known as uniaxial materials.

The development of birefringence when an isotropic transparent substance in placed in an electric field is the main electro-optic effect behind sensors that is envisaged to measure voltage or current. It is used in constructing Kerr cells, which function as variable wave plates with an extremely fast response time, and find use in high-speed camera shutters. Because the effect is quadratic with respect to E, is sometimes known as the quadratic electro optical effect.

The amount of birefringence (as characterized by the change in index of refraction) due to the Kerr effect can be parameterized by where K is the Kerr constant (in cgs units of cm) and is the vacuum wavelength. The phase change introduced in a Kerr cell of thickness d under an applied voltage V is given by

$$\Delta n = \lambda_0 K E^2 \tag{3.26}$$

$$\Delta \phi = \frac{2\pi K \lambda V^2}{d^2} \tag{3.27}$$

Therefore Kerr effect is an anisotropic change in the index of refraction of a substance in response to an electric field. A practical implementation has the Kerr substance (often nitrobenzene, which has a very high Kerr Constant) between two crossed polarizers. The polarization of the light is rotated in proportion to the square of the E field, allowing some light to pass through the polarizers. As a shutter, the response time of the Kerr Cell is limited mainly by how fast the E field can be changed. The problems

with a Kerr Cell are: nitrobenzene is a volatile solvent which is remarkably toxic; the effect is proportional to the square of the E-field, which is no problem for a shutter application, but not as appropriate for a measurement application.

3.3.5 Pockels Cells

The Pockels effect is an electro-optical effect in which the application of an electric field produces a birefringence which is proportional to the field (Giallorenz & Bucaro, 1982.) Only crystals which lack a center of symmetry (20 out of the 32 classes) may show this effect. (These are, incidentally, the same classes which are piezoelectric). The Pockels cell is used in ultra fast shutters. For the longitudinal arrangement, the phase shift is given by Equation (3.28) where r_{eo} is the electro-optical constant measured in m/V.

$$\Delta\phi = \frac{2\pi n_0^3 r_{eo} V}{\lambda_0} \tag{3.28}$$

The Pockels effect is similar to that of the Kerr effect, except that the change in index is linearly proportional to the electric field. Substances such as KDP (Potassium Dihydrogen Phosphate), KD*P (Deuterated KDP) and LiNbO3 (Lithium Niobate) show large Pockels effects and are very popular as electro-optic modulators for laser work.

One problem with Pockels sensors is the cost of the crystals, particularly in large sizes. A small 1 cm diameter crystal suitable for turning on and off a laser beam is not particularly expensive (several hundreds of dollars), but a larger one for use as a photographic shutter would be prohibitively expensive. For a HV measuring application, the cell could be on the scale of millimeters, particularly if fiber optic cables are used.

3.3.6 Faraday Rotation

Faraday rotation is a magnetic effect. Notable in high density lead glass, the rotation is proportional to the magnetic field. A chunk of lead glass 2.4 cm thick and 5cm in diameter would need a field of .5 Tesla (5000 Gauss) to rotate the polarization 90 degrees. (This is about 10,000 ampere turns for that physical size). The rotation is proportional to the length of the optical path and to the magnetic field, so a longer piece of glass makes a more sensitive detector.

Faraday rotation does provide a handy way to measure the current in EHV or UHV power lines. A piece of lead glass (which can be quite long) is placed near the power cable and a polarized laser is used to measure the rotation. In a Tesla coil application, lead glass sensors connected by fiber optic cables could be used to measure the current at various parts of the coil. For that matter, a glass fiber of the appropriate material could be used as the sensor itself.

3.3.7 The Fabry Perrot Cavity as a current transducer

The Fabry-Perot (FP) cavity is formed as discussed above, and may be constructed by using a single mode fiber and a multimode fiber sealed inside a hollow core tube. The single mode fiber acts as the input-output fiber whereas the multimode fiber is used solely as a reflector. If the multimode fiber is replaced by a magnetostrictive material with the one side polished and acting as a reflector, the gap length will vary according to the externally applied current. The hollow core tube acts as a guide tube in addition to protecting the cavity from external elements. Light enters the single mode fiber and it is partially reflected from the first glass-air interface as R_1. The transmitted light travels through the cavity, is reflected from the second air-glass interface and enters the single mode fiber again as R_2. These reflections then interfere in the single mode fiber. The output depends on the difference in the optical path lengths traveled by the two interfering waves. The effect of subsequent reflections inside the cavity are negligible. Output intensity is approximately given by equation (3.28).

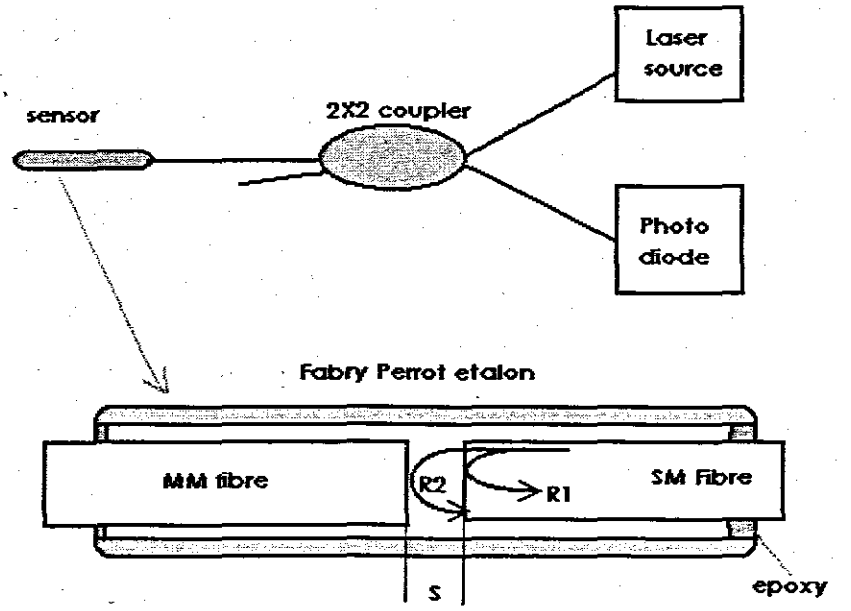

Figure 3.3 Schematic of an EFPI-based current sensor if MM fibre is replaced by magnetostrictive material.

$$I_{pd} = A^2\left[1+\frac{2ta}{a+(2g)\tan(\sin^{-1}(NA))}\cos(\frac{4s\pi}{\lambda})+(\frac{ta}{a+(2g)\tan(\sin^{-1}(NA))})^2\right] \quad (3.28)$$

where I_{pd} is the detected signal intensity, A is the reference reflection coefficient, g is the length of the air gap, t is the transmission coefficient of the air-glass interface, a is the core-radius of the fiber and NA is the numerical aperture of the single mode fiber Figure 3.4 shows the variation in the detected intensity as a function of air gap length.

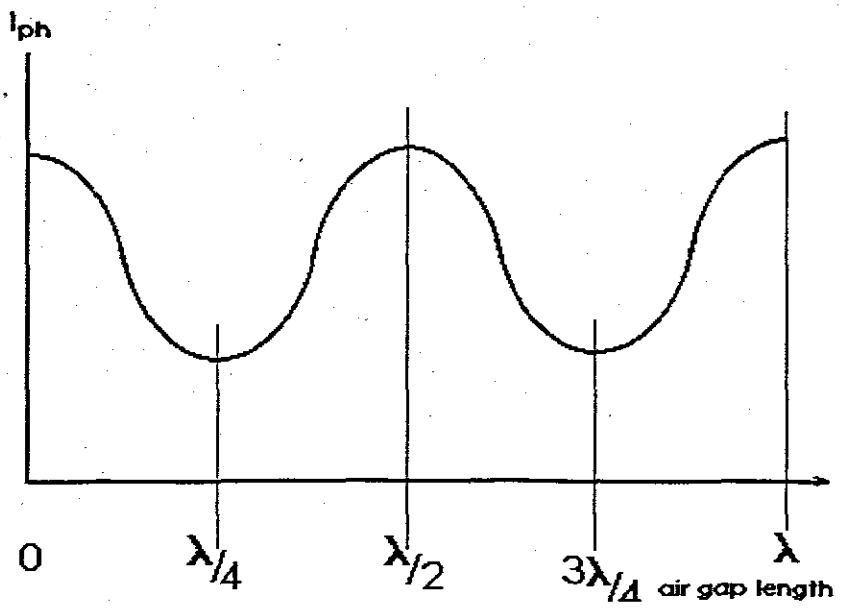

Figure 3.4 Detected intensity as a function of air gap length.

The small interaction length is the major advantage of an Fabry Perrot sensor. This gives it the ability to effectively monitor various external parameters (in this case current) as a point sensor. Since the single mode fiber carries the light signal both to and from the sensor, no separate electrical biasing is required. Hence an EFPI can be used in environments not suitable for other kinds of active sensors and can be deployed at larger distances from the laser source and demodulation circuitry without having to worry about EMI. It can be easily bonded to other materials for measurement applications and can also be embedded in composite materials. The ability of being embedded makes it an ideal candidate for smart structure and smart systems applications. A typical EFPI can have a gage length of 2 to 3 mm with an air gap separation of about 30-40 μm. It is relatively easy to fabricate, compact and light weight. An EFPI has a wide frequency response, limited only by the signal processing circuitry at the detector end. As can be seen in Figure 3.4, the variation in the output signal of an EFPI with change in the length of the air gap, is sinusoidal. Thus when the length of the air gap is any multiple of $\lambda/4$, the output is at the maximum or minimum and the sensitivity (slope of the curve at that point) is zero. The sensor thus exhibits varying sensitivity to external perturbation depending on the operating point. This

phenomenon is common to all interferometric sensors and is known as 'signal fading'. Figure 3.5 shows the signal fading phenomenon in detail.

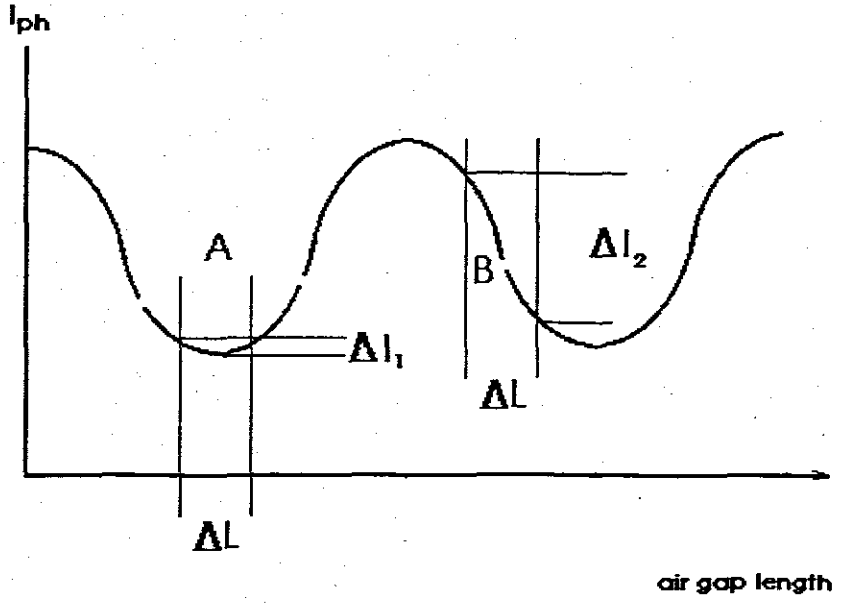

Figure 3.5 Signal fading in fiber interferometers.

As can be seen from the above figure, at operating point A, an air gap change of ΔL causes and output variation of ΔI_1. However at operating point B, the same change in air gap length causes a much larger output variation of ΔI_2. Thus, the EFPI has to be biased at the quadrature point to achieve maximum sensitivity. Moreover, this operating point has to be maintained at all times during the actual operation of the sensor. This limitation can be eliminated using a Quadrature Phase Shifted (QPS) demodulation scheme, making the sensor much more complex. Source intensity fluctuation is another important factor since it causes a change in the EFPI output without any change in the air gap length g.

3.4 Conclusion

The above sections of this chapter provided a specific theoretical basis for EFPI point sensor design and also highlighted the effects that would be of interest to the design of EFPI's to measure current or voltage. Limitations of the Fabry Perrot type sensor were discussed and presented. The limitation of air gap length g however, will be taken up further and it will be proved in subsequent chapters, can be overcome by using the real time signal processing technique which is contributed by this thesis. Hence a very sensitive and somewhat "intelligent" current sensor is proposed using this technique in the chapters that follow.

Chapter 4

DEVELOPMENT OF A MODEL FOR LIGHT BEAM PROPAGATION IN OPTICAL FIBRES FOR APPLICATIONS IN NOVEL CURRENT AND VOLTAGE TRANSDUCER DESIGN.

4.1 Introduction

Building on the principles out lined in chapters 2 and 3 we will now look at confining the optical wave to an optical fibre and develop a novel light beam propagation model which can be numerically implemented for designing the sensors. In the design of sensors for a large system such as the national grid, the modelling of the waveguide structure for developing generic sensor deployment and sensor data telemetry become important. Several waveguide types was found to be in use, but most often graded index multi-mode (GRIN) and single mode fibre were deployed. Considering the fact that we are looking at optical fibre (OF) sensors, deployed over large areas, and that this method of interrogation is not limited to simple optical time domain reflectometry (OTDR) techniques, but interferometric, it is imperative that the light beam propagation in the fibre be studied with the worst case scenario of index of refraction that varies with distance z. This will play a role in shaping the assumptions for multiplexing techniques, as well as Fabry Perrot sensor heads that make use of electro-optic effects for voltage and current measurements, which is an essential consideration in this research. The alternating direction implicit method is introduced as a numerical solution that involves a monoiterative procedure for solving multidimensional partial differential equations, and the matrices for such a solution are developed herewith.

4.2 Optical Waveguides and Light propagation

An optical waveguide is a structure that "guides" a light wave by constraining it to travel along a certain desired path. Usually the light is guided by Total Internal Reflection (TIR). Recall that TIR occurs when light is incident on a dielectric interface at an angle greater than the critical angle θ_c. A waveguide traps light when more than one TIR interface (for planar waveguides and rectangular waveguides), or an interface that surrounds the guiding region (for optical fibers) is present.

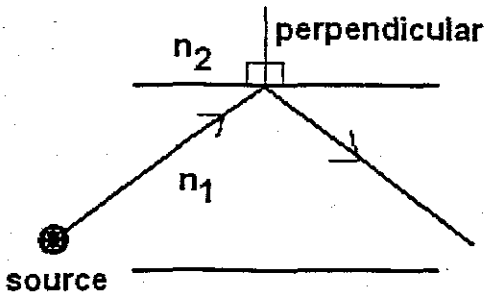

Figure 4.1: Total internal reflection

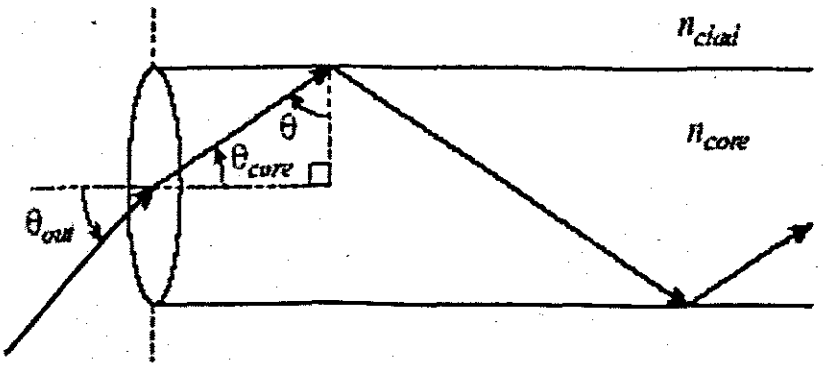

Figure4.2 : Light propagation in optical fibre

When light is shone on the end of an optical fiber, ray optics tells us which rays may be

guided. It is known that inside the fiber total internal reflection occurs only for rays with $\theta > \theta_c$. We can work backwards to see what this condition tells us about the outside ray angle θ_{out}. Snell's law requires that

$$n_{out} \sin\theta_{out} = n_{core} \sin\theta_{core}$$

but

where we use

$$\sin\theta_{core} = \cos\theta = \sqrt{1-\sin^2\theta}$$

$$\sin^2\theta + \cos^2\theta = 1$$

The largest ray angle incident on the end of the fiber that may be guided, which is denoted as $\theta^{out}{}_{max}$, corresponds to the internal angle θ that is just equal to θ_c, the critical angle.. Therefore

$$n_{out} \sin\theta_{out}^{max} = n_{core}\sqrt{1-\sin^2\theta_c} = n_{core}\sqrt{1-\frac{n_{clad}^2}{n_{core}^2}} = \sqrt{n_{core}^2 - n_{clad}^2}$$

This result is often stated in terms of an important quantity in optics called the Numerical Aperture of an optical system. In summary, if the indexes of refraction of the core and cladding of an optical fiber or waveguide is known, then we can immediately determine the numerical aperture *(NA)* of the waveguide, which tells us the largest cone of rays that may be successfully guided. Single mode fibre for instance , confines only about 80% of the optical power to the core.

We note that even though glass fibers are remarkably flexible (they truly are the optical analog of electrical wiring!), because the light is guided by total internal reflection an optical fiber or waveguide may not be bent arbitrarily tightly without allowing some or all of the light to escape from the waveguide. We will consider z axis propagation of the

electromagnetic wave in an optical fiber in developing a model. Intramodal dispersion will be accounted for in our model as the main cause of signal distortion that may have an impact on channel capacity in our application of an intelligent sensor system employing optical fiber. We will therefore consider the case of a slowly varying index of refraction with regard to the z axis in the model.

4.3 Model development

The generalized nonlinear Schrödinger equation (Marcuse, 1991) describing a propagation of signals in optical fibers is given by

$$\frac{\partial E(z,t)}{\partial z} = [D + I_p] \cdot E(z,t) \tag{4.1}$$

where E denotes the electric field of the light wave, I_p characterizes its power, z the distance along the fibre and D is the dispersion operator.

Light wave propagation is studied in classical waveguide theory by means of the z axis propagation wave, known as the Helmholz equation, defined earlier in chapter 2. This z-axis propagating wave is therefore given as

$$\frac{\partial^2 \mathrm{E}}{\partial z^2} + \nabla^2 E + k^2 n^2 E = 0 \tag{4.2}$$

where n is the refractive index and k as defined in chapter 2 equation (2.27)

Taking the square root of equation (4.2), gives:

$$\frac{\partial E(x,y,z)}{\partial z} = \pm\sqrt{\nabla^2 + k^2 n^2(x,y)}\,E(x,y,z) \tag{4.3}$$

which has a solution of the type:

$$E(x,y,z+\Delta z) = \exp\left(\pm j\sqrt{\nabla^2 + k^2 n^2(x,y)}\Delta z\right)E(x,y,z) \tag{4.4}$$

This expression can be handled to give the relationship between the z separated fields,

$$E(x,y,z+\Delta z) = \exp\left(\pm j(M+k)\frac{\Delta z}{2}\right)\exp[\pm jN\Delta z]\cdot\exp\left(\pm j(M+k)\frac{\Delta z}{2}\right)E(x,y,z) \tag{4.5}$$

where the operators M and N are given by:

$$M = \frac{\nabla^2}{k + \sqrt{\nabla^2 + k^2}} \tag{4.6}$$

$$N = k\Delta n(x,y) \tag{4.7}$$

If E is expressed by $E(x,y,z)=e(x,y,z)e^{jkz}$, for the envelope $e(x,y,z)$ the propagation is defined by

$$e_{\pm}(x,y,z+\Delta z) = \exp\left(\pm j(M+k)\frac{\Delta z}{2}\right)\exp[\pm jN\Delta z]\cdot\exp\left(\pm j(M+k)\frac{\Delta z}{2}\right)e_{\pm}(x,y,z) \tag{4.8}$$

The step propagation is, therefore, divided into three parts: a first half-step propagation through a homogeneous medium of index n_s, followed by a phase correction process due to the non homogeneity of the propagation medium and, finally, by another half-step propagation through a medium with refractive index n_s.

Using the property of the *Fourier* transform,

$$F\left[\left(\nabla^2\right)^n f\right] = \left[-\left(k_x^2 + k_y^2\right)\right]^n F[f] \tag{4.9}$$

where k_x and k_y are the frequency domain variables, equations (4.5) and (4.8) can be rewritten in the form:

$$E_F(k_x,k_y,z+\Delta z) = \exp\left(j\Delta k_z \frac{\Delta z}{2}\right)\cdot F\left\{\exp[jk\Delta n(x,y)\Delta z\cdot F^{-1}\left\{\exp\left(j\Delta k_z \frac{\Delta z}{2}\right)E_F(k_x,k_y,z\right\}\right\} \tag{4.10}$$

$$\Delta k_z = \sqrt{k_B^2 - (k_x^2 + k_y^2)} \tag{4.11}$$

The above method is also applicable in the simulation of general optical transmission devices as introduced by Feit and Fleck (Haus, 1984))in the late seventies to solve optical waveguide problems, known as the *Beam Propagation Method.* This beam propagation method has proved to be a very powerful simulation tool, making possible to determine the response of wave guiding devices to arbitrary optical inputs. The beam propagation method (BPM) is at present also the most widely used tool employed in the study of optical devices, largely owing to its numerical speed and simplicity (Yevick ,1994). Basically, it constructs a relation between the electromagnetic fields in two axially separated parallel planes, i.e., the field distribution in one plane is calculated numerically from the distribution in the preceding plane. This procedure is recursively implemented and ideally suited to embedded controller or computers, thus completing the simulation of wave propagation step by step with an arbitrary excitation. One can descretise the BPM formulas in three dimensions via the standard Crank–Nicholson scheme.

To develop the model for general application with the BPM, the Helmoltz equation can also be presented as

$$\left[\frac{\partial^2}{\partial z^2} + \frac{\partial^2}{\partial y^2} + k_0^2\left(\frac{n^2(x,y,z)}{n_0^2} - 1\right)\right]\varphi(x,y,z) = -2jk_0\frac{\partial\varphi(x,y,z)}{\partial z} \tag{4.12}$$

where φ is the generalised field strength.

A solution of this form of the Helmholtz equation can be introduced as

$$\Lambda(x,y,z')\varphi(x,y,z',z)=j\frac{\partial\varphi(x,y,z',z)}{\partial z} \tag{4.13}$$

Where z' acts as an additional co-ordinate and Λ is defined as

$$\Lambda(x,y,z')=-j\frac{\partial}{\partial z'}+E(x,y,z') \tag{4.14}$$

Here k_0 is the wave number and n_0 the cladding index of refraction and E is defined as before. The core index of refraction is given by $n_{(x,y,z)}$. We will take into account the possibility of losses in the fiber as a slow variation of n with regard to the fiber axis z. For this we assume that the ration between the spatial variation of $n_{(x,y,z)}$ and the cladding index of refraction n_0 is much smaller than one. Under this assumption the second derivative of the field with respect to z is ignored in the Laplacian operator. With this we observe the equivalence of the Helmholz equation with that of the time dependent Schrodinger equation.

The solution of equation (4.12) can be given by

$$\varphi(x,y,z)=\phi(x,y,z',z)\Big|_{z'=z} \tag{4.15}$$

Where $E(x,y,z=0)=\phi(x,y,z=0)$ is the field in the entrance to the fibre at z=0. Since Λis z independent the electric field of generalised index of refraction is given by

$$E(x,y,z)=e^{jk_0z}\left[e^{-j\Lambda(x,y,z')z}E(x,y,z=0)\right]_{z'=z} \tag{4.16}$$

As can be determined from equation (4.16) , a new Beam Propagation Method (BPM) is thereby introduced which avoids the need for introducing the longitudinal or distance operator z and coupled mode formalism,(Marcuse, 1991) (Snyder & Love, 1983) when the index of refraction is z dependent. This allows one to use the technique to calculate the propagation of light through an inhomogeneous medium by using computational methods that were originally developed for light beam propagation where index of refraction were z-independent.

4.4 Numerical solution of the model:

A discretization of the above BPM formulas in three dimensions via the standard Crank–Nicholson scheme results in an implicit relation between two axially separated parallel planes, and it requires operator inversions to complete the propagation. Yamauch (Yamauch et al,1991) proposed a three dimensional (3-D) BPM algorithm based on the alternate direct implicit method, which was a scalar algorithm with the operator inversion implemented via the alternate direct implicit method. In this chapter is further proposed a 3-D full-vectorial BPM algorithm purely based on the standard Crank–Nicholson scheme and the alternate direct implicit method for simplicity. In so doing, the proposed algorithm was of second order accuracy in the z direction, and numerical stability was also assured thanks to the pure implicit form. Because of the non-iterative nature of the alternate direct implicit method, this algorithm also has a very good performance in speed of computation in real time applications.

Starting from Maxwell's equations, the vector wave equation for the time-harmonic electric field in a linear, isotropic, and time-invariant medium is derived as shown in equations (4.1) to (4.3) where n is the refractive index as a function of position, and k_o is the wave number in vacuum. If the refractive index does not vary along the z direction, or if the variation is very slow as taken into account with the proofs in equations (4.12) to (4.16), the propagation of the electromagnetic wave is governed by two coupled equations with x and y components only.

By defining an envelope field such that $\overline{E} = \overline{E}e^{-jnkz}$ (the slowly varying envelope approximation as discussed in chapter 2), and considering the components in (4.1), we obtain

$$\left(\frac{j}{2n_0k_0}\frac{\partial^2}{\partial z^2}+\frac{\partial}{\partial z}\right)\begin{bmatrix}\overline{E}_x\\ \overline{E}_y\end{bmatrix}=\frac{-j}{2n_0k_0}\begin{bmatrix}P_{xx} & P_{xy}\\ P_{yx} & P_{yy}\end{bmatrix}\begin{bmatrix}\overline{E}_x\\ \overline{E}_y\end{bmatrix} \tag{4.17}$$

where

$$P_{xx}\overline{E}_x=\frac{\partial^2\overline{E}_x}{\partial y^2}+\frac{\partial}{\partial x}\left(\frac{1}{n^2}\frac{\partial\left(n^2\overline{E}_x\right)}{\partial x}\right)+\left(n^2-n_0^2\right)k_0^2\overline{E}_x \tag{4.18}$$

$$P_{yy}\overline{E}_y=\frac{\partial^2\overline{E}_y}{\partial x^2}+\frac{\partial}{\partial y}\left(\frac{1}{n^2}\frac{\partial\left(n^2\overline{E}_y\right)}{\partial y}\right)+\left(n^2-n_0^2\right)k_0^2\overline{E}_y \tag{4.19}$$

$$P_{xy}\overline{E}_y=\frac{\partial}{\partial x}\left(\frac{1}{n^2}\frac{\partial n^2}{\partial y}\overline{E}_y\right) \tag{4.20}$$

$$P_{yx}\overline{E}_x=\frac{\partial}{\partial y}\left(\frac{1}{n^2}\frac{\partial n^2}{\partial x}\overline{E}_x\right) \tag{4.21}$$

From equations (4.17) to (4.21) it is clear that P_{xy} and P_{yx} denote the cross coupling effects between the two transverse fields.

For simplicity, we rewrite equation(4.17) as

$$\left(\frac{j}{2n_0k_0}\frac{\partial^2}{\partial z^2}+\frac{\partial}{\partial z}\right)\overline{E}_t=\frac{-j}{2n_0k_0}\overline{PE}_t \tag{4.22}$$

which we have already seen in equation (4.12) above and which is a second-order partial differential equation describing the transverse field E_t. If we adopt the paraxial

assumption here, the second-order derivative term is dropped off, and equation (4.22) becomes the full-vectorial paraxial BPM equation

$$\frac{\partial}{\partial z}\overline{E}_t = \frac{-j}{2n_0 k_0}\overline{PE}_t \tag{4.23}$$

which is a first-order partial differential equation to be solved as an initial value problem.

We shall discretize equation (4.23) via the Crank–Nicholson scheme and evaluate it step by step with the aid of the alternate direct implicit method. Equation (4.23) can be rewritten in an alternative form

$$\frac{\partial}{\partial z}\begin{bmatrix}\overline{E}_x \\ \overline{E}_y\end{bmatrix} = \frac{-j}{2n_0 k_0}\begin{bmatrix}P_{xx} & P_{xy} \\ P_{yx} & P_{yy}\end{bmatrix}\begin{bmatrix}\overline{E}_x \\ \overline{E}_y\end{bmatrix} \equiv \begin{bmatrix}A_x + A_y & C \\ D & B_x + B_y\end{bmatrix}\begin{bmatrix}\overline{E}_x \\ \overline{E}_y\end{bmatrix} \tag{4.24}$$

where A_x and A_y denote the x-dependent and the y-dependent parts of P_{xx}, respectively, with

$$A_x\overline{E}_x = \frac{-j}{2n_0 k_0}\left(\frac{\partial}{\partial x}\left(\frac{1}{n^2}\frac{\partial\left(n^2\overline{E}_x\right)}{\partial x}\right) + \frac{1}{2}\left(n^2 - n_0^2\right)k^2{}_0\overline{E}_x\right) \tag{4.25}$$

$$A_y\overline{E}_x = \frac{-j}{2n_0 k_0}\left(\frac{\partial^2\overline{E}_x}{\partial y^2} + \frac{1}{2}\left(n^2 - n_0^2\right)k_0^2\overline{E}_y\right) \tag{4.26}$$

Similarly, B_x and B_y denote the x-dependent and the y- dependent parts of P_{yy}, respectively, with

$$B_x\overline{E}_y = \frac{-j}{2n_0 k_0}\left(\frac{\partial}{\partial y}\left(\frac{1}{n^2}\frac{\partial\left(n^2\overline{E}_y\right)}{\partial y}\right) + \frac{1}{2}\left(n^2 - n_0^2\right)k_0\overline{E}_y\right) \tag{4.27}$$

$$B_y\overline{E}_y=\frac{-j}{2n_0k_0}\left(\frac{\partial}{\partial y}\left(\frac{1}{n^2}\frac{\partial\left(n^2\overline{E}_y\right)}{\partial y}\right)+\frac{1}{2}\left(n^2-n_0^2\right)k_0\overline{E}_y\right) \tag{4.28}$$

while C and D denote the cross-coupling terms. In the semivectorial formulation the cross-coupling terms are assumed negligible, resulting in

$$\frac{\partial}{\partial z}\overline{E}_x=\left(A_x+A_y\right)\overline{E}_x \tag{4.29}$$

$$\frac{\partial}{\partial z}\overline{\mathrm{E}}_y=\left(\mathrm{B}_x+\mathrm{B}_y\right)\overline{\mathrm{E}}_y \tag{4.30}$$

Equations (4.29) and (4.30) can be individually evaluated via the standard alternate direct implicit method (Liu & Li, 1992). For equation (4.29), the discretization form becomes

$$\frac{\overline{E}_x^{n+1}+\overline{E}_x^{n}}{\Delta z}=\left(A_y+A_x\right)\frac{\overline{E}_x^{n+1}+\overline{E}_x^{n}}{2} \tag{4.31}$$

or

$$\left(1-\frac{\Delta z}{2}\left(A_x+A_y\right)\right)\overline{E}_x^{n+1}=\left(1+\frac{\Delta z}{2}\left(A_x+A_y\right)\right)\overline{E}_x^{n} \tag{4.32}$$

Implementing the alternate direct implicit method by adding second-order error terms to (32) yields

$$\left(1-\frac{\Delta z}{2}\left(A_x+A_y\right)+\left(\frac{\Delta z}{2}\right)^2A_xA_y\right)\overline{E}_x^{n+1}=\left(1+\frac{\Delta z}{2}\left(A_x+A_y\right)+\left(\frac{\Delta z}{2}\right)^2A_xA_y\right)\overline{E}_x^{n} \tag{4.33}$$

or

$$\left(1-\frac{\Delta z}{2}A_x\right)\left(1-\frac{\Delta z}{2}A_y\right)\overline{E}_x^{n+1}=\left(1+\frac{\Delta z}{2}A_x\right)\left(1+\frac{\Delta z}{2}A_y\right)\overline{E}_x^{n} \tag{4.34}$$

In so doing, it becomes not difficult to perform the operator inversion in each sub-step, and the inserted error terms do not reduce the accuracy, since the Crank–Nicholson scheme is also of second-order accuracy. But in the full-vectorial formulation the extra cross-coupling terms become an impediment to implement the alternate direct implicit method. Discretizing equation (4.24) with the well known Crank–Nicholson scheme the following is obtained

$$\frac{\overline{E}_x^{n+1}+\overline{E}_x^{n}}{\Delta z}=\left(A_x+A_y\right)\frac{\overline{E}_x^{n+1}+\overline{E}_x^{n}}{2}+C\frac{\overline{E}_y^{n+1}+\overline{E}_y^{n}}{2} \tag{4.35}$$

$$\frac{\overline{E}_y^{n+1}+\overline{E}_y^{n}}{\Delta z}=\left(B_x+B_y\right)\frac{\overline{E}_y^{n+1}+\overline{E}_y^{n}}{2}+D\frac{\overline{E}_x^{n+1}+\overline{E}_x^{n}}{2} \tag{4.36}$$

If C and D are neglected, equations (4.35) and (4.36) reduce to the semivectorial formulation discussed above. On the contrary, if C and D are considered, it is not so trivial to implement the operator inversion with the alternate direct implicit method, since and can not be inversed via the alternate direct implicit method. In (Mansour et al, 1996) , equations (4.35) and (4.36) are approximated by

$$\frac{\overline{E}_x^{n+1}+\overline{E}_x^{n}}{\Delta z}=\left(A_x+A_y\right)\frac{\overline{E}_x^{n+1}+\overline{E}_x^{n}}{2}+C\overline{E}_y^{n} \tag{4.37}$$

$$\frac{\overline{E}_y^{n+1}+\overline{E}_y^{n}}{\Delta z}=\left(B_x+B_y\right)\frac{\overline{E}_y^{n+1}+\overline{E}_y^{n}}{2}+D\overline{E}_x^{n} \tag{4.38}$$

that is CE_y^n, and DE_x^n are used to replace $C(E_y^{n+1}+E_y^n)/2$ and , $D(E_x^{n+1}+E_x^n)/2$ respectively, in order to avoid performing the operator inversion of C and D. Such treatment of the cross-coupling terms is similar to the simple Euler method, and hence is only of first-order accuracy in the z direction. Furthermore, because of the explicit form, the stability is doubtful. In fact, the algorithm of equation (4.37) and (4.38) was proposed to work together with a digital low-pass filter in order to filter out extra numerical noises in (Mansour et al, 1996). Here, we propose an alternative formulation to achieve an algorithm of second-order accuracy.

Rewrite (4.24) as

$$\frac{\partial}{\partial z}\begin{bmatrix}\overline{E}_x\\ \overline{E}_y\end{bmatrix}=\begin{bmatrix}A_x+A_y & C\\ D & B_x+B_y\end{bmatrix}\begin{bmatrix}\overline{E}_x\\ \overline{E}_y\end{bmatrix}=\left(\begin{bmatrix}A_x & C\\ 0 & B_x\end{bmatrix}+\begin{bmatrix}A_y & 0\\ D & B_y\end{bmatrix}\right)\begin{bmatrix}\overline{E}_x\\ \overline{E}_y\end{bmatrix} \tag{4.39}$$

After discretizing , we obtain

$$\frac{1}{\Delta_z}\left(\begin{bmatrix}\overline{E}_x\\ \overline{E}_y\end{bmatrix}^{n+1}-\begin{bmatrix}\overline{E}_x\\ \overline{E}_y\end{bmatrix}^{n}\right)=\left(\begin{bmatrix}A_x & C\\ 0 & B_x\end{bmatrix}+\begin{bmatrix}A_y & 0\\ D & B_y\end{bmatrix}\right)\cdot\frac{1}{2}\left(\begin{bmatrix}\overline{E}_x\\ \overline{E}_y\end{bmatrix}^{n+1}+\begin{bmatrix}\overline{E}_x\\ \overline{E}_y\end{bmatrix}^{n}\right) \tag{4.40}$$

Adopting the alternate direct implicit method, equation (4.40) becomes

$$\begin{bmatrix}\overline{E}_x\\ \overline{E}_y\end{bmatrix}^{n+1}=\left(\frac{1+\frac{\Delta}{2}\begin{bmatrix}A & 0\\ D & B\end{bmatrix}}{1-\frac{\Delta}{2}\begin{bmatrix}A & C\\ 0 & B\end{bmatrix}}\right)\cdot\left(\frac{1+\frac{\Delta}{2}\begin{bmatrix}A & C\\ 0 & B\end{bmatrix}}{1-\frac{\Delta}{2}\begin{bmatrix}A & 0\\ D & B\end{bmatrix}}\right)\cdot\begin{bmatrix}\overline{E}_x\\ \overline{E}_y\end{bmatrix}^{n}=\frac{\Gamma_3}{\Gamma_4}\cdot\frac{\Gamma_1}{\Gamma_2}\cdot\begin{bmatrix}\overline{E}_x\\ \overline{E}_y\end{bmatrix}^{n}=\Gamma_4^{-1}\Gamma_3\Gamma_2^{-1}\Gamma_1\begin{bmatrix}\overline{E}_x\\ \overline{E}_y\end{bmatrix}^{n} \tag{4.41}$$

It can be easily proven that Γ_2^{-1} and Γ_3 are interchangeable. To accomplish propagation, the electric field E is multiplied by Γ_1, divided by Γ_2, multiplied by Γ_3, and finally divided by Γ_4 or

$$\begin{bmatrix} \overline{E}_x \\ \overline{E}_y \end{bmatrix}^{n+1} = \Gamma_4^{-1}\Gamma_3\Gamma_2^{-1}\Gamma_1 \begin{bmatrix} \overline{E}_x \\ \overline{E}_y \end{bmatrix}^{n} \tag{4.42}$$

The operator multiplication in equation (42) is trivial, and the operator inversion is also not difficult. For example, if we are going to perform the inversion of Γ_2

$$\begin{bmatrix} \overline{E}_x \\ \overline{E}_y \end{bmatrix}^{m+1} = \Gamma_2^{-1} \begin{bmatrix} \overline{E}_x \\ \overline{E}_y \end{bmatrix}^{m} \tag{4.43}$$

or

$$\begin{bmatrix} \overline{E}_x \\ \overline{E}_y \end{bmatrix}^{m} = \Gamma_2 \begin{bmatrix} \overline{E}_x \\ \overline{E}_y \end{bmatrix}^{m+1} = \left(1 - \frac{\Delta}{2}\begin{bmatrix} A_y & 0 \\ D & B_y \end{bmatrix}\right) \begin{bmatrix} \overline{E}_x \\ \overline{E}_y \end{bmatrix}^{m+1} \tag{4.44}$$

We can formally solve the equation $(1-\Delta z A_y/2)E_x^{m+1} = E_x^m$ first in order to obtain E_x^{m+1}, and then solve $(-\Delta z D/2)E_x^{m+1} + (1-\Delta z B_y/2)E_y^{m+1} = E_y^m$ to obtain E_y^{m+1}. Since this formulation is a pure Crank–Nicholson scheme together with the alternate direct implicit method, it is a scheme of second-order accuracy in the forward direction. It can theoretically be shown that equation (4.42) is numerically unconditionally stable. In this implementation the reference refractive index is adaptively chosen during propagation. To fulfill the slowly varying envelope approximation, should be chosen such that the variations of transverse fields along the longitudinal direction are minimized, and the optimum refractive index should be the average of the effective indexes of all the propagating modes involved in the propagation process. The Rayleigh quotient may be

used at each step to adaptively choose the optimum reference refractive index. From the Rayleigh quotient the reference refractive index can be obtained by

$$n_0 = \sqrt{\frac{\overline{E^A P E}}{k_0^2 \overline{E^A E}}} \tag{4.45}$$

Where E^A is the adjoint of the electric field E.

To implement the transverse derivatives for operator P, instead of using the graded-index assumption which is questionable especially in strongly guiding structures, we use the finite difference schemes in x and y directions , in which the finite difference schemes can assure truncation errors of second order in the transverse directions. For boundaries of the numerical window, both the transparent boundary condition (Mansour et al,1996) and the perfectly matched layer (Yamauchi et al, 1991) boundary condition can be adopted in this algorithm.

4.5 Conclusion

The above solutions to the Helmholz equation and propagation of light in waveguides, was achieved and a non-iterative procedure was developed that was easily coded in C or Matlab for characterizing the Fabry Perot sensor head discussed in the following chapters. An algorithm to design code for this method is indicated in appendix 7. Due to the non-iterative nature of the method, the algorithm has good performance in efficiency compared with that of other (relaxation) approaches.

Chapter 5

DEVELOPMENT OF DIGITAL DATA CAPTURE FOR A NON-MONOCHROMATIC EFPI OPTICAL FIBRE CURRENT SENSOR.

5.1 Introduction

An extrinsic Fabry Perot etalon sensor head using a single sensing EFPI was developed, analysed and constructed from the principles depicted in the previous three chapters. In this chapter the signal response, and the signal processing techniques for the non-monochromatic lightwave extrinsic Fabry-Perot interferometric (EFPI) sensor system is presented. Equations are derived to model the behavior of the non-monochromatic lightwave EFPI sensor system, which provide an insight into the modulation of the signal responses and their demodulation techniques, applicable for digital signal processing to be applied to the sensor. With this absolute value of the EFPI gap measurable, it is proved that the digital data capture is possible and may be algorithmically implemented by means of digital signal processing techniques. The EFPI sensor developed in this application is for the measurement of current in power system applications.

5.2. Reason for sensor choice

In the design presented in this chapter, the opto-electronic technique developed in (Kahn, March 1999) would be aimed at to measure current changes. Fibre-optic interferometric sensors can be designed as compact and robust transducers. In general the transduction mechanism involves the phase modulation of coherent or monochromatic light propagating through a fibre-optic cable, and detecting the changes in the energy that is associated with this phase change. A review of technology in chapter 1 suggests that the four different interferometric sensor configurations, namely the Michealson, Mach Zehnder, Sagnac and Fabry-Perot interferometers, have been most popular in fibre-optic sensor development. In the

Fabry Perot etalon the sensing element is the optical cavity defined by the two reflecting surfaces. This sensor configuration can be easily constructed by extrinsic as well as intrinsic means, and renders itself a viable candidate for an embeddable sensor technology. In this application the external Fabry Perrot (EFPI) cavity is used as the sensing element but may be applied to other forms of the FPI.

5.3. Description of the Non-monocromatic lightwave EFPI Sensor System

The sensor discussed here was based on ideas developed as an extension of a previous design (Khan, December 1999), and the material of chapters 2, 3 and 4, where a sense and measurement FPI was modeled and developed. Figure 5.1 shows the basic functional block diagram of a non-monochromatic lightwave EFPI optical fiber sensor system, in this case without a reference cavity. A broadband super luminescent light-emitting diode is employed as an optical source to launch light into a single-mode optical fiber. The broadband light propagates to an EFPI sensor through an optical coupler, and reflects back, first, from the glass-air interface of the input/output fiber, and second, from the air-glass interface of the reflector fiber. The first reflection is termed as the *reference reflection* while the second reflection is termed as the *sensing reflection* (Murphy et al, 1991) A reflection of desired percentage can be achieved from the 2nd interface by applying appropriate coating material to the reflector fiber. The other end of the reflector fiber is shattered roughly to scatter away any light that transmits through it, and thus there is no reflection from that end.

The EPFI is mounted on a specimen where the cavity will be induced to change in accordance with the current that is to be measured as discussed in chapter 3. Interference occurs in the input/output fiber between the backward propagating waves of the reference reflection and the sensing reflection, and depending on the length of the EFPI air gap some wavelengths add with a phase difference 360^0(or a multiple of 360^0) producing fringe peaks, and some wavelengths add with a phase difference of 180^0(or an odd multiple of 180^0) producing fringe troughs, and the rest add with a phase difference other than 360^0 or 180^0 producing values within the peaks and troughs. The interfered light propagates back to the end of a fiber through the optical coupler. Normally at this stage a PIN photo-diode or avalanche photo

detector is used in conjunction with a transimpedence amplifier to convert the light intensity back to an electrical measurement. In this design the light from the fibre is interfaced to a reflection diffraction grating, which separates the light components by diffracting different wavelengths at different angles on to a screen or charge coupled device array, as shown in Figure 5.1. The charge coupled device array senses the intensity of different wavelength components of the light at different elements of the array and makes an electrical signal pattern with discrete amplitude pulses which corresponds to the linear fringe pattern of the interfered waves, the shape of the pattern depends mainly on the length of the EFPI air gap, the profile of the light launched from the LED, the responsivity profile of the charge coupled device photo-diodes, and the optical characteristics of the fiber and the coupler. The discrete analog pulses are digitized and transferred to the digital signal processing (DSP) unit, which does all the necessary processing of the digital signal in real-time to find out the length of the air gap of the EFPI sensor. The sensor system shown in Figure 5.1 is also called an Absolute EFPI (AEFPI) system as it can measure the length of the EFPI air gap and hence the movement (both in direction and in displacement) of the reflector fiber, with respect to the input/output fiber. This capability is unlike the single frequency phase measurement interferometry (PMI), where the direction and the total displacement of the reflector fiber becomes ambiguous over a displacement in excess of $\lambda/4$ (λ being the wavelength of the light in free space) and also where the absolute position of the reflector with respect to the reference is never known.

5.4. Gaussian Signal Characteristic

The signal responses of the non-monochromatic lightwave EFPI sensor system is shown in Figure 5.2. This is illustrated for a EFPI air gap of 50.0 micrometere only. Due to the Gaussian profile of the LED optical source, the shape of the signal responses also look like Gaussian, but having the fringe peaks and troughs added with the Gaussian. As the length of the EFPI air gap increases, the number of wavelengths which can satisfy the condition of in-phase addition, after being reflected from the reference interface and the sensing interface, also increases, increasing the number of fringe peaks, and decreasing the distance (in terms of wavelength) between adjacent fringe peaks. Note that, the frequency of occurrence of fringe peaks decreases gradually towards the higher end of wavelength values,

i.e., there is a chirp present in the frequency of the fringe pattern. This chirp is due to the fact that the condition of in-phase addition, after being reflected from the reference interface and the sensing interface, is met more frequently (in terms of wavelength distances) at lower wavelengths, and gradually decreases with the increase of wavelength.

5.5. Modeling the Non-monochromatic lightwave EFPI Sensor System

Before developing the model equations for the non-monochromatic lightwave EFPI sensor system we need to make the assumptions as stated below.

5.5.1 The model assumptions:

5.5.1.1 Negligible variation in refractive index and insignificant total dispersion:

A non-monochromatic light source is a wide band source and hence the optical wave spectrum launched into the single-mode fiber is also wide. If light of wavelength λ , where λ varies over a range, is launched into the single-mode fiber the index of refraction of the fiber will be different for different values of λ, and for wavelengths less than 1.0 μm the refractive index n corresponding to any wavelength λ can be found by using the Sellmeier relation (Didomenico ,. 1972),

$$n^2 = 1 + \frac{E_0 E_d}{E_0^2 - E^2}, \qquad (5.1)$$

where $E = hc/\lambda$ is the photon energy corresponding to wavelength λ, and E_0 and E_d are material oscillator energy and dispersion energy parameters, respectively. For SiO_2 glass E_0 = 13.4 eV and E_d = 14.7 eV, and also hc = 1.24 m-eV (Didomenico , 1972). For wavelengths ranging from 0.8 to 0.9 μm, the refractive index of the fiber core varies from 1.4532 to 1.4521. The total material dispersion due to this variation of refractive index, though very significant for long-haul fibers having lengths in kilometers, is insignificant for our short length fiber and is neglected. As material dispersion is very dominant over waveguide dispersion at wavelengths lower than 1.0 μm (Keiser,1991), the waveguide dispersion is neglected also.

5.5.1.2 Negligible attenuation along the fiber:

As the commercial single-mode silica fibers have an attenuation about in the range of 0.1 to 0.4 dB/km, and the length of the fiber being used for the system in Figure 5.1 is very short, usually measured only in meters rather than in kilometers, we neglect any attenuation of signal along the fiber.

5.5.1.3 Source power launched into the fiber is independent of the power reflected back to source:

We assume that there is negligible effect on the source due to incidence of optical power propagating back to the source after the reflections. An optical isolator can also be used to hinder the optical power that may propagate back to the source.

5.5.1.4 Only the first order reflection in the EFPI cavity is significant:

There can be multiple reflections inside the EFPI cavity, but the second and the higher order reflections have been shown to have negligible amplitude if compared to the first order reflection (Claus et al, 1992), and hence are neglected. We assume only a simple two beam interference system.

5.5.1.5 A wavelength independent coupler is used:

For the wavelength range of our interest we assume that the behavior of the optical coupler, shown in Figure 1, is independent of wavelength.

5.5.2. Development of the model equations:

If g is the length of the EFPI air gap, and λ is the free space wavelength of any particular light component, then the field amplitude $y(\lambda)$ of the interfered light corresponding to wavelength λ, propagating from the EFPI sensor to the reflection grating, under the above assumptions and as shown in Figure 5.1, can be expressed as,

$$y(\lambda) = r_{pr} f_s(\lambda) \cos\left(2\pi \frac{ct}{\lambda n_1}\right) + t_{pr} f_a(g) f_s(\lambda) \cos\left(2\pi \frac{ct}{\lambda n_1} - \frac{4\pi g}{\lambda} - \varphi_2 + \varphi_1\right), \quad (5.2)$$

where,

i) $f_s(\lambda)$ is the profile (in terms of amplitude, not intensity) of the non monocromatic light output coupled into the input/output fiber,

ii) $f_a(g)$ is a attenuation factor which can be thought as the square root of the ratio of the light intensity being transmitted out through the first interface to the light intensity being coupled back again into the fiber through the same interface;

iii) n_1 is the refractive index of the fiber core (note that n_1 varies negligibly with distance)

iv) φ_1 and φ_2 are the reflection phase shifts at the reference and the sensing interfaces respectively (for the first interface of glass-air and for the second interface of air-glass, we get $\varphi_1 = 0^0$ and $\varphi_2 = 180^0$ (Moller , 1988),and,

v) r_{pr} and t_{pr} are Fresnel's amplitude reflection and amplitude transmission coefficients, respectively, for p polarization, at the reference interface. For normal incidence $r_{pr} = (n_1\text{-}1)/(n_1+1)$, and $t_{pr} = 2n_1/(n_1+1)$ (Moller, 1988).

$(4\pi g/\lambda)$ is the phase delay, for any wave of wavelength λ, incurred in traversing the gap length g forward and backward.

Note that Equation (5.2) assumes that, for any wavelength, the wave reflecting back from the first interface and the wave coupling back again into the fiber through the same interface, are linearly polarized and they have their electric field vectors polarized in the same plane and same direction. The first term in Equation (5.2) is the reference term while the second term is the sensing term, and both the terms add together to make constructive and destructive fringes for continuous values of λ. The $f_a(g)$ factor can be approximated with the help of the method expounded by (Keiser,1991), as,

$$f_a(g) = r_{ps}\left(\frac{a}{a + g\tan[\sin^{-1}(NA)]}\right)^2, \qquad (5.3)$$

where r_{ps} is Fresnel's amplitude reflection coefficient at the sensing interface, a is the core radius of the input/output fiber, g is the gap length between the reference and the sensing reflection interfaces, and NA is the numerical aperture of the

input/output fiber. $NA = \sqrt{(n_1^2 - n_2^2)}$, where n_1 and n_2 are the core and the cladding refractive indices respectively. Note that $f_a(g)$ is an attenuation factor of amplitude (not intensity) and is independent of

$$y(\lambda) = f(\lambda)\left[r_{pr} \cos\left(2\pi \frac{ct}{n_1 \lambda}\right) + t_{pr} f_a(g) \cos\left(2\pi \frac{ct}{n_1 \lambda}\right) - \delta \right] \tag{5.4}$$

where $\delta = \left(\frac{4\pi g}{\lambda} + \varphi_2 - \varphi_1\right)$. Note that Equation (4) has two phasor terms of amplitude r_{pr} and $t_{pd} f_a(g)$ having the same frequency $\frac{2\pi c}{n\lambda}$ with a phase difference of δ. The two terms of Equation (5.4) can be added together with the help of phasor geometry as, and the resultant vector $y(\lambda)$ can be written as,

$$y(\lambda) = f_s(\lambda)\left\{ r_{pr} \cos\theta + t_{pr} f_a(g) \cos(\delta - \theta) \right\} \cos\left(2\pi \frac{ct}{n\lambda} - \theta\right) \tag{5.5}$$

where θ is calculated as,

$$\theta = \sin^{-1}\left[\frac{t_{pr}^2 f_a^2(g) \sin^2 \delta}{\left(r_{pr} + t_{pr} f_a(g) \cos\delta\right)^2 + t_{pr}^2 f_a^2(g) \sin^2 \delta} \right]^{0.5} \tag{5.6}$$

As light intensity is proportional to the square of the amplitude of the field, by squaring both sides of Equation (5.5) we can write,

$$\begin{aligned} y^2(\lambda) &= f_s^2(\lambda)\left\{ r_{pr} \cos\theta + t_{pr} f_a(g) \cos(\delta - \theta) \right\}^2 \cos^2\left(2\pi \frac{ct}{n\lambda} - 2\theta\right) \\ &= \frac{1}{2} f_s^2(\lambda)\left\{ r_{pr} \cos\theta + t_{pr} f_a(g) \cos(\delta - \theta) \right\}^2 \left(1 + \cos 4\pi \frac{ct}{n\lambda} - 2\theta\right) \end{aligned} \tag{5.7}$$

The signal current of the photodiode is proportional to the light intensity incident upon the photodetector. Usual photodiodes are not able to respond to double the

frequency of light as expressed by the time varying cosinusoidal term of Equation (5.7), and hence the photo-current, I_p, sensed by a photodiode can be written as,

$$I_p(\lambda) = A\Re(\lambda) f_s^2(\lambda)\left\{r_{pr}\cos\theta + t_{pr} f_a(g)\cos(\delta-\theta)\right\}^2 \qquad (5.8)$$

where A is a proportionality constant and $\Re(\lambda)$ is the responsivity of the photodiode. Responsivity is independent of the power level incident on the photodetector, and is a function of wavelength (or in another way is a function of photon energy h_n), and is defined in (Keiser,1991). For the charged coupled device the charge of the photocurrent is stored across a capacitor and accumulated for a period of time to generate a voltage. Using Equation (5.8) the voltage, Vc, across the charge coupled device capacitor can be written as,

$$V_c(\lambda) = B\Re(\lambda) f_s^2(\lambda)\left\{r_{pr}\cos\theta + t_{pr} f_a(g)\cos(\delta-\theta)\right\}^2 \qquad (5.9)$$

where B is a constant and can be calculated as, $B = AT/C$, where T is the integration period and C is the capacitance of the charge coupled device elements. Note that the $f^2_s(\lambda)$ factor of Equation (5.9) can be thought as the optical source profile in terms of intensity, as the $f_s(\lambda)$ factor in Equation (1) was considered as the source profile in terms of amplitude. For practical systems there will be a Gaussian random noise added with the signal of Equation (5.9). Assuming that the noise added is independent of λ and g, We can write,

$$V_c(\lambda) = B\Re(\lambda) f_s^2(\lambda)\left\{r_{pr}\cos\theta + t_{pr} f_a(g)\cos(\delta-\theta)\right\}^2 + G(\mu,\sigma^2) \qquad (5.10)$$

where μ is the mean and σ^2 is the variance of the Gaussian random process.

5.6. Conclusion:

Equation (5.10) completely models the signal of the non-monocromatic lightwave EFPI sensor system of Figure 5.1. For a set of discrete values of λ a set of signals Vc (λ) from Equation (5.10) is achieved. The number of signals in the set is the number of elements of the charge coupled device array, each charge coupled device array element corresponding to a particular λ. Figure 2 shows the simulated signal response of the non-monocromatic lightwave EFPI sensor system, modeled by Equation (5.10), for an EFPI gap of 50.0 micrometers. With this absolute value of the gap measureable, the digital data capture is possible and may be algorithmically implemented by means of digital signal processing techniques. This will be the topic of the next chapter.

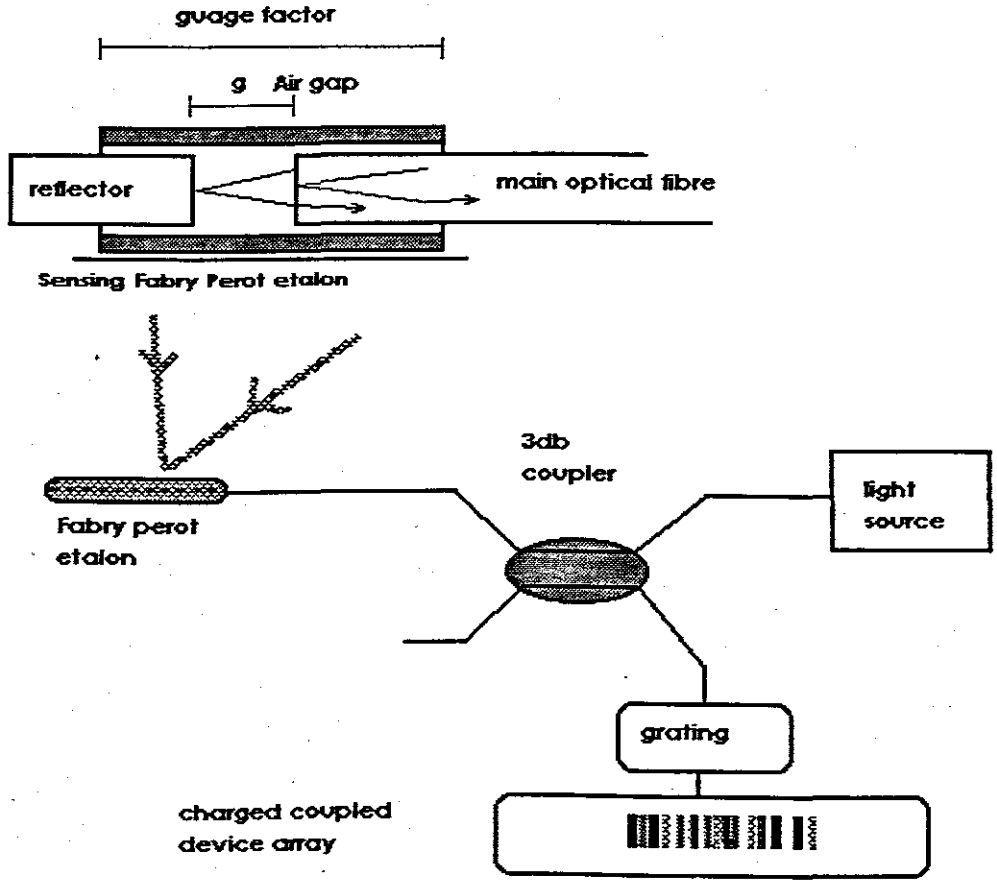

Figure 5.1 The Fabry Perrot sensor set-up with digital data capture

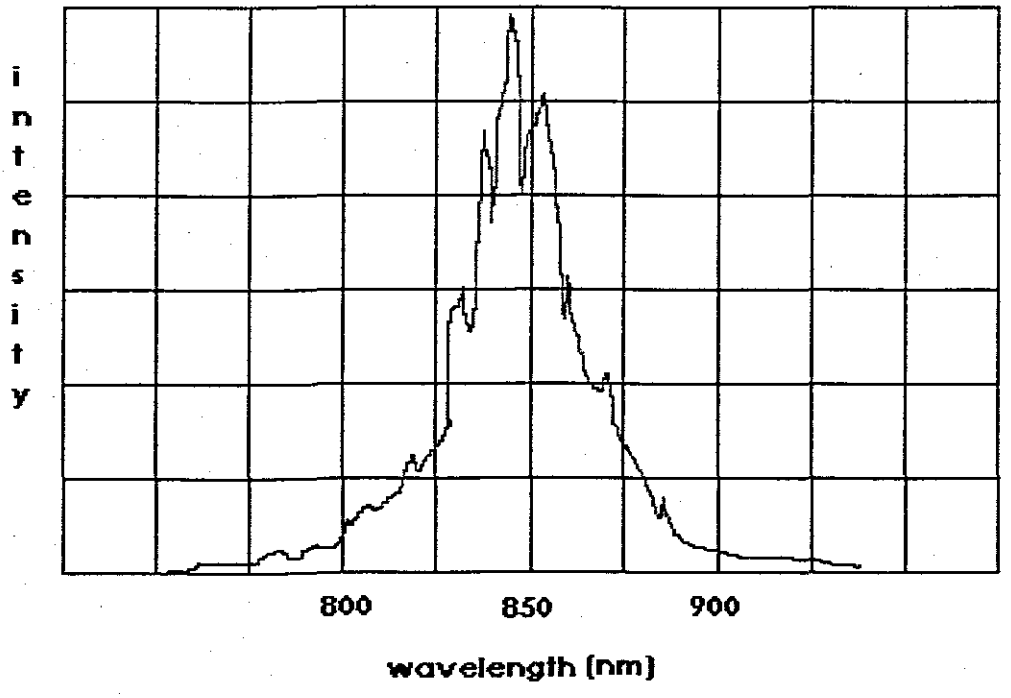

Figure 5.2 Wavelength characteristic of the sensor

Chapter 6

DEVELOPMENT OF SIGNAL DEMODULATION TECHNIQUES FOR THE EFPI BASED CURRENT SENSOR

6.1 Introduction

It was a challenge to find out the value of the External Fabry Perot Interferometer air gap length *g*, from the complex signal response of the non-monochromatic lightwave EFPI sensor system proposed for our generic current sensor. It is known that due to the Gaussian profile of a broadband optical source, the shape of the signal response is somewhat Gaussian, but modulated with the fringe pattern, including peaks and troughs. With the increase of the EFPI gap, the number of fringe peaks within the same wavelength range, of the signal response, gets increased, decreasing the distance (in terms of wavelength) between adjacent fringe peaks. Also, the non-monochromatic lightwave EFPI sensor system has a signal response where the frequency of occurrence of fringe peaks decreases gradually towards the higher end of the wavelength values, i.e., there is a chirp in the frequency of the fringe pattern, distancing any two adjacent fringe peaks further for larger values of wavelengths. We present below several methods in reference to process this complicated signal response of the non-monochromatic lightwave EFPI sensor system, to find the EFPI gap length *g*, and as such any measurand (in this case current) that relates to that.

6.2 EFPI signal demodulation and gap length

In the design presented in this chapter, the opto-electronic technique developed in chapter 5 based on the proposal in (Kahn, 1999) was in need of a suitable demodulation technique for real time sensor applications. The digital data capture technique was used to transduce a suitable signal proportional to current change. Fibre-optic interferometric sensors can be designed as compact and robust transducers. In general the transduction mechanism involves the phase modulation of coherent or monochromatic light propagating through an optical fibre, and detecting the changes in the energy that is

associated with this phase change. A review of technology suggests that the four different interferometric sensor configurations, namely the Michealson, Mach Zehnder, Sagnac and Fabry-Perot interferometers, have been most popular in fibre-optic sensor development (Kahn, 1998).

Many fiber optic interferometers in general depend on the interference between two light beams obtained from reflections within or outside the fiber. These are the reference and sensing waves in the sensor. Secondary reflections do exist but are generally negligible. External parameters cause a change in the optical path length of the sensing wave, thus causing a phase difference between the two interfering waves. In the Fabry Perot etalon the sensing element is the optical cavity defined by the two reflecting surfaces. This sensor configuration can be easily constructed by extrinsic as well as intrinsic means, and renders itself a viable candidate for an embeddable sensor technology. In this application the external Fabry Perrot (EFPI) cavity is used as the sensing element

The output signal can be demodulated to obtain absolute or relative information about the external parameter. The electronic signal processing system in the general purpose optical fiber based sensor essentially consists of the opto-electronic conversion circuitry, the signal demodulation scheme and the display. The opto-electronic interface converts the optical signal output from the sensors into electrical form and the signal demodulation scheme (Thompson & Khan, 2000) obtains phase information from it. After appropriate scaling and calibration the output is displayed in terms of the external parameter measured. Figure 6.1 shows the various components of the electronic signal processing involved in a standard fiber optic sensor system.

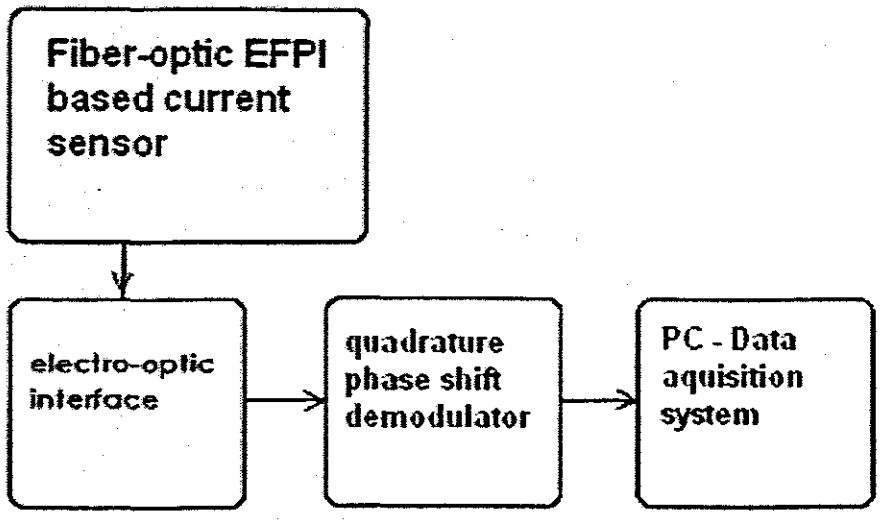

Figure 6.1 The electronic signal processing system.

In our set-up a charged coupled device was used to directly assess the interference pattern after suitable pre-processing with a grating. This is where we pick up the development of chapter 5 and continue with the development of a suitable signal demodulation scheme. This leads us to the following model as derived in (Keiser, 1991) where, for the charged coupled device the charge of the photocurrent is stored across a capacitor and accumulated for a period of time to generate a voltage. The voltage, Vc, across the charge coupled device capacitor can be written as,

$$V_c(\lambda) = B\Re(\lambda) f_s^2(\lambda)\left\{r_{pr}\cos\theta + t_{pr} f_a(g)\cos(\delta-\theta)\right\}^2 \qquad (6.1)$$

where B is a constant and can be calculated as, $B = AT/C$, where T is the integration period and C is the capacitance of the charge coupled device elements. Note that the $f^2_s(\lambda)$ factor of Equation (6.1) can be thought as the optical source profile in terms of intensity, as the $f(g)$ factor in Equation (6.1) was considered as the source profile in terms of amplitude. For practical systems there will be a Gaussian random noise added with the signal of Equation (6.1). Assuming that the noise added is independent of λ and g, We can write,

$$V_c(\lambda) = B\Re(\lambda) f_s^2(\lambda)\left\{r_{pr}\cos\theta + t_{pr} f_a(g)\cos(\delta-\theta)\right\}^2 + G(\mu,\sigma^2) \qquad (6.2)$$

where μ is the mean and σ^2 is the variance of the Gaussian random process.

It is in general not easy to find out the value of the External Fabry Perot Interferometer air gap length g, from the complex signal response of a non-monochromatic lightwave EFPI sensor system. It is known that due to the Gaussian profile of a broadband optical source, the shape of the signal response is somewhat Gaussian, but modulated with the fringe pattern, including peaks and troughs. We present below several methods in reference to process this complicated signal response of the non-monochromatic lightwave EFPI sensor system, to find the EFPI gap length g, and as such any measurand that relates to that.

6.3. The Peak-to-Peak Method

Any free space wavelength of value λ_1 can make a fringe peak, i.e., can add in-phase after being reflected from the reference interface and the sensing interface, only if it satisfies the condition,

$$2\pi\frac{2g}{\lambda_1}+\varphi_2 = 2m_1\pi+\varphi_1 \tag{6.3}$$

where, g is the EFPI gap length, φ_1 and φ_2 are the reflection phase shifts at the reference and the sensing interfaces respectively, and m_1 is an integer (m_1 represents the number of full wavelengths the wave λ_1 travels before adding back in phase). A free space wavelength of value $\lambda_2(\lambda_2>\lambda_1)$ to make the fringe peak just adjacent to the fringe peak of λ_1 must satisfy the condition,

$$2\pi\frac{2g}{\lambda_2}+\varphi_2 = 2(m_1-1)\pi+\varphi_1 \tag{6.4}$$

where it is assumed that the reflection phase shifts are independent of wavelengths. Now subtracting Equation (6.4) from Equation (6.3) we get,

$$g=\frac{\lambda_1\lambda_2}{2(\lambda_2-\lambda_1)} \tag{6.5}$$

Thus one can easily find out the EFPI gap length g, just by finding the wavelengths of the adjacent fringe peaks. Equation (6.5) also applies for adjacent fringe troughs, and that can easily be shown using the similar derivation. As we have observed earlier, the fringe peaks are not uniformly-spaced in wavelengths, rather the wavelength spacing between adjacent fringe peaks increases gradually towards the higher end of wavelength values causing a chirp in the frequency of the fringe pattern. Using Equation (6.3) and (6.4) we can easily get,

$$\lambda_2 - \lambda_1 = \frac{8\pi^2 g}{\{2(m_1 - 1)\pi + \varphi_1 - \varphi_2\}\{2m_1\pi + \varphi_1 - \varphi_2\}} \tag{6.6}$$

For simplicity lets assume that the reflection phase shifts, $\varphi_1=\varphi_2=0$, then we can write the equation (6.6) as,

$$\lambda_2 - \lambda_1 = \frac{2g}{(m_1 - 1)m_1} \tag{6.7}$$

Equation (6.7) is of significant importance for the understanding of the chirp phenomena of a non-monochromatic lightwave EFPI sensor system. It says that the spacing in wavelength between two adjacent fringe peaks is proportional to the EFPI gap g, and is inversely proportional to the product of the numbers of full wavelengths the waves, forming the fringe peaks, travels before adding in phase. When g is constant, as m decreases for the fringes of the higher wavelengths, the spacing between the adjacent fringe peaks increases. And when g increases, m_1 increases in the same proportion as evident from equation (6.3), causing the spacing between adjacent fringe peaks $\lambda_2 - \lambda_1$ to decrease almost with the same proportion. Note that Equation (6.7) can be written as,

$$\lambda_2 - \lambda_1 = \frac{2g}{m_1 m_2} = \frac{2g}{m_1(m_1 - n)} \tag{6.8}$$

where mn represents the number of full wavelengths the wave λn ($\lambda\ n > \lambda_1$) travels before adding back in phase, and (n-1) is the number of fringe peaks in between λ_1 and λn. Now, to quantify the amount of chirp, lets assume a free space wavelength of value λ_3 ($\lambda_3 > \lambda_2$) makes the fringe peak just adjacent to the fringe peak of λ_2, then we can write, like Equation (6.7),

$$\lambda_3 - \lambda_2 = \frac{2g}{(m_1 - 1)(m_1 - 2)} \tag{6.9}$$

Using Equation (6.7) and (6.9), we get the spacing difference of the non-uniform spacing of adjacent peaks as,

$$(\lambda_3 - \lambda_2) - (\lambda_2 - \lambda_1) = \frac{4g}{m_1(m_1 - 1)(m_1 - 2)} \tag{6.10}$$

For the condition of fringe peak, as stated by equation (6.1), the parameter δ of Equation (6.3) gets the value as,

$$\delta = \frac{4g}{\lambda} + \varphi_2 - \varphi_1 = 2m\pi \tag{6.11}$$

where m is an integer. Thus for the wavelengths of the fringe peaks, Equation (6.2) can be written as,

$$V_c(\lambda) = B\Re(\lambda) f_s^2(\lambda)\{r_{pr} + t_{pr} f_a(g)\}^2 + G(\mu, \sigma) \tag{6.12}$$

Similarly, for the condition of fringe troughs, the parameter δ of Equation (6.2) must have the value as,

$$\delta = \left(\frac{4\pi g}{\lambda} + \varphi_2 - \varphi_1\right) = (2m+1)\pi \tag{6.13}$$

And thus for the wavelengths of the fringe troughs, Equation (6.2) can be written as,

$$V_c(\lambda) = B\Re(\lambda) f_s^2(\lambda)\{r_{pr} + t_{pr} f_a(g)\}^2 + G(\mu, \sigma) \tag{6.14}$$

Even if we ignore the Gaussian noise and assume that the responsivity characteristics of the photodiodes are independent of wavelengths, i.e. $\Re(\lambda)$is a constant, we may not find

the intensity values of Equation (6.12) and (6.14) as the peaks and the troughs in the output of our linear array CCD spectrometer due to the modulation of the signal by the profile of the optical source $f_s^2(\lambda)$.

The achievement of a perfectly white optical source is not very practical yet, and the demodulation of the signal response using the profile of the optical source to undo the modulation effects, is not practical for real time applications due to the fact that the source intensity may vary over time and the profile may not follow a fixed curve (either analytic or numeric). When the optical source is Gaussian but of pretty wide band, an estimate of the EFPI gap length g can be made though, by assuming the peaks of the modulated signal response as the fringe peaks, and troughs of the modulated signal response as the fringe troughs.

6.4 The Fast Fourier Transform Method

The frequency of the fringe pattern of the signal response of the non-monochromatic lightwave EFPI sensor system, though modulated by the profile of the optical source and a chirp, varies with the variation of the EFPI gap g. The fast Fourier transformation (FFT) method uses this variation of the frequency of the fringe pattern of the response to find out the EFPI gap length g. After implementing a high-pass filtering on the EFPI signal response, to filter out any DC value, a fast Fourier transformation is implemented on the filtered data. Applying a Gaussian interpolation technique (Shin et al, 1992) , zero padding the data before doing the FFT, the resolution or accuracy of finding the EFPI gap can be increased by at least an order of magnitude. Matlab code (appendix 6) was used for the implementation of the FFT method using Gaussian interpolation technique, and Figure 6.3 and 6.4 show the filtered data and the FFT magnitude values respectively, for the non-monochromatic lightwave EFPI sensor system, using the Ocean Optics S100 linear array spectrometer of SIE-687 (see appendix 1), With an EFPI air gap of 50 micrometer. the wavelength spacing between adjacent CCD diode elements are not uniform, as depicted in Figure 6.2

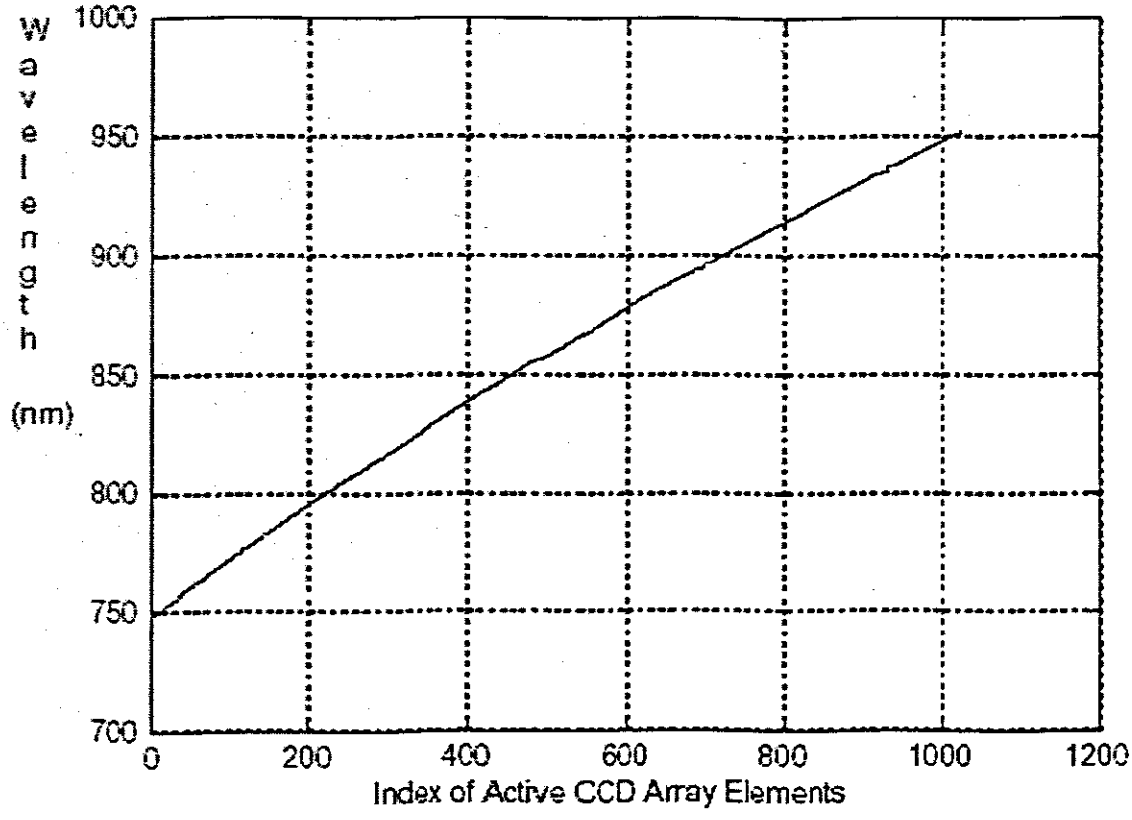

Figure 6.2 Wavelength versus CCD active index

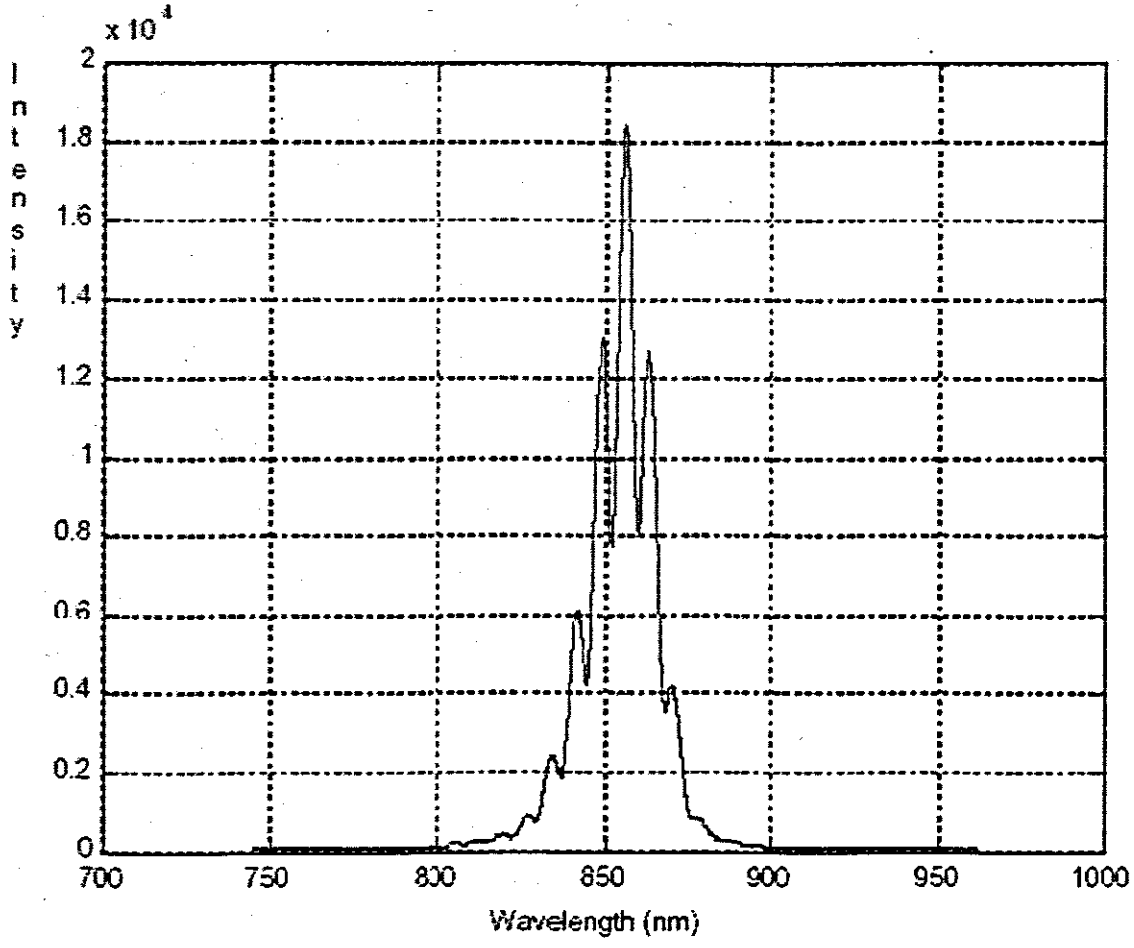

Figure 6.3 Wavelength versus intensity of filtered profile

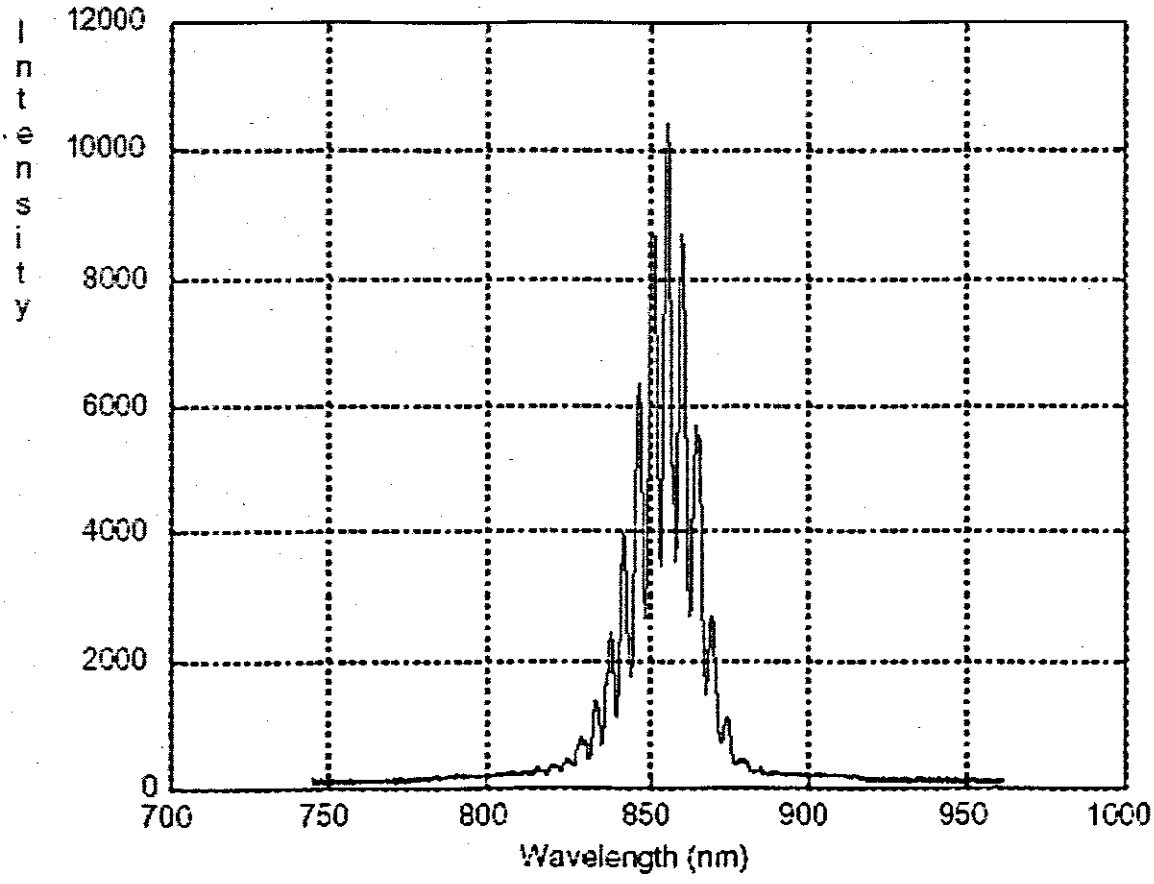

Figure 6.4 Wavelength versus Intensity of unfiltered profile.

The FFT method of finding the EFPI gap g, though very fast for real-time applications, is not very precise, mainly may be due to its dependence on the curve fitting coefficients, which must be derived from a set of data associated with known EFPI gap values. A self-calibrated method which uses a special transformation, instead of FFT, can find the EFPI gap g with more precision and is presented below.

6.5 The Discrete Gap Transformation Method

A special transformation, termed here as *discrete gap transformation* (DGT), based on the parameter $\frac{4\pi g}{\lambda}$ of Equation (6.2), is given as (Shin et al, 1992),

$$I(g_m) = \sum_{n=1}^{N} x(n) \exp\left(j \frac{4\pi g_m}{\lambda(n)} \right) \tag{6.15}$$

where $x(n)$ are the intensity sequence of the elements of the linear array CCD spectrometer, $\lambda(n)$ are the wavelengths corresponding to the elements, g_m is any EFPI gap length, and N is the total number of active elements in the CCD spectrometer (which is 1024 in our wavelength modulated EFPI sensor system). To get the square of the magnitude of the DGT transformation, using Equation (6.15), we get,

$$\left|I(g_m)\right|^2 = \left|\sum_{n-1}^{N} x(n)\cos\left(\frac{4\pi g_m}{\lambda(n)}\right)\right|^2 + \left|\sum_{n-1}^{N} x(n)\sin\left(\frac{4\pi g_m}{\lambda(n)}\right)\right|^2 \qquad (6.16)$$

For any given set of acquired data with an EFPI gap of g, the magnitude of the DGT transformation of Equation (6.16) is maximum when g_m equals g. As in the discrete Fourier transformation (DFT) where the transform magnitude is the maximum at the frequency which corresponds to the dominating frequency of the data set, in the DGT transformation the transform magnitude is the maximum at the gap which corresponds to the gap of the data set. Thus for any given data set to find out the associated EFPI gap, we find the magnitude of the DGT transformation for a discrete set of values (with an incremental step of our expected precision) of g_m, and the value for which the transformation magnitude is the maximum is the EFPI gap. Matlab code was developed for finding the EFPI gap for any set of data, acquired from a wavelength modulated EFPI sensor system, using the DGT method. Figure 6.5 shows the calculated EFPI gap using the FFT method and the DGT method, both using the same 7 sets of data acquired from the wavelength modulated EFPI sensor system with the same nominal EFPI gap of about 50 micrometer.

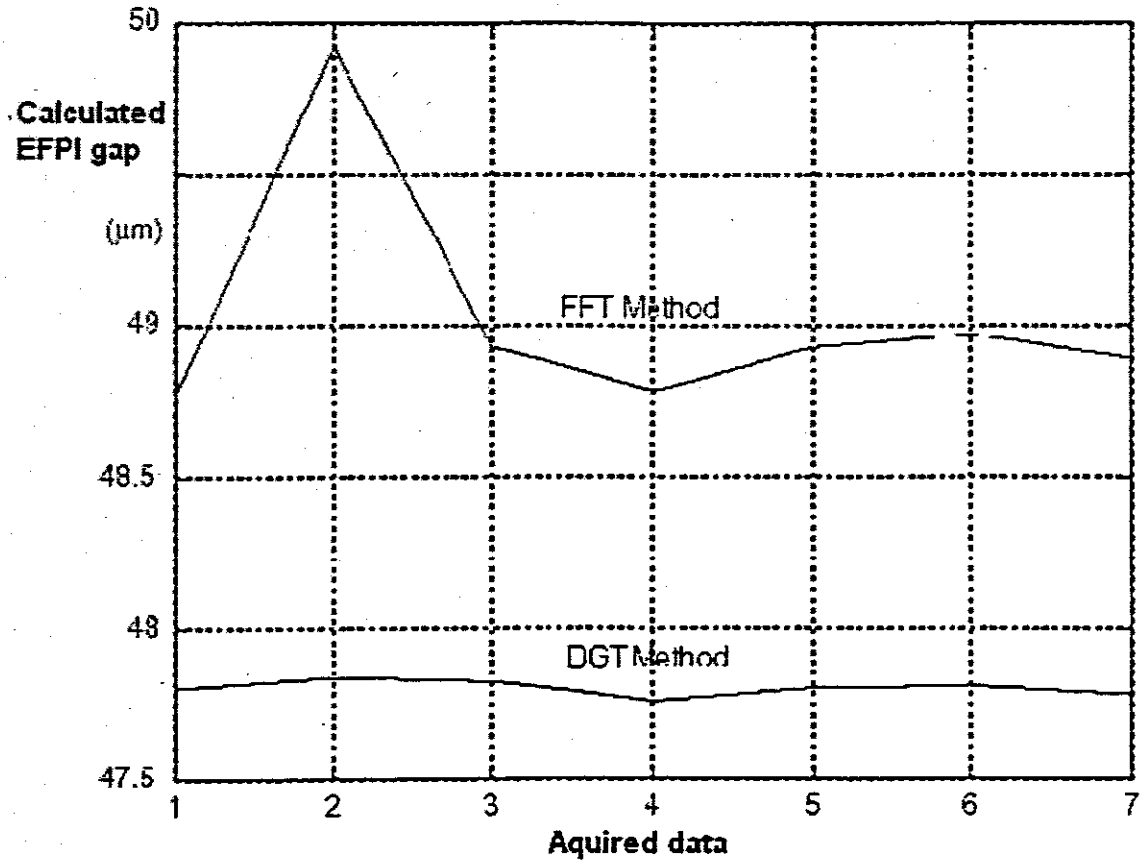

Figure 6.5 . Calculated EFPI gap using the FFT method and the DGT method

Though the DGT method is precise, it is very computation intensive. As the EFPI gap can be of any value in the range 30 micrometer to 300 micrometer, to find out the gap for a given data set with a desired precision of say 1 nanometer, one must calculate the DGT magnitude using the Equation (6.16) starting with a value of g_m of 30 micrometer and then increasing it by one nanometer at each step until 300 micrometer, entailing the computation of Equation (6.16) for 270,000 times, which is unrealistic for real-time applications.

6.6 Conclusion : FFT and then DGT with Golden Search Rule

To use the Gausian monotonocity of the magnitude of the DGT transformation to our advantage, we apply a peak search method rather than calculating Equation (6.16) at fixed increments of g_m. A peak search method named *golden search rule* (Press et al, 1998), is applied to find the value of g_m for which the magnitude of the transformation is the maximum, as coded in C. The iteration of calculation of Equation (6.16) is further reduced by reducing the range of the EFPI gap to be searched, by first making a rough estimate of the EFPI gap using the FFT method, which is pretty fast. The range of the EFPI gap to be searched, is assumed the EFPI gap found from the FFT method plus/minus 5 mm. And such, for the same precision of 1 nanometer, the iteration of calculation of Equation (6.16) is reduced to only about 20, rather than 270,000 as stated earlier. As depicted in Figure 6.6, the magnitude of the DGT transformation is very much like a Gaussian curve having only one peak. The real-time application of the DGT method is thus now made very feasible. In this way the EFPI gap can be adequately modelled for the application.

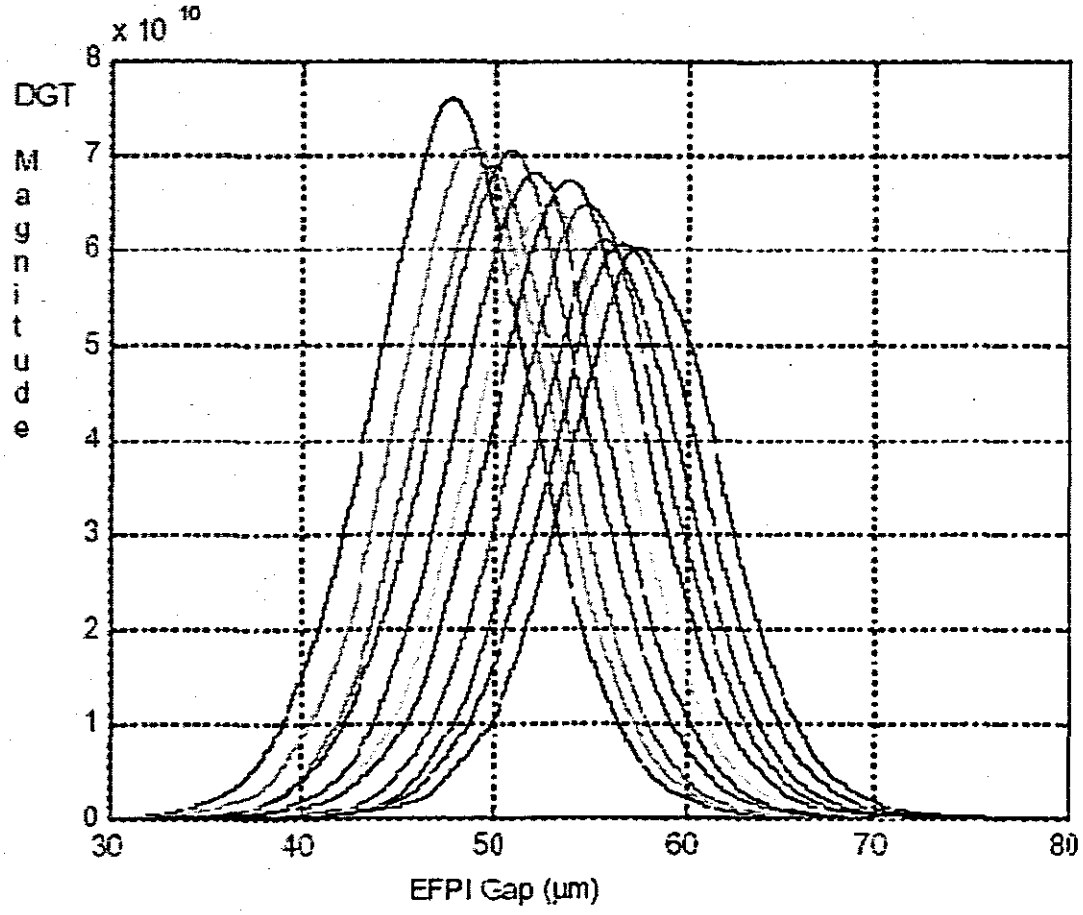

Figure 6.6. Magnitude of discrete gap transformation for different gap length.

Chapter 7

OPTICAL CURRENT SENSOR RESULTS AND FEATURES

7.1 Introduction

Our previous development resulted in a rudimentary but new real time optical current sensor. In a more deregulated and competitive market, generation companies are now looking for different solutions or alternatives to support strategies that focus on improving service reliability and reducing the costs of operation and maintenance. To maximise the benefit capability of an automation solution, existing infrastructure must be leveraged, functionality and benefits must be maximised, the cost of end use devices must be minimised. Furthermore, the estimated benefits must be captured, and a migration path must be developed that will support the transition to new technology. The first phase however is to examine the feasibility of this new kind of current sensor telemetry. Optical current sensors are achieving increased acceptance and use in high voltage substations due to their superior accuracy, bandwidth, dynamic range and inherent isolation. Once deemed specialized devices intended for novel applications, optical sensors have risen to a performance level exceeding conventional magnetic devices. A specific area where optical current sensors outperform conventional iron core transformers is the measurement of very high currents that occur during a fault on the power system. Conventional instrument transformers utilize an iron core and windings ratio to step down the current measured in the primary to a more manageable current level for secondary devices such as meters and relays. This signal may be distorted due to saturation of the magnetic core. In a pure optical current sensor, no such mechanism for saturation exists. However, optical sensors must be used and applied properly to provide distortion free signal replication well into the hundreds of kiloamp region. This chapter discusses the characteristics of optical current sensors,

specifically for relaying applications where measurement of fault-level currents may be required.

7.2 Conventional Current Transformer technology and optical techniques

In the past, current transformers with iron cores were used for current measurement in protection, measuring and metering applications. The known draw backs of current transformers had to be accepted, because the available technology did not allow the use of other principles like the Rogowski coil with its superior saturation characteristics, as well as other more exotic optical fibre techniques, which is the subject of this paper. The fast progress in digital technology now provides the possibility to use other measurement principles and in this way get rid of the disadvantages of the conventional current transformers. There is also an increase in the application of capacitive voltage sensors to replace the oil-filled inductive voltage transformers.

When faults on a power system occur, they must be isolated quickly to maintain the safe operation of the system, minimize damage to equipment, and maintain stability of the system. Therefore, the accurate measurement of fault current is a critical input to protection relays which monitor the current and/or voltage signals to determine whether the monitored portion is faulted and should be isolated, or whether conditions are normal and should remain closed to maintain the flow of power. If protection relays receive the "true" representation of current flowing on a transmission line, or into transformers, capacitor banks, or reactor banks, they will make decisions based on the current that is actually flowing, not based on a distorted representation of the current which the relay may need to compensate for. An undistorted view could improve the ability of the relay to trip when it should and to prevent false trips. Additionally, analyzing the power system as a whole, optical current sensors make design and analysis easy since no current transformer saturation will ever be encountered. Optical sensors behave in a simple and predictable manner known for every situation. (A pure optical sensor is defined in this chapter to be a current sensor which uses only optical sensing methods to measure the current. There are optical sensors available which use iron core or air core transformers to measure the current, and an optical path to bring

the signal from high voltage to ground potential.) Our real time sensor was the one developed in chapters 5 and 6.

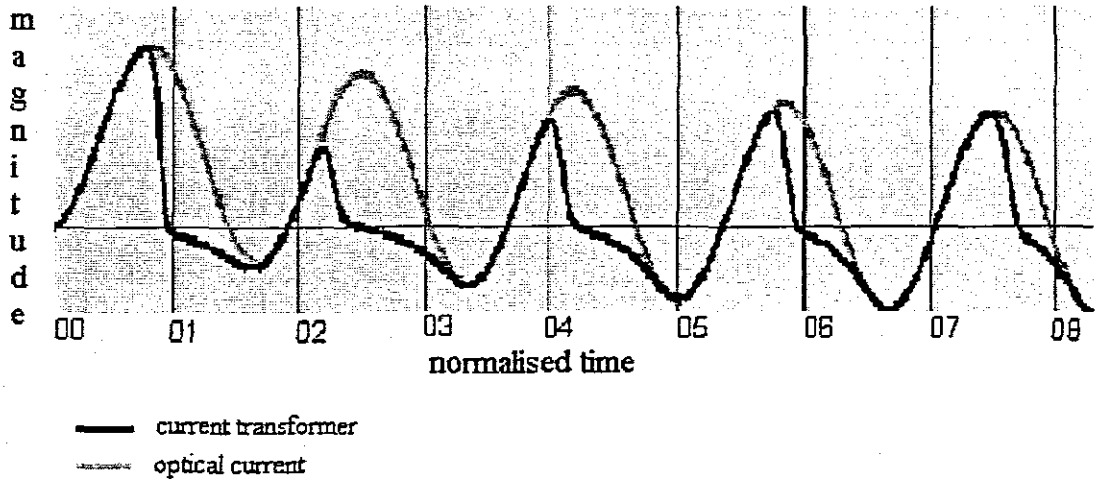

Figure 7.1 Optical current versus current transformer during peak overloading

7.3 Drawbacks associated with conventional Current transformers

During fault conditions a well-known phenomenon occurs: the iron core in a transformer "saturates" due to a large magnetic field caused by high fault currents. This saturation of the iron core prevents the transformer from accurately representing the primary current in the current transformer secondary, and therefore distorts current measurement. It is not the intent of this paper to explain saturation or analyze when and why it occurs. Readers not familiar with saturation should reference the many papers, books, and standards that deal directly with this subject in detail to fully understand the phenomena. Additionally, many good reference sources discuss the problems of current transformer saturation with respect to relaying, avoidance of saturation and methods to deal with saturation. The underlying problem surrounding the phenomena is that essentially all current transformers will saturate unless they are built with an excessive amount of steel to prevent it. This method of mitigation is impractical and must be dealt with by knowing how, when, and why a current transformer will saturate, then taking appropriate measures to prevent any false relay operations. The mechanism for current transformer saturation is not a simple relationship. Saturation depends on the physical

design of the current transformer, the amount of steel in the "core" of the transformer, the connected burden, the winding resistance, the remanence flux in the iron core, the fault level, and the system X/R ratio (which can cause a larger DC offset to occur). Taken together, these dependencies make the analysis of current transformer saturation complex. Figure 1 below shows an example of a current transformer with a saturated output against a plot of actual current. Scale is not given on the y-axis since it could apply to a variety of current transformers with various currents. The plots are shown only to illustrate a saturated current transformer waveform.

7.4 Current Measurement using optical technology

The problem of current transformer saturation in iron core instrument transformers can be avoided altogether by using an optical current sensor. Optical current sensors contain no magnetic components and do not have any saturation effects associated with them. Optical current sensors also have no iron core to saturate. Depending on the design of the sensor, these types of sensors have the ability to give a near perfect representation of the primary current. An optical sensor uses light to measure the magnetic field surrounding a current carrying conductor and, based on this measurement, electronics associated with the optics calculate the current flowing in the conductor. If done optimally, an optical measurement of current has the ability to measure fault currents exceeding 400 kA peak. Additionally, using advanced techniques, both AC and DC currents can be measured to this level.

An optical current sensor using light to measure the magnetic field surrounding a conductor has a transfer function with a sine wave characteristic. With normal load current flowing on the conductor, the measurement of the magnetic field by light is maintained essentially within the linear portion of the sine wave. Once the current increases substantially (for example, when a fault occurs) the transfer function of the light no longer traverses the linear portion of the sine wave, but enters a non-linear portion. In this non-linear portion of the sine wave, the electronics compensate for the non-linearity. Since this non-linear "sine wave" characteristic is well defined,

electronics can easily adjust, in order to maintain overall linearity of the current measurement throughout the dynamic range. Although this compensation technique permits excellent accuracy, it has an inherent limit. As the current reaches the "end" of the sine wave (or at an angle of plus and minus π radians) and continues to increase, the electronics may interpret the current to be higher than its previously measured current, or may interpret the current to be at the opposite end of the sine wave transfer function. The sensor will show a severe jump in the measurement of the current to a current of negative polarity with respect to its previous value. This phenomena is illustrated in Figures 7.2, 7.3 and 7.4 which show sensor outputs for 1 current loop, 3 loops, and 5 loops.

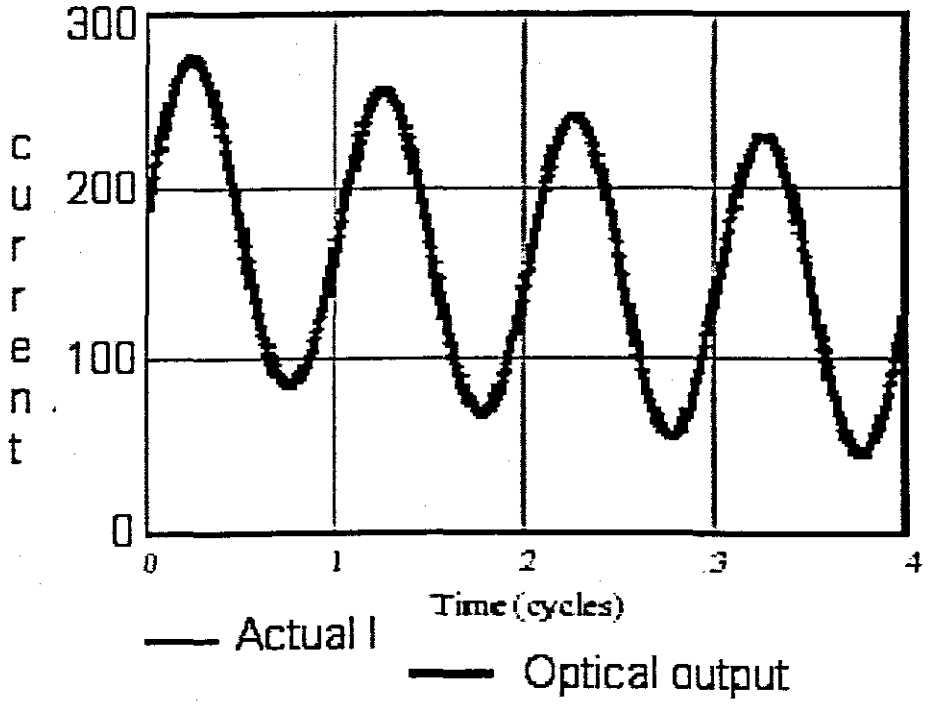

Figure 7.2 Optical and actual current on primary

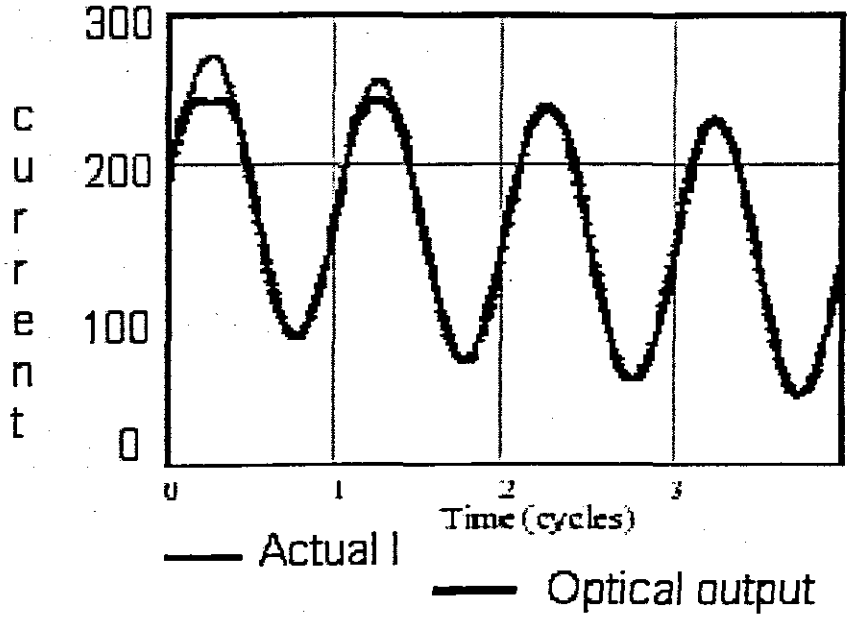

Figure 7.3 Optical and actual current on primary

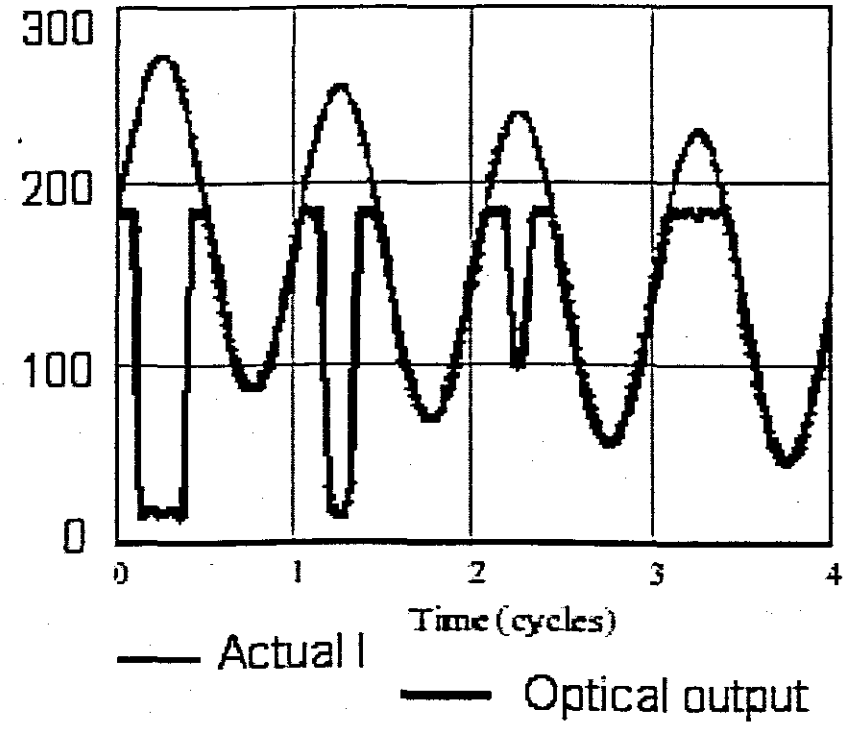

Figure 7.4 Optical and actual current on primary

As more current loops are added to the sensor design, the signal-to-noise ratio of the output increases, though not detectable in the figures. A better signal to noise ratio has certain distinct advantages, especially in metering applications (Hrabliuk, J.D.P., 2001). However, as the fiber turns are increased and the fault level is maintained at a constant level, operating range on the optical transfer function approaches the limit of plus and minus π radians. If exceeded, the sensor can record a current "jump", or move to the next optical "fringe" and thus appear as a different current value. To avoid this situation, which cannot be tolerated by relays, either special processing algorithms can be introduced to keep track of which fringe the sensor is on or the sensor can be designed to reduce possibility of such an occurrence. Fortunately, for typical fault current levels, reducing the probability of the sensor exceeding the "fringe" is simple, since the point at which the optical sensor reaches this point is precisely known based on the number of fiber turns used in an optical current sensor. This would eliminate the distortions seen in figures 7.2 and 7.3, provide an accurate current waveform representation free from saturation effects, and provide a high signal-to-noise ratio so the signal is also optimized for metering and power quality analysis applications. To a user of fiber based optical current sensors, the situation will never be observed unless a sensor is driven to a value beyond its specifications.

Our fiber optic current sensor (as shown in figure 7.5) consists of a light source, photo detector, optics and electronics coupled to a fiber sensor head around which is wound a current carrying conductor. The real time signal processing by means of the digital data capture is the "heart" of the current sensor technology and it, along with the electronics and optics, provide a highly accurate measurement of current.

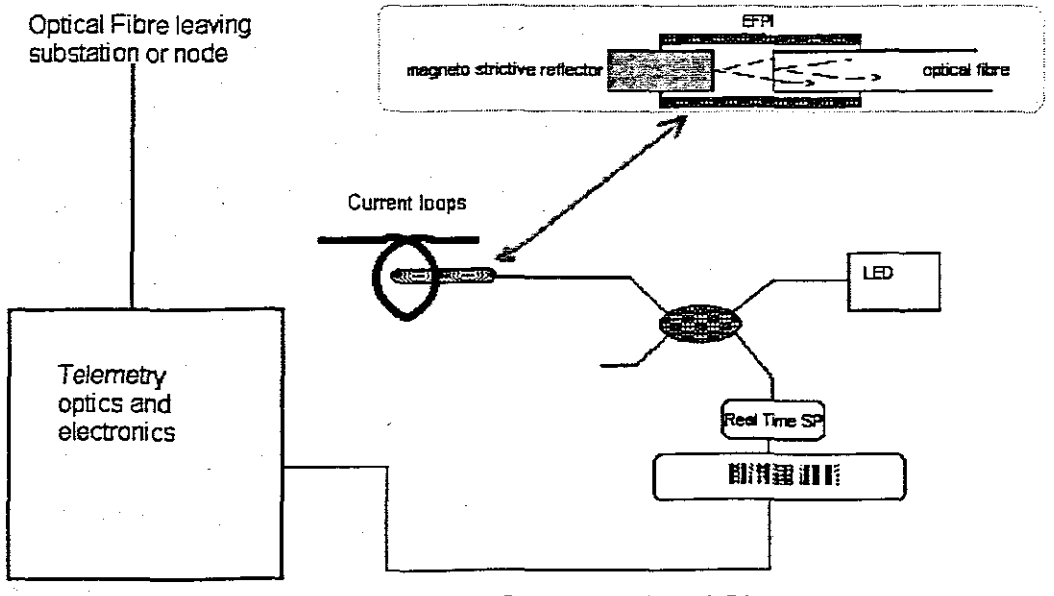

Figure 7.5: Fiber Optic Current Sensor Optical Block Diagram

A light source sends light through a waveguide to a EFPI with a magnetostrictive reflector, thereby transducing current to gap length modulation of the EFPI. The phase shift between the two light waves of the EFPI is proportional to current The optical phase shift is then processed and encoded and made available as a read-out or sent further along by optical fibre to other nodes in the national grid network or end user.

7.5 Conclusion

It was shown that the optical current sensors provide a reliable method of measuring very high fault currents with significant DC offsets without any type of saturation, as is understood with conventional current transformers. Depending on the design of the sensor, several turns of current carrying conductor can be wound around the EFPI to increase the signal to noise ratio of the sensor. This gain in signal to noise ratio is traded with the ability of the sensor to measure extremely high fault currents without fringe management algorithms. However, if desired, advanced processing techniques such as fringe management techniques can be implemented in sensors, and high signal to noise ratios and high fault current measurements can be achieved simultaneously.

Chapter 8

OPTICAL FIBRE SENSOR TELEMETRY FOR LARGE NETWORKED SENSOR TOPOLOGY: an overview

8.1 Introduction

Given the enormity of the work that has recently transpired in fibre optic sensors, it is relevant to introduce sensor telemetry for intelligent systems using the code division multiplexing techniques commonly employed in cellular telephone networks. In this paper, this code division multiplexing is explored with the idea of expanding it to a more desirable large scale sensor network using optical fibre for applications in electrical energy distribution systems.

8.2 Topology of the sensor network

In this chapter the establishment of a feasible optical bus for multiple sensor multiplexing, without the synchronisation problems associated with time division multiple access, was achieved. For this purpose code division multiplexing was used.

Most popular electrical data networks have a ring or bus topology because of power budget considerations. Due to present advances in ebrium doped fibre amplifiers, optical fibre busses for sensor data, have become feasible (Wagner, 1987) (Khan, 1998). The principle of optical CDM is based on spread spectrum techniques, which have been widely used in digital cellular communication systems (Dixon, 1994). In this technique the energy in the optical signal is spread over a frequency band that is much wider than the minimum band that is needed to send the information. The spreading is usually done by a code that is signal independent and an encoder is used to map each bit of information into a high rate optical sequence. This set of optical sequences becomes a set of unique address codes for individual sensor nodes. The symbols in the spreading code are known as chips. Time domain optical CDM allows a number of different sensor nodes to be networked through the use of a common wavelength. This method

will aim to be on par with WDM and is more than sufficient for sensor data transmission.

8.3 Modelling the network

In this model, rectangular E field vectors are considered for simplicity. For incoherent correlation it is necessary according (Ohlson, 1989) to assume that the photo detector in the sensor data bus receive two broadband signals. In the method developed for this paper I depart from Ohlson's theory by considering the autocorrelation function and then to derive the power spectrum.

The signal and noise fields can therefore be represented as follows.

$$S_E(t) = \sqrt{2P_S}\eta_S(t)e^{-j\omega_0 t} \tag{8.1}$$

$$N_E(t) = \sqrt{2P_N}\eta_N(t)e^{-j\omega_0 t} \tag{8.2}$$

where η is the normalised signal and noise complex envelopes.
The combined field will then be:

$$E_{S,N}(t) = S_E(t) + N_E(t) \tag{8.3}$$

and the photo diode output

$$v(t) = \tfrac{1}{2}\Re E_{S,N}(t)E^*_{S,N}(t) \tag{8.4}$$

Therefore

$R_v(\tau) = \overline{v(t)v(t+\tau)}$ is the auto correlation function of $v(t)$ and

$$\frac{4R_v(\tau)}{\Re^2} = \overline{(S_E(t)+N_E(t))(S_E(t)+N_E(t))^*((S_E(t+\tau)+N_E(t+\tau))(S_E(t+\tau)+N_E(t+\tau))^*} \tag{8.5}$$

An expression of 16 terms is created if we expand the brackets on the right hand side of the equation which is simplified as,

$$\overline{S_E(t)S_E^*(t)N_E(t+\tau)N_E^*(t+\tau)} = \overline{|S_E(t)|^2}\,\overline{|N_E(t+\tau)|^2} = 4P_S P_N \tag{8.6}$$

This simplification is possible because we consider that the fields in the waveguide are statistically independent so that averages of products may be replaced with products of averages. If both fields have zero mean then:

$$\overline{S_E(t)} = \overline{S_E(t+\tau)} = \overline{N_E(t)} = \overline{N_E(t+\tau)} = 0 \tag{8.7}$$

All unbalanced terms will therefor be zero. In the book, Statistical Optics, (Goodman, 1985), for thermal like signals the signal and noise electric fields may be modelled as circular complex Gausian random processes. Therefore:

$$\overline{|S_E(t)|^2|S_E(t+\tau)|^2} = \overline{|S_E(t)|^2}.\overline{|S_E(t+\tau)|^2} + \overline{|S_E^*(t)S_E(t+\tau)|^2} \tag{8.8}$$

The first term in the right hand side of the equation is indirectly $4P_s^2$ while the second term is the modulus of the self coherent function $\Gamma_s(\tau)$. Using the equation from (Goodman,1985), and remembering power spectral density to be constant over bandwidth we get,

$$\Gamma_S(t) = \int_0^\infty 4D_S(f)e^{-j2\pi f\tau}df \tag{8.9}$$

$$\Gamma_S(t) = \frac{2P_S}{B_S}\int_{f_0-\frac{B_S}{2}}^{f_0+\frac{B_S}{2}} e^{-j2\pi f\tau}df \tag{8.10}$$

$$\Gamma_S(t) = 2P_S e^{-j2\pi f_0\tau}\frac{Sin(\tau\pi B_S)}{(\tau\pi B_S)} \tag{8.11}$$

where $(\tau\pi B_S) = \alpha$

Interchanging in equation (8.5) gives us therefore,

$$\frac{R_v(\tau)}{\Re^2} = (P_S + P_N)^2 + P_S{}^2\left(\frac{Sin(\alpha_S)}{\alpha_S}\right)^2 + P_N{}^2\left(\frac{Sin(\alpha_N)}{\alpha_N}\right)^2 + 2P_SP_N\left(\frac{Sin(\alpha_S)}{\alpha_S}\right)\left(\frac{Sin(\alpha_N)}{\alpha_N}\right) \tag{8.12}$$

To get the power spectrum of $v(t)$ we take the Fourier Transform of $R_v(\tau)$. We then consider the contribution to the combined spectrum with $(P_S + P_N)^2$ being the DC equivalent voltage. In this case the signal times the beating is presented as $P_S{}^2\left(\frac{Sin(\alpha_S)}{\alpha_S}\right)^2$. Spectrally this can be represented as triangular baseband of width B_s.

Figure 1 shows the physical implementation of the code division multiple access system proposed for optical fibre sensor data telemetry over vast distances.

8.4 Conclusion

In the proposed sensor system the optical fibre sensors are coupled by CDMA to a single optical bus on a typical transmission line. At any remote location the data can be extracted uniquely. This is possible for any NxN sensors deployed in such a large scale system and as shown in equation (8.12) it is possible to isolate each sensor data from the rest of the signals on the bus.

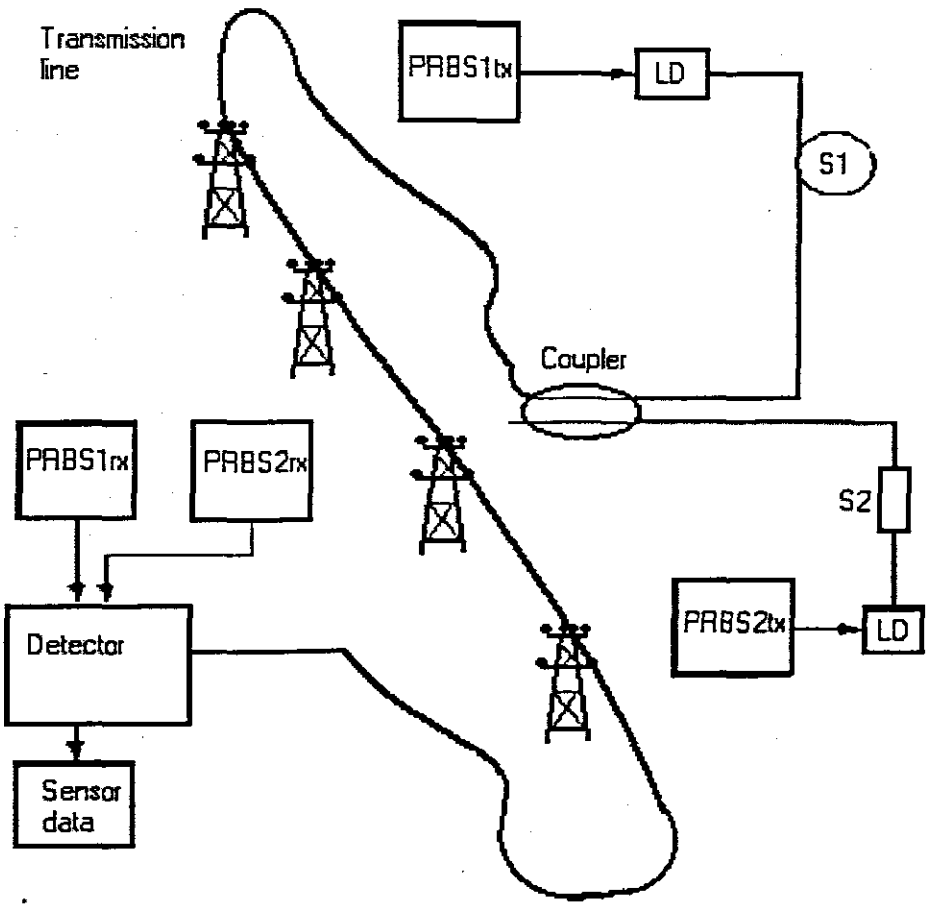

Figure 8.1. Sensor system deployment

Chapter 9

THE DESIGN OF A MULTIPLEXING TECHNIQUE FOR NETWORKED POINT SENSORS BY MEANS OF CODE DIVISION MULTIPLEXING

9.1 Introduction

In order to network many sensors as discussed in chapter 8, it is necessary to explore successful multiplexing methods and multiplexing algorithms that have been used on same-signal devices. Code division multiplexing has been used to multiplex same-signal communications devices for some time. Closely related research has resulted in the multiplexing of fiber optic sensors onto the same network. Given the enormity of the work that has in the process of this research transpired, this makes sense. In this chapter, this same-signal multiplexing work is explored with the idea of expanding it to a more desirable mixed-signal network, for the optical fiber sensor design for large networks which is the topic of this thesis.

9.2 Code Division Multiplexing History

Code division multiplexing utilizes pulse compression and cross-correlation techniques, originally developed for radar, to reduce signal to noise ratios (Whitesel et al ,1997). The technology provides for the increase of the number of optical sensors one can monitor with a single optical source. It was adapted to multiplexing optical sensors on an experimental basis starting in the 1980's (Mlodzianowski et al, 1988) (Kersey et al, 1992) (Street & Edwards, 1995) (Walker et al, 1992). It is also used in cellular telephone networks where it is called Code Division Multiple Access (CDMA).

9.3 Pseudo-random Bit Sequences

At the heart of code division multiplexing is the pseudo random bit sequence which is a series of pulses that appear to mimic white noise. These lend themselves to being incorporated into digital signal processing. A maximal length pseudorandom bit sequence is one that has a length of 2^m-1 where m is an integer. Maximal length pseudorandom bit sequences satisfy certain postulates of randomness. They are:

- In every sequence period, the number of +1's shall not differ from the number of -1's by more than one.
- For every sequence period, half of the runs (a run being a subsequence of -1 or +1) have a length of one, a quarter of the runs have a length of 2, one eighth of the runs have a length of 3 and so on as long as the number of runs exceeds one.
- Furthermore, for each of the runs there are equally many runs of +1's and −1's
- The autocorrelation function is binary valued; that is

$R(m) = p, m = 0,$

$R(m) = c, 0 < |m| < p$

We desire $p>>c$ so that the sequences look white (Dixon,1994:99). The autocorrelation function for a 7 bit length code is shown in Figure 9.1.

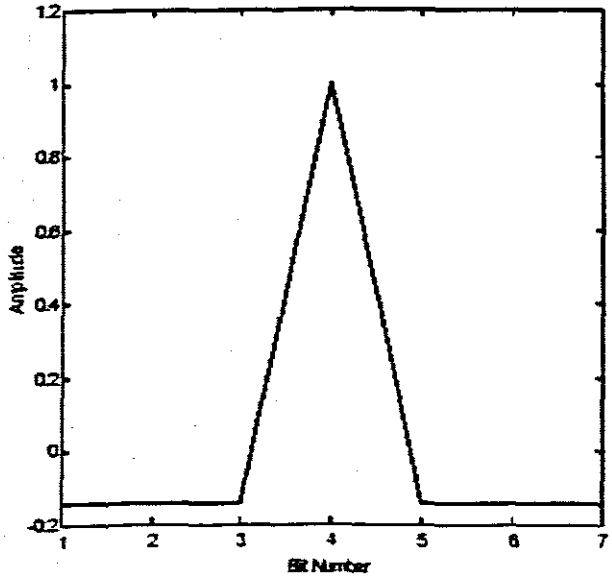

Figure 9.1 Autocorrelation of a 7 bit sequence

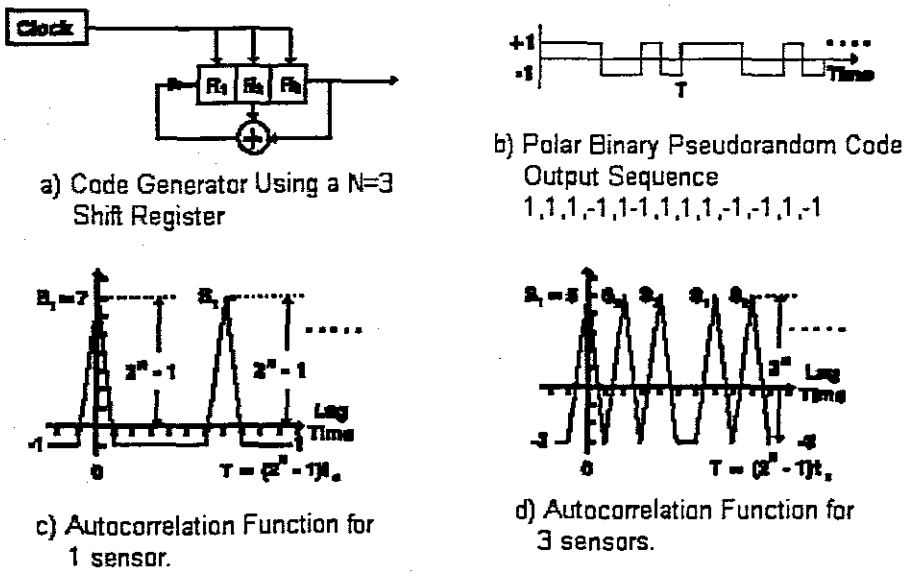

a) Code Generator Using a N=3 Shift Register

b) Polar Binary Pseudorandom Code Output Sequence
1,1,1,-1,1-1,1,1,1,-1,-1,1,-1

c) Autocorrelation Function for 1 sensor.

d) Autocorrelation Function for 3 sensors.

Figure 9.2 Autocorrelation functions for 1 and 3 sensors

9.4 Code Generation

Code generation is key to this form of multiplexing. These are typically generated in hardware, by the use of clocks and logical flip-flop circuits. Figure 9.2(a) (Whitesel et al, 1997) shows the design of a code generator made up of a 3 stage shift register. The pseudorandom pulse sequence repeats every 7 pulse times, labeled T in Figure 9.2(b). The pulses are also polar binary, meaning they return to a negative number, not to zero. The calculated autocorrelation functions, shown below, for both a single optical sensor and for 3 optical sensors repeats every 7 pulse times. Three sensors are the maximum number of sensors that can be interrogated for a 3 stage shift register, because each correlation function requires 2 pulse times and the sequence repeats every 7 pulse times. Calculating the autocorrelation function is simply a matter of adding the number of agreements and then subtracting the number of disagreements as the code is compared

with itself. For example, with a 3-stage register, the code that is generated is 0111001. If one compares this code with an identical code, the number of agreements is 7, i.e. 0 agrees with 0, 1 agrees with 1, 1agrees with 1, and so on. The number of disagreements is 0. If the code is now compared with a version of itself that has been slipped one pulse time, for example 1011100, the same calculation is performed. The number of agreements is 3 and the number of disagreements is 4, leading to a correlation of -1. This is also shown in Table 9.1. After the code has been compared with a slipped version 7 times, the sequence repeats. The same is true for 3 identical codes in a row, ie. the 3 fiber optic sensor system.

Table 9.1 Shift of a 7 bit sequence

Shift	Sequence	Agreements	Disagreements	A-D
1	0111001	3	4	-1
2	1011100	3	4	-1
3	0101110	3	4	-1
4	0010111	3	4	-1
5	1001011	3	4	-1
6	1101001	3	4	-1
7	1110100	7	0	7

9.5 Code Correlation

Table 9.1 shows how timing slip affects autocorrelation. When the code is shifted by one or more bits, the correlation is -1. When the code is in the zero-shift condition, the correlation is 7. Sometimes these numbers are divided by the code length to normalize the maximum autocorrelation. Obviously normalization would lead to a zero-shift correlation of 1 and the shift correlation of -1/7 in this case. Another important characteristic is cross correlation with other codes. A desirable property is for two codes to have low cross correlation no matter what the time difference is between them. This is necessary if one wants to send two codes without regard to timing and have the resultant signals have low cross talk between them. An example of two 31 bit length codes that show low cross correlation regardless of timing slip is shown in Table 9.2. Here the maximum cross correlation is 7 whereas the maximum auto correlation is 31. These codes could be used, without regard to timing, in a system together, unless the power of one was sufficiently larger than the other to cause a cross correlation close to the peak value 7.

Table 9.2 Correlation of two 31 bit length codes

Shift	Agreements (A)	Disagrrements(D)	A-D
0	15	16	-1
1	19	12	7
2	15	16	-1
3	11	20	-9
4	19	12	7
5	15	16	-1
6	19	12	7
7	15	16	-1
8	15	16	-1
9	15	16	-1
10	15	16	-1
11	19	12	7
12	19	12	7
13	15	16	-1
14	15	16	-1
15	19	12	7
16	15	26	-1
17	15	16	-1
18	11	20	-9
19	11	20	-9
20	11	20	-9
21	19	12	7
22	11	20	-9
23	15	16	-1
24	19	12	7
25	19	12	7
26	15	16	-1
27	15	16	-1
28	15	16	-1
29	15	16	-1
30	19	12	7
31	15	16	-1

9.6 Interfacing to the sensor systems

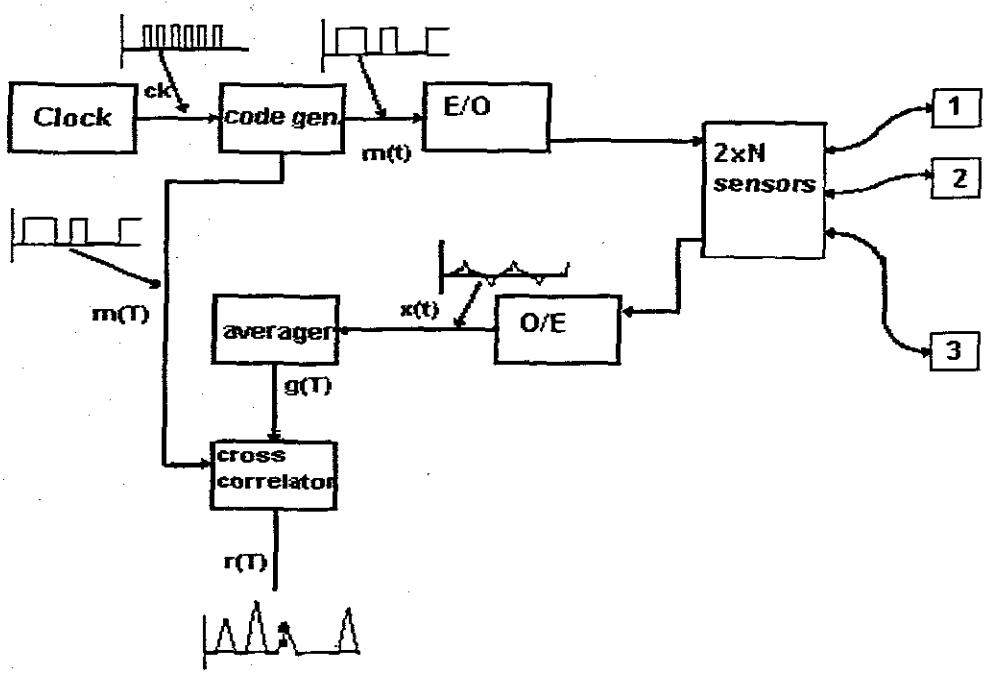

Figure 9.3 : Secure demodulation of N sensors in a network

In an effort to network same-signal sensors using software and signal processing, (Whitesel et al, 1997) have demonstrated a system that multiplexes 32 fiber optic sensors using code division multiplexing, and information for much of this design is taken directly from that work. The operating schematic for the system that was developed for the research of this dissertation, which differs from that of Whitesel et al in that more sensors are allowed on the network, is shown in Figure 9.3

Here, a master clock continuously puts out high frequency, on-off pulses into the code generator which changes these regularly occurring pulses into a seemingly irregular sequence of pulses m(t). The zero states (or zero crossings) occur at pseudorandom times that are some multiple of the pulse time, the period of the master clock. The code generator then drives an electro-optic (E/O) interface which may be either LED or Laser based, thereby generating a pseudorandom optical pulse sequence transmitted through the 2 x N optical coupler to each of the N sensors. Each sensor is connected with slightly

different lengths of fiber cable, causing the reflected signal from each Fabry-Perot sensor to each arrive at the receiver at slightly different times, as determined by the optical transit time through the different length cables. The 2 x N optical coupler divides the optical power to the point where the received signal (O/E) , *x(t),* appears like random noise mixed with several versions of the transmitted pseudorandom pulse sequence. The sensor response at this point is not visually discernable. The averager enhances the sensor signals by reducing incoherent noise, generating an ensemble averaged signal *g(T).*

The cross correlator calculates the correlation of the reflected sensor signals with the transmitted pseudorandom pulse sequence, $P_{mg}(\tau)$, which peaks in value when the time delay corresponds to the round trip optical transit time from the optical source to each optical sensor and back to the receiver. Noise that is not coherent to the transmitted pseudorandom pulse sequence is rejected. Each sensor peak occurs at a different point in time corresponding to the optical time delay in each sensor channel. The sensor signals can then be displayed.

The cross correlation function, $P_{mg}(\tau)$, can be expressed as the sum of scaled and delayed versions of the autocorrelation function,

$$P_{mg}(\tau) = \int_{-\infty}^{+\infty} m(t)\,g(t+\tau)\,dt \tag{9.1}$$

$$p_{mg}(\tau) \approx \int_{-\infty}^{+\infty} \{S_1[m(t)\cdot m(t-t_1+\tau)\} + \{S_2[m(t)\cdot m(t-t_2+\tau)\} + \ldots \{S_M[m(t)\cdot m(t-t_M+\tau)\}dt$$

$$\text{hence} = \sum_{n=1}^{N} S_n p_{mm}(\tau - t_n) \tag{9.2}$$

where

S = Reflection coefficient from sensor k, (k = 1, 2,.....N),

m(t) = Transmitted pseudorandom pulse sequence,

g(t) = Ensemble averaged reflected signal from all sensors and

t = Time delay for sensor k, (k = 1, 2,.....N) and J = Lag-time variable k

The response of each sensor can then be determined by simply measuring the peak values of the calculated autocorrelation function at the appropriate delay times. However, there are residual errors that arise from cross coupling of the autocorrelation response of each sensor.

When there is no time delay match between the reflected pulses and the transmitted pulses, the autocorrelation function returns to a value of −1 times the sensor reflectivity, S_1, as shown in Figure 9.2(c). This is the residual value of the autocorrelation function and in general is given by $1/2^M$ for each sensor. For the 3-stage shift register shown in Figure 9.2(a) connected to 1 sensor, this residual value is 12.5%. Adding 2 more sensors for a total of three gives a residual error of $3/2^M$ .In general the residual value of the autocorrelation function is given by $N/2^M$, where N is the number of sensors. Three sensors with a 3 stage shift register gives a residual value of the autocorrelation function that increases to 3/8 of S_1 , or 37.5%, as shown in Figure 9.2(d).

9.7 Benefits from using the proposed CDMA telemetry technique.

Innovative solutions need to focus on the integration of functionality while at the same time reducing the number of parts. When we look in more detail behind the move to more economic solutions by means of new technology, then there are two main drivers that form the basis of a total cost analysis. These two main factors are Initial investment costs and Operation and Maintenance (O&M) costs:

9.7.1 Initial Investment Cost

The initial investment costs include the resource and monetary cost to a utility when establishing a new investment such as a replacement of existing current transformers in the system. Reducing these factors lead to a decreased initial investment cost based on:

1.) Reduced consumption of resources,

2.) Reduced effort in engineering,

3.) Safe handling of a complex system like a substation,

4.) Reduced number of different designs,

5.) Reduced installation time,

6.) Scalable architecture

9.7.2 Impact on Asset Management

The advantage of the new solutions are visualized thorough evaluation of operational and maintenance costs. The new systems allow for simple and clear direction in operation and maintenance policies for the asset owner. Items such as:

1.) Lower maintenance cost due to monitoring functions. Monitoring leads to new concepts of maintenance on demand.

2.) Reduced operational costs due to availability of online and detailed data direct from the station and the process and the related optimization of operational procedures

3.) Increased availability created from self supervision functions

4). Reduced spare parts stock, reduced inventory

5.) Scalable architecture advantageous for all size of installations and extensions

9.8 Summary of Code Division Multiplexing Telemetry

Code division multiplexing of same-signal devices, here basic optical fiber Fabry-Perrot sensors, has been successfully demonstrated. Key points of consideration are timing, slip, power budget, code length, autocorrelation, and cross correlation between two codes. The benefit of code division multiplexing as applied to optical fiber sensors is increased system signal to noise ratio thus allowing the multiplexing of a large number

of sensors to one optical source (Whitesel et al, 1997). With computing power continually decreasing in cost, code division multiplexing becomes more attractive since the complexity of the technique is inherently in the signal processing software as opposed to the optics. This means optical systems can be constructed without the manufacture of special optical devices which add cost. This chapter has spelled out in detail the mathematics and algorithms behind code division multiplexing of a same-signal sensor source. These algorithms can be included in signal processing software to multiplex different type sensor signals. For this research we have chosen one of these to be any standard current transformer with digital interfacing as a sensor.

Chapter 10

SYSTEMS DESIGN AND ANALYSIS OF THE NETWORKED FIBRE OPTIC SENSOR TOPOLOGY.

10.1 Introduction

One of the prime aims of this thesis was to model the multiplexing of different Optical Fiber and other electrical sensor signal sources using a software and signal processing approach. An analysis was performed to determine the issues involved in multiplexing the different sensor signal sources, and how those issues could be resolved using good software design. The systems analysis also determined the correct operating parameters.

10.2 Description

A schematic of the effort is shown in Figure 10.1. There are two code generators, one for the subsystem of fiber optic sensors, and one for the simulated sensor. These sensors generate different codes so the digital interface sensor can send information without regard to the timing of the fiber optic sensors and vice versa. The optical signals from the digital interface and fiber optic sensors are fed through couplers into the receiver where they are converted to electrical signals and then fed into the computer. There the cross correlation is taken and the measurand computed and displayed. The simulated digital interface sensor consists of a commercially available accelerometer, the Analog Devices ADXL-05, which was identical to the ADXL-50 air bag sensor, but has a lower operating range of approximately 5 g's as opposed to the ADXL-50's 50 g range (Koester et al, 1996)(ADXL-05 Specification Sheet: 1996). This sensor modulates an LED with a 0 to 5 volt output which is pulsed by the pseudorandom bit generator. This was the manner in which the digital interface sensor was used to simulate the second

type of sensor after fiber optics sensor. Other components were chosen to ensure the system was compatible with the overall goal of multiplexing different sensors signal sources. The components selected for the system include the Hewlett Packard 1414T LED and the companion 2416T detector . The optical fiber selected during testing was 62.5/125 μm multimode graded index:22 and the couplers were Gould 2x2 with approximately 4db overall insertion loss. These components were chosen due to their availability , ease of breadboarding and relatively low cost testing of the concept. This may be expanded to single mode fibre systems. and results may easily be correlated for our national grid based optical fibre sensor topology.

10.3 Power Budget

In order for the sensor system network to operate with compatibility of at least two different sensor types, a power budget was performed which is shown below. Referring to Figure 10.1, the system is divided into two sections, A and B, and then analyzed for the power budget.

SECTION A:

The parameters are LED output: -11dBm, total coupler insertion loss 4dB each, connector loss 1dB each. Taking the case of the fiber optic intensity sensors first and going from the LED to the detector, the power budget calculation is:

$P_{FO} - 1 - 4 - 4 - 4 - 1 = P_{FO} - 14dB_m$ at the detector

SECTION B:

Going from the LED in the simulated digital interface sensor, we have:

$P_{digital} - 1 - 4 - 1 = P_{digital} - 6dB_m$

From this, in order to have signals of approximately equal power at the detector,

$$P_{FO} = P_{digital} - 8dB_m$$

This means that the power in the fiber optic sensor LED must be 8 db higher than the power in the sensor with digital interface LED. This can be accomplished by correct circuit design and is not the subject of this thesis.

10.4 Correlation and timing

In order to allow both types of sensors to send and receive signals on the same transmission path, the issue of using software to determine signal correlation was studied. The study found that a major issue in code division multiplexing as applied to fiber optic and digital interface sensors is calculating the cross correlation of two signals. While the calculation can be performed in the time domain, the total number of calculations can be rather high. What is desired is an expression of the cross correlation in the frequency domain. Performing the cross correlation in the time domain takes approximately N calculations where N is the code length, and performing the entire calculation in the frequency domain requires approximately $3N\log_2(N)$ calculations. (Porat, 1997). The expression for the time domain calculation of the cross correlation of two signals is derived below (Stremler, 1996).

The cross correlation function is defined as

$$p_{fg} = \int_{-\infty}^{+\infty} f(t)g(t+\tau)dt \qquad (10.1)$$

Taking the Fourier transform of equation (10.1) we obtain

$$F(p_{fg}(\tau) = \int_{-\infty}^{+\infty}\int_{-\infty}^{+\infty} f(t)g(t+\tau)dt \cdot e^{-j\omega\tau}d\tau \qquad (10.2)$$

Interchanging the order of integration in equation (10.2) we have

$$F(p_{fg}(\tau) = \int_{-\infty}^{+\infty} f(t) \int_{-\infty}^{+\infty} g(t+\tau) \cdot e^{-j\varpi\tau} d\tau dt \tag{10.3}$$

Use of the time delay property gives

$$F(p_{fg}(\tau)) = \int_{-\infty}^{+\infty} f(t) G(\varpi) \cdot e^{-j\varpi\tau} dt \tag{10.4}$$

and finally, using the definition of the Fourier transform, we have

$$F(p_{fg}(\tau)) = F(\varpi) G(\varpi) \tag{10.5}$$

From this we can see that the cross correlation is simply the inverse Fourier transform of the products of the Fourier transforms of both the transmitted and returned signal. Thus we have obtained the necessary expression to allow efficient software to be developed for the signal processing.

Not only is it necessary to have different types of sensors signals multiplexed together, it is also necessary to have the same type of sensors multiplexed onto the system. Here the fiber optic sensors need to have a delay in order for the software to be able to separate out the signals.

To obtain different codes for each sensor, two code generators were used, one for the fiber optic sensors and one for the simulated digital sensor. Since the fiber optic sensors are in the same line, the output of fiber optic sensor 1 can be discerned from that of fiber optic sensor 2 simply by putting in the delay coil in line with sensor 2.

If the length of this delay coil is adjusted to make the delay greater than one pulse time, the outputs of both sensors can be detected using the original code. This set-up is shown in Figure 10.1

Formulae used in calculating the delay coil length are as follows:

$$s = vt$$

$$v = \frac{c}{n}$$

$$s = \frac{ct}{n}$$

where c = $3x10^8$ meters per second, n = index of refraction in the fiber core = 1.468,

and t = pulse time = 1/frequency = 1/1.8432Mhz. From this we obtain 111m

$$s = \frac{3 \times 10^8}{1.468} \frac{1}{1.8432 \times 10^6}$$

Therefore we need a delay coil of at least 111 meters in length to provide the new code.Thus we are able to create a physical design that allows for correct code timing of the two fiber optic sensors and also allows for the signal processing to separate them.

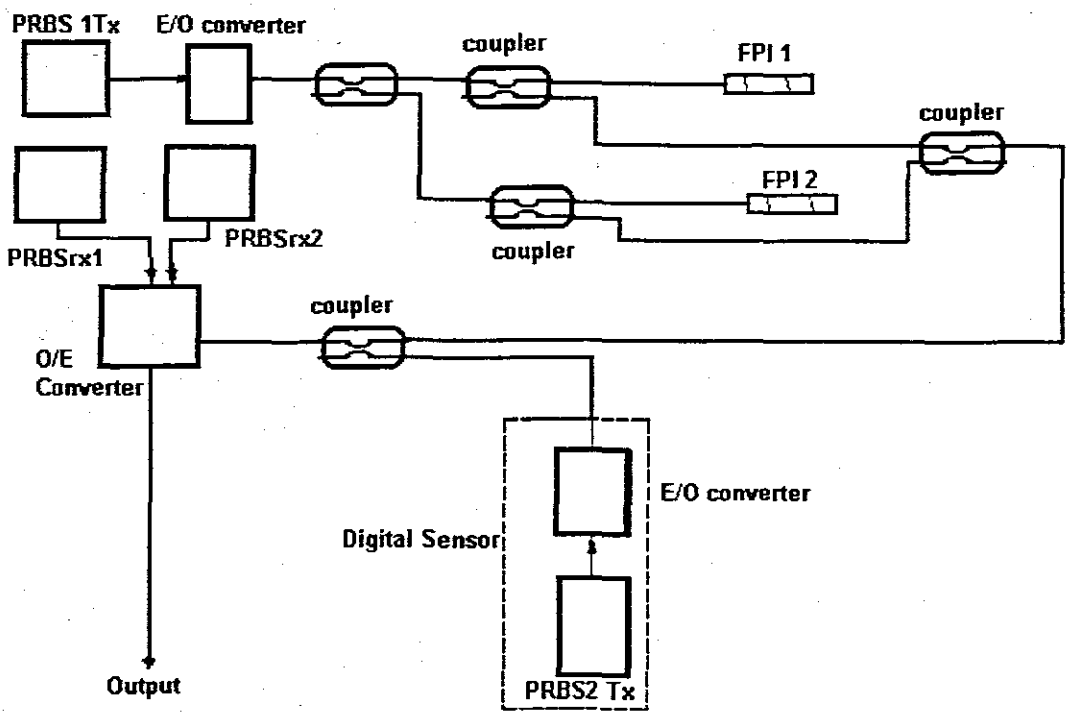

Figure 10.1. : Typical multiple sensor implementation

10.5. Code Selection

In this mixed-signal system it is necessary to allow all types of sensors to be received, and this is where code selection comes into play. If the correct codes are not implemented in the software design, the system will not work. In view of this, a detailed analysis of all possible codes was undertaken. A systems analysis was performed to determine the proper codes to use and to predict the experimental results. A MATLAB computer program was written to generate code pairs and their correlation plots, and to generate theoretical code pulses and correlation functions. Code selection is extremely important. The best codes to use are those that have already been determined to have characteristics attractive to signal processing (Dixon, 1994:99). It is desired to have pairs of codes that have a high degree of autocorrelation and a low degree of cross correlation, and certain codes lend themselves to this application because they have these properties. For ease of experimentation, a code length of 127 bits was chosen. All maximal bit length codes of this length were compared to determine the low cross correlation. The

results are shown in Figures 10.2 through 10.19. As can be seen, the lowest cross correlation was -17 and this was for several code pairs. Code taps of 7 1 and 7 3 were chosen in order to facilitate the experimentation. The correlation shows that both signals can be discerned, even though they are from different sensor sources.

10.6. Predicted Results

A MATLAB computer program was written to predict the actual results. These are illustrated in Figures 10.20 through 10.23. The output of a 127 bit length code is shown in Figure 10.20. This is the code that is sent out from either fiber optic or digital interface sensor. Figure 10.21 shows the same code after noise is added. This simulates the code received at the detector. Figure 10.22 shows the 7 1 and 7 3 codes after correlation. Figure 10.23 shows the 7 1 received code correlated with another 7 1 code. Note the correlation peak on the left hand side. The correlation is quite discernible to the naked eye, whereas the correlation between the 7 1 and 7 3 codes does not reveal any peak. This is desirable since cross talk between the fiber optic and digital interface sensors should be kept as low as possible.

10.7. Summary of the Systems Analysis and Design

In designing the software package, the MATLAB computer program was used because it possesses sophisticated signal processing capabilities necessary for a mixed signal sensors system. The signal processing was used to filter out the noise and the unwanted sensor signals to allow one to discern the desired sensor signal. Some issues that were uncovered were how to keep the signals separate and how to transform the sensor output of one system into an ouput that is compatible with the other system. Further, one could combine signals with a simple time domain or wavelength division method, but these would limit the number of possible maximum number of sensors since there is no inherent gain in these methods. That is why code division mutilpexing was chosen.

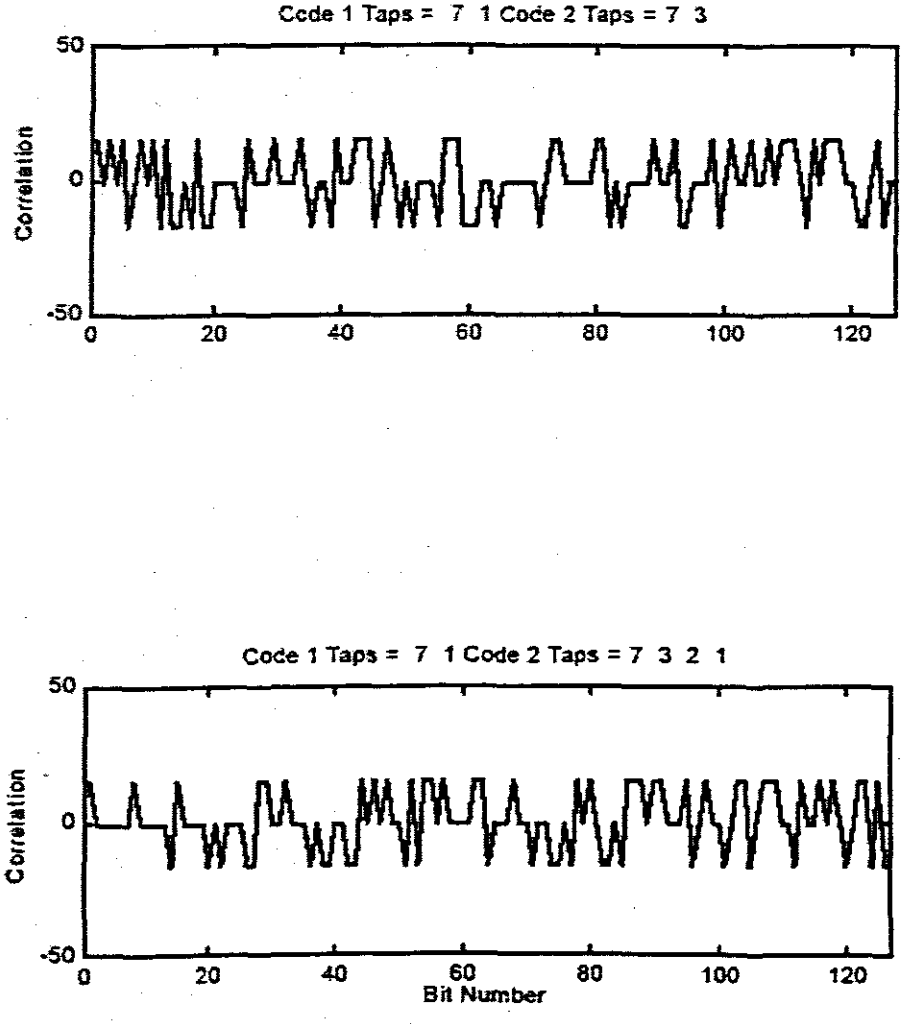

Figure 10.2 Correlations of code pairs 71,73 and 71,7321

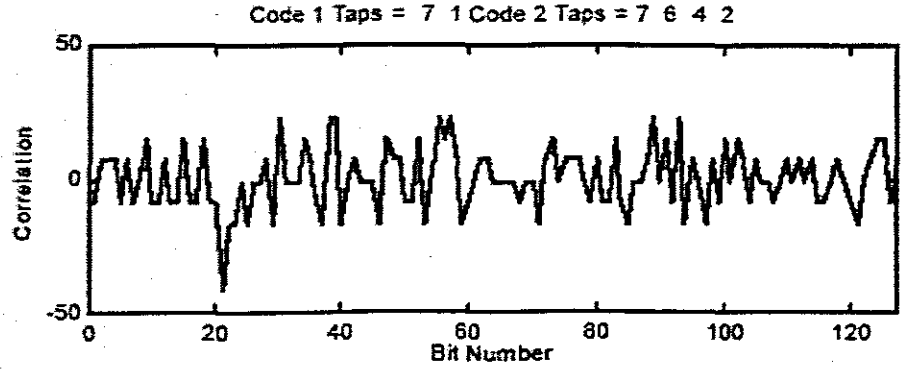

Figure 10.3(a) correlations of acode pairs 71, 7432

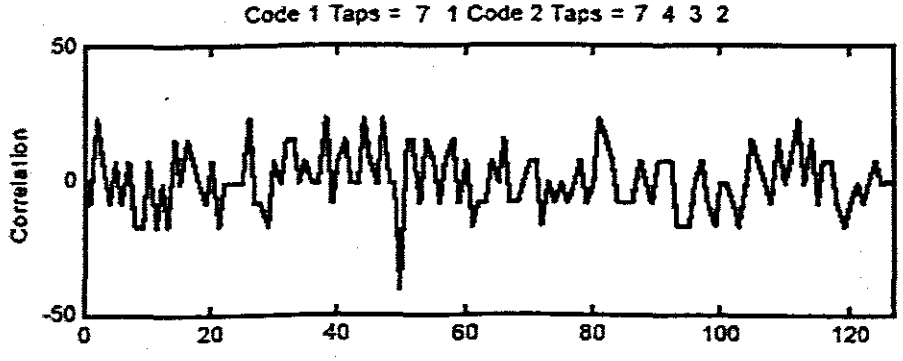

Figure 10.3(b) code pairs 71, 7642

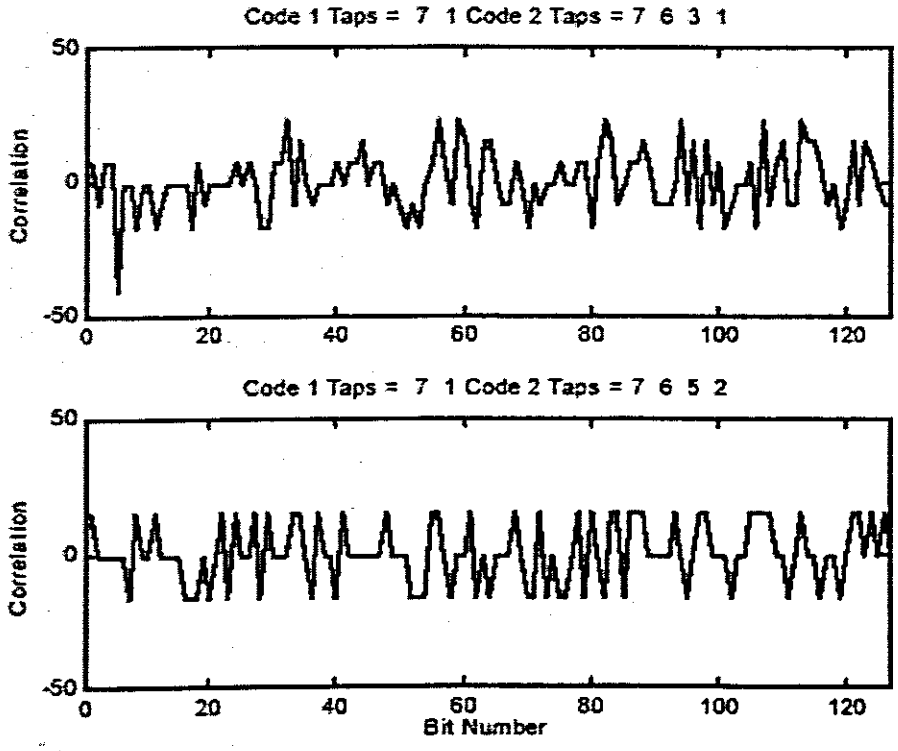

Figure 10.4 correlations of code pairs 71, 7631 and 71 7652

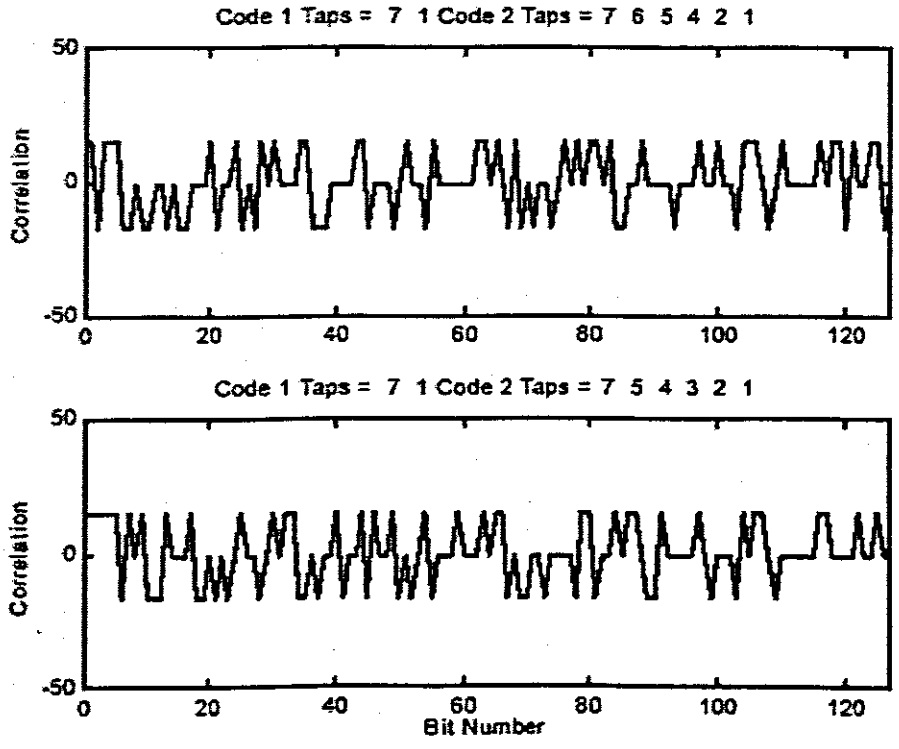

Figure 10.5 correlations for dode pairs 71, 765421 and 71, 75432

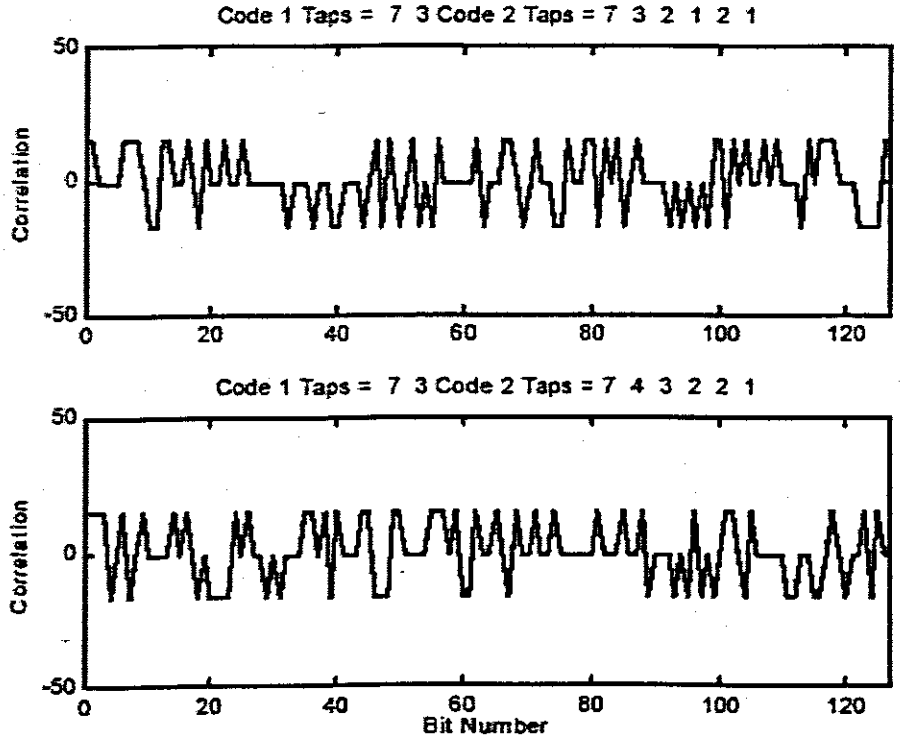

Figure 10.6 Code pairs 73,7321 and 73,74321

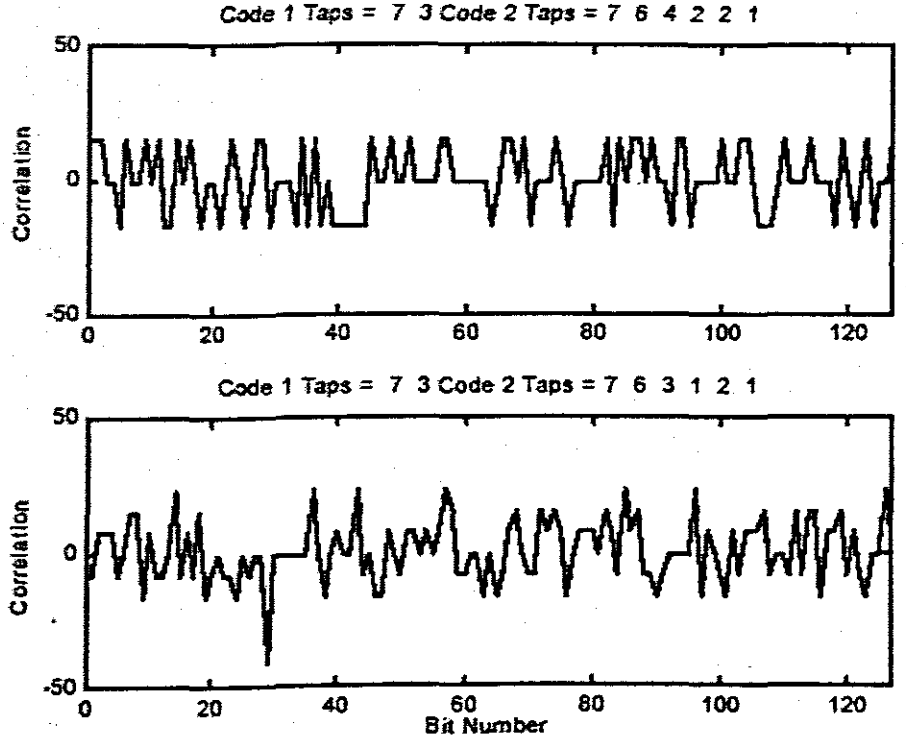

Figure 10.7 : Code pairs 76,76421 and 76, 76321

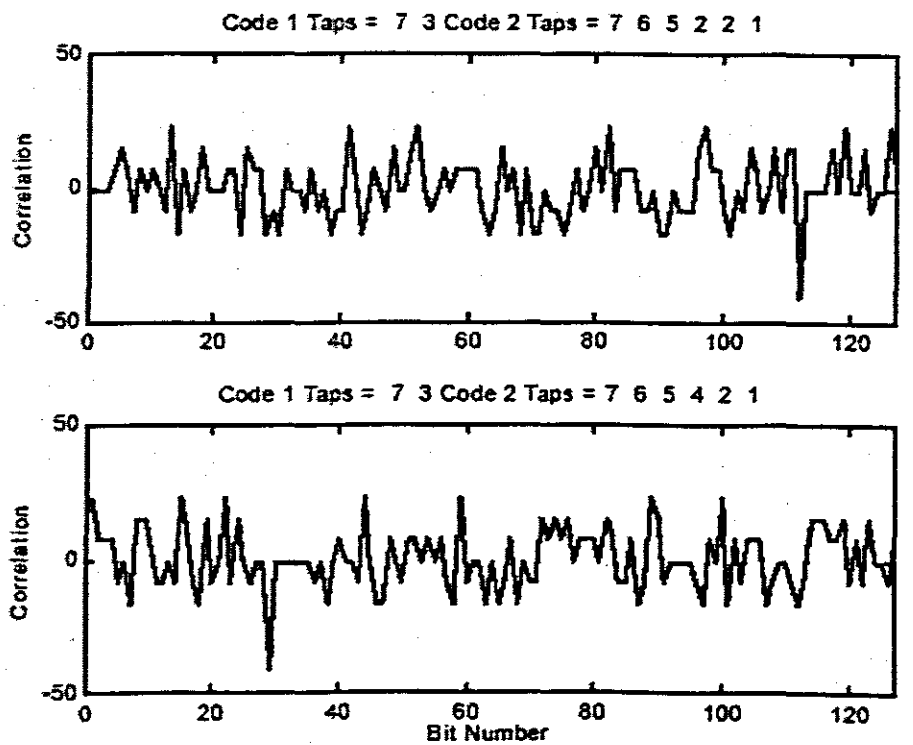

Figure 10.8 :code pairs 73,7621 and 73765421

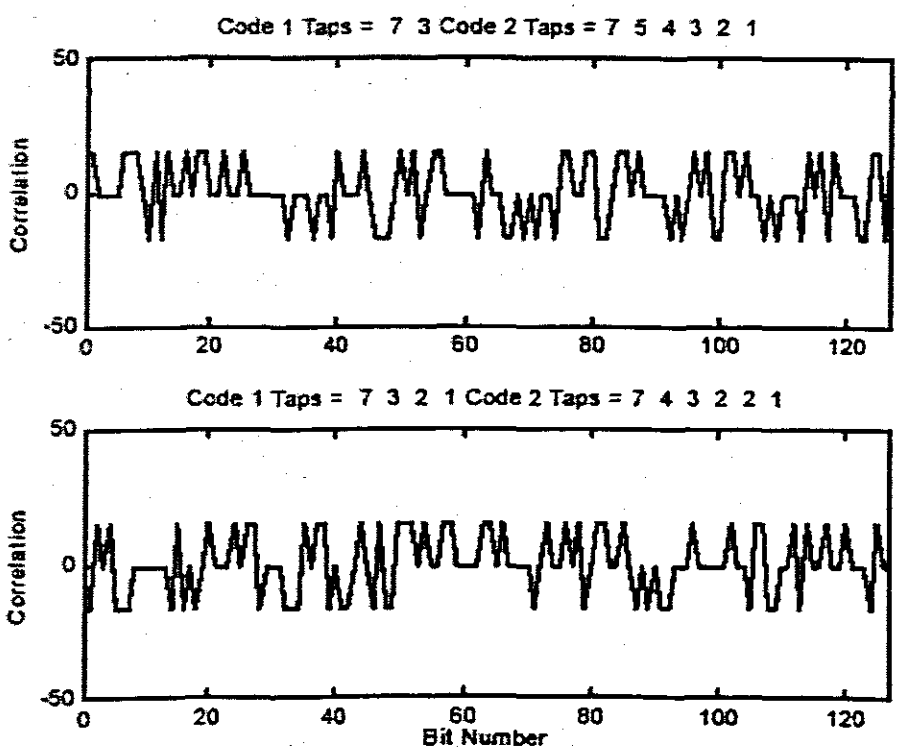

Figure 10.9 : code piars 73,754321 and 7374321

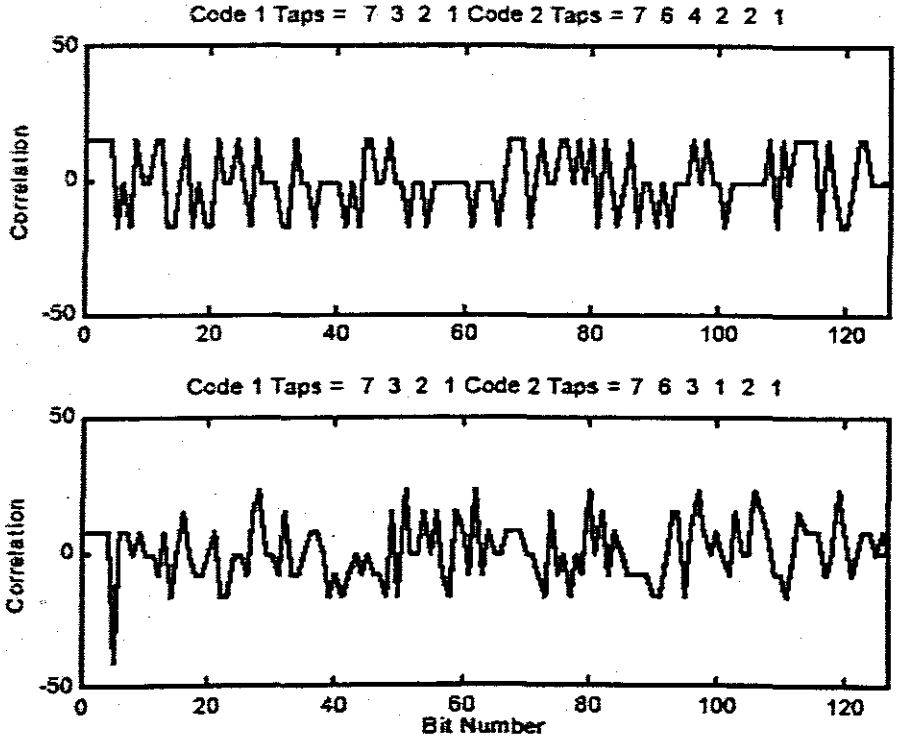

Figure 10.10 code pairs 7321,76421 and 7321, 76321

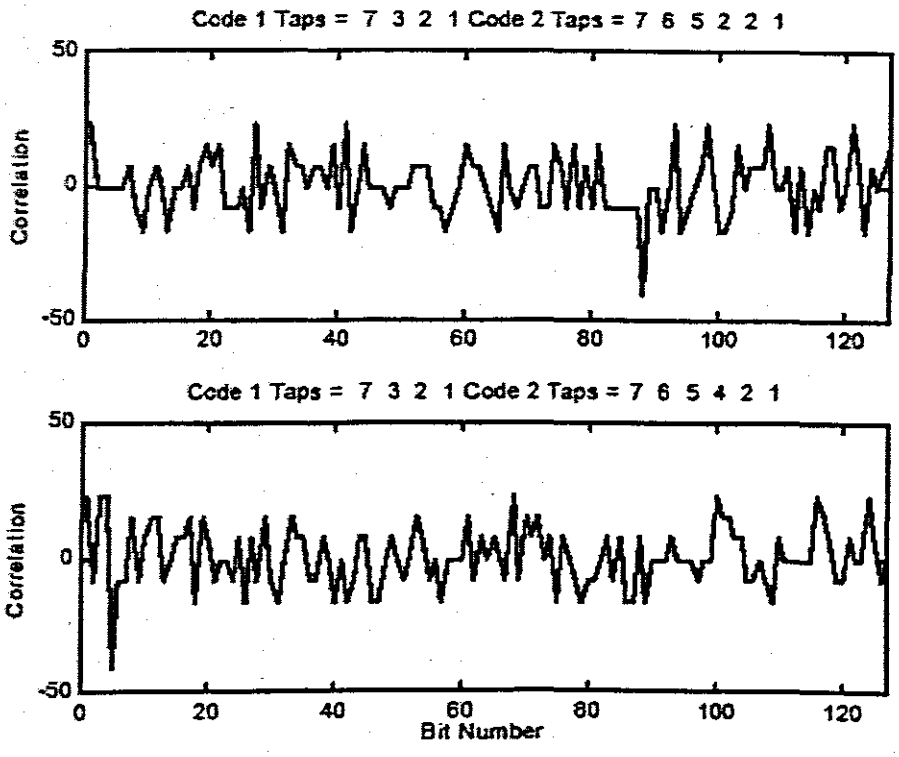

Figure 10.11 Code pairs 7321,7321 and 7321,765421

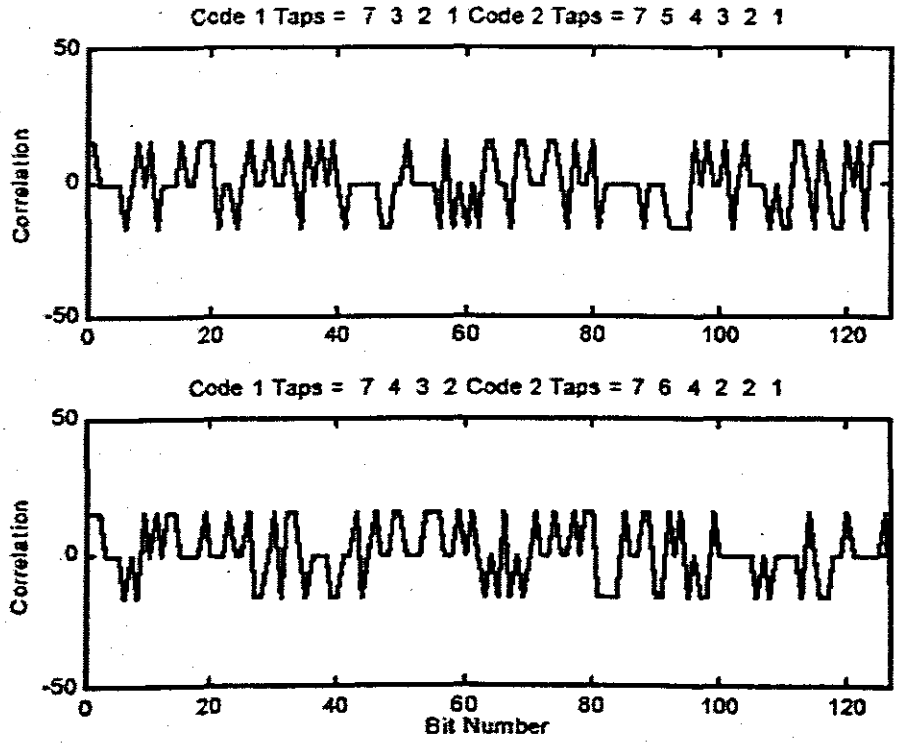

Figure 10.12 code piars 7321,754321 and 7432,764221

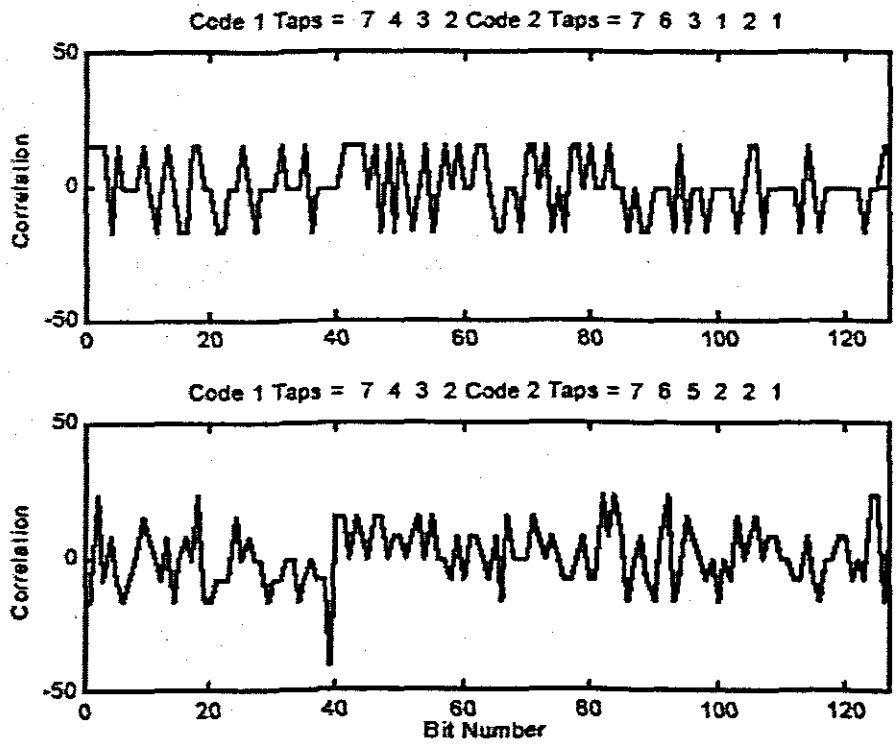

Figure 10.13 Code Pairs 7 4 3 2, 7 6 3 2 1 and 7 4 3 2, 7 6 2 2 1 .

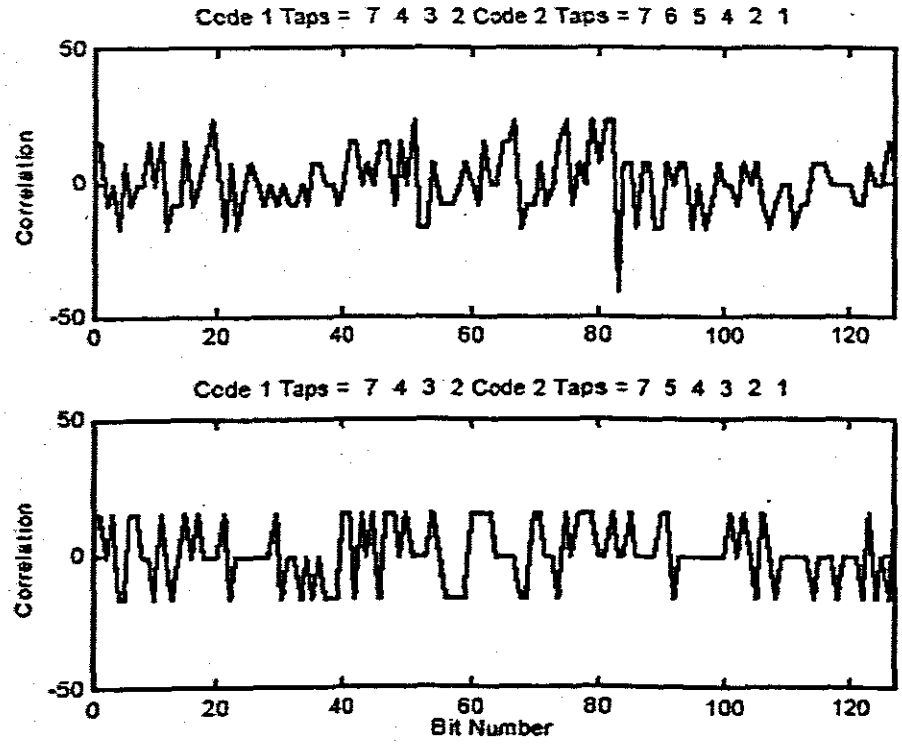

Figure 10.14 Code Pairs 7 4 3 2, 7 6 4 2 1 and 7 4 3 2, 7 5 4 3 2 1

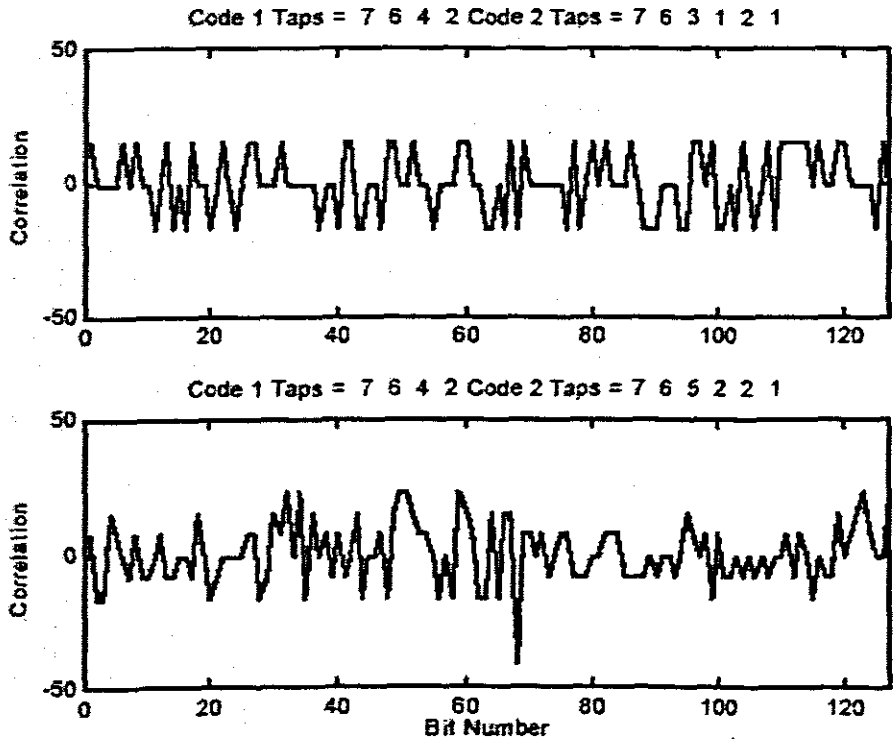

Figure 10.15 Code Pairs 7 6 4 2, 7 6 3 1 2 1 and 7 6 4 2, 7 6 5 2 2 1

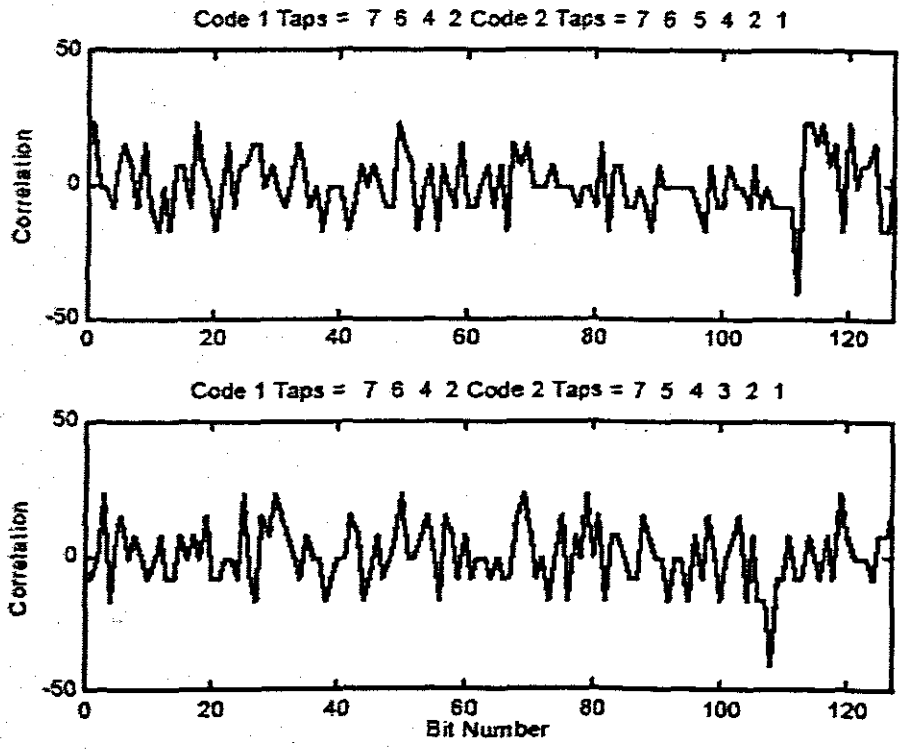

Figure 10.16 Code pairs 7 6 4 2, 7 6 5 4 2 1 and 7 6 4 2, 7 5 4 3 2 1

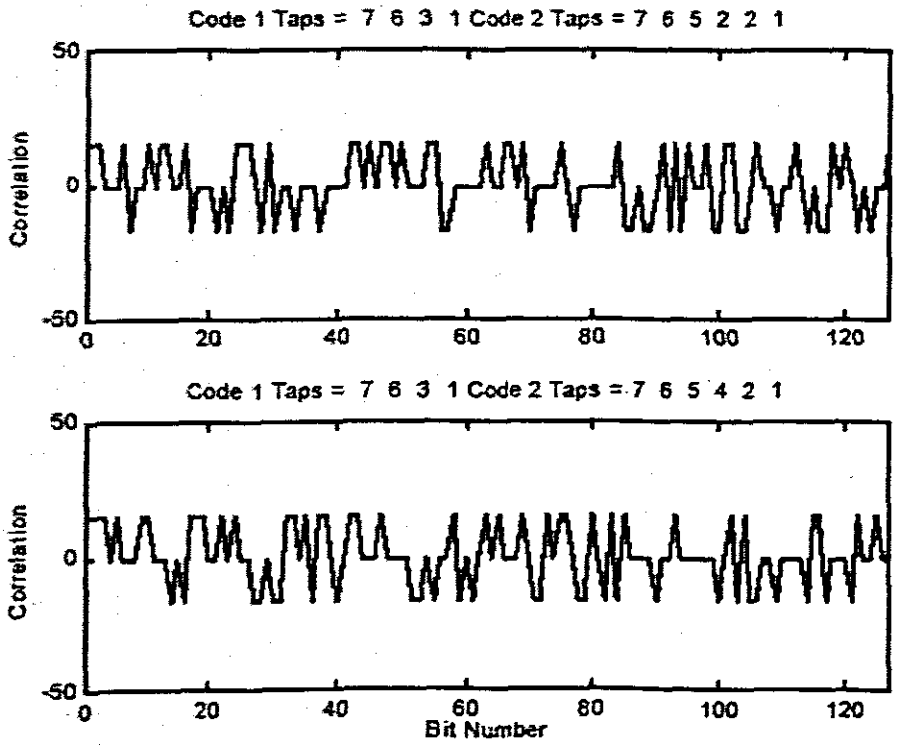

Figure 10.17 Code Pairs 7 6 3 1 ,7 6 5 2 1 and 7 6 3 1, 7 6 5 4 2 1

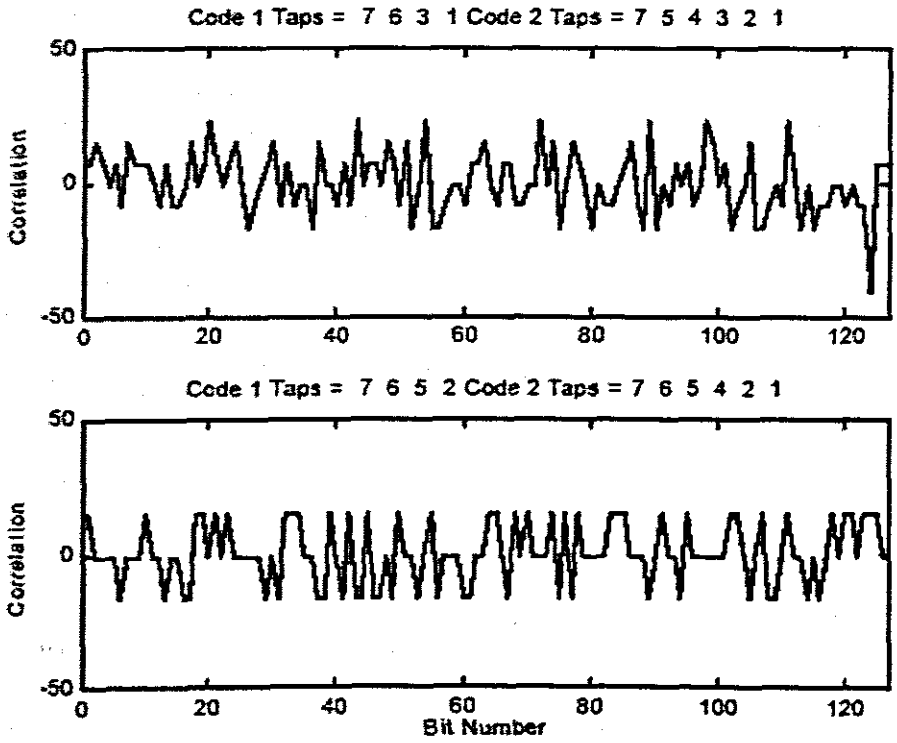

Figure 10.18 Code Pairs 7 6 3 1, 7 5 4 3 2 1 and 7 6 5 2, 7 6 5 4 2 1.

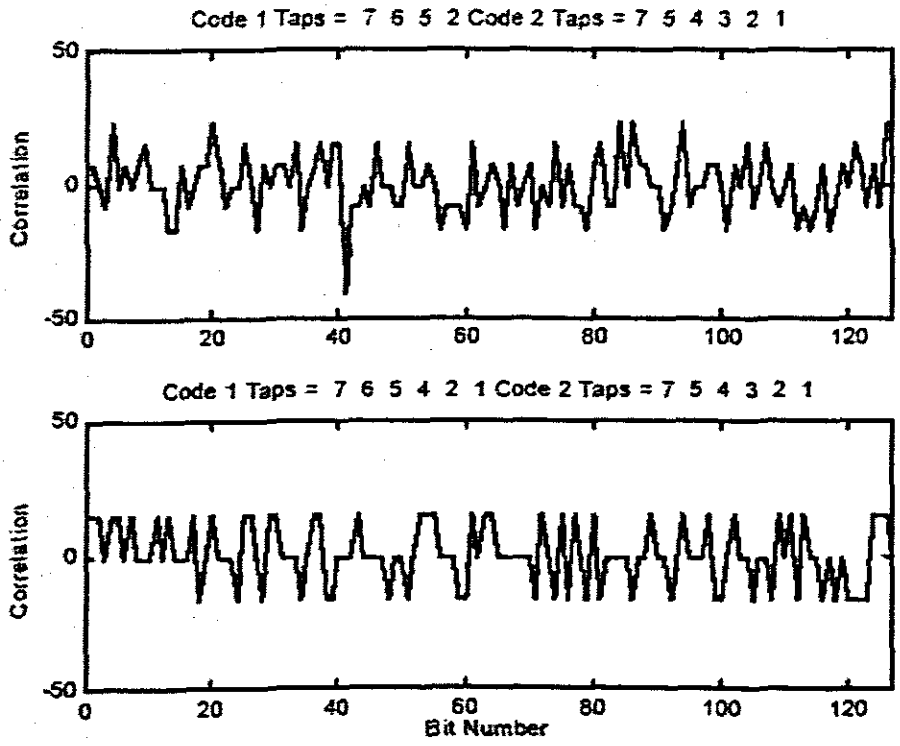

Figure 10.19 Code Pairs 7 6 5 2, 7 5 4 3 2 1 and 7 6 5 4 2 1, 7 5 4 3 2 1

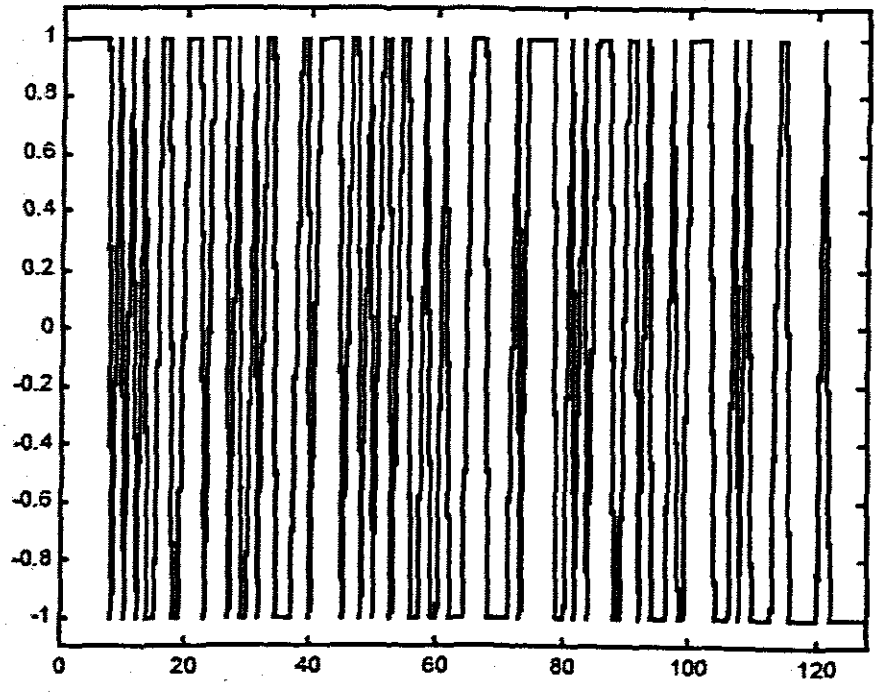

Figure 10.20 Code with Taps 71, no noise

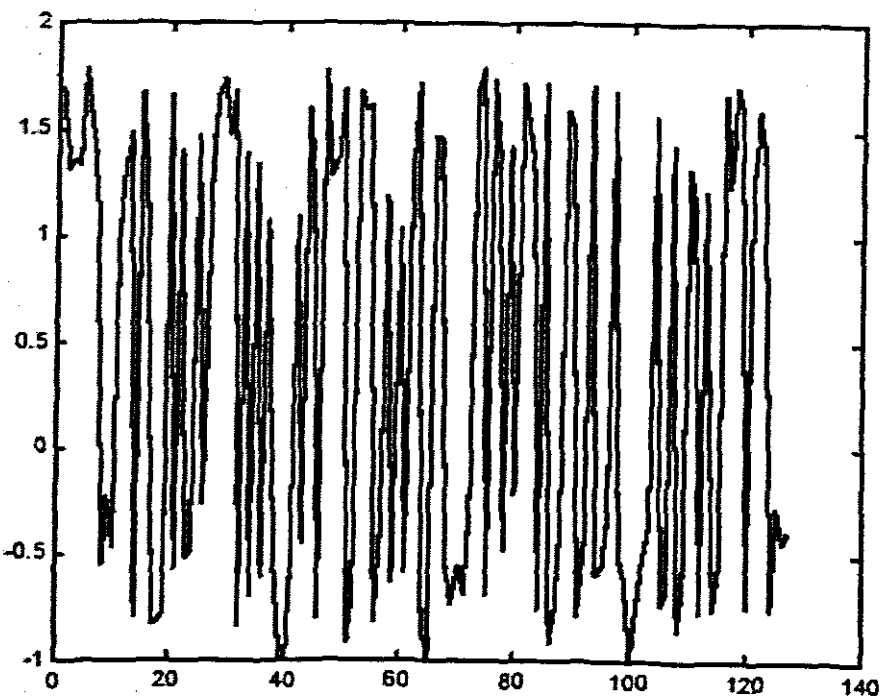

Figure 10.21 Code with taps and noise added, 71

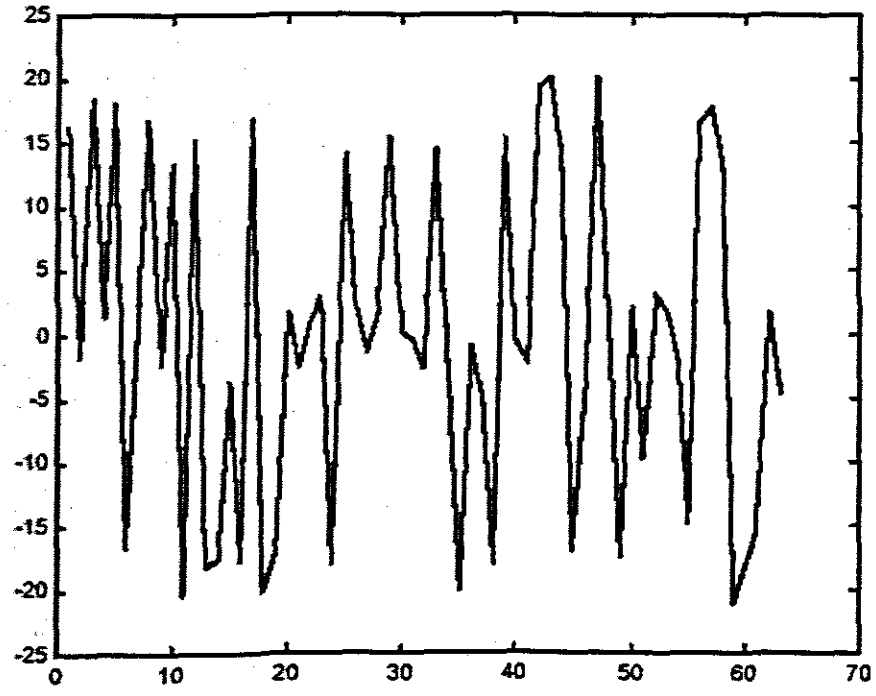

Figure 10.22: Correlated code with taps at 71 and 73

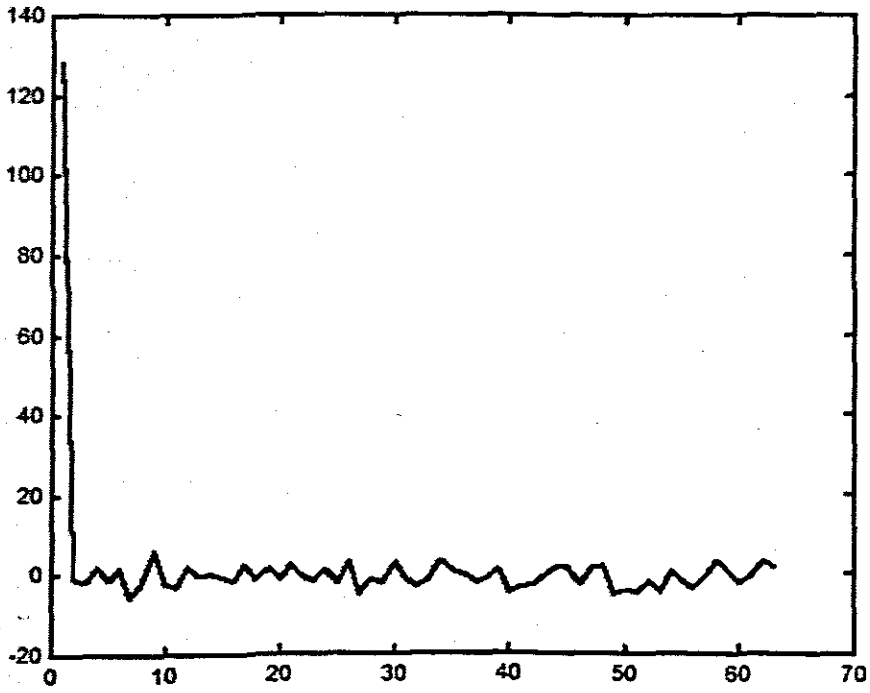

Figure 10.23 Code with taps at 71, noise added and reference code with taps at 71 as well

Chapter 11

EXPERIMENTAL DEVELOPMENT AND RESULTS OF NETWORKED SENSORS

11.1 Introduction

The proof of this networked sensor system is, of course, with the experimental effort to see what results can be obtained when breadboarded hardware and software were combined together and tested. The only drawback here was that testing was limited to the period spent at Nebuweb Sciencepark Laboratories. In performing the experimentation, the two distinct sensors were placed in the optical fiber communications system in such a way that they had their respective signals sent to the same fiber. The codes were generated using standard flip flop registers and the signals received at the detector were analyzed with Nebuweb software specifically designed to receive the different sensor signals.

11.2 Experimental Setup

As mentioned in Chapter 10, the experimental setup is shown diagrammatically in Figure 10.1.The two different sensors have code generators associated with them and these send pseudorandom pulses to the LED's which then emit light at 820nm into the 62.5/125 multimode graded index optical fiber. The light from the fiber optic sensor LED goes through a coupler and then into the intensity-based sensors. The modulated light from the sensors is then combined through another coupler so that information from both sensors is now on one fiber. Note the delay coil in one arm of the fiber optic sensor setup. This is to delay the transmitted light approximately one pulse time so the detector can discern one fiber optic sensor signal from the other. The light from the

digital interface code generator is modulated by the digital interface sensor as shown in the figure. The modulated light from this sensor is combined with the light from the fiber optic sensors and is then coupled into the receiving fiber via an optical coupler. The combined light pulses are then sent optically to the detector where they are converted into analog electrical information, read by the oscilloscope, and to the computer for signal processing. Figure 11.1 is a diagrammatic representation of the two code generators. Two 4 bit shift registers are connected together to provide a shift register capable of operating at 2 through 8 shift sequences. For ease of experimentation, both registers were connected using 7 stages total per generator. Taps 1 and 7 were used for the fiber optic sensor generator, and taps 3 and 7 for the digital interface sensor generator. This resulted in codes that have a relatively low cross correlation of 17.This was necessary so the software could separate or de-multiplex the two different signals.

11.2.1 Design of the Code Generators

The schematic of code generators is shown in Figure 11.2. The generators for both the fiber optic and digital interface sensors are identical except for the taps which control the type of code generated. The digital interface sensor also has a modulation circuit to vary the intensity of its LED. The pulsed output of the clock is inputted into the clock connections of both of the four stage shift registers. The output of the first shift register, pin 12, is connected into the first stage of the second four-stage shift register. The output of this shift register (here stage 3 which, when added to the first shift register, gives 7 total stages) is fed into the adder. In the case of the fiber optic sensor, stage 3 of the first shift register is also fed into the adder. In the case of the digital interface generator, the output of stage 1 is also fed into the adder. The output of the adder is then fed into the input of the first shift register. The maximal bit length sequences are then taken from the stage 7 output (pin 13 on the second register) and fed into the LED drivers. In both cases, the drivers are set up so that the LED input is shorted out by transistor Q1 as the pulses are generated. In the case of the digital interface sensor, the LED output is modulated by transistor Q_2connected to the digital interface sensor.

11.2.2 Digital interface Sensor Modulation and Code Generation

Code generation and modulation of the digital interface sensor is accomplished by the circuit shown in Figure 11.3. Here the code is generated by a circuit identical to the fiber optic sensor code generator, but the LED is triggered by an additional NPN transistor. The LED is shorted out with each pulse and the amplitude is controlled by the ADXL-05 sensor providing voltage to the base of the transistor. As the voltage changes, the amplitude of the light from the LED is varied as a function of input voltage which is controlled by the transistor. This modulation scheme was chosen in favor of a simple on off switch since the operational frequency upper limit of the ADXL-05 is Hz and the LED is switched on and off at a rate of 1.8 MHz. The overall experimental setup is shown pictorially in Figure 11.4. On the left is the spool of fiber containing the fiber optic sensor delay coil. To the right of the delay coil is the fiber optic sensor and coupler assembly consisting of three couplers and two intensity-based fiber optic sensors. To the right of that are the code generators constructed on the breadboard assembly. The digital interface generator is on the left and the fiber optic sensor generator is on the right. The digital interface sensor assembly is in the foreground. Next to the breadboard assembly is the oscilloscope which is connected to the Hewlett Packard detector. The oscilloscope reads the voltage across the detector which is proportional to the incoming optical signal. A view of the fiber optic sensor assembly, code generators and digital interface sensor assembly is shown in Figure 11.5.

11.3 Experimentation

The steps in the experimentation were as follows: As part of the overall signal processing, the reference codes from each code generator were sent separately into the detector and stored as a file on the computer. These codes were normalized and then converted to RMS, and then the autocorrelation of each of these resultant normalized RMS codes was taken to ensure that a valid code was indeed sent out and then stored. The returned signal was correlated with each of the sent codes to determine the sensor

values. This was done using the Nebuweb platform but could also be implemented using Labview in future enhancements.

11.3.1 Results

The system succeeded in multiplexing the two different signal sources and then separating them out with the software. The results are shown in Figures 11.6 through 11.19. Figure 11.6 , and the corresponding return, Figure 11.7 show the theoretical output of the initial pulse that is used to interrogate the fiber optic sensors and the corresponding theoretical return. Figure 11.8 shows the theoretical correlation of the two pulses. Figures 11.9 and 11.10 show experimental pulses sent out and then received at the detector. Figure 11.9 show the actual pulses that were sent out and the raw return data is shown in Figure 11.10. It is this raw return data that is fed into the software-based signal processor. The results of the cross correlation is shown in Figure 11.11. There are two peaks, each representing one fiber optic sensor. Note how this output compares with the raw return data. The raw return data appears virtually unintelligible to the naked eye, however, the correlated data contains the two well defined peaks. This is to be expected and closely parallels the expected theoretical output.

11.3.2 Digital interface Sensor Results

A key to success was to discern the digital interface sensor with the system, in view of the fact that the main goal was multiplexing different sensor signal sources using software and signal processing. The results of the digital interface sensor running through the code division multiplexer are shown in Figures 11.12 through 11.14. Figure 11.12 is the outgoing digital interface sensor pulse and Figure 11.13 is the received pulse. Figure 11.14 is the cross correlation of the received pulse with the outgoing pulse. Note the peak at approximately t=170. This represents the output of the digital interface sensor. Note that it is quite similar, as one would expect, to the triangular peaks of the two fiber optic sensors shown before. Figure 11.15 shows the same raw return data where the correlation is now taken to discern the two fiber optic sensors. Notice that

again there are two peaks, each representing a fiber optic sensor. It is also important to have no peak when there is no signal. Figure 11.16 shows what happens when the digital interface sensor signal is zero and the received signal is correlated with the digital interface sensor outgoing code. There is no discernible correlation. The same is true for Figure 11.17 when the fiber optic sensor is zero.

11.3.3 Timing

The signal processing system was modified and the experiments described above were repeated using a non-synchronized set of codes. A separate 1.8432 Mhz crystal was installed to drive the fiber optic sensor code generator. Key results are shown in Figures 11.18 and 11.19. Here, again, the digital interface and fiber optic sensors are readily discernible when correlated with their respective codes. It should be pointed out here that the synchronized code generators were synchronized in terms of pulse times only. That is to say that both the digital interface and fiber optic sensor codes differed by exact multiples of pulse times. With the non-synchronized approach, the difference was of a continuous variety. The issue of timing is important since the use of the system to multiplex a large number of different type sensors would not allow for synchronization of each code generator.

11.4. Summary of Experimental Results

The overall goal of discerning the two different types sensors, digital interface and fiber optic was achieved through the use of signal processing software specifically written for this research Alexander Carberry and myself. Unprocessed received signals are so weak before being processed that they cannot be discerned by the naked eye. After the signal processing performs the autocorrelation, the signal can be read and converted to an actual sensing value.

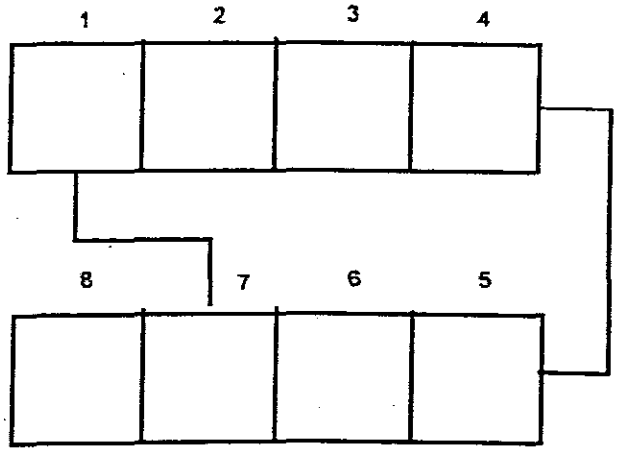

Figure 11.1 Diagrammatic representation of a Shift register with taps 1 and 7 connected

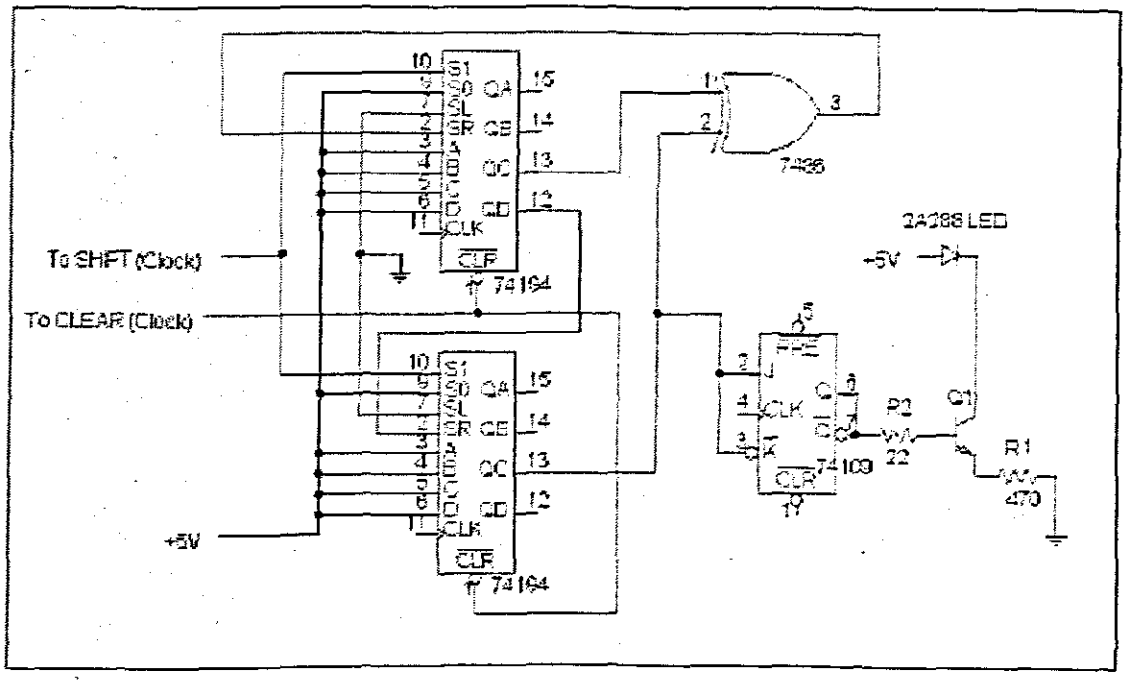

Figure 11.2 Code generator for the optical fibre sensor

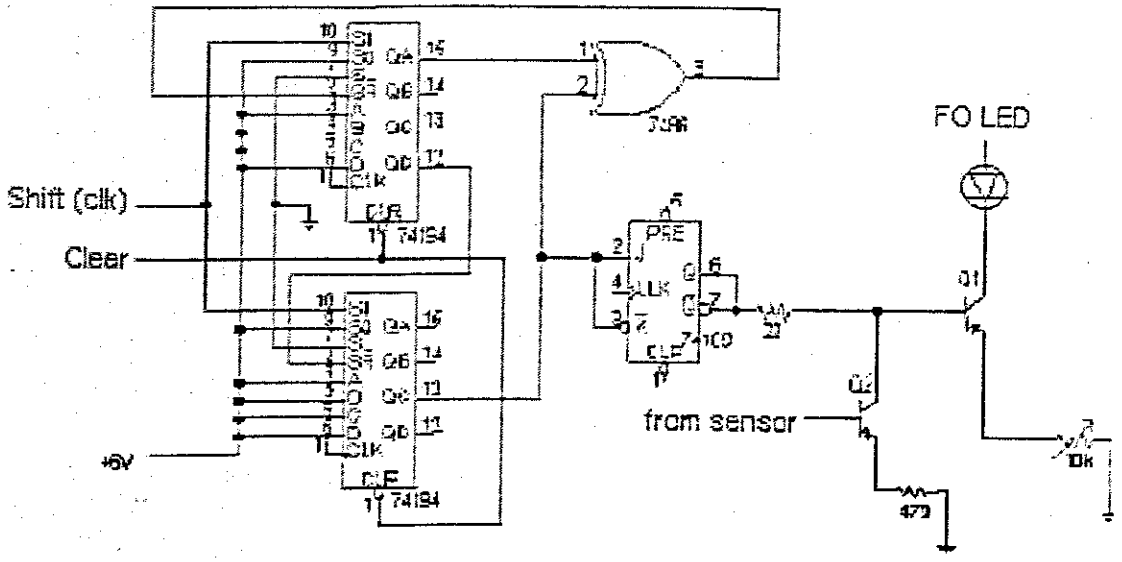

Figure 11.3 Code generator for general purpose sensor to add to the network

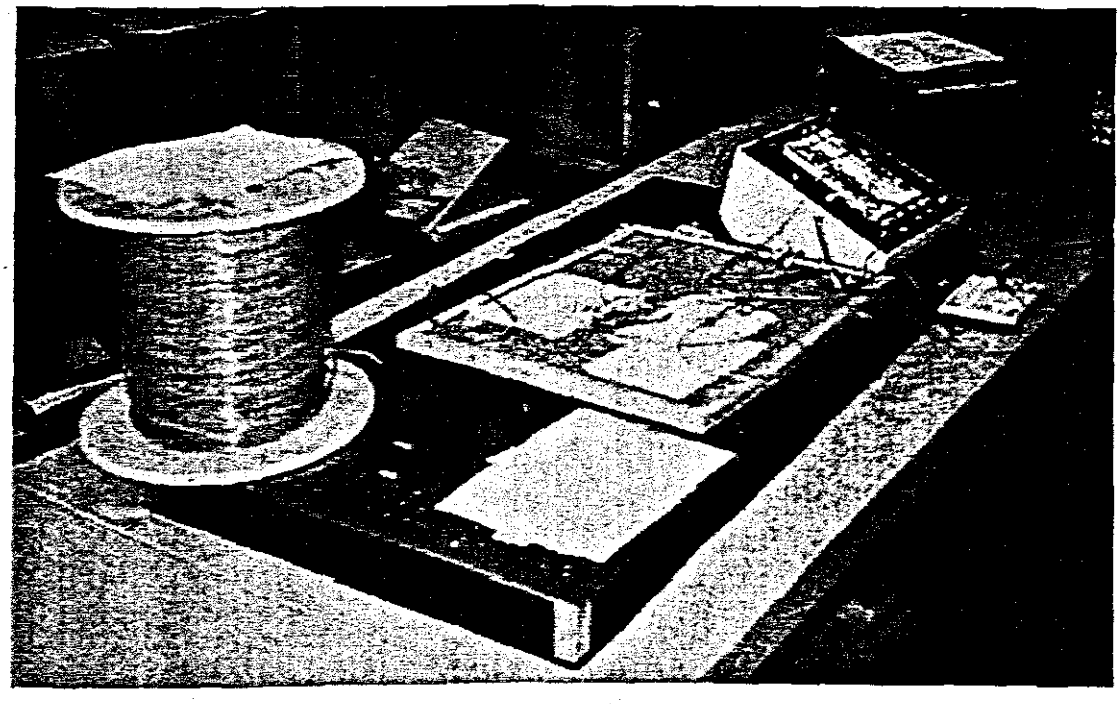

Figure 11.4 Overall Experiment

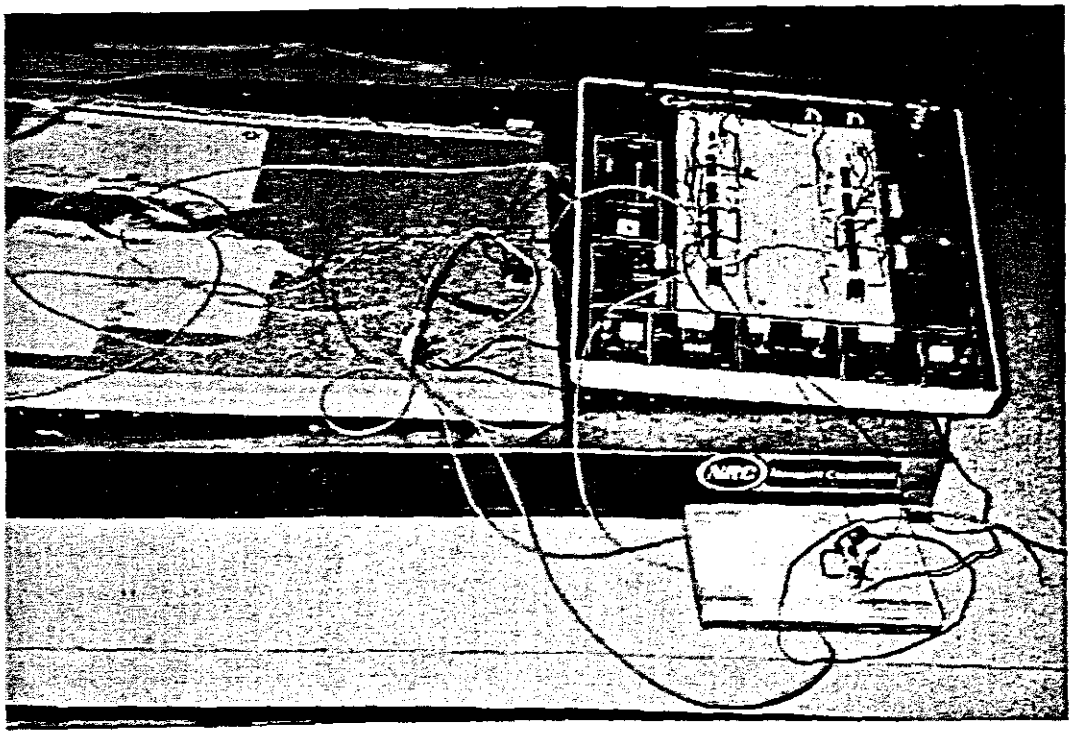

Figure 11.5 Experimental Setup

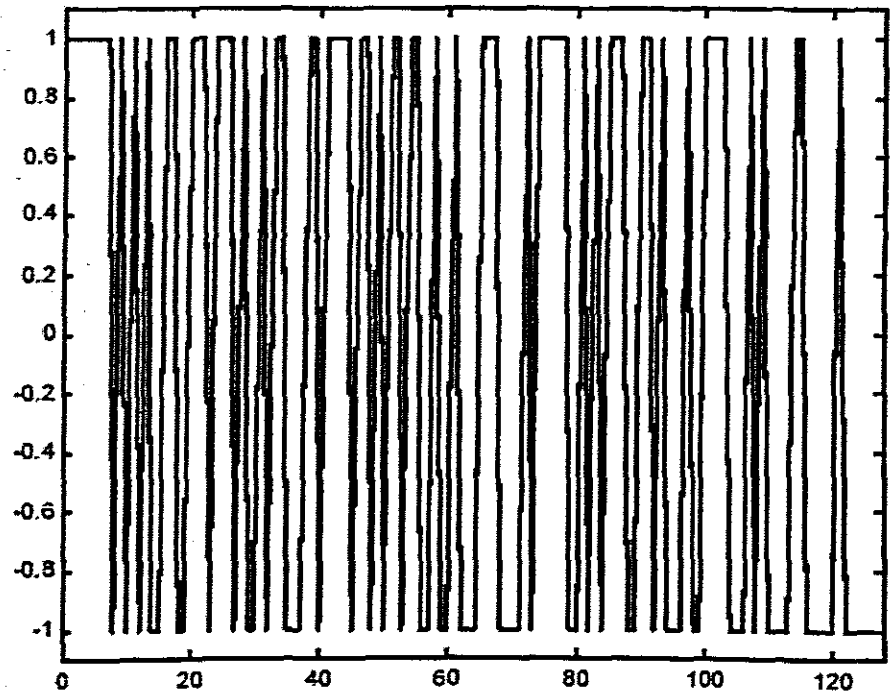

Figure 11.6 Theoretical pulse output

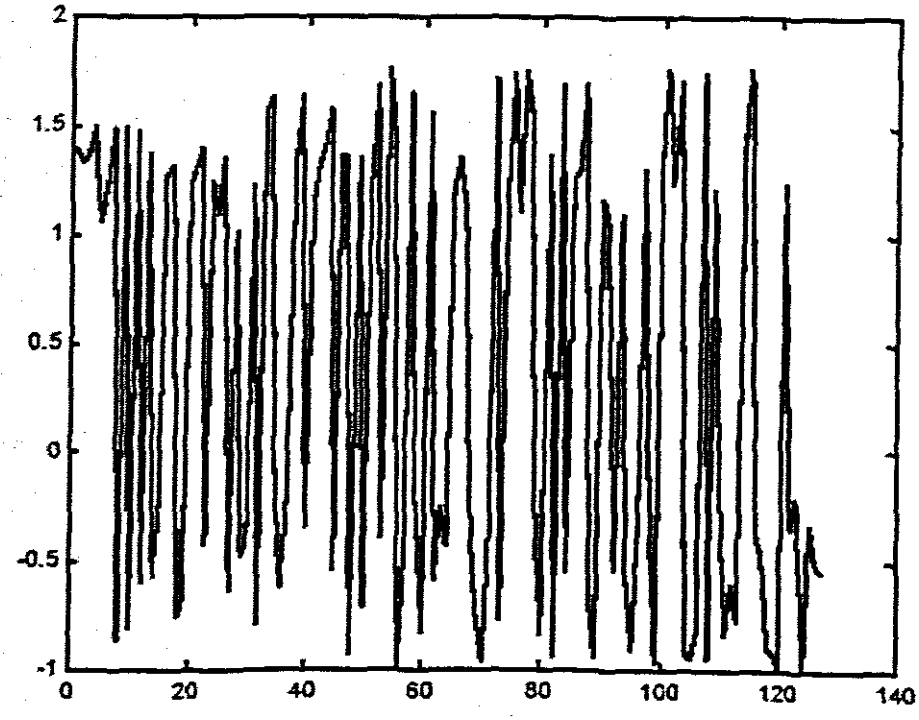

Figure 11.7 Theoretical return (simulated noise)

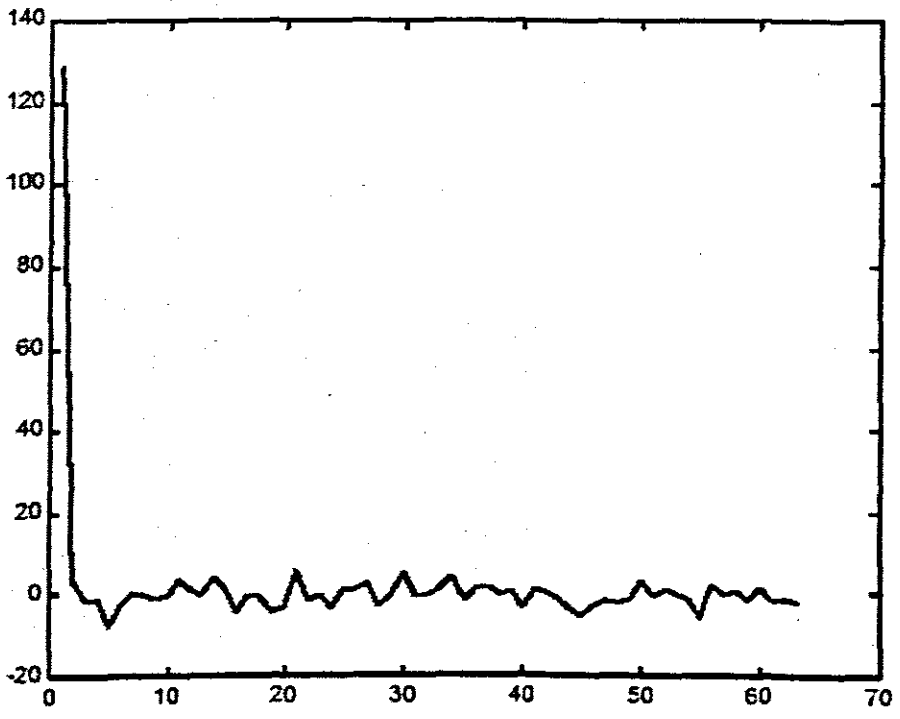

Figure 11.8 Theoretical peak for FO sensor

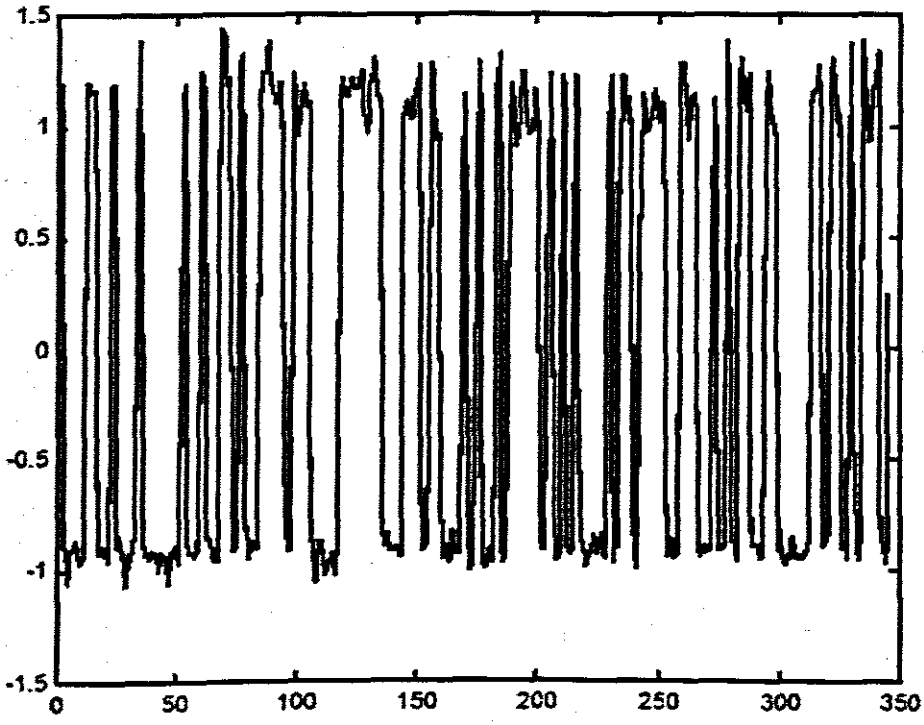

Figure 11.9 Experimental FO sensor transmitted pulse

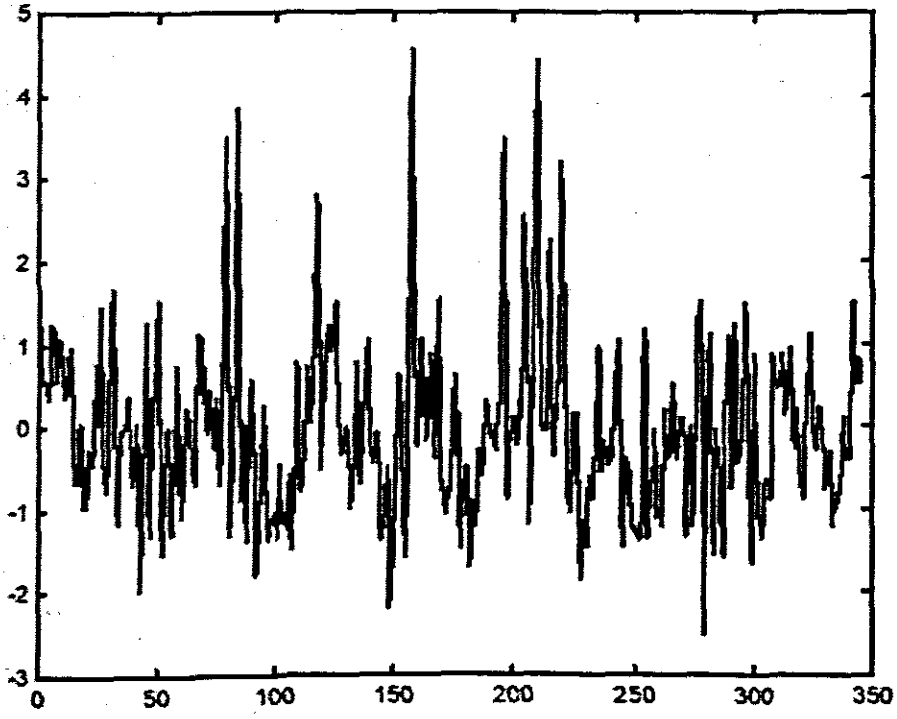

Figure 11.10 Experimental FO sensor return pulse

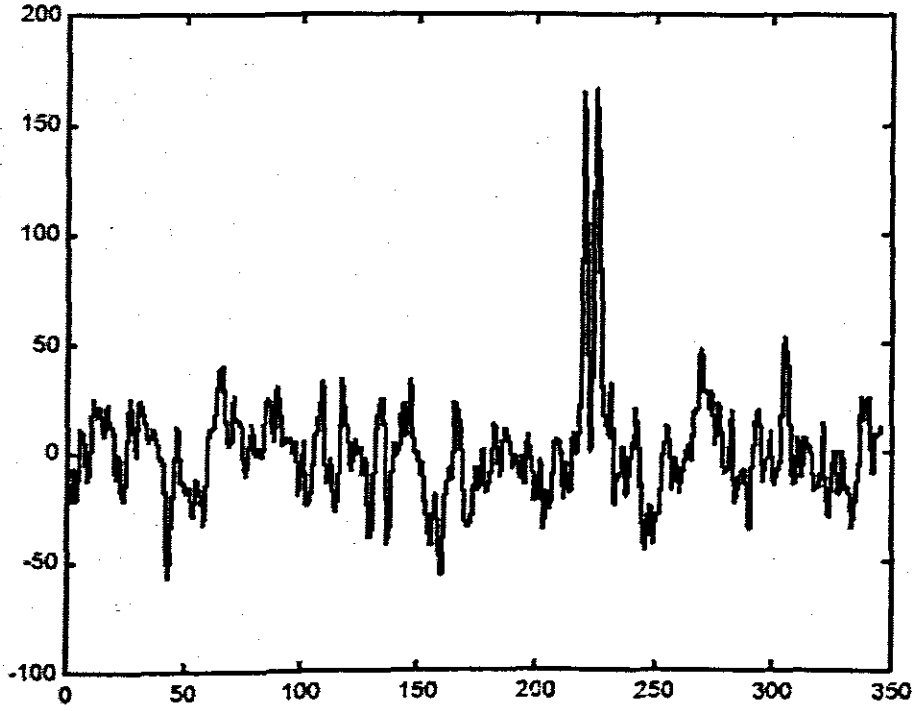

Figure 11.11 corresponding correlations (FO sensors only)

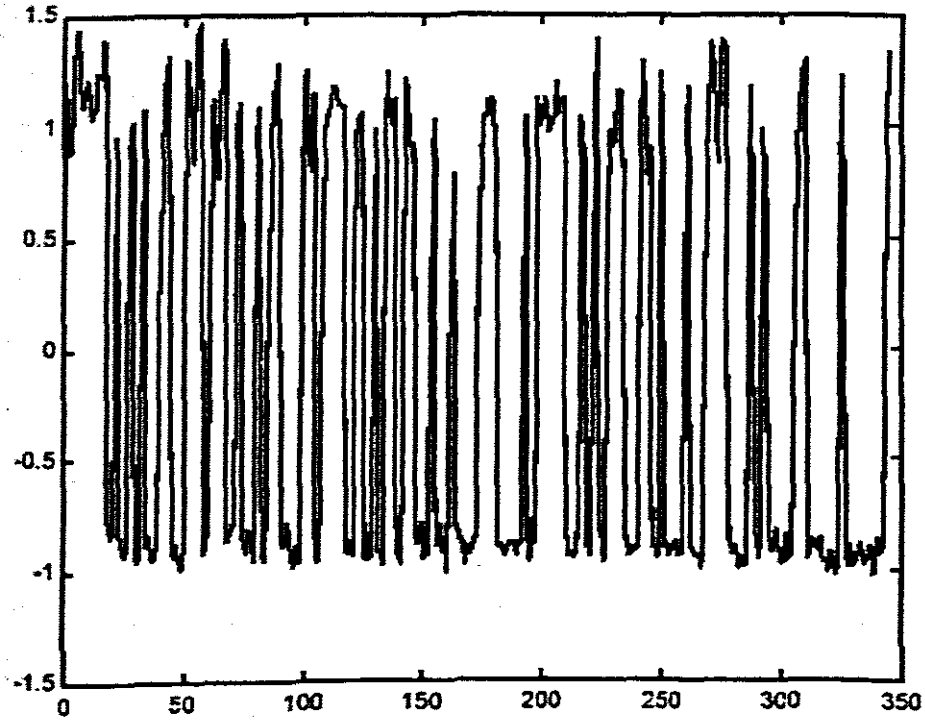

Figure 11.12 ADXL sensor outgoing pulse

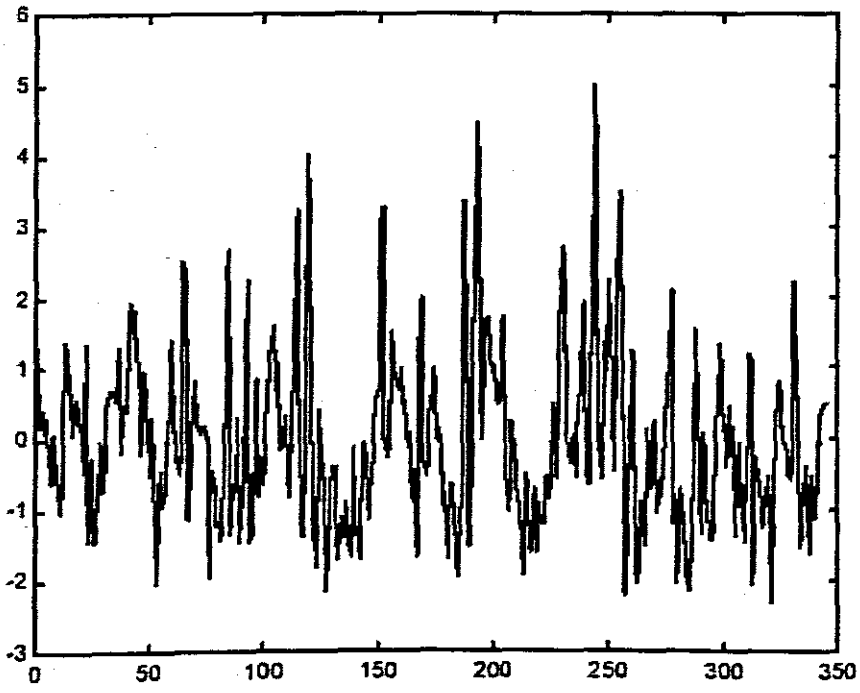

Figure 11.13 Experimental ADXL sensor return pulse

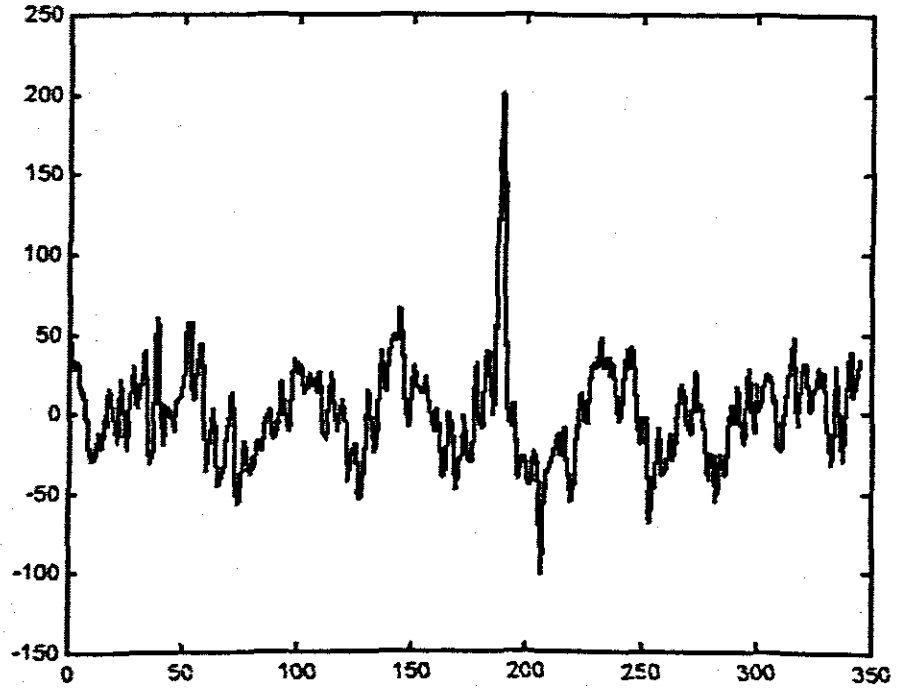

Figure 11.14 Correlations of ADXL pulse (peak at 170)

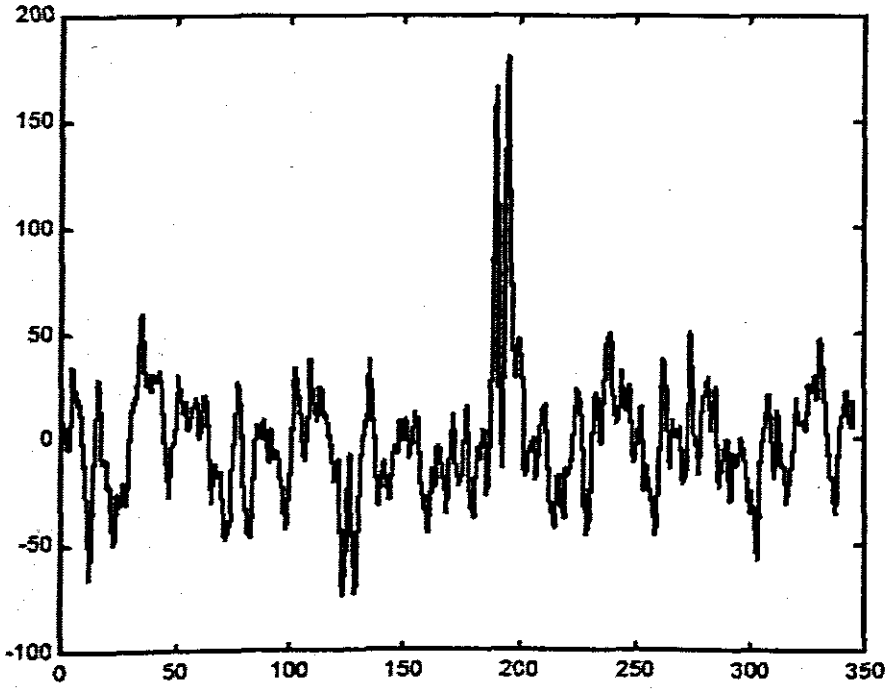

Figure 11.15 Same pulse returned correlated to detect FO sensors only

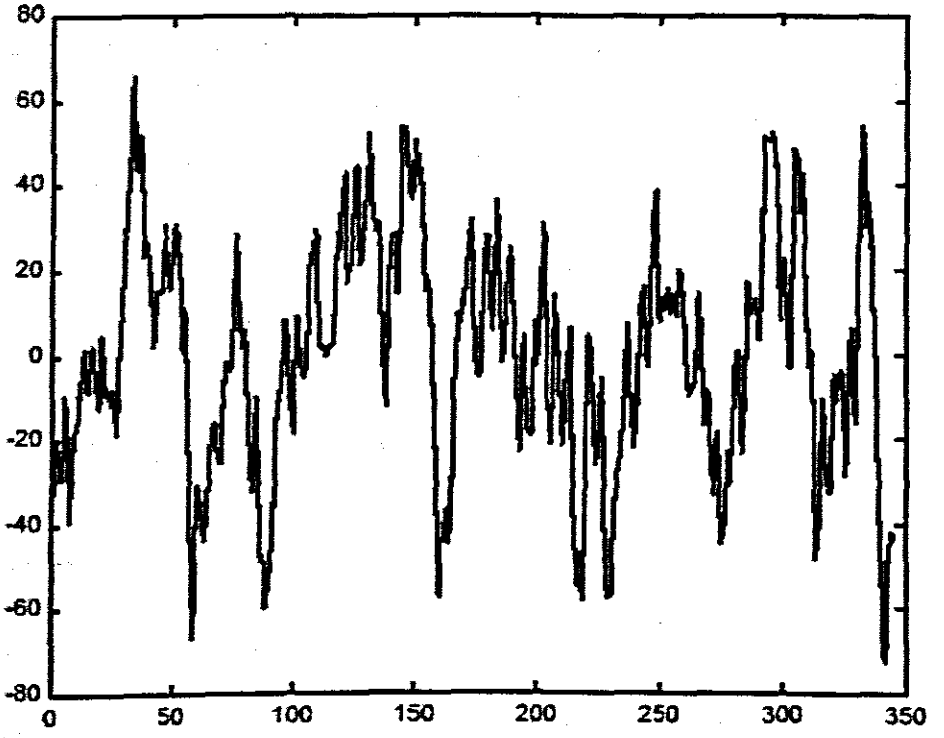

Figure 11.16 Correlation of ADXL senor with 0 ADXL signlal (no correlatiobn)

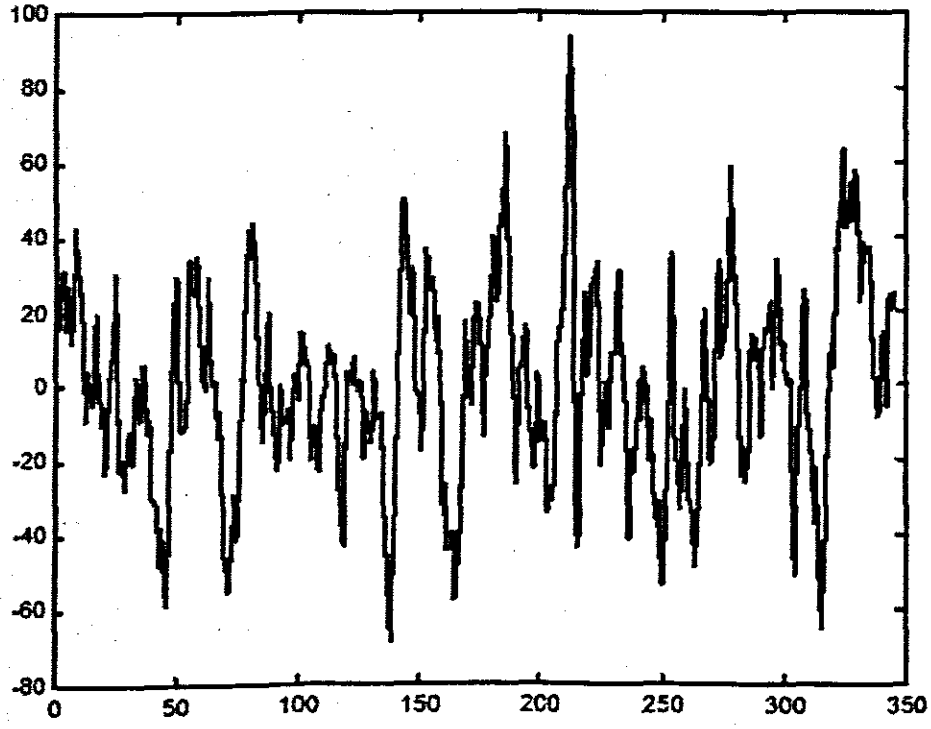

Figure 11.17 Lack of correlation of FO sensor with zero signal

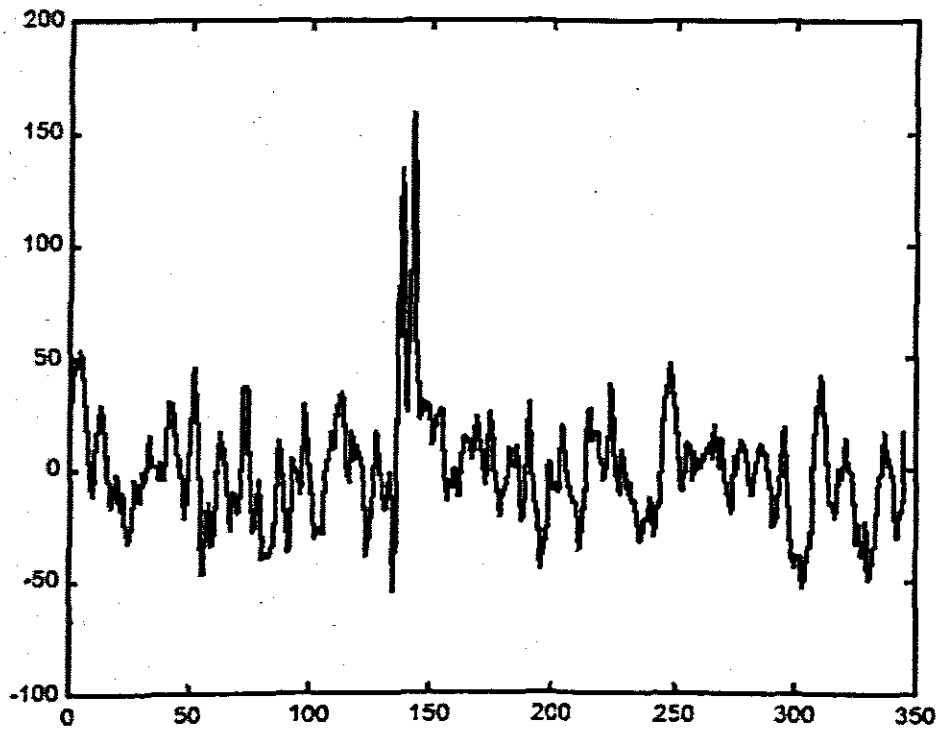

Figure 11.18 Unsynchronised generators of FO sensors

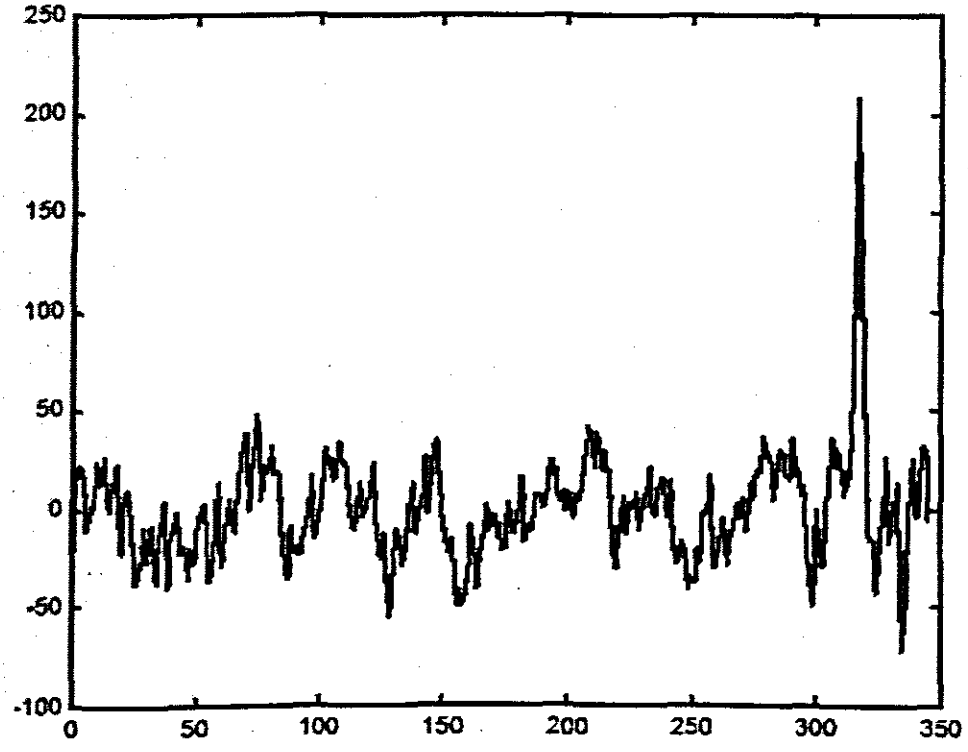

Figure 11.19 ADXL sensors with unsynchronised generators

Chapter 12

ANALYSIS OF SYSTEM LIMITATIONS

12.1 Introduction

In this chapter the large networked sensor system is analyzed and the system limitations explored. When considering a system of the type described in this dissertation, it becomes imperative to consider the results when the system is expanded. The primary limit is the number of sensors, and if the system is expanded beyond what was demonstrated, i.e. the two fiber optic and one digital interface sensors, other limitations come into play. Recall that the desire was to have a large system of optical fiber and other digital interface sensors. These limitations include bit error rate limitation on sensor resolution, time jitter, number of codes, physical device limitation, response time, and system topology.

12.2 Limit on the number of sensors

There are two limits to consider when looking at the upper bounds of the number of sensors: fiber optic sensor limits and digital interface sensor limits. With the fiber optic sensors, half the power is lost as the number of sensors doubles. This can be expressed by,

$$P = \frac{P_T}{P_R} = N \tag{12.1}$$

where P is the ratio of optical output power P_T and the received optical power, P_R and N is the number of fiber optic sensors connected in a tree network.

As the number of sensors is doubled, twice as much optical power is required for a given code length. As the code length is increased, the number of sensors can be increased. The correlation is similar to that of the power increase and is given by

$$P = \frac{P_T}{P_R} = CL \tag{12.2}$$

where CL is the code length and is given by

$$CL = 2^{BL} - 1 \tag{12.3}$$

where BL is the bit length of the shift register. For most code lengths we can ignore the -1 and, combining equations, we obtain

$$N = 2^{BL} \tag{12.4}$$

This again means that as the code length doubles, the maximum number of sensors doubles, or, as the bit length of the shift register increases by one, the maximum number of sensors doubles. A graphical representation of this is shown in Figures 12.1 through 12.4. We can see that when increasing the power 8 times over what is required for one sensor, we can have a maximum of 250 fiber optic sensors. But when we go from 8 to 12 times over the original power level, we can get 4000 sensors. Similar increases are true when the code register length is increased, as shown in Figures 12.2 and 12.4. However, notice what happens when both the code length and the optical power are increased by a factor of 12 as shown in Figure 12.5. The total maximum number of sensors is over 8 million. The limit on the number of digital interface sensors is a different story. The limit is not governed by power since each digital interface sensor has its own optical transmitter. Also, each sensor adds to the noise when the detector is attempting to discern a particular sensor. So as long as there is adequate power to overcome a few couplers, the number of digital interface sensors can be increased without respect to power. What is an issue, though, is the number of allowable codes.

For a given code length, there is a finite number of codes that can be used to transmit information. The number of allowable codes versus code length is plotted in Figures 12.6 and 12.7 below.

12.3 Limitations of the optical fiber current sensor systems

The three main limiting factors in the real-time performance of our current sensor systems are: (a) the speed and the integration time of the linear array CCD spectrometer, (b) the speed of the analog-to-digital converter, and, (c) the speed of the TMS320C40 DSP processor. If the speed of all these three components can be increased by a factor, the refresh cycle time of the real-time systems can be improved with the same factor, assuming that the memory interfacing is still of zero wait-state for the DSP processor.
The code was designed for a project specific to Alexander Carberry of Nebuweb, and was started fairly early in the development of this project. Subsequent to that, faster CCD spectrometers and DSP processors were released on the market.

The limitations on the performance of the accuracy and the precision of the measurements are imposed by two factors: (a) the number of bits used for the analog-to-digital conversion (ADC) of the intensity amplitude, and (b) the total number of elements in the CCD spectrometer and also the spacing in wavelengths between the adjacent elements. Increasing the number of bits for the ADC and the number of elements for the CCD spectrometer the accuracy and the precision can be improved, but with a price of increased computation, which may slow the real-time performance. Another limitation of our systems is that the LED optical source has a output profile like a Gaussian curve. A perfectly white source having a constant output profile, though not practical in reality, would provide a better performance in absence of the amplitude modulation of the optical intensity of the CCD spectrometer elements.
The EFPI based real time current sensor proved to be expensive and needed to be refined for multiplexing purposes. The digital output could be easily encoded with optical CDMA and re-transmitted over an optical network like the national grid. The optical CT is at this stage still unsuitable for field trial on the national electrical distribution systems.

12.4 Bit Error Rate limitation on sensor resolution

This system is a combination of digital and analog components, i.e. while the overall sensor signal measured is indeed analogue, a digital code is also used. If some bits are transmitted in error, it will affect the code received and will also affect the analog signal that is received. It may well mean that no signal is received at all. An accepted figure for bit error rate of a system is 10 which means one bit is transmitted in error for every 10 bits transmitted. If codes can be kept to a maximum length of 10 , the system will perform satisfactorily. This is a new limitation on the code length since earlier it was shown that it was desired to make codes as long as possible. The tradeoff is a maximum code length of 10 which corresponds to a register length of 33. Looking again at the figures of the three dimensional plot, we see that this is not a problem since the maximum length required would be a register of length 12. If bit error rate did become a problem, i.e. we did decide to use extremely long codes, error correction could be used. Another scheme would be to modify the system so that the codes were continuously transmitted and an average taken.

12.5 Physical device limitations

One of the difficulties with my choice of optical fibre sensor is the concentration on the Fabry Perot sensor which has a reflectivity of 1 to 10 percent depending on the particular type, and would therefore required longer codes or more power for the CDMA multiplexing scheme. In laboratory trials, I concentrated on feasibility tests however since I had only limited time at my disposal. Our Fabry-Perot sensor with the real time interface was connected as a digital output sensor to the CDMA multiplexing system. We found that, in short, any device that reduces power significantly should be avoided, but even these can be used if code length and/or power are increased. As far as the digital interface sensors go, they could be used with few limitations. The digital interface sensors can have artificial intelligence at the sensor, but this is not a requirement. One issue that arises though, is that as the code length grows, the digital interface sensors will have to have more computing power at the sensor just to generate a longer code.

This could mean a higher speed processor and resultant cooling problems. But, as computing power limits continue to increase, this should not be a major issue. Also, since the power output of the digital interface sensors does not have to increase, the LED portion of the sensor can remain relatively simple.

12.6 Time jitter

Time jitter is a factor in that it can lead to the wrong code being received if the jitter is greater than one pulse time. It is important to note, though, that synchronization of the digital interface sensors is not necessary due to their inherently different codes. A sample calculation shows the effect of jitter. If a 1.8 MHz clock is used, each pulse length is 5.5×10^{-7} seconds or .55 microseconds. Since jitter is typically in the picosecond range, there would not be a problem until a frequency of 100 MHz was reached.

12.7 Response time o f the sensor network

As the system is expanded, the overall network response time could become an issue. Since sensors typically sample at low data rates (one measurement per second or less is not uncommon) and the system can be constructed with high speed communications devices, response time is not an issue as long as a receiver is fabricated that reads the signals continuously.

12.8 System topology

Five basic topologies; bus, tree, ring, star and mesh were considered. The system in the experimentation used a tree topology for the networked sensors, and although other topologies could also be used caution should be exercised. The ring and mesh topologies could lead to multiple signals being received due to a ghosting effect. If there is more than one path from the optical source to the receiver, ghosting will be a problem. One solution to this would be for the receiver to expect the multiple signals and allow for them. This would require much more sophisticated and expensive detection circuitry. The advantage of using a mesh or ring topology is that redundancy is built in. If there is a break in one of the fibers, the others could take over the task of maintaining communication. The feasibility of these other topologies in our smart power system must still be investigated.

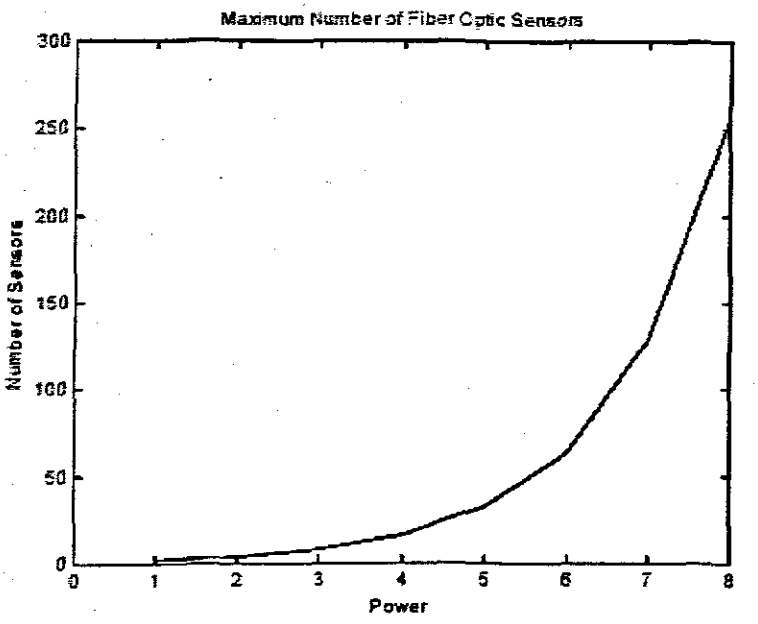

Figure 12.1 Maximum Number of Fiber Optic Sensors vs Power

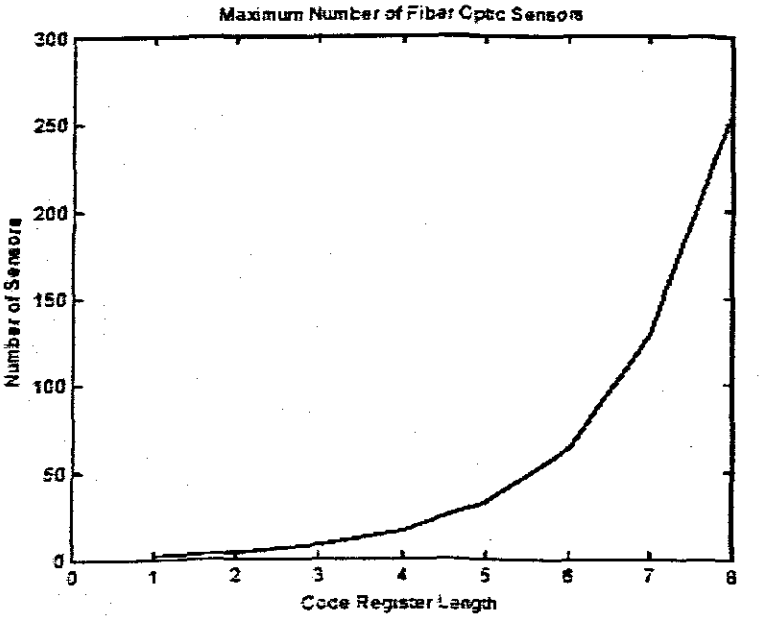

Figure 12.2 Maximum Number of Fiber Optic Sensors vs Code Register Length

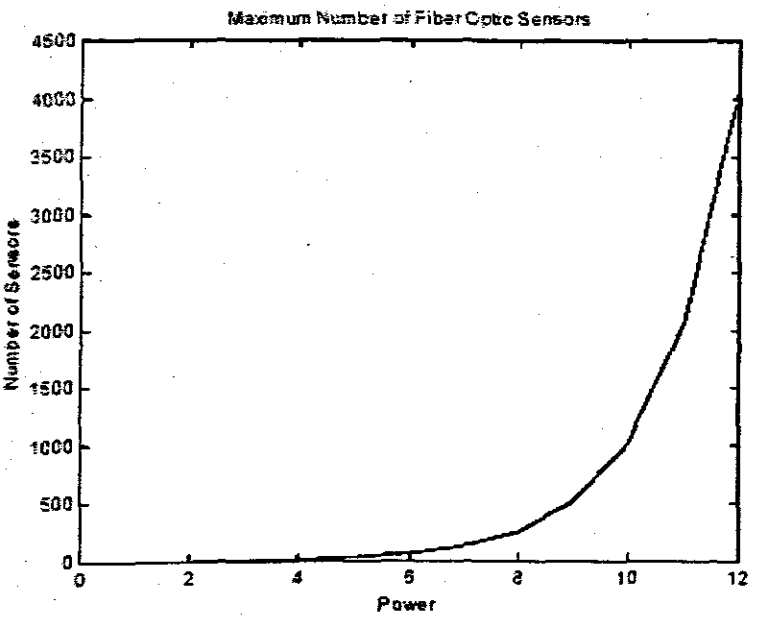

Figure 12.3 Maximum Number of Fiber Optic Sensors vs Power

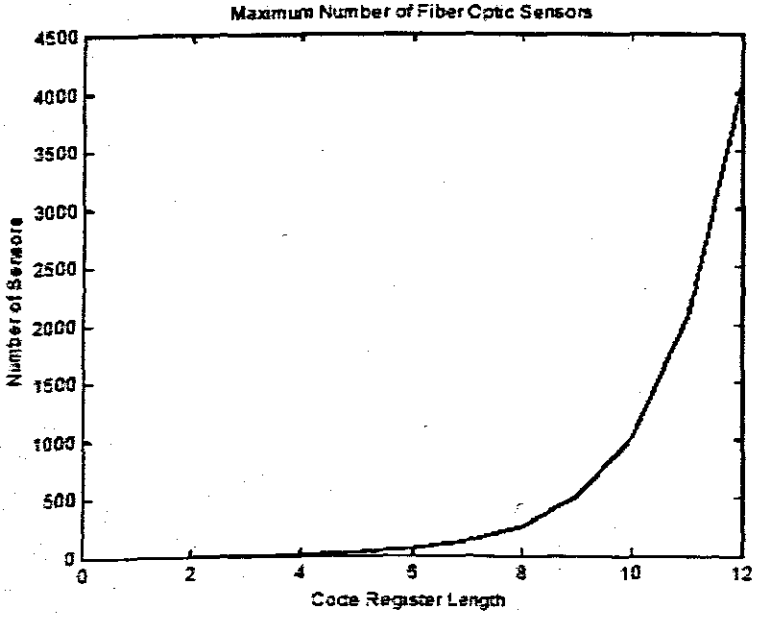

Figure 12.4 Maximum Number of Fiber Optic Sensors vs Code Register Length

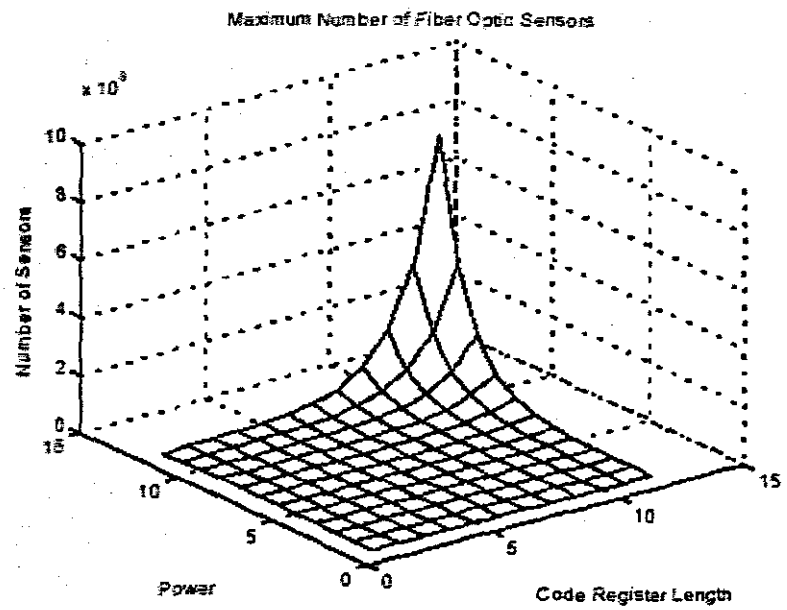

Figure 12.5 Fiber optic sensors versus code register length

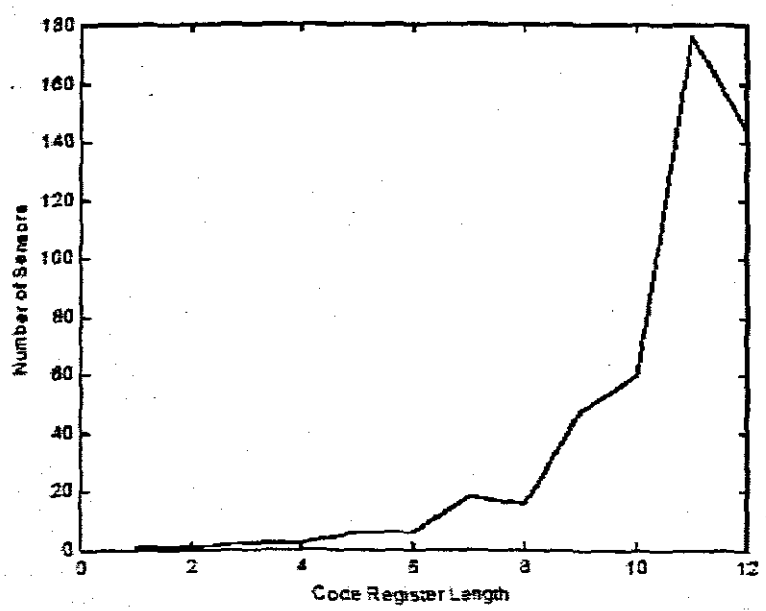

Figure 12.6 Number of digital sensors with regard to code length

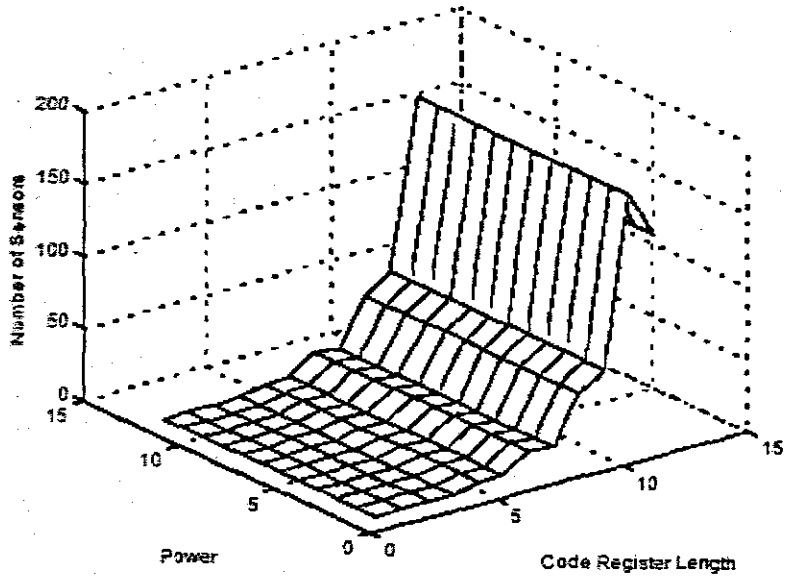

Figure 12.7 Maximum number of ADXL sensors *vs* power and code register length

Chapter 13

CONCLUSIONS AND RECOMMENDATIONS

13.1 Summary

The research undertaken for this dissertation is summarized herewith and the achievements of the study and conclusions are made. As knowledge based techniques are introduced in supervision and control of power systems, the need for structured methodical approaches in the development of these systems as smart systems are expected to increase. A smart system is dependent on sensor systems and particularly sensors that can be multiplexed and networked to provide overall systems status to control elements within the system.

With the dilemma of providing electricity supply through hazardous environmental conditions, and with prospects of supplying power even beyond South African borders, the need for a comprehensive damage assessment strategy becomes all the more relevant. In recent years power system networks have grown in complexity in order to extend the supply of electricity to wider networked areas. Energy control centers must therefore retain highly skilled operators to provide power system control and proper analysis of power system phenomena. The rapid growth being made in the evolution of so called "intelligent" structures, with inherent sensor, actuator and control mechanisms built in can have a direct influence on power distribution networks.

It was found reasonable to determine if opto electonic sensors for electrical parameter and damage assessment in large scale networks, such as an electricity supply and power system network, were applicable. These sensors were miniature by nature and much smaller than conventional current transformers. Since motivation existed for miniature opto electronic sensor applications , it was therefore feasible to develop topologies for

fibre-optic sensor deployment in power systems as well as an implementation of such sensors with reliable multiplexing technology in a large network (such as a power system).

The research objectives that was adhered to in this study are summarised below as:

- development, modeling and analysis of sensor deployment and electronic signal processing in optical fiber based sensors that would be suitable for use in a large networked applications.
- development of a complete model of a wide-band extrinsic Fabry-Perot interferometric (EFPI) sensor system, along with the development of all the associated equations.
- derivation of parameters for the development of real time optical fibre sensors for the measurement of current and voltage in high voltage applications.
- modelling and development of techniques to multiplex and network the sensors developed herewith, with an analysis of performance.

It was generally not possible to address these objectives on a strictly chapter-by-chapter basis as the topic involved a large networked system with several detailed design processes that followed a functional order. How these objectives were addressed in each chapter is summarized below:

Chapter 2 dealt with optical electromagnetic principles pertaining to this study and provided the necessary theoretical background to the work that followed. The chapter started with Maxwell's equations and derived pertinent relationships from that. The relationship between Maxwell's equations and the Helmholtz equation is introduced and optical wave propagation in freespace as well as dielectrics (optical fibre) with associated boundary constraints are explored. The discussion is rounded off with a treatise on Jones and Stokes vector notation that is commonly employed in optical wave propagation analysis.

Chapter 3 analysed the theoretical basis of the Fabry Perot etalon as well as how electrical quantities could be measured using optical fibres. The Fabry Perrot etalon as a current transducer was then explored and a model developed for a generic sensor for high voltage applications later on and forms an essential part of the main research objective.

Chapter 4 built on the principles out lined in chapters 2 and 3. The optical wave is confined to an optical fibre and what follows is a development of a novel light beam propagation model which can be numerically implemented for use in designing the sensors. Using this model was not essential, but it provided such a useful technique and was computationally simple to implement that it was included as a chapter. This model proved useful in the calculation of wave anomalies in the EFPI gap as discussed in chapter 3 and thus useful in the design of the EFPI. A Matlab or other program could implement the method. What remained then was the development of an EFPI and looking at the signal processing techniques to extract real time information from it.

In Chapter 5 the signal response, and the signal processing techniques for the non-monochromatic lightwave extrinsic Fabry-Perot interferometric (EFPI) sensor system was presented. This technique was essential to the main research objective as well as objective 2. Equations were derived to model the behavior of the non-monochromatic lightwave EFPI sensor system, which provide an insight into the modulation of the signal responses and their demodulation techniques, applicable for digital signal processing to be applied to the sensor. With this absolute value of the EFPI gap measurable, it was proved that the digital data capture was possible and may be algorithmically implemented by means of digital signal processing techniques. The EFPI sensor developed in this application was for the measurement of current in high voltage applications.

It was a challenge to find out the value of the External Fabry Perot Interferometer air gap length g, from the complex signal response of the non-monochromatic lightwave EFPI sensor system proposed for the generic current sensor. This is largely the topic of

concern in Chaper 6. It is known that due to the Gaussian profile of a broadband optical source, the shape of the signal response is somewhat Gaussian, but modulated with the fringe pattern, including peaks and troughs. With the increase of the EFPI gap, the number of fringe peaks within the same wavelength range, of the signal response, gets increased, decreasing the distance (in terms of wavelength) between adjacent fringe peaks. Also, the non-monochromatic lightwave EFPI sensor system has a signal response where the frequency of occurrence of fringe peaks decreases gradually towards the higher end of the wavelength values, i.e., there is a chirp in the frequency of the fringe pattern, distancing any two adjacent fringe peaks further for larger values of wavelengths. In this chapter there were presented several methods to process this complicated signal response of the non-monochromatic lightwave EFPI sensor system, to find the EFPI gap length g, and as such any measurand (in this case current) that relates to that This formed an essential part of research objective 1 and 2.

The previous development resulted in a rudimentary but new real time optical current sensor. In chapter 7 the characteristics of optical current sensors, specifically for relaying applications where measurement of fault-level currents may be required were discussed. Research objective 3, derivation of parameters for the development of real time optical fibre sensors for the measurement of current and voltage in high voltage applications, was addressed in this chapter.

Chapter 8 introduces sensor telemetry for intelligent systems using the code division multiplexing techniques commonly employed in cellular telephone networks. In this chapter, this code division multiplexing is explored with the idea of expanding it to a more desirable large-scale sensor network using optical fibre for applications in electrical energy distribution systems. In this way research objective 1 was together with chapter 7, theoretically fully addressed, by standardising a sensor topology and proving that networked sensor topology as feasible. What remained was development of simulation and comparison of results with actual tests when several sensors were networked.

In order to network many sensors as discussed in Chapter 8, the matter is taken further in Chapter 9 with an exploration of successful multiplexing methods and multiplexing algorithms that have been used on same-signal devices. In this chapter research objective 4 is addressed theoretically. Code division multiplexing has been used to multiplex same-signal communications devices for some time. Closely related research has resulted in the multiplexing of fiber optic sensors onto the same network. Given the enormity of the work that has in the process of this research transpired, this makes sense. In this chapter, this same-signal multiplexing work is explored with the idea of expanding it to a more desirable mixed-signal network, for the optical fiber sensor design for large networks which is part of the objectives of this thesis.

Chapter 10 follows as a logical continuation of chapter 9. One of the prime aims of this thesis was to model the multiplexing of different optical fiber and other electrical sensor signal sources using a software and signal processing approach in a large (smart) network. An analysis was performed to determine the issues involved in multiplexing the different sensor signal sources, and how those issues could be resolved using good software design. This completes the theoretical part of research objective 4. The systems analysis also determined correct operating parameters.

Chapter 11 discuss the experimental development and brings together the ideas of objective 1, 2, 3, and 4 on a practical platform. The proof of this networked sensor system is, of course, with the experimental effort to see what results can be obtained when bread boarded hardware and software were combined together and tested. In performing the experimentation, two distinct sensors were placed in the optical fiber communications system in such a way that they had their respective signals sent to the same fiber. The codes were generated using standard flip flop registers and the signals received at the detector were analyzed with Nebuweb software specifically designed to receive the different sensor signals.

When considering the evolution of a smart system of the sort described in this dissertation, one must consider the results when the system is expanded. This is the

topic of chapter 12. The primary limit is the number of sensors, and if the system is expanded beyond what was demonstrated, i.e. the two fiber optic and one digital interface sensors, other limitations come into play. Previously the desire is to have a large system of optical fiber and mixed signal sensors in the system was expressed. These limitations include bit error rate limitation on sensor resolution, time jitter, number of codes, physical device limitation, response time, and system topology and is discussed in this chapter, which essentially forms an analysis of results.

13.2 Conclusions

The application of fibre-optic EFPI sensors, as a class of miniature opto electronic sensor, was explored with regard to the development of an intelligent power system. A major part of the research depended on the development of a complete model of a wide-band extrinsic Fabry-Perot interferometric (EFPI) sensor system, along with the development of all the associated equations. This objective was achieved in chapters 4, 5 and 6.

The derivation of parameters for the development of real time optical fibre sensors for the measurement of current and voltage in high voltage applications was achieved in chapters 2, 3 and 7 respectively.

The modelling and development of techniques to multiplex and network the sensors developed, with an analysis of performance, was achieved in chapters 8, 9 and 10 respectively.

The overall research objective, being the development, modeling and analysis of sensor deployment and electronic signal processing in optical fiber based sensors, which was addressed as part of many chapters, but which was solved in chapter 8, was brought together in chapters 11 and 12 where it was proven workable and suitable for use in a large networked applications.

13.3 Technical problems

The technical barriers in this research were similar to multiplexed communications systems with the primary limit being the number of sensors one can multiplex together and reliably identifying the appropriate measurands. That limit affected a number of interrelated parameters such as network topology, physical device limitations, code size, code configuration, increased complexity of the sensor devices, bit error rate limitations on sensor resolution and response time of the sensor network. Networking a combination of fiber optic and digital interface sensors using code division multiplexing required that tradeoffs be made in the system design. The upper limit on the number of fiber optic sensors is primarily governed both by power to the optical transmitter and by the code length. Increasing one of these parameters can increase the maximum number dramatically, and increasing both power and code length by several orders of magnitude gives an upper limit of approximately eight million sensors. The maximum number of digital interface sensors in the network, on the other hand, depends solely on the code length. Each digital interface sensor has its own optical transmitter, say for instance a fault relay with a digital output. While it was desirable to have long codes to increase the maximum allowable number of sensors, there is an upper bound to code length that is dictated by bit error rate limitations on sensor resolution. It was found that as long as the code length was less than 109, the bit error rate issue was not significant and the system performed satisfactorily. The physical device limitations on the sensors include an adequate amount of fiber optic sensor reflectivity to keep code lengths and power at a reasonable level. The commercially available digital interface sensors have little physical device limitations when used on this system, but increased computing power on the sensor could lead to some trade offs. Time jitter is not an issue below 100 MHz and system response time was adequate since high-speed communications designs were used on low speed systems. The tested system topology was a tree network, but other topologies could be used. Topologies that are multi-path in nature would have ghosting issues to overcome, but these same topologies have an inherent redundancy that can allow for fiber breakage by rerouting signals through undamaged fiber.

13.4 Recommendations for future work

Further development of this research could indeed lead to technological advances that parallel those we have seen in the communications industry. One prediction is thousands of mixed-signal sensors in say a substation environment in an enclosed area, multiplexed together with one notable exception: No fiber. The transmissions would be made via optical transmitters and receivers, but the overall gain one gets by increasing both the power and the code lengths could over come the effect of no fiber. The received optical signal would be that which has been reflected off the walls of the space. This would make the system useful in areas where high electromagnetic interference is an issue, but wireless sensor interconnection is desired. Another prediction is that the codes could become so long due to increased computing power that this system could be used to multiplex high speed computers with the wireless optical effect noted above. Since this research involved pulling signals out of the noise, one could envision portable communications devices that communicate long distances optically. All that would be needed would be for the light, after many lossy reflections, to end up at the receiver. Perhaps one of the biggest implementations of this technology in next generation systems would be devices that communicate optically over a long distance, say over a continent, as would be possible with optical fibre conduit carried in High Voltage electrical distribution cable. One could envision a sensor planted at a strategic location say at an electrical generation plant in North Africa, and being monitored in Pretoria, all through the code division process. One can also envision passive and active sensors being multiplexed, perhaps by wireless means, to a central receiving point. Artificial intelligence on some of the sensors would process data, say distribution faults or overloads, and send it optically through high EMI fields along with the passive sensor data to the central receiving point. From here actuation and control could take place, but this is the next step in the evolution of smart systems using optical sensor technology!

Suggestions for future enhancements on this work are made to lead someone to add to the performance of the real time current sensor and expand it to a voltage sensor for multiplexed sensor systems. Another possible enhancement to increase the real-time

performance of the optical fiber current sensor system would be to use a faster CCD array than the linear array spectrometer used in this project. It would also be necessary to develope a faster 16-bit analog-to-digital converter. A faster DSP processor will of course improve the real-time performance of the system significantly. A proper low cost, low power consumption DSP implementation of this sensor requirements needs to be undertaken on the basis of the theoretical models developed in this dissertation.

References

ABEL, E.; LARESGOITI, I. & ECHEVARRI, J. 1993: A multi-agent approach to analyse disturbances in electrical networks. Proceedings of Expert Systems Applications to Power Systems, vol 2, pp 127-128.

ANNOVAZZI-LODI, V.; DONATI S.; & MERLO S. 1992: Coiled-fiber sensor for vectorial measurment of magnetic field. Journal of Lightwave Technology, vol. 10, pp. 2006-2010.

ARDITTY H. J; BOURBIN Y.; MAPUCHON M. & PUECH C. 1981: Current Sensor Using State-of-the-art Fiber-optic Interferometric Techniques. Technical Digest, 3 rd International Conference on Integrated Optics and Optical Fiber Communication, San Francisco,vol 2, pp 78-81.

ARREGUI, F.J.; LENAHAN K. M.; LIU Y; MATIAS, R. & CLAUS,O. 1999:Self-assembled optical fiber sensors, Proceedings of the SPIE on Sensory Phenomena and Measurement Instrumentation for SmartStructures and Materials, vol. 3670, pp. 74-81.

ADXL-50 Specification Sheet 1996, Analog Devices, Inc., Norwood, MA.

ADXL-05 Specification Sheet 1996, Analog Devices, Inc., Norwood, MA.

BERTHOLD, J. W.; GHERING, W. L. & VARSHNEYA, D. 1987: Design and characterization of a high-temperature fiber-optic pressure transducer, Journal of Lightwave Technology, vol.5, pp.1-6.

BORN, M. & WOLFE, E. 1975: Principles of Optics, Pergamon Press, New York, 5ªEdition.

BUCARO, J. A.; DARDY, H. D. & CAROME E.F. 1977: Fiber optic hydrophone, Journal of the Acoustic Society of America, vol. 62, pp. 1302.

BUCHOLTZ, F.; VILLARRUEL, C. A.; DAVIS, A. R.; KIRKENDALL, C.K.; DAGENAIS, D.M.; MCVICKER,A.M.; PATRICK, S.S.; KOO, K.P; WANG, G.; VALO, H.; LUND, T.; ANDERSEN, A. G.; GJESSING, R.; EIDEM, E. J. AND KNUDSEN T. 1995: Multichannel fiber-optic magnetometer system for undersea measurements, Journal of Lightwave Technology, vol. 13, pp. 1385-1395.

CHAN, K.; ITO, H. & INABA, H. 1984: An optical fiber based gas sensor for remote absorption measurement of low-level CH_4 gas in the near-infrared region, Journal of Lightwave Technology, vol. 2, pp. 234-237.

CLAUS, R. O.; GUNTHER, M. F.; WANG, A. & MURPHY, K. A. 1992:Extrinsic Fabry-Perot sensor for strain and crack opening displacement measurements from -200 to 900°C, Smart Materials and Structures, vol. 1,pp. 237-242.

CLAUS, RO.; HOLTON, C E.; ZHAO, W. 1998:Performance of optical fiber sensors embedded in polymer matrix composites for 15 years. Proceedings of the SPIE Sensory Phenomena and Measurement Instrumentation for Smart Structures and Materials, vol. 3330, pp. 8-11.

CLAUS, R.O. 1997: Optical fiber instrumentation and applications, Proceeding of the SPIE on Smart Electronics and digital interface ,vol. 3242,pp. 20-24.

COLE, J. H.; JOHNSON, R. L.; AND BHUTTA,P. G. 1977: Fiber optic detection of sound, Journal of the Acoustic Society of America, vol. 62, pp. 1136.

CRAWLEY, E.F. 1994:Intelligent structures for Aerospace: A technology overview and assessment. AIAA Journal, vol.32, no 8, pp 1689-1899.

CULSHAW, B. 1995: Introduction to special issue on optical fiber sensors, Journal of Lightwave Technology, vol. 13, no 6, pp. 1187.

DAVIS, M. 1998:An international review of institutional reform in the power sector. EDRC Report, University of Cape Town.

DAY, G. W; DEETER, M. N.; ROSE, A. H. & ROCHFORD K. B. 1994: Faraday Effect Sensors for Magnetic Field and Electric Current, SPIE Proceedings, Vol. 2292, pp. 42-47.

DEBOUX, B. J. C.; LEWIS, E. ; SCULLY, P. J. ; & EDWARDS R. 1995,:A novel technique for optical fiber pH sensing based on Methylene blue adsorption, Journal of Lightwave Technology, vol. 13, pp. 1407-1414.

DIDOMENICO, M. Jr. 1972: Material dispersion in optical fiber waveguides, Applied Optics, vol. 11, no3, pp. 652-654.

DILLS, R. 1983:Temperature measurement by lightwaves, Journal of Applied Physics, vol. 84, no3, pp1198-1202.

DIXON, R.C. 1994: Spread Spectrum Systems, 3 Edition, New York, Wiley and Sons.

DIXON, R.C. 1994: Spread Spectrum systems with commercial Applications, New York Wiley & Sons

DOOLEY, R. 1998: Unintended consequences of energy R&D in a deregulated market. Energy Policy, vol. 26, no 7, pp 547-555.

DRUY, M. A. & STEVENSON, W. A. 1988: In situ composite cure monitoring using IR transmitting optical fibers, Proceedings of the SPIE, vol. 986, pp. 130.

DRYAGIN, Y. A., PARSHIN, V. ;. KRUPNOV, A. F; GOPALSAMI, N. & RAPTIS, A.C. 1996:Precision broadband wavemeter for millimeter and submillimeter range, IEEE Transactions on Microwave Theory and Technology., Vol. MTT-44, pp1610–1613,.

DE MELO, M. T.; LANCASTER, M. J.; YOKOTA, H. & GOUGH C. E. 1995:High temperature superconducting microstrip resonators for the measurement of .lms made by pyrolysis, Proceedings of the 1995 IEEE MTT-S, pp868–872,

FENG, G.; KLEIN, M. V.; KRUSE, J. & FENG, M. :1996:Mode coupling in superconducting parallel plate resonator in a cavity with outer conductive enclosure. IEEE Trans. Microwave Theory and Technology., Vol. MTT-44, pp 944–952,.

FARBER, E.; DEUTSCHER, G. ; KOREN, G. & JERBY, E. 1996:Microwave measurements of high Tc superconductors. 9th Conference. Electrical and Electronics Engineering. in Israel,pp 444–447,

FLAVIN, D. A.; MCBRIDE, R. & JONES, J. D. C. 1995:Interferometric fiber-optic sensing based on the modulation of group delay and first order dispersion: application to strain-temperature measurand. Journal of Lightwave Technology, vol. 13, pp.1314-1323.

FEHER K, 1981: Digital Communications, Prentice Hall, New York.

FOX, A. G. & LI, T. 1961:Resonant modes in a maser interferometer. Bell Systems Technical Journal, Vol. 40, pp453–458,.

FUHR, P.L & HUSTON, D.R. 1995:Fiber Optic Smart Civil Structures, SPIE Proceedings, Vol. 2574, pp. 6-11,.

FUJII, T.; MAZAKI, H. ; TAKEI, F.; BAE, J. ; NARIHIRO, M. ; NODA, T. ; SAKAKI, H. ; MIZUNO, K. & RANSON, R. G. 1996:Coherent power combining of millimeter wave resonant tunneling diodes in a quasioptical resonator. IEEE MTT-S Digest, pp919–922,

GIALLORENZI, T.G & BUCARO, J. A. 1982 :Optical Fiber Sensor Technology, IEEE Journal of Quantum Electronics, Vol. QE-18, No. 4, pp. 626-664,.

GRATTAN, K.T.V.& MEGGIT, B.T. 1995: Optical Fiber Sensor Technology, Chapman & Hall, London.

GOODMAN, TW. 1985: Statistical Optics, Wiley Series in Pure and Applied Optics, NewYork

GREEN, P.E Jr.1993: Fiber Optic Networks, Prentice-Hall Inc., New Jersey,.

GOTTLIEB, M. & BRANDT, G. B 1981:Fiber-optic temperature sensor based on internally generated thermal radiation. Applied Optics, vol. 20, pp. 3408.

GORDEON, M. & REDMON, J.R. 1991: Electric co-operatives and distribution automation- a survey. IEEE Rural Electric Power Conference, pp A1.1 – A 1.6

GUENTHER, R. 1990: Modern Optics, John Wiley and Sons, New York.

HABEL, W. R. & POLSTER H. 1995:The influence of cementitious building materials on polymeric surfaces of embedded optical fibers for sensors. Journal of Lightwave Technology, vol. 13, pp. 1324-1330.

HILL, K.O.; MALO, B.; JOHNSON, D.C. & SKINNER, I. 1990:Efficient mode conversion in telecommunication fibre using externally written gratings. Electronics Letters, vol. 26, pp. 1270-1272.

HORDRIK, A., BERG, A. & THINGBO, D. 1983: A fiber optic gas detection system, European Conference on Optical Communications, Geneva, pp. 317-320.

HAUS, H. A. 1984: Waves and Fields in Optoelectronics, Prentice& Hall,Inc., Englewood Cliffs, New Jersey,

HORIGUCHI, T.; SHIMIZU, K. ;KURASHIMA, T.; TATEDA, M. & KOYAMADA, Y. July 1995 :Development of a distributed sensing technique using Brillouin scattering. Journal of Lightwave Technology, vol. 13, pp. 1296-1302.

HRABLIUK, J.D.P. 2001 : Interfacing Optical Current Sensors in a Substation, IEEE PES Summer Power Meeting, Vancouver, B.C., pp89-92.

JACOBSON, C. P. February 1997:U.S. Navy Fiber Optic Sensor Technology. Photonics West SPIE, SanJose,pp 234-240.

JEFFERS, L. A.1985:Fiber optic SO_2 analyzer. Proceedings of the SPIE, vol. 566.

JENKINS, F. A. & WHITE, H. E. 1957, Fundamentals of Optics, 3rd ed., McGraw-Hill, New York.

KAHN, MTE. 1998, Development of a non-monochromatic lightwave micro-interferometric, etalon based, vibration sensor for applications in smart structures, Masters Degree Thesis, Peninsula Technikon

KAHN, M.T.E, September 1997:Intelligent structures with opto-electronic sensor systems. Elektron Journal of the SAIEE, pp 35-37,

KHAN, MTE . September 2000:Electronic Signal Processing Techniques for Optical Fibre sensors, SATCAM 2000, Somerset West, South Africa,.

KAHN, MTE. 1999: Development of a non-monochromatic lightwave Fabry Perrot etalon for smart structure applications, ISA Transactions, vol.38, pp 337-345

KHAN, MTE. 1998:Electro-optic Technologies for Sensor Applications, Advances in Systems, Signals, Control & Computers, vol.3, Durban, South Africa,.

KAHN, MTE , March 1999:Lightwave acoustic vibration sensor for smart structures.Mechanical Technology Journal

KEISER, G. 1991: Optical Fiber Communications, Second Edition, McGraw-Hill Inc., New York,.

KERSEY, A. D.; DANDRIDGE, A & DAVIS M. A., January 1992:Code-Division Multiplexed Interferometric Array With Phase Noise Reduction and Low Crosstalk. Optical Fiber Sensors: IEEE and Optical Society of America, pp 266-269.

KIM C. G & RYU, K. S. November 1996 :Low Magnetic field Measurement by NMR Using Polarized Flowing Water", IEEE Transactions on Magnetics, Vol. 29, No. 6,.

KOSTIC, A.; HOLTON, E.; CLAUS, O. 1999:Optical fiber magnetic fieldsensors and signal processing for vehicle detection and classification. Proceedings of the SPIE on Mobile Robots XIII and Intelligent Transportation Systems, Vol. 3525,pp. 381-392,

KURIBARA, M. 1983:Liquid-core optical fiber for voltage measurement using the Kerr effect. Electronics Letters, vol. 19, pp. 133-135.

LAGAKO N., LITOVITZ, T. MACEDO, P. & MOHR, R. 1981: Multimode optical fiber displacement sensor. Applied Optics, vol. 20, pp. 167-168.

LAWSON, C. M. & TEKIPPE, V. J 1983: Environmentally insensitive diaphragm reflectance pressure sensor. Proceedingsof the SPIE, vol. 412, pp. 96-103.

LENZ, J.E. June 1990:A review of Magnetic Sensors", Proceedings of the IEEE, Vol. 78, pp. 973-989.

LIMANOVA, N. I. 1996: Multichannel fiber optic sensors for precision measurements of vibration and linear position. Proceedingsof the SPIE, vol. 2839, pp. 342-349.

LIU, P.L. & LI, B.J. 1992:Semivectorial beam-propagation method for analyzing polarized modes of rib waveguides. IEEE Journal of Quantum Electronics, vol. 28, pp. 778–782

LIU, Y; WANG, Y. X.; ZHAO, W; CLAUS, R O.; LENEHAN, K; HEFLIN, JR. 1998:Ionically self-assembled second-order nonlinear optical thin film materials and devices. Proceedings of the SPIE on Sensory Phenomena and Measurement Instrumentation for Smart Structures and Materials, Vol. 3330, p. 75-79

LIU, Y; ZHAO, W; WANG, Y. X.; CLAUS, RO. 1998 :Functionally tailored nano particle-based ionically self-assembled multilayer thin films. Proceedings of the SPIE Smart Materials and Technologies, vol. 3324, pp. 45-48.

LI, T; MAY, RG.; WANG, A; CLAUS, R O. 1998:Multimode interference and a white light scanning Michelson interferometer with a 400-mm sapphire fiber sensing head. Proceeings of the SPIE:Optical and Fiber Optic Sensor Systems ,vol. 3555, pp. 217-224.

LORRAIN,P & CORSON, D.R. 1979: Electromagnetism. Principles and Applications. W.H. Freeman and Company, San Francisco.

LUO, F.; MENG, A.; LIU, J.; KIM, K. & PARK, D. 1996:Optical fiber sensing method for the in-situ cure monitoring of composite materials. Proceedings SPIE, vol. 2839, pp. 413-419

MAY, G.; CLAUS,O.1996: Nondestructive Evaluation for Process Control in Manufacturing, Proceedings of the SPIE ,vol. 2948, pp. 24-34.

MARCUSE, D.1991,Theory of Dielectric optical Waveguides, Academic Press, Boston

MANSOURI, S. & SCHULTZ, J. S. 1984: A miniature optical glucose sensor based on affinity binding. Bio Technology, vol 46,no3, pp 885-889.

MANSOUR I; CAPOBIANCO,C.B.; ROSA, C. 1996.:Noniterative vectorial beam propagation method with a smoothing digital filter: Journal of Lightwave Technology., vol. 14, pp. 908–913.

MARKS, J. 1999: Use of fibre optic cable grows for T & D applications. Electrical World, pp44-45

MARKLE, D.R; MCGUIRE, D. A.;GOLDSTEIN, S. R. ; PATTERSON, R. E. &. WATSON, R. M 1997:A pH measurement system for use in tissue and blood employing miniature fiber optic probes. Advances in Bioengineering, Ed: Viano, D. C., pp. 123.

MARSHALL,R.H. 1996: Mach-Zehnder electronically scanned white-light interferometer. Journal of Lightwave Technology, vol. 14, no 3, pp. 397-402.

MAY, G.; SHINPAUGH, K A.; DUNCAN, PG.; LOOS, AC.; CLAUS,R.O. 1997 : Multifunctional fiber optic sensor for manufacturing of thermoset matrix compositematerials. Proceedings of the SPIE Smart Structures and Materials ,vol. 3044, pp. 244-251.

MCCLEARY, J., LI, M. Y & CHANG, K. 1994:Ka-band slot-fed higher order mode low-loss Fabry-Perot filters. IEEE Transactions on Microwave Theory and Technology, Vol. MTT-42, pp1423–1426,.

MEASURES, R. M. 1992:Advances toward fiber optic based smart structures. Optical Engineering, vol. 31, no 1,. pp. 34-47.

MELLER, SA.; DE VRIES, MJ.; ARYA, V; CLAUS.; ZABARONICK R.O. 1998:Advances in optical fiber sensors for vehicle detection. Proceedings of the SPIE Intelligent Transportation Systems, vol. 3207, pp. 318-322.

MELTZ, G. 1996:Overview of fiber grating-based sensors. Proceedings of the SPIE, vol. 2838, pp. 2-22.

MLODZIANOWSKI, D., & CULSHAW, B. 1988: Multiplexing System for Frequency Modulated Fibre Optic Sensors Using Pseudorandom Sequences. Fiber Optic Sensors III,SPIE,vol 1011, pp 26-29.

MICHIE, W. C., CULSHAW, B. ; KONSTANTAKI, M. ; MCKENZIE, I.; KELLY, S. ; GRAHAM, N. B. & MORAN, C. 1995: Distributed pH and water detection using fiber optic sensors and hydrogels. Journal of Lightwave Technology, vol. 13, no 7, pp. 1415-1420.

MIGNANI, A. G. & BALDINI, F. 1995:In-vivo biomedical monitoring by fiber-optic system. Journal of Lightwave Technology, vol. 13, pp. 1396-1406.

MILANOVICH F. P, & HIRSCHFELD, T. 1983:Process, product, and waste stream monitoring with fibre optics. Advances in Instrumentation, Proceedings ISA Int. Conf. vol. 38, pp. 407-418.

MOLLER K. D. 1991, Optics, University Science Books, California,. pp. 273-275.

MOURACHKINE, A. P. & BAREL, A. R. F. 1995:Microwave measurement of surface resistance by the parallel-plate dielectric resonator method. IEEE Transactions on Microwave Theory Technology, vol. MTT-43, pp 544–551,

MURPHY, K. A.; FOGG, B.R.& VENGSARKAR, A.M. 1992 :Spatially weighted vibration sensors using tapered two-mode optical fibers. Journal of. Lightwave Technology, vol. 10, pp. 1680-1687.

MELLER, S.A.; ZABARONICK, N.; GHOREISHIAN, I.; ALLISON, J.; ARYA, V.; DE VRIES, J.; CLAUS, R.O. 1997: Performance of fiber optic vehicle sensors for highway axle detection: Proceeding of the SPIE Transportation Sensors and Controls: CollisionAvoidance, Traffic. Management, and ITS ,vol. 2902, pp. 166-172.

NELLEN, P. M., BRONNIMANN, R. ; SENNHAUSER, U. J.; ASKINS, C. G.&. PUTNAM, M. A 1996: Strain measurement on concrete beam and carbon fiber cable with distributed optical fiber Bragg grating sensors. Optical Engineering, vol. 35, pp. 2570-2577.

OLIVER, S. A. & DIMARZIO, C. A. 1993 :Magnetooptic Kerr Effect Sensors for Fiber Optic Applications, SPIE Proceedings, Vol. 2, pp. 429-437.

OH, K.D.& RANADE J, November 1996:Fiber Optic EFPI-based Sensor for Low Magnetic Field Measurement", Conference Proceedings, 9th Annual Meeting of the IEEE Lasers and Electro-Optics Society, vol. 1, pp. 236-237.

OH, K.D.; RANADE, J., ARYA V; WANG A; CLAUS, R.O. 1999:Miniaturized fiber optic magnetic field sensors. Proc. SPIE Vol. 3538, p. 136-142, Process Monitoring with Optical Fibers and Harsh Environment Sensors, Michael A. Marcus; Anbo Wang; Eds.

OH, K D.; RANADE, J. ; ARYA, V. ; WANG A. &. CLAUS R. O. 1999: Fiber Optic EFPI-basedSensor for Low Magnetic Field Measurement. IEEE/LEOS Conference Proceedings,vol.1, pp. 236-237.

OH, K. D.;RANADE, J.; ARYA, V. ;WANG, A. & CLAUS, R. O. 1997:Optical Fiber Fabry-Perot Interferometric Sensor for Magnetic Field Measurement. IEEE Photonics Technology Letters, vol. 9,no. 6, pp. 797-799.

OH, K.D.; RANADE, J; ARYA, V; WANG, A; CLAUS, RO. 1999:Miniaturizedfiber optic magnetic field sensors. Proc. SPIE Vol. 3538, p. 136-142, Process Monitoring with Optical Fibers and Harsh Environment Sensors, Michael A. Marcus; Anbo Wang; Eds., 01/1999

OHLSON, N.A, July 89:Lightwave systems with optical amplifiers. Journal of Lightwave Technology. vol 7, pp1071-1082

PETERSON I.J. & C. G. VUREK, 1984:Fiber optic sensors for biomedical applications. Science, vol. 224, pp. 123-127.

PRESS, W.H. 1998: Numerical Recipes in C. The art of Scientific Computing, Cambridge University Press, London.

PETERSON, R; GOLDSTEIN, S. R.; FITZGERALD, R. V & BUCKHOLD, D. K. 1980: Fibre optic pH probe for physiological use. Analytical. Chemistry., vol. 52, pp. 864.

PORAT, B. 1997:A Course in Digital Signal Processing, New York, Wiley and Sons.

PICON, L.L.; KOLESAR, E. S. & BRIGHT, V. M. 1994:Low-Intensity Magnetic Field Detection with a Magnetostrictive Fiber Optic Interferometric Sensor", SPIE Proceedings. Vol. 2292, pp. 14-25.

QUIST, S, MARTINELLI, V. & IKEDA, R. 1996:Fiber-Optic Gyroscopes in Automotive and Industrial Applications, Sensors, Vol. 13, No. 4, pp. 42-46.

RAMAKRISHNAN, S., UNGER, L. & KIST, R. 1988: Line loss independent fiber optic displacement sensor with electrical sub carrier phase encoding. 5th Int. Conf. Optical Fiber Sensors, OFS '88, New Orleans, pp. 133-136.

RHYNE, V.T. 1982: Field demonstrations of communication systems for distribution automation. Electric Power research Institute, vol 2, pp 45-56.

ROGERS, A. 1997:Essentials of Opto-electronics, Chapman and Hall,London

ROAN, G. T. & ZAKI, K. A. July 1997:Calculation of losses in a super conductive resonator using FDTD. IEEE AP-S Digest, pp 384–387,

RUDOLPH, D.L. 1998:An integrated solution to substation automation. IEEE Rural Electric Power Conference, pp C2.1- C2.9

SANAGI, M.; YAMAMOTO, E.; NOGI, S. &. RANSON, R.G 1996:Axially symmetric Fabry-Perot power combiner with active devices mounted on both the mirrors. IEEE MTT–S Digest, vol 66,pp 1259–1262,

SCHAWLOW, A. L. & TOWNES, C. H. 1958: Infrared and optical masers. Physics Review., Vol. 112, 1940–1949

SHINPAUGH, K.A., R. L. SIMPSON, A. L. WICKS, S. M. HA, & J. L. FLEMING 1992:Singal-processing techniques for low signal-to-noise ratio laser Doppler velocimetry signals. Experiments in Fluids, vol. 12, pp. 319-328.

SNYDER, A.W. & LOVE J.D 1983: Optical waveguide Theory, Chapman and Hall, London

SWART,P.L.;SPAMMER, S.J. & THERON,S. 1997:Multiplexed Mach-Zender interferometer for multiphase current measurement. Optical Engineering, vol. 36, no 6, pp 1135.

SIRKIS, J.; BERKOFF, T.A. ; JONES, H.; SINGH, A. ; KERSEY, A.D. ; FRIEBELE, K. & PUTNAM, E. July 1995 :In-line fiber etalon (ILFE) fiber-optic strain sensors. Journal of Lightwave Technology, vol. 13, no 6, pp.1256-1263.

SHIN, K.A. 1992: Signal processing techniques for low SNR ratio laser Doppler velocimetry signals, Experiments in Fluids, vol 32,no 2, pp 319-328

STREMLER, F. G. 1996: Introduction to Communication Systems ,(3rd ed), Addison-Wesley, Toronto.

STREET, A. M. & EDWARDS, D. J. 1995:Bandwidth Requirements for M-Sequence Codes used in Fibre Optic Multiplexing Systems. IEE Proceedings on Optoelectronics., vol 142, No 4, pp 202-206.

THOMPSON, A. 2000: Programmable , Multi-purpose Opto-Electronic Sensor System, IEEE Aerospace & Electronic Systems, pp 13-16

TANAKA, T. & BENEDECK, G. B. 1975:Measurement of the velocity of blood flow (in vivo) using a fiber optic catheter and optical mixing spectroscopy. Applied Optics, vol. 14, pp. 189.

UDD, E. 1991:Fiber Optic Sensors An Introduction for Engineers and Scientists, John Wiley & Sons Inc.,New York.

UDD, E. 1995: Fibre optic Smart Structures, John Wiley and Sons,New York.

URRUTI, E.H; BLASZYK, P.E. & HAWK, R. M. 1988:Optical fibers for structural sensing applications. Proceedings SPIE, vol. 986, pp. 158.

VENGSARKAR, A.M.; LEMAIRE, P. J. ;JUDKINS, J. B. ; BHATIA, V. ; ERDOGAN, T. &. SIPE, J. E 1996:Long-period gratings as band-rejection filters. Journal of Lightwave Technology, vol. 14, pp. 58-65.

WANG, G. Z.; WANG, A. ;MAY, R. G. & CLAUS, R. O. 1995: Self-referenced fiber optic sensor for microdisplacement measurement. Optical Engineering, vol. 34, pp. 240-243.

WANG, A.; HE, S. ; FANG, X. ;JIN, X. & LIN, J. Oct. 1992:Optical fiber pressure sensor based on photoelasticity: application. Journal of. Lightwave Technology, vol. 10, pp. 1466-1472.

WAGNER, S.S. April 1987:Optical amplifier applications in fibre optic networks. IEEE Transactions on Communications, vol 35, pp 419-426

WALKER, J. C.; HOLMS, R. & JONES, G. R. 1992 :Network of 12 Optical Sensors Using Code-Division Multiplexing.. Electronic Letters, vol 28, No 22, pp 2074-2075.

WAIT, J. R. 1962: Electromagnetic Waves in Stratied Media, Pergamon Press, New York.

WHITESEL, H.K.; SARKADY, A. A.; OVERBY, J.K.; JACOBSON, C.P. 1997:Code Division Multiplexing of Fiber Optic Sensors with LED Sources. Photonics West, Proceedings of the SPIE San Jose, vol.144,pp 201-205

WOOD,R.L.; TAY, A. K. &. WILSON, D.A 1989:Design and Fabrication considerations for composite structures with embedded fiber optic sensors. Proceedings SPIE, vol. 1170, pp. 160.

YU F.T., J. ZHANG, K. PAN, D. ZHAO, AND RUFFIN, P. B. 1995:Fiber vibration sensor that uses the speckle contrast ratio. Optical Engineering, vol. 34, pp. 236-239.

YEVICK, D. 1994:A guide to electric field propagation techniques for guided wave optics. Optics and Quantum Electron., vol. 26, pp. S185–S197.

YAMAUCHI, J; ANDO, T. & NAKANO, H. 1991:Beam-propagation analysis of optical fibers by alternating direction implicit method. Electronics. Letters, vol. 27, pp. 1663–1665

ZIMMERMAN B. D., R. O. CLAUS, D. KAPP, AND. MURPHY, K. A 1989, "Optical time domain reflectometry for local strain measurements. Proceedings of the SPIE, vol.1170, p534.

ZHAO, W.; CLAUS, R.O.,1998:Long-period grating fiber sensor with fiber Bragg gratingdemodulator. Proceedings of the SPIE Vol. 3330, pp. 231-236, Smart Structures and Materials 1998: SensoryPhenomena and Measurement Instrumentation for Smart Structures and Materials, Richard O.Claus; William B. Spillman; Eds..

The Big Squeeze available from http://bama.ua.edu/~trieland/tcf355/connections /tsld018.htm. INTERNET. Accessed March 16, 2000.

Advanced control of energy and power systems (ACEPS) from http://www.mines.edu/Research/aceps.htm. INTERNET. Accessed January 25, 1999.

History of Internetworking, . available from http://www.cisco.com/cpress/ cc/td/cpress/fund/ith/ith01gb.htm. INTERNET.Accessed November 16, 2002.

Farely, T., Digital Wireless Basics II available from http://www.privateline.com/PCS/Multiplexing.htm. INTERNET. Accessed July 16, 2002.

Appendix 1

S1000 Linear Array CCD Spectrophotometer used at Nebuweb Labs.

The picture below is that of the S100 linear array spectrometer of Ocean Optics, Inc., which is used for diffracting (with reflection diffraction gratings) the optical frequency components, of the fiber sensor, at different angles and collecting the corresponding optical intensities to a linear CCD array. Each element or pixel of the CCD array corresponds to a particular optical frequency. The S100 has a maximum clock input rate of 2 MHz. The video output pin of the S1000 sequentially outputs 1100 CCD pixel voltages in analog pulses, at half the input clock rate, with a range of 0 to 10 volts (added with a user selective offset), at intervals of 8192 input clock pulses. At the beginning of each integration period, all pixel charges are transferred at once to CCD registers for sequential read out through the video output pin. After the transfers, the photodiodes continue to conduct again, and charge is stored proportional to the light intensity over the integration period. An enable input signal allows to output triggers, synchronized with the 1100 analog video output pulses, which is at half the rate of the input clock frequency. The rising edge of the trigger pulses are used as the conversion triggers for the analog-to-digital conversion of the 1100 analog video output pulses.

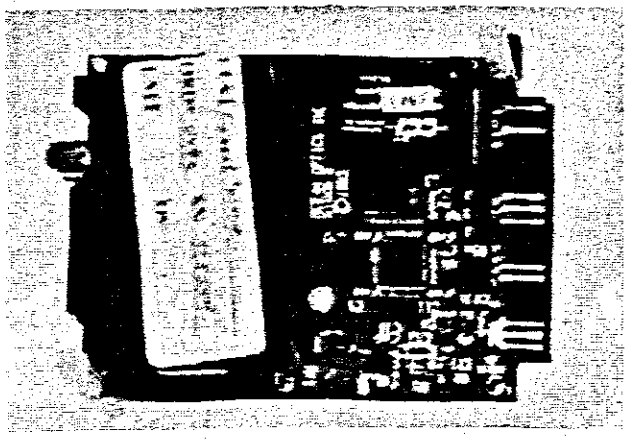

Figure A1: Picture of Spectrophotometer used to gain experimental data at Nebuweb.

Appendix 2

Analog-to-Digital Conversion Board

An analog-to-digital conversion board, as shown in the picture of Figure A2.1, was designed and developed at Nebuweb. The analog-to-digital conversion (ADC) board interfaces the CCD spectrometer with the TMS320C40 board. It digitizes the pulse amplitude signals from the spectrometer using the conversion trigger pulses, also coming from the spectrometer. The ADC board converts the analog pulses, each pulse corresponding to a particular CCD element and hence representing the intensity of a particular optical frequency, into 12-bit parallel digital signals which are interfaced with the communication ports of the TMS320C40 (henceforth also known as just 'C40) DSP chip. The interfacing connections are as shown in the figure below.. There are six communication ports in the 'C40 chip, and each port can handle 8 parallel data bits. For parallel interfacing of our 12-bit data we need two communication ports of the 'C40 chip, Figure A2.2 shows the interfacing with the Port 3 and 4. Note that after reset, the communication Ports 3, 4, and 5 are configured as input ports, and the communications Ports 1, 2, and 3 are configured as output ports A token forcing circuit is provided, if necessary, in the ADC board, which is required for an output port to be configured as an input port, or vice versa. For the data acquisition and processing advantages, the 12-bit data of the ADC board is read as 16-bit data by the 'C40 chip, the least significant 4 bits being always zero (i.e. grounded). As the speed of the 'C40 chip is very high (40 MHz) if compared to the speed of the ADC chip (800 kHz), only a one way handshaking is implemented for transferring data from the ADC board to the 'C40 communication ports.

The Burr-Brown 12-bit analog-to-digital converter, ADS7810, is used for the ADC board. A brief description of this analog-to-digital converter is provided below. *Analog-to-Digital Converter ADS7810*: The speed of the Ocean Optics' S1000 spectrometer allows an analog-to-digital converter no faster than 1 MHz. After extensive vendor search the most suitable ADC chip, for interfacing with the TMS320C40 communication ports, was decided to be 28-pin Burr-Brown CMOS 12-bit parallel converter, ADS7810, which is specified at 800 kHz sampling rate, having an industry standard ±10 V analog input voltage range and a power dissipation under 250 mW .Though a 16-bit ADC were more appropriate for our system, a suitable chip did not exist at the time of our design with a sampling rate of around 1 MHz.

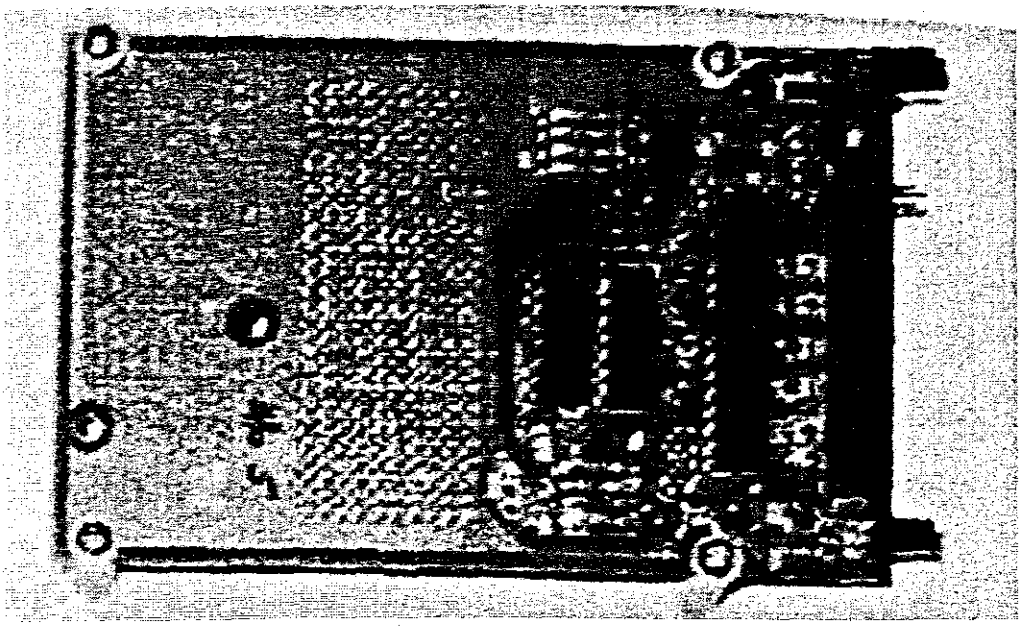

Figure A2.1 The analog-to-digital conversion (ADC) board.

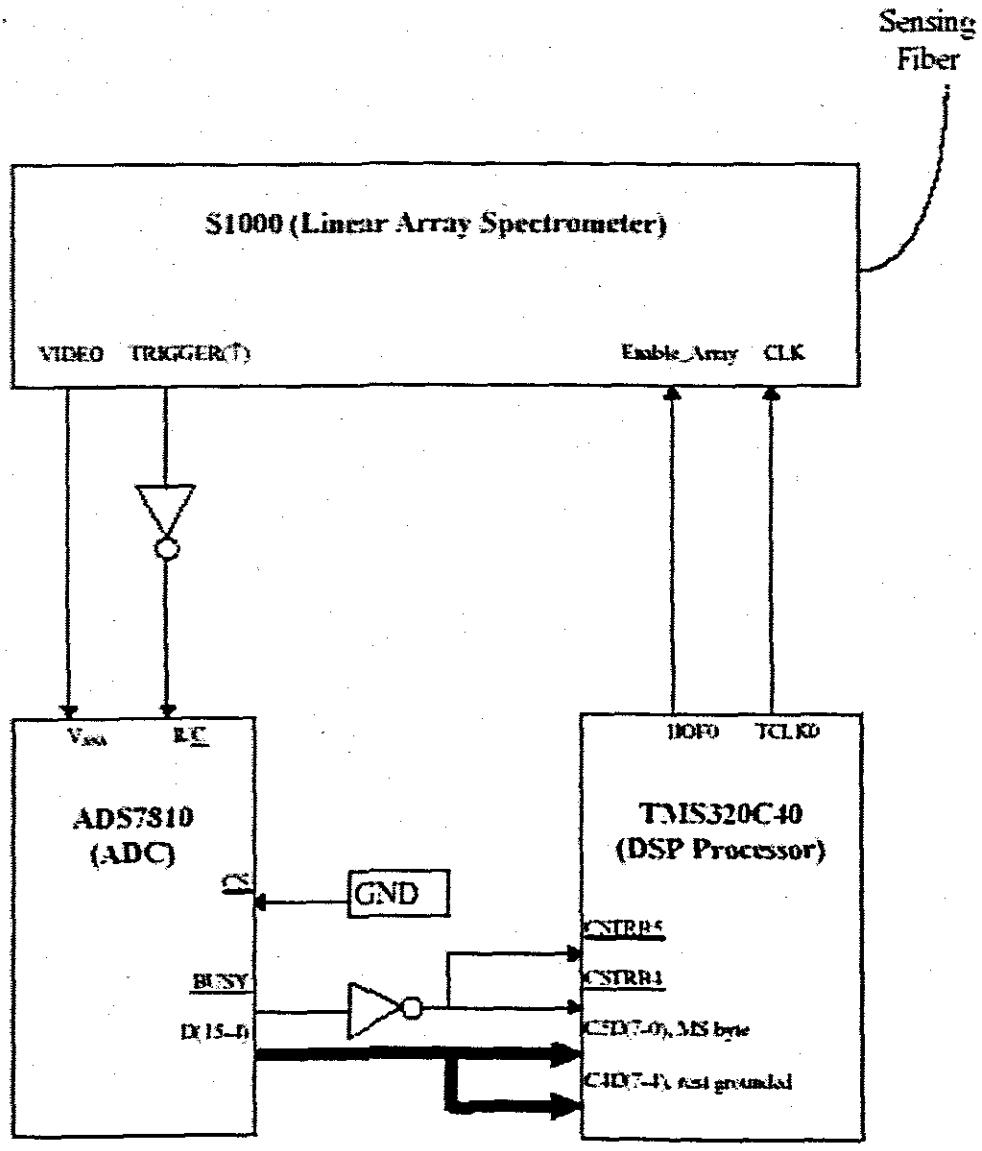

Figure A2.2

Interface connections of the CCD Spectrometer, the ADC chip, and the TMS320C40 chip.

Appendix 3

TMS320C40 Board

A real-time signal processing board, named the TMS320C40 board, as shown in Figure A3, was used in the project. The 'C40 board is the mother board of our sensor system. This board hosts the Texas Instrument's TMS320C40 (or just 'C40) floating point digital signal processor, which is used as the main processor for real time signal processing of the wavelength modulated optical fiber sensor system. The JTAG (or Boundary Scan) interface of the 'C40 chip is used to debug and/or upload/download programs to memory. The 'C40 board has a universal asynchronous receiver/transmitter (UART) to connect the system to any computer using the RS232 communication ports . The RS232 connection is used for the TCP/IP server in any computer to get access to the sensor system so that the server can send the sensor data in realtime if requested by any TCP/IP client through the Internet. The RS232 connection can also be used for any general purpose operations like uploading/downloading programs to/from the sensor system, or running a small operating system for the sensor system from any host computer. 128K of 32-bit words of Non-volatile SRAM and 512K of 32-bit words of fast SRAM is provided on the 'C40 board. The non-volatile RAM keeps the system programs and data intact at power off, and such the system can run by itself at power on. The SRAM can be used for running programs faster as it has a very small access time. A watchdog timekeeper is provided which keeps track of time, and can be used to time stamp any data if required, or to put an interrupt to the 'C40 processor at any predetermined time intervals. Xilinx field-programmable gate arrays are used as programmable glue logic for timing and interfacing all the components of the 'C40 board. A brief description of all the major components of the board are given below.

TMS320C40 DSP Processor:

325-pin grid array TMS320C40 of Texas Instruments, a 32-bit RISC architecture floating point DSP processor ,is used as the main processor for our wavelength modulated optical fiber sensor system. Our processor has a speed rating of 40 MHz, i.e. 50-ns instruction cycle times. The 'C40 processor has an instruction set of 145 instructions, the instruction

set being especially well suited to digital signal processing and other numeric-intensive applications. Most of the instructions take only a single cycle to execute. The floating point instructions are implemented using 12 (R0-R11) 40-bit wide extended-precision registers. Another 8 (AR0- AR7) 32-bit wide auxiliary registers are used primarily for address generation. Both the extended-precision and auxiliary registers can also be used as general purpose 32-bit integer registers. The 'C40 processor has two identical data (32-bit wide) and address (31 bit wide) buses, termed global and local buses, which support shared memory systems. It has a JTAG interface for IEEE Boundary Scan and other standard connections. 512 byte of instruction cache and 8 K-byte single-cycle dual access program or data RAM are provided as on-chip memory in the 'C40 processor. The 'C40 processor has six bi-directional communications ports and a six-channel DMA coprocessor for concurrent I/O and CPU operations. Separate internal data, program, and DMA coprocessor buses support parallel data, program, and I/O operations.

UART PC16550D:

14-pin PC16550D universal asynchronous receiver/transmitter (UART) with FIFOs of National Semiconductor [Nati95], is used with the 'C40 board for interfacing the stand alone real-time signal processing system with any serial communication ports of computers. The PC16550D performs parallel-to-serial conversion on data characters received from the CPU, and serial-toparallel conversion on data characters received from any peripheral device or any MODEM. It has all the modem control functions, CTS, RTS, DSR, DTR, RI, and DCD. The CPU is capable of reading the status of the UART (e. g., the error conditions, and the type and conditions of the transfer), at any time of operation. It can generate and detect even, odd, or no parity, and can add or delete start, stop, and parity bits. The UART can generate a programmable baud rate ranging from DC to 1.5M baud, and is capable of handling 5-, 6-, 7-, or 8-bit characters.

SRAM mPD434008 and Nonvolatile SRAM DS1245:

12K-word by 8 bits CMOS fast static RAMs μPD434008LE-20 , of NEC Electronics Inc., are used to design 512K of 32-bit words of SRAM memory. The chips have a small

plastic package of 36 pin. They have a very fast access time of 20-ns maximum. 128K x 8-bit nonvolatile static RAMs DS1245 of Dallas Semiconductor , are used to design 128K of 32-bit words of nonvolatile memory. It has direct interface with the 'C40 exactly like fast SRAM. Each nonvolatile SRAM has a self-contained lithium energy source, which automatically protects the data in the memory whenever the external power is turned off. It has 10 years minimum data retention capability in the absence of external power, and has unlimited write cycles with an access time of 70-ns.

Watchdog Timekeeper DS1286:

Watchdog timekeeper DS1286 of Dallas Semiconductor is used as watchdog timer, to keep track of time, or to time-stamp any data, if required. It keeps track of hundredths of seconds, seconds, minutes, hours, days, date of the month, months, and years, and can generate separate interrupts at any programmable time intervals and/or when the watchdogged processor goes out of control. It has an embedded lithium battery source which has a greater than 10 years of timekeeping in the absence of any external source.

Xilinx FPGA X'C4003A:

Two of the Xilinx field-programmable gate arrays (FPGAs) X'C4003A-4PC84 , are used to generate, buffer, and interface the control signals of the 'C40 processor, the PC16550D UART, and the memory devices. The X'C4003A-4PC84 is a 84-pin PLCC package with approximate gates count of 3000 and flip-flops count of 360 in a 10 x 10 configurable logic block (CLB) matrix. These FPGAs are configured by loading a binary file in it, and have unlimited reprogrammability. The X'C4003A chips provide programmable input pull-up or pulldown resistors, and programmable output slew rates. The X'C4003A can handle up to 24-mA sink current per output.

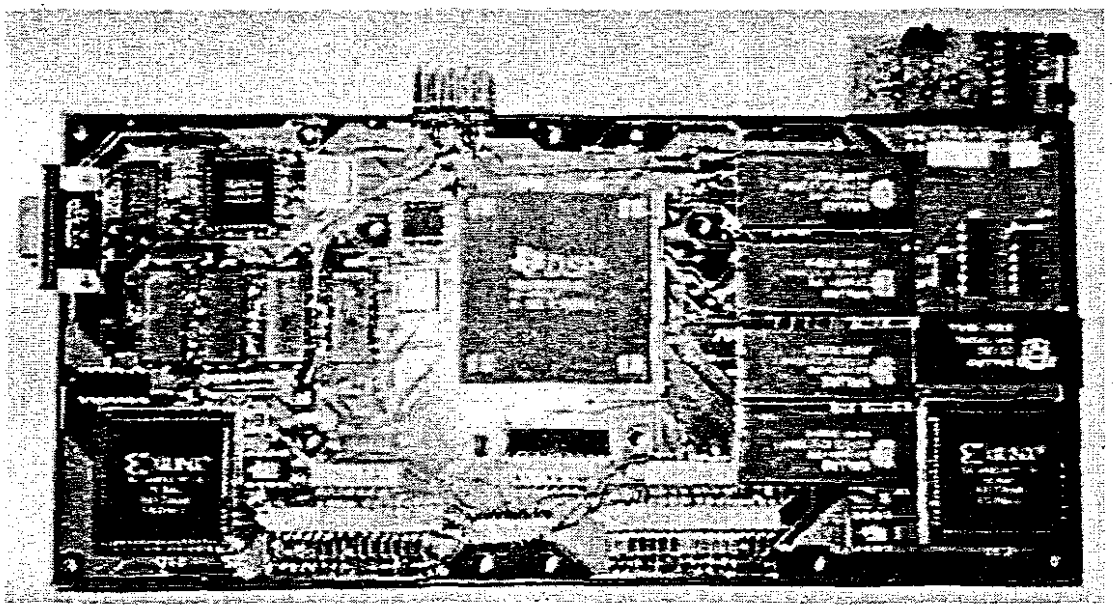

Figure A3

The TMS320C40 real-time signal processing board, which holds the 'C40 processor, the UART, SRAM, non-volatile SRAM, watchdog timekeeper, and the Xilinx FPGAs.

Appendix 4

Programming the Logic for the Xilinx FPGA XC4003A-4PC84

The base package of the Xilinx Foundation Series 6.0.1 software is used to program the logic of the FPGAs. The programming of the logic can be implemented by using VHDL or by using schematic capture from the library provided with the Foundation package. The schematic capture method is used for programming the Xilinx FPGAs as the logic required for our system is simple. Figure A4.1 and Figure A4.2 shows the schematics of the logic which are implemented in the Xilinx FPGAs. Once the schematic is drawn and a library for the schematic components is built, the Foundation software performs full automatic partitioning, placement, and routing of the FPGA available resources to implement the logic. The software finally produces a *.bit* file which when loaded into the FPGA, the chip gets programmed as the logic of the schematic. The software has the provision of pre-selecting pins for specific signals

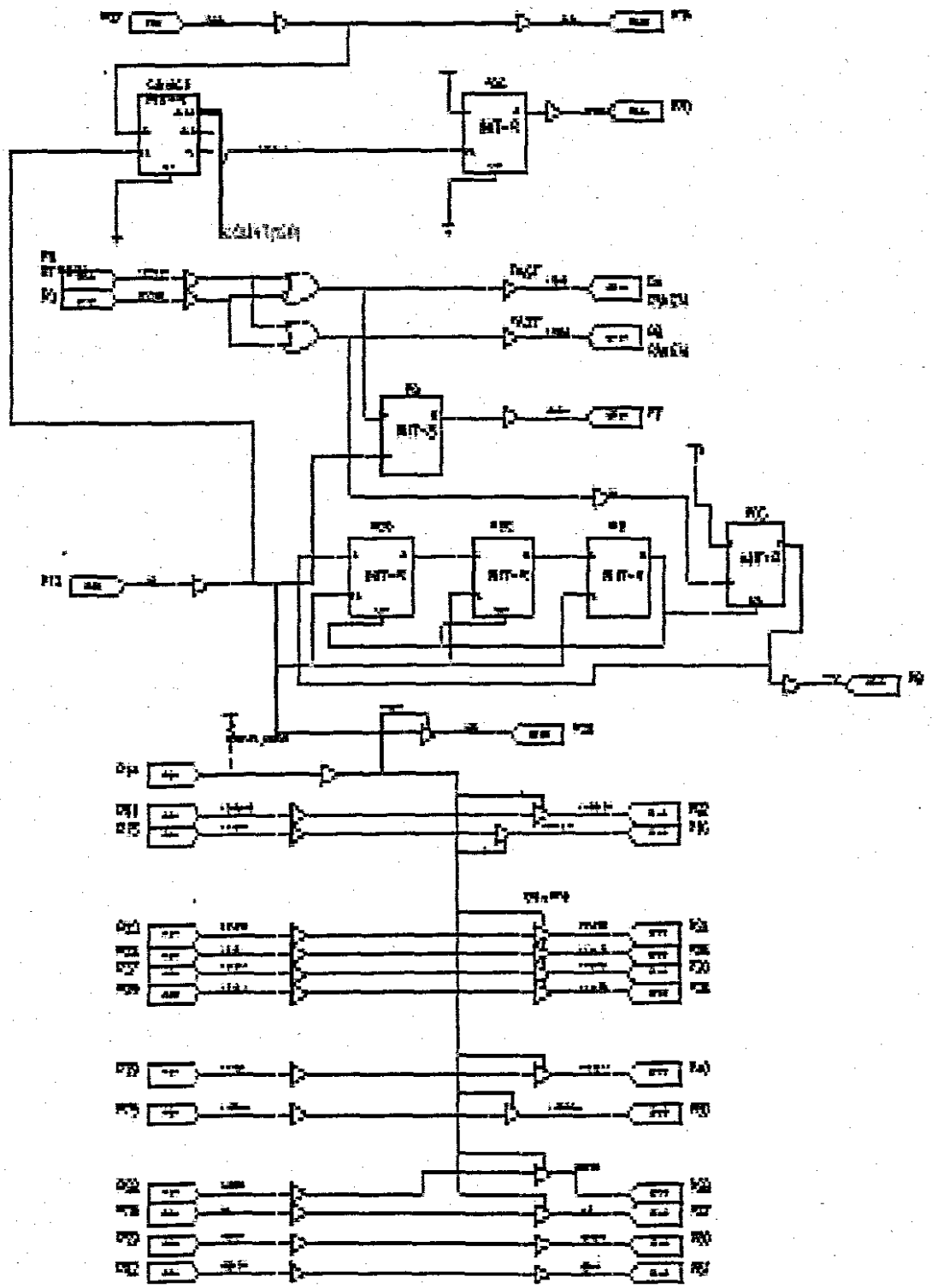

Figure A4.1 Top level schematic of the programmed logic for the Xilinx FPGA XC4003A-4PC84 to generate, buffer, and interface the control signals of the 'C40 local buses, the PC16550D UART, and the SRAM memory devices.

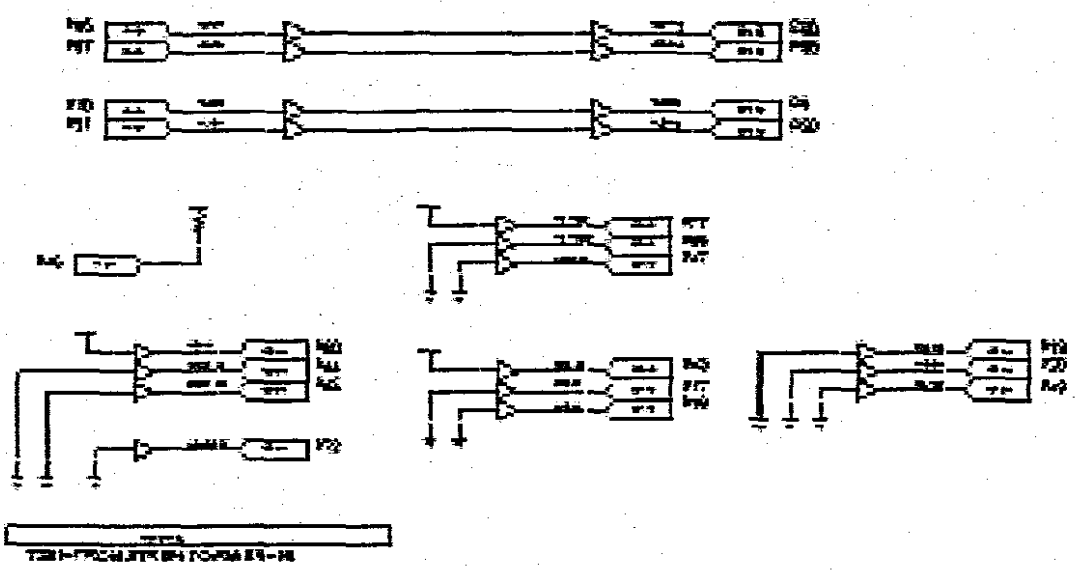

Figure A4.1 Continued Top level schematic of the programmed logic for the Xilinx FPGA XC4003A-4PC84 to generate, buffer, and interface the control signals of the 'C40 local buses, the PC16550D UART, and the SRAM memory devices.

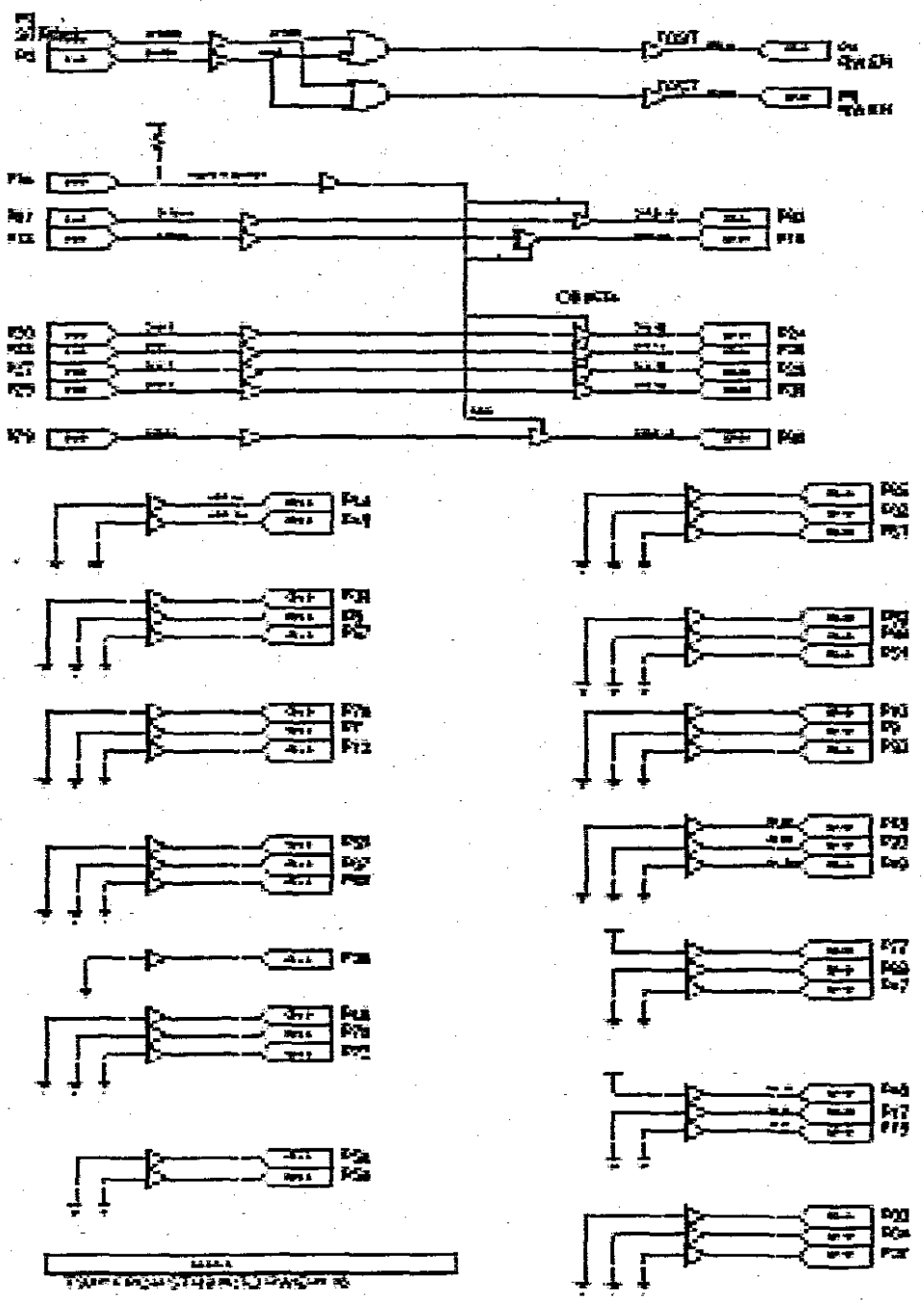

Figure A4.2 Top level schematic of the programmed logic for the Xilinx FPGA XC4003A-4PC84 to generate, buffer, and interface the control signals of the 'C40 global buses, and the non-volatile SRAM memory devices.

The Xilinx FPGA data sheet is not attached to this document and may be obtained from the supplier, Xilinx Inc., or their registered agent Avnett Kopp Ltd.

Appendix 5

Real Time Signal Processing Software

5.1 Real-Time Signal Processing Routines for the EFPI Sensor System

```
/*************************************************************************

Function Prototype:
void main (void)
Author and Date Started: Alexander Carberry, MTE Kahn 3/01/2000
Description:
The main() program calls all the initialization, data acquisition, and
signal processing functions. The functions could either be in C, or in
C4x assembly language.
Method:
The InitC4x() function initializes all the necessary registers of the
TMS320C4x DSP processor. The InitUART() function initializes all the
necessary registers of the UART for communicating with the comport or
computers. The CalbPxls(flaot *) function calibrates the 1100 CCD
pixels to wavelengths and the table is loaded at the input pointer. It
uses the Ocean Optics CCD spectrometer calibration coefficients. Every
individual CCD spectrometer, having a unique SIE number has its own
calibration coefficients.
(Note that the FFT calibration coefficients are not the CCD calibration
coefficients.) The AcqData(int iaData[],DMA3_DEST,DMA4_DEST) acquires
the 1100 data set at the given pointer iaData. There must be at least
275 (0x44c) memory locations both at iaDMA3_DEST and iaDMA4_DEST.
The rest of the functions are for the real-time signal processing for
the EFPI wavelength modulated optical fiber sensor.
Any new functions can easily be added in main() at it's proper place,
if necessary. Input Parameters and Ranges:
None.
Called By:
None.
*************************************************************************/



#include <stdlib.h>
#include <math.h>
/* If the stack is small, then large arrays must not be kept as local
variables. Local variables are placed on stack for processing. The
following variables are kept out of main() for monitoring from the
'watch' window. */
float
faData[1024],
faFourPiByLamda[1024],
faFltrdData[1024],
faFFTMag[1024];
float
fGapEst,
fTruGap,
fMaxPix,
fMaxVal;
short
nStatus;
```

```
int
iIndexOfMax,
iaData[1100],
iaDMA3_DEST[275],
iaDMA4_DEST[275];
typedef struct
{
float r;
float i;
} complex;
complex
FFTData[1024];
void main(void)
{
float
fMaxPix,fMaxVal;
int
i;
float
C2=-5.0963e-6,
C1=1.8196,
C0=-2.354;
/* FFT calibration coefficients for CCD of SIE687 */
vInitC4x();
vInitUART();
vCalbPxls(faFourPiByLamda);
for (;;){
nStatus = nAcqData(iaData,iaDMA3_DEST,iaDMA4_DEST);
/* nStatus = 0 , if nAcqData() is successful */
nStatus = nServUART(iaData);
/* nStatus = 0 , if nServUART() sends data to UART at the
request of server */
vFloatData(iaData+16,faData);
/* Type conversion, converts data from int to float */



/* Actual data starts 16 pixel later */
vFltrBw3(faData,faFltrdData,1024); /* High-Pass filter */
fftr(faFltrdData,FFTData,1024,0); /* SigTar function */
cvabs(FFTData,2,faFFTMag,1,512); /* VecTar function */
maxv(faFFTMag,1,&fMaxVal,&iIndexOfMax,512); /* VecTar function */
vFindFloatPix(iIndexOfMax,faFFTMag,&fMaxPix);
/* Gaussian interpolation */
fGapEst = C0 + C1*fMaxPix + C2*fMaxPix*fMaxPix;
vFindTruGap(fGapEst,&fTruGap,faData,faFourPiByLamda);
}
}
*****************************************************************************
*****
* Function Prototype:
* void vInitC4x(void),
* called from C environment.
*
* Author and Date Started: Alexander Carberry, 3/1/2000
*
* Description:
* The function vInitC4x( ) initializes all the necessary CPU and
peripheral
```

```
* bus registers of the C4x processor. After setting the timer TCLK0 as
an
* output clock, vInitC4x( ) waits for a while for the timer to be
stable,
* before acquiring any data from the CCD. TCLK0 is used as the input
clock
to the CCD. The global memory interface control register (GMICR) and
the
* local memory interface control register (LMICR) are set properly with
* appropriate strobe sectioning and wait state conditions for the
memory
* sections.
*
* Input Parameters and Ranges:
* None.
*
* Returns:
* None.
*
* Called By:
* main ().
*
*************************************************************************

DIER .word 0h ;DMA interrrupt enable register
IIER .word 0h ;Internal interrupt enable register
IIFR .word 00002202h ;Flag register
PERIPH .word 00100000h ;Base address of the peripheral registers
TIM0CTL .word 000003C1h ;Timer 0 control Register (1 MHz CLK) (20h)
TIM0PRD .word 00000003h ;Timer 0 period register (28h)
GMICR .word 3E39D952h ;Global memory interface control register (0h)
LMICR .word 3E39F852h ;Local memory interface control register (4h)
.def _vInitC4x
_vInitC4x:
LDI 0A000h,ST ;GIE=1,SET COND=1



LDI @DIER,DIE
LDI @IIER,IIE
LDI @IIFR,IIF
LDI @PERIPH,AR7
LDI @GMICR,R0
STI R0,*+AR7(0h) ;Init global memory interface control register
LDI @LMICR,R0
STI R0,*+AR7(4h) ;Init local memory interface control register
LDI @TIM0PRD,R0
STI R0,*+AR7(28h) ;Set timer 0 period register
LDI @TIM0CTL,R0
STI R0,*+AR7(20h) ;Set timer 0 control
;wait for a while for the TCLK0 output clock signal to be stable
LDHI 06h,R0
OR 0FFFFh,R0;(This wait is very crucial for correct acquisition)
HERE
SUBI 1h,R0
BLE THERE
BR HERE
THERE
RETS
```

```
*************************************************************************
*****
* Function Prototype:
* void vInitUART(void),
* called from C environment.
*
* Author and Date Started: Alexander Carberry, MTE Kahn,, 3/1/99
*
* Description:
* The function vInitUART( ) initializes all the necessary registers of
the
* UART and also sets a baud rate for the UART. Note that three NOPs are
* required after any read or write to the UART.
*
* Input Parameters and Ranges:
* None.
*
* Returns:
* None.
*
* Called By:
* main ().
*
*************************************************************************
****
.def _vInitUART
UARTADDR .word 00300000h ; Address of RS232
IER .set 4 ; Interrupt Enable Register (changed from 1)
IIR .set 2 ; Interrupt Identification Register(read only)
FCR .set 2 ; FIFO Control Register(write only)
LCR .set 6 ; Line Control Register (changed from 3)
MCR .set 1 ; MODEM Control Register (changed from 4)
LSR .set 5 ; Line Status Register
MSR .set 3 ; MODEM Status Register (changed from 6)



SCR .set 7 ; Scratch Register
DLL .set 0 ; Divisor Latch Least(significant byte)
DLM .set 4 ; Divisor Latch Most(significant byte)(changed from 1)
DLAB .set 80h ; Divisor Latch Access Bit value in the LCR
* Baud rate constants for 18.432MHz clock and 38400bps
BAUD_HI .set 00
BAUD_LO .set 30
_vInitUART:
* We initialize all of the UART's registers by reading them.
* This clears any flags and removes any previous characters that
* were entered.
LDI @UARTADDR,AR0 ; Load RS232 base address to AR0
LDI *AR0,R0 ; Clear the receive register
NOP
NOP
NOP
LDI *+AR0(IER),R0 ; Clear all registers by reading them
NOP
NOP
NOP
LDI *+AR0(IIR),R0
NOP
```

```
NOP
NOP
LDI *+AR0(FCR),R0
NOP
NOP
NOP
LDI *+AR0(LCR),R0
NOP
NOP
NOP
LDI *+AR0(MCR),R0
NOP
NOP
NOP
LDI *+AR0(LSR),R0
NOP
NOP
NOP
LDI *+AR0(MSR),R0
NOP
NOP
NOP
STI 0h,*+AR0(SCR)  ; Clear scratch register
NOP
NOP
NOP
STI 2,*+AR0(MCR)  ; Enable RTS
NOP
NOP
NOP
* The following code sets the baud rate (38400bps) for the UART


LDI DLAB,R0
STI R0,*+AR0(LCR)  ; Set DLAB
NOP
NOP
NOP
LDI BAUD_HI,R0
STI R0,*+AR0(DLM)  ; Set the divisor latch MSB
NOP
NOP
NOP
LDI BAUD_LO,R0
STI R0,*AR0  ; Set the divisor latch LSB
NOP
NOP
NOP
STI 3h,*+AR0(LCR)  ; Reset DLAB and set 8,none,1
NOP
NOP
NOP
RETSU
/*************************************************************************
*****
Function Prototype:
void vCalbPxls(float *pfFourPiByLamda)
Author and Date Started: Alexander Carberry, MTE Kahn,, 4/12/99
```

```
With suggestions added by MTE Khan in 2001
Description:
The function, vCalbPxls(float *pfFourPiByLamda), initializes the array
of 1024
floating point values with the w (4*pi/lamda) vlaues of the 1024
elements
(starting at element 17) of the Ocean Optics CCD. The first 16 CCD
elements
are not photodiodes. Note that the conversion coefficients (fCoeff1,
fCoeff2,
and fIncept) are different for different CCDs. Make sure to put the
right
coefficients using the SIE# of the CCD being used. All the lamda values
are
in nm.
Input Parameters and Ranges:
float *pfFourPiByLamda:
pfFourPiByLamda must be a pointer to an array of 1024 floating point
values.
Returns:
None.
Called By:
main ().
*************************************************************************
*****/
void vCalbPxls(float *pfFourPiByLamda)
{



float
fCoeff1 = 0.24256929,
fCoeff2 = -4.176e-5,
fIncept = 744.837472;
/* Coefficients for the CCD of SIE687 */
float
fLamda,
fPi = 3.141592654;
int i,
iPix,
iPixOffset=16;
/* iPixOffset is the index of the first photodiode element of the
CCD array in the 1100 acquired data vector */
for (i=0; i<1024; i++)
{
iPix = i + iPixOffset;
fLamda = fIncept + fCoeff1*iPix + fCoeff2*iPix*iPix;
/* fLamda in nm */
*(pfFourPiByLamda+i) = (4000*fPi)/fLamda;
}
}
```

```
*************************************************************************
*****
* Function Prototype:
* short nAcqData(int *iaData,int *iaDMA3_DEST,int *iaDMA4_DEST),
* called from C environment.
*
* Author and Date Started: Alexander Carberry, 11/20/99
*
* Description:
* The function, nAcqData(int *iaData,int *iaDMA3_DEST,int
*iaDMA4_DEST),
* acquires 1100 integer data set from the CCD spectrometer, and saves
them
* in the array pointed by iaData.
*
* Method:
* DMA3 and DMA4 are initialized, after reseting, to take 275 word of
data each
* from comport 3 and comport 4, at locations pointed by iaDMA3_DEST and
* iaDMA4_DEST respectively. (iaDMA3_DEST holds the least significant
bytes
* of the 1100 CCD data as full 32-bit words in consecutive (1100/4 =
275)
* memory locations. iaDMA4_DEST holds the most significant bytes of the
* 1100 CCD data as full 32-bit words in consecutive (1100/4 = 275)
memory
* locations.) After enabling the CCD spectrometer
* and the DMA interrup enable, the CPU waits in a loop (WAITLOOP) until
the
* data set is acquired completely. Then it disables both the CCD enable
and
* the DMA interrupt enable, and calls the UNMINGLE subroutine, after
proper
* register initializations, to unmingle the byte mingled data in 1100
* sign-extented 16-bit integer numbers at location pointed by iaData.
*
* Note that, in the WAITLOOP it watis only a predetermined amount of
time
* (determined by WAITCOUNT), and if the complete data set is not
acquired
* within that time, the routine nAcqData() returns with an error code
of -1,
* otherwise if successful it returns with a value of 0.



*
*Input Parameters and Ranges:
*
* int *iaData:
* iaData points to the integer array where the 1100 acquired data set
* be saved.
*
* int *iaDMA3_DEST:
* iaDMA_DEST points to the integer array where the least significant
bytes
* of the 1100 CCD data is acquired as full 32-bit words in consecutive
```

```
* 1100/4=275 memory locations.
*
* int *iaDMA3_DEST:
* iaDMA_DEST points to the integer array where the most significant
bytes
* of the 1100 CCD data is acquired as full 32-bit words in consecutive
* 1100/4=275 memory locations.
*
* Returns:
* A short integer, 0 if succesful, and -1 if data acquisition is
failed.
*
* Called By:
* main ().
*
*************************************************************************
****
.def _nAcqData
* Initilize all necessary CPU registers
DIER .word 00104000h ;DMA3-DMA4 read through ICRDY3-ICRDY4 interrupts
* Initilize all necessary internal peripheral registers
DMA3_CTL .word 00C00047h ;START=11, TCC=0, SYNC_MODE=01, and,
;TRANSFER_MODE=01, DMA_PRI=11 (D0h)
DMA3_SRC .word 00100071h ;source reg (D1h)
DMA3_SRCI .word 0h ;source index register value (D2h)
DMA3_COUNT .word 275 ;counter register value, 275*4=1100 (D3h)
;DMA3_DEST .word 80005000h ;destination address (raw LS data) (D4h)
DMA3_DESTI .word 1h ;destination index register value (D5h)
DMA4_CTL .word 00C00047h ;START=11, TCC=1, SYNC_MODE=01, and,
;TRANSFER_MODE=01, DMA_PRI=11 (E0h)
DMA4_SRC .word 00100081h ;source reg (E1h)
DMA4_SRCI .word 0h ;source index register value (E2h)
DMA4_COUNT .word 275 ;counter register value, 275*4=1100 (E3h)
;DMA4_DEST .word 80005200h ;destination address (raw MS data) (E4h)
DMA4_DESTI .word 1h ;destination index register value (E5h)
* Initilize other variables required
PERIPH .word 00100000h ;Starting address of internal peripheral-
;bus memory
WAITCOUNT .word 003FFFFFh ;The maximum delay allowed for the data
;acquisition
_nAcqData:
PUSH DIE ;Save DMA Internal Interrup register
PUSH IIF ;Save Internal Interrupt Flag register
PUSH AR0 ;Save AR0



PUSH AR1 ;Save AR1
PUSH AR2 ;Save AR2
PUSH AR3 ;Save AR3
PUSH AR4 ;Save AR4
PUSH AR5 ;Save AR5
PUSH AR6 ;Save AR6
PUSH AR7 ;Save AR7, points to peripheral registers
PUSH R1 ;Save the lower 32 bits of R1
PUSH R2 ;Save the lower 32 bits of R2
ANDN 0400h,IIF ;Put IIOF2 output to 0,
;IIOF2 is the CCD enable input
* Reset C40 COM3 and COM4 FIFOs
```

```
RST_FIFO3
LDI *+AR7(070h),R0 ;Load CPCR3 to R0
AND 01E00h,R0 ;Input level is bit 9,10,11,12
BZ RST_FIFO4
LDI *+AR7(071h),R0 ;Read input FIFO
BR RST_FIFO3
RST_FIFO4
LDI *+AR7(080h),R0 ;Load CPCR4 to R0
AND 01E00h,R0 ;Input level is bit 9,10,11,12
BZ DONE_FIFO4
LDI *+AR7(081h),R0 ;Read input FIFO
BR RST_FIFO4
DONE_FIFO4
STI 0h,*+AR7(0D0h) ;Reset DMA 3 control register
STI 0h,*+AR7(0E0h) ;Reset DMA 4 control register
* set DMA channel 3 to read data from Com Port 3
LDI @DMA3_CTL,R0 ;Set DMA 3 control register
STI R0,*+AR7(0D0h)
LDI @DMA3_SRC,R0 ;Set DMA 3 source register
STI R0,*+AR7(0D1h)
LDI @DMA3_SRCI,R0 ;Set DMA 3 source index register
STI R0,*+AR7(0D2h)
LDI @DMA3_COUNT,R0 ;Set DMA 3 counter register
STI R0,*+AR7(0D3h)
LDI SP,AR0;
LDI *-AR0(14),R0 ;Load the DMA3_DEST argument to R0.
;(12 PUSHes + 2 = 14)
;R0 points to LS-byte of data.
;LDI @DMA3_DEST,R0
STI R0,*+AR7(0D4h) ;Set DMA 3 destination register
LDI @DMA3_DESTI,R0 ;Set DMA 3 destination index register
STI R0,*+AR7(0D5h)
* set DMA channel 4 to read data from Com Port 4
LDI @DMA4_CTL,R0 ;Set DMA 4 control register
STI R0,*+AR7(0E0h)
LDI @DMA4_SRC,R0 ;Set DMA 4 source register
STI R0,*+AR7(0E1h)
LDI @DMA4_SRCI,R0 ;Set DMA 4 source index register



STI R0,*+AR7(0E2h)
LDI @DMA4_COUNT,R0 ;Set DMA 4 counter register
STI R0,*+AR7(0E3h)
LDI SP,AR0
LDI *-AR0(15),R0 ;Load the DMA4_DEST argument to R0.
;(12 PUSHes + 3 = 15)
;R0 points to MS-byte of data.
;LDI @DMA4_DEST,R0
STI R0,*+AR7(0E4h) ;Set DMA 4 destination register
LDI @DMA4_DESTI,R0 ;Set DMA 4 destination index register
STI R0,*+AR7(0E5h)
LDI @DIER,DIE ;Enable ICRDY3-ICRDY4 read sync
;(DIE is initialized after starting DMA)
OR 0400h,IIF ;Put IIOF2 output to 1 (enable CCDs)
* Check and wait until a fixed time, for the 1100 data be acquired
LDI @WAITCOUNT,R2 ;R2 holds the maximum waitcount
WAITLOOP
LDI *+AR7(0D3h),R0 ;Load DMA3 transfer counter in R0
```

```
LDI *+AR7(0E3h),R1 ;Load DMA4 transfer counter in R1
OR R0,R1
BZ DATA_ACQD
SUBI 1,R2 ;Decrement the waitcount by 1
BNN WAITLOOP ;Go to WAITLOOP if waitcount is not yet
;counted all down
LDI 0h,DIE ;Disable ICRDY3-ICRDY4 read sync
ANDN 0400h,IIF ;Put IIOF2 output to 0 (disable CCDs)
LDI -1,R0
BU NOT_ACQD ;Return with -1, if data not acquired
DATA_ACQD
LDI 0h,DIE ;Disable ICRDY3-ICRDY4 read sync
ANDN 0400h,IIF ;Put IIOF2 output to 0 (disable CCDs)
* Call UNMINGLE subroutine after proper register initializations
LDI SP,AR0;
LDI *-AR0(14),AR4 ;Load the DMA3_DEST argument to AR4
;(12 PUSHes + 2 = 14)
;DMA3_DEST points to LS-bytes of data
LDI *-AR0(15),AR5 ;Load the DMA4_DEST argument to AR5
;(12 PUSHes + 3 = 15)
;DMA4_DEST points to MS-bytes of data
LDI *-AR0(13),AR6 ;Load the iaData[] argument to AR6
;(12 PUSHes + 1 = 13)
;AR6 points to the unmingled data
CALL UNMINGLE
NOP
LDI 0,R0 ;return with 0, when data is acquired.
NOT_ACQD
POP R2 ;Restore the lower 32 bits of R2
POP R1 ;Restore the lower 32 bits of R1
POP AR7 ;Restore AR7
POP AR6 ;Restore AR6
POP AR5 ;Restore AR5
POP AR4 ;Restore AR4
POP AR3 ;Restore AR3



POP AR2 ;Restore AR2
POP AR1 ;Restore AR1
POP AR0 ;Restore AR0
POP IIF ;Restore IIF
POP DIE ;Restore DIE
RETS
```

```
*************************************************************************
*****
* Function Prototype:
* UNMINGLE, called from C4x assembly environment.
*
* Author and Date Started: Alexander Carberry, MTE Kahn,, 11/20/2000
*
* Description:
* Subroutine UNMINGLE unmingles the raw data (saved by the DMA3 and
DMA4),
* and converts them in 16-bit sign-extented integer values.
*
*
* Input Parameters and Ranges:
*
* It is assumed that:
* (a) AR4 already points to the address of least significant bytes
* of the 1100 CCD data as full 32-bit words in consecutive (1100/4 =
275)
* memory locations
* (a) AR5 already points to the address of most significant bytes
* of the 1100 CCD data as full 32-bit words in consecutive (1100/4 =
275)
* memory locations
* (c) AR6 already holds the address pointing to the destination of the
* final integer data values.
*
* Returns:
* None.
*
* Called By:
* nAcqData().
*
*************************************************************************
****
UNMINGLE:
;Save all the registers being used and modified
PUSH AR0 ;Save AR0
PUSH AR1 ;Save AR1
PUSH R0 ;Save the lower 32 bits of R0
PUSH R1 ;Save the lower 32 bits of R1
PUSH R2 ;Save the lower 32 bits of R2
PUSH R3 ;Save the lower 32 bits of R3
PUSH R4 ;Save the lower 32 bits of R4
PUSH R5 ;Save the lower 32 bits of R5
PUSH R6 ;Save the lower 32 bits of R6
PUSH R7 ;Save the lower 32 bits of R7
PUSH R8 ;Save the lower 32 bits of R8
PUSH R9 ;Save the lower 32 bits of R9
LDI AR6,AR0 ;Copy the address of final destination to AR0
LDI AR6,AR1 ;Copy the address of final destination to AR1



;Start unmingling the byte-mingled data
```

```
;(The Com Port keeps the first received byte as the LS-byte of the
word)
LDI 1100/4-1,RC ;Load the repeat counter
NOP
RPTB UNPACK
LDI *AR5++(1),R5 ;R5 has the 4 MS bytes of 4 data values
|| LDI *AR4++(1),R4 ;R4 has the 4 LS bytes of 4 data values
LDI 0FFh,R6 ;Load 0000 00FFh to R6
AND3 R5,R6,R8
AND3 R4,R6,R7
LDI 0h,R0
LWL2 R7,R0
LWL3 R8,R0 ;First data is in the MS 16 bits of R0
LH1 R0,R0 ;First data is in the LS 16 bits of R0 and
;sign extended
STI R0,*AR6++(1)
LDI 0FF00h,R6
AND 0FF00h,R6 ;Load 0000 FF00h to R6
AND3 R5,R6,R9
LDI 0h,R8
LWR1 R9,R8 ;Shifted right to help merge
AND3 R4,R6,R7
LDI 0h,R1
LWL1 R7,R1
LWL3 R8,R1 ;Second data is in the MS 16 bits of R1
LH1 R1,R1 ;Second data is in the LS 16 bits of R1
;and sign extended
STI R1,*AR6++(1)
LDHI 0FFh,R6 ;Load 00FF 0000h to R6
AND3 R5,R6,R9
LDI 0h,R8
LWR2 R9,R8 ;Shifted right to help merge
AND3 R4,R6,R7
LDI 0h,R2
LWL0 R7,R2
LWL3 R8,R2 ;Third data is in the MS 16 bits of R2
LH1 R2,R2 ;Third data is in the LS 16 bits of R2 and
;sign extended
STI R2,*AR6++(1)
LDHI 0FF00h,R6 ;Load FF00 0000h to R6
AND3 R5,R6,R9
LDI 0h,R8
LWR3 R9,R8 ;Shifted right to help merge
AND3 R4,R6,R7
LDI 0h,R3
LWR1 R7,R3
LWL3 R8,R3 ;Fourth data is in the MS 16 bits of R3
LH1 R3,R3 ;Fourth data is in the LS 16 bits of R3
;and sign extended
UNPACK STI R3,*AR6++(1)
NOP
;Restore all the stacked registers



POP R9 ;Restore the lower 32 bits of R9
POP R8 ;Restore the lower 32 bits of R8
POP R7 ;Restore the lower 32 bits of R7
POP R6 ;Restore the lower 32 bits of R6
```

```
POP R5';Restore the lower 32 bits of R5
POP R4 ;Restore the lower 32 bits of R4
POP R3 ;Restore the lower 32 bits of R3
POP R2 ;Restore the lower 32 bits of R2
POP R1 ;Restore the lower 32 bits of R1
POP R0 ;Restore the lower 32 bits of R0
POP AR1 ;Restore AR1
POP AR0 ;Restore AR0
RETS

*************************************************************************
*****
* Function Prototype:
* short nServUART(int *iaData),
* called from C environment.
*
* Author and Date Started: Alexander Carberry, 3/1/97
*
* Description:
* The function nServUART( ), if called from the main( ),
* checks if there is any request for sending the 1100 integer data set
* through the UART. If it finds the request 'S' it sends the data
* with the preamble (123456789) and the postamble (987654321).
* Otherwise it returns from the subroutine doing nothing.
* Note after every read or write of the UART needs 3 NOPs
* to be followed by.
*
* Input Parameters and Ranges:
*
* int *iaData:
* iaData points the 1100 integer data set to be sent through the UART.
*
* Returns:
* It returns with 0 if it finds a request and sends the data, otherwise
it
* returns with -1.
*
* Called By:
* main ().
*
*************************************************************************
****
.def _nServUART
UARTADDR .word 00300000h ; Address of RS232
DATAADDR .word 80004000h ; Address of 1100 data location
BEGINING .word 123456789; ; Preamble of the Data set to be sent
ENDING .word 987654321; ; Postamble of the Data set to be sent
MCR .set 1 ; MODEM Control Register (changed from 4)
LSR .set 5 ; Line Status Register


100
MSR .set 3 ; MODEM Status Register (changed from 6)
_nServUART:
PUSH AR0
PUSH AR1
PUSH R1
PUSH RC
LDI @UARTADDR,AR0 ; Load RS232 address to AR0
```

```
;STI 0h,*+AR0(MCR) ; Disables the RTS bit
NOP
NOP
NOP
LDI *+AR0(LSR),R0 ; Check the received character bit of PC16550
NOP
NOP
NOP
AND 1h,R0
BZ RETURNM ; If the result is zero there are no
; characters in the buffer
LDI *AR0,R0 ; Else, we have a character. Load it into R0
NOP
NOP
NOP
AND 0FFh,R0
SUBI3 'S',R0,R1 ; Check to see if the character is an 'S'(53h);
BZ SENDDATA
LDI -1,R0
BU RETURNM ; If not, return with -1
; If the character is an 'S', go ahead and send the data
SENDDATA
LDI @BEGINING,R1 ; Send the preamble first
CALL XMIT_WORD
LDI SP,AR0
LDI *-AR0(5),AR1 ; Load the iaData[] argument to AR1
LDI 1100-1,RC ; Load the repeat counter
RPTB SENDIT
LDI *AR1++(1), R1 ; Puts data in R1
CALL XMIT_WORD
NOP
SENDIT
LDI @ENDING,R1
CALL XMIT_WORD
NOP
LDI 0h,R0 ; Return with 0 if data is sent
RETURNM
STI 2h,*+AR0(MCR) ; Enable the RTS bit
NOP
NOP
NOP
POP RC
POP R1
POP AR1
POP AR0
RETSU



*************************************************************************
*****
* Function Prototype:
* XMIT_WORD,
* called from C4x assembly environment.
*
* Author and Date Started: Tracy Cramer & Alexander Carberry, 3/1/97
*
* Description:
* The function XMIT_WORD transmits the contents of R1 to the UART. It
```

```
* first reorders the bytes of R1 to send the MS byte first.
*
* Input Parameters and Ranges:
* It is assumed that the word be sent is already in R1 before calling
this
* function.
*
* Returns:
* None.
*
* Called By:
* vServUART().
*
*******************************************************************************
****
XMIT_WORD:
PUSH R0
PUSH R2
PUSH R3
PUSH R4
PUSH AR0
* Reverse the contents of R1 (i.e. R1=B3B2B1B0h becomes R1=B0B1B2B3h),
* to send the MS byte first.
LDI 0h,R0 ; R0=0000 0000h
LDI 0h,R2 ; R2=0000 0000h
LHU0 R1,R2 ; R2=0000 B1B0h, R1=B3B2 B1B0h
LSH -8,R2,R0 ; R0=0000 00B1h
AND 0FFh,R2 ; R2=0000 00B0h
LWL1 R2,R0 ; R0=0000 B0B1h
LHU1 R1,R2 ; R2=0000 B3B2h
LSH -8,R2,R1 ; R1=0000 00B3h
AND 0FFh,R2 ; R2=0000 00B2h
LWL1 R2,R1 ; R1=0000 B2B3h
LWL2 R0,R1 ; R1=B0B1 B2B3h (reversed)
; End of reversing the contents of R1
LDI @UARTADDR,AR0
LDI -8,R3
LDI 4,R4
LP0:
LDI *+AR0(LSR),R0 ; Read the Line Status Register
NOP
NOP
NOP



AND 20h,R0 ; If the THRE bit is high we are ok to put the
; byte in the buffer.
BZ LP0
LP1:
LDI +AR0(MSR),R0 ; Read the MODEM Status Register
NOP
NOP
NOP
AND 10h,R0 ; If the CTS bit is high we are clear to send
; the character
BZ LP1
STI R1,*AR0 ; Sends the eight LSB
NOP
```

```
NOP
NOP
LSH R3,R1 ; Shifts R1 eight bits right (see header)
SUBI 1h,R4 ; Decrement counter
BNZ LP0 ; Transmit four bytes
POP AR0
POP R4
POP R3
POP R2
POP R0
RETSU
*******************************************************************************
****
* Function Prototype:
* void vFloatData(int *piData,float *pfData);
*
* Author and Date Started: Alexander Carberry, MTE Kahn,, 2/13/99
*
* Description:
* vFloatData(int *piData,float *pfData) converts 1024 integer data
pointed
* by piData to floating point values and stores them to memory pointed
* by pfData.
*
* Input Parameters and Ranges:
*
* int *piData:
* The array of 1024 integer data to be converted is pointed by piData.
*
* float *pfData:
* The memory location where the converted floating point values be
stored
* is pointed by pfData.
*
* Returns:
* None
*
* Called By:
* main ().
*
*******************************************************************************
*****/



.def _vFloatData
_vFloatData:
PUSH AR0
PUSH AR1
PUSH R0
PUSH R1
LDI SP,AR0
LDI *-AR0(5),AR1 ;AR1 is a pointer to the data we need to convert
LDI *-AR0(6),AR0 ;AR0 contains the converted data
LDI 1024-1,RC ;Init repeat counter
RPTB FLTIT ;Repeat RC+1 times
LDI *AR1++(1),R0
FLOAT R0,R1
FLTIT:
```

```
STF R1,*AR0++(1)
POP R1
POP R0
POP AR1
POP AR0
RETS
/*************************************************************************
*****
Function Prototype:
void vFltrBw3(float x[], float y[], int iNumPts)
Author and Date Started: Alexander Carberry and MTE Khan, 2/13/2000
Description:
vFltrBw3(float x[], float y[], int iNumPts) is a 3rd order butter worth
high
pass filter with a normalized cutoff frequency of fc=0.03. x[] points
to the
input data, and y[] points to the filtered output data. The length of
the
output array is equal to the length of the input array.
Input Parameters and Ranges:
float x[]:
The array of floating point data values, to be filtered, is pointed by
x.
float y[]:
y points to the array of filtered data values.
int iNumPts:
iNumPts is the length of the input array of x[].
Returns:
None
Called By:
main ().
*************************************************************************
*****/


void vFltrBw3(float x[], float y[], int iNumPts)
{
float b[4] = {0.91002543068616,
-2.73007629205848,
2.73007629205848,
-0.91002543068616};
float a[4] = {1.00000000000000,
-2.81157367732469,
2.64048349277834,
-0.82814627538626};
int i;
y[0] = b[0]*x[0];
y[1] = b[0]*x[1] + b[1]*x[0] - a[1]*y[0];
y[2] = b[0]*x[2] + b[1]*x[1] + b[2]*x[0] - a[1]*y[1] - a[2]*y[0];
for (i=3; i<iNumPts; i++)
{
y[i] = b[0]*x[i] + b[1]*x[i-1] + b[2]*x[i-2] + b[3]*x[i-3]
- a[1]*y[i-1] - a[2]*y[i-2] - a[3]*y[i-3];
}
}
*************************************************************************
*****
* Function Prototype:
```

```
* void vFltrBw3(float x[], float y[], int iNumPts)
* (Implemented in C4x Assembly)
*
* Author and Date Started: Alexander Carberry, 4/12/2000
*
* Description:
* vFltrBw3(float x[], float y[], int iNumPts) is a 3rd order butter
worth
* high pass filter with fc=0.03. x[] points to the input data, and y[]
* points to the filtered output data. The length of the output array
* is equal to the length of the input array.
*
* Input Parameters and Ranges:
*
* float x[]:
* The array of floating point data values, to be filtered, is pointed
by x.
*
* float y[]
* y points to the array of filtered data values.
*
* int iNumPts:
* iNumPts is the length of the input array of x[].
*
* Returns:
* None
*
* Called By:
* main (), (afss.c)



*************************************************************************
******
.def _vFltrBw3
b0 .float 0.91002543068616
b1 .float -2.73007629205848
b2 .float 2.73007629205848
b3 .float -0.91002543068616
a2 .float -2.81157367732469
a3 .float 2.64048349277834
a4 .float -0.82814627538626
_vFltrBw3:
PUSH AR0
PUSH AR1
PUSH AR2
PUSH AR3
PUSH R0
PUSH R1
PUSH R2
PUSH R3
PUSH R4
PUSH R5
PUSH R6
PUSH R7 ; general purpose register
PUSH R8 ; general purpose register
PUSH R9 ; general purpose register
LDI SP,AR3
LDI *-AR3(15),AR0 ; Pointer to input array
```

```
LDI *-AR3(16),AR1 ; Pointer to output array
LDI *-AR3(17),AR2 ; Number of points
* Load constants for quicker access
LDF @b0,R0
LDF @b1,R1
LDF @b2,R2
LDF @b3,R3
LDF @a1,R4
LDF @a2,R5
LDF @a3,R6
* y[0] = b[0]*x[0];
MPYF3 R0,*AR0,R7
STF R7,*AR1
* y[1] = b[0]*x[1] + b[1]*x[0] - a[1]*y[0];
MPYF3 R0,*+AR0(1),R7
MPYF3 R1,*AR0,R8
ADDF R7,R8
MPYF3 R4,*AR1,R7
SUBF R7,R8
STF R8,*+AR1(1)
* y[2] = b[0]*x[2] + b[1]*x[1] + b[2]*x[0] - a[1]*y[1] - a[2]*y[0];
MPYF3 R0,*+AR0(2),R7
MPYF3 R1,*+AR0(1),R8


ADDF R7,R8
MPYF3 R2,*AR0,R7
ADDF R7,R8
MPYF3 R4,*+AR1(1),R7
SUBF R7,R8
MPYF3 R5,*AR1,R7
SUBF R7,R8
STF R8,*+AR1(2)
* for (i=0; i<iNumPts-3; i++)
SUBI 4,AR2
LDI AR2,RC
RPTB FILTER_LOOP
* y[i+3] = b[3]*x[i] + b[2]*x[i+1] + b[1]*x[i+2] + b[0]*x[i+3]
* - a[2]*y[i] - a[1]*y[i+1] - a[0]*y[i+2];
MPYF3 R3,*AR0++,R7
MPYF3 R2,*AR0++,R8
ADDF R8,R7
MPYF3 R1,*AR0++,R8
ADDF R8,R7
MPYF3 R0,*AR0++,R8
ADDF R8,R7
SUBI 3,AR0
MPYF3 R6,*AR1++,R9
MPYF3 R5,*AR1++,R8
ADDF R8,R9
MPYF3 R4,*AR1++,R8
ADDF R8,R9
SUBF R9,R7
STF R7,*AR1
FILTER_LOOP:
SUBI 2,AR1
POP R9 ; general purpose register
POP R8 ; general purpose register
POP R7 ; general purpose register
POP R6
```

```
POP R5
POP R4
POP R3
POP R2
POP R1
POP R0
POP AR3
POP AR2
POP AR1
POP AR0
RETS
/*************************************************************************
*****
Function Prototype:

void vFindFloatPix(int iIndexOfMax, float *pfFftMag, float
*pfIndexOfMax)
Author and Date Started: Alexander Carberry and MTE Kahn, 2/13/2000
Description:
vFindFloatPix(int iIndexOfMax, float *pfFftMag, float *pfIndexOfMax),
finds
the index of the peak value of the FFT magnitude of CCD data more
precisely
than just an interger. It uses a Gaussian approximation of the FFT
magnitude
of three pixels having the index iIndexOfMax-1, iIndexOfMax, and
iIndexOfMax+1. The more precise peak value floating point index is
stored at
lcoation pointed by pfIndexOfMax.
Input Parameters and Ranges:
int iIndexOfMax:
The integer index having the maximum value of the FFT magnitude.
float *pfFftMag:
pfFfftMag points to (array of 1024) FFT magnitude of the 1024 float
data.
float *pfIndexOfMax
The more precise floating point index value which corresponds to the
maximum FFT magnitude.
Returns:
None
Called By:
main ().
*************************************************************************
*****/
void vFindFloatPix(int iIndexOfMax, float *pfFftMag, float
*pfIndexOfMax)
{
float fLgVal0b1,
fLgVal2b1,
fVal0,
fVal1,
fVal2,
fOffset;
fVal0 = pfFftMag[iIndexOfMax - 1];
fVal1 = pfFftMag[iIndexOfMax];
fVal2 = pfFftMag[iIndexOfMax + 1];
fLgVal0b1 = log(fVal0 / fVal1);
fLgVal2b1 = log(fVal2 / fVal1);
fOffset = (fLgVal0b1 - fLgVal2b1)/(2*(fLgVal0b1 + fLgVal2b1));
*pfIndexOfMax = (float)iIndexOfMax + fOffset;
```

```
}
/*************************************************************************
*****


Function Prototype:
void vFindTruGap(float fEstGap, float *pfTruGap, float *pfRawData,
float
*pfFourPiByLamda)
Author and Date Started: Alexander Carberry, MTE Kahn,, 3/15/2000
Description:
vFindTruGap( ) finds the more precise gap of the EFPI sensor using the
estimated gap provided. It does the 4*pi*Gap/lamda transformation (+/-
5
micrometer) around the estimated gap on the 1024 data pointed by
pfRawData.
It calls the vDGT( ) function to do the transform, and uses the Golden
Search
rule to reduce the number of calls for the vDGT( ) function. The EFPI
gaps
are assumed in micrometer.
Input Parameters and Ranges:
float fEstGap:
fEstGap is the estimated EFPI gap found from the FFT transform.
float *pfTruGap:
pfTruGap points to floating point value where the calculated true gap
be saved.
float *pfRawData:
pfRawData points to the array of 1024 unfiltered CCD data values.
float *pfFourPiByLamda:
pfFourPiByLamda points to the array of 1024 wavelength values which
corresponds
to the 1024 CCD data values pointed to by pfRawData.
Returns:
None
Called By:
main ().
*************************************************************************
*****/
#define R 0.61803399
#define C (1.0 - R)
void vFindTruGap(float fEstGap, float *pfTruGap, float *pfRawData,
float
*pfFourPiByLamda)
{
float fAx, fBx, fCx;
float f0 ,f1 ,f2 ,f3 ,fX0 ,fX1 ,fX2, fX3, *fp1, *fp2;
float tol = 1e-3;
fAx = fEstGap - 5.0;
fBx = fEstGap;
fCx = fEstGap + 5.0;
fp1 = &f1;
fp2 = &f2;
fX0 = fAx;
fX3 = fCx;
if (fabs(fCx-fBx) > fabs(fBx-fAx)){
fX1 = fBx;
fX2 = fBx + C * (fCx - fBx);}
```

```
else {
fX2 = fBx;
fX1 = fBx - C * (fBx - fAx);
}
vDGT( pfRawData, fX1, pfFourPiByLamda, fp1);
vDGT( pfRawData, fX2, pfFourPiByLamda, fp2);
while (fabs(fX3-fX0) > tol)
{
if (f2 > f1){
fX0 = fX1;
fX1 = fX2;
fX2 = R * fX1 + C * fX3;
f1 = f2;
vDGT(pfRawData, fX2, pfFourPiByLamda, fp2);}
else {
fX3 = fX2;
fX2 = fX1;
fX1 = R * fX2 + C * fX0;
f2 =f1;
vDGT(pfRawData, fX1, pfFourPiByLamda, fp1);
}
}
if (f1 > f2){
*pfTruGap = fX1;}
else {
*pfTruGap = fX2;
}
}


/*************************************************************************
*****
Function Prototype:
void vDGT(float *pfData, float fGap, float *pfFourPiByLamda, float
*pfDGTMag)
Author and Date Started: Alexander Carberry, MTE Kahn, 2/13/2000
Description:
The function, vDGT(float *pfData, float fGap, float *pfFourPiByLamda,
float
*pfDGTMag), finds the 4*pi*Gap/lamda transform magnitude,for an EFPI
gap value
of fGap, and saves the magnitude in location pointed to by pfDGTMag.
All the lamda values are assumed in nm.
Input Parameters and Ranges:
float *pfData:
pfData is the pointer to the array of 1024 floating point data values
for
which the transform magnitude is to be found.

float fGap:
fGap is the EFPI gap (usually 20.0 to 300.0).
float *pfFourPiByLamda:
pfFourPiByLamda points to the 1024 wavelength values which corresponds
to the
data
values pointed by pfData.
float *pfDGTMag:
The location where the Transform magnitude be saved is pointed by
pfDGTMag.
Returns:
```

```
None
Called By:
vFindTruGap().
*************************************************************************
*****/
#include <math.h>
void vDGT(float *pfData, float fGap, float *pfFourPiByLamda, float
*pfDGTMag)
{
float fParam,
fReal,
fImag,
fSumReal,
fSumImag;
int i;
fSumReal = 0.0;
fSumImag = 0.0;
for (i=0; i<1024; i++){
fParam = fGap*pfFourPiByLamda[i];
fReal = pfData[i] * cos(fParam);
fImag = pfData[i] * sin(fParam);
fSumReal = fSumReal + fReal;
fSumImag = fSumImag + fImag;
}
*pfDGTMag = (fSumReal*fSumReal + fSumImag*fSumImag);
}
*************************************************************************
*****
* Function Prototype:
* void vDGT(float *pfData, float fGap, float *pfFourPiByLamda,
* float *pfDGTMag),
* (Implemented in C4x Assembly)
*
* Author and Date Started: Alexander Carberry, Tracy Cramer, 4/15/2000
*
* Description:
* The function, vDGT(float *pfData, float fGap, float *pfFourPiByLamda,
float
* *pfDGTMag), finds the 4*pi*Gap/lamda transformation magnitude,for an
EFPI



* gap value of fGap, and saves the magnitude in location pointed to by
* pfDGTMag.
*
* All the lamda values are assumed in nm.
*
*
* Input Parameters and Ranges:
*
* float *pfData: (AR4)
* pfData is the pointer to the array of 1024 floating point data values
for
* which the transformation magnitude is to be found.
*
* float *fGap: (AR5)
* fGap is the EFPI gap (usually 20.0 to 300.0).
*
```

```
* float *pfFourPiByLamda: (AR6)
* pfFourPiByLamda points to the 1024 wavelength values which
corresponds
* to the data values pointed by pfData.
*
* float *pfDGTMag: (AR7)
* The location where the Transform magnitude be saved is pointed by
pfDGTMag.
*
* Returns:
* None
*
* Called By:
* vFindTruGap (), (findtrugp.c)
*
*******************************************************************************
******
.def _vDGT
_vDGT:
.file "C:\TI_DSP\TI_TOOLS\MATH.H"
.globl _cos
PUSH R4 ; fParam
PUSH R5 ; fReal & fImag
PUSH R6 ; fRealSum
PUSH R7 ; fImagSum
PUSH R8
PUSH AR4 ; pfData
PUSH AR5 ; pfGap
PUSH AR6 ; pfFourPiByLamda
PUSH AR7 ; pfDGTMag
* Initialize the pointer registers
LDI SP,AR0
LDI *-AR0(9),AR4 ; pfData
LDI *-AR0(10),AR5 ; pfGap
LDI *-AR0(11),AR6 ; pfFourPiByLamda
LDI *-AR0(12),AR7 ; pfDGTMag
* Initialize the summing registers to zero
LDF 0.0,R6 ; (SumReal)
LDF 0.0,R7 ; (SumImag)
LDF *AR5,R8 ;Load Gap in R8
* (C-statement) for (i=256; i<769; i++)



* We are only using 512 array values from the middle of data, so
* we offset the pointers by 256
ADDI 256,AR6 ; (pfFourPiByLamda)
ADDI 256,AR4 ; (pfData)
* Load the repeat register with (512-1)
LDI 511,RC
RPTB DFT_LOOP
LDF *AR6++,R1 ; R1 = 4*pi/lamda
* (C-statement) fParam = fGap * pfFourPiByLamda[i];
MPYF3 R1,R8,R4 ; R4 contains fParam
* (C-statement) fReal = pfData[i] * cos(fParam);
PUSH R4 ; We need to push the parameter for the call to cos
CALL _cos ; The return value is in R0 by convention
SUBI 1,SP ; Decrement stack now that the call is over
LDF *AR4++,R4 ; Retrieving fData[i]
```

```
MPYF R0,R4,R5 ; R5 contains fReal
* (c-statement) fSumReal = fReal + fSumReal;
ADDF R5,R6 ; R6 contains fSumReal
* (C-statement) fImag = pfData[i] * sin(fParam);
* Using the identity sin(x) = sqrt(1-cos(x)*cos(x))
MPYF R0,R0 ; cos(x)*cos(x)
SUBRF 1,R0 ; 1-cos(x)^2
RSQRF R0,R0 ; 1/sqrt(1-cos(x)^2) (reciprocal square root)
* Newton-Raphson Iteration
RCPF R0,R1
MPYF3 R1,R0,R2
SUBRF 2.0,R2
MPYF R2,R1 ; End of 1st iteration (16-bit precision)
MPYF3 R1,R0,R2
SUBRF 2.0,R0
MPYF3 R2,R1,R0 ; End of 2nd iteration (32-bit precision). R0 = sin(x)
MPYF R0,R4,R5 ; R4 contains pfData[i],R5 contains fImag
DFT_LOOP:
* (c-statement) fSumImag = fImag + fSumImag;
ADDF R5,R7 ; R7 contains fSumImag
* (C-statement) *pfDGTMag = (fSumReal*fSumReal + fSumImag*fSumImag)
MPYF R7,R7,R1 ; R1 contains fSumReal^2
MPYF R6,R6,R2 ; R2 contains fSumImag^2
ADDF R1,R2 ; R2 contains DGTMag
STF R2,*AR7 ; Store the result in memory
POP AR7 ; pfDGTMag
POP AR6 ; pfFourPiByLamda
POP AR5 ; pfGap
POP AR4 ; pfData
POP R8
POP R7 ; fImagSum
POP R6 ; fRealSum
POP R5 ; fReal & fImag
POP R4 ; fParam
RETS
```

A.2 Real-Time Signal Processing Routines for the FBG type Sensor System

```
/*************************************************************************
Function Prototype:
void main (void)
Author and Date Started: Alexander Carberry, MTE Kahn,, 5/9/99
Description:
The main() program calls all the initialization, data acquisition, and
signal processing functions. The functions could either be in C, or
in C4x assembly language.
Method:
The InitC4x() function initializes all the necessary registers of the
TMS320C4x DSP processor. The InitUART() function initializes all the
necessary registers of the UART for communicating with the comport or
computers. Ocean Optics CCD spectrometer calibration coefficients are
used to convert any pixel index to wavelenght values.
Every individual CCD spectrometer, having a unique SIE
number has its own conversion coefficients. The nServUart() serves
the UART request, if any.
The AcqData(int *,DMA3_DEST,DMA4_DEST) acquires the 1100 data set at
the given pointer. There must be at least 275 (0x44c) memory locations
both at DMA3_DEST and DMA4_DEST.
The rest of the functions are for real-time signal processing.
```

```
Any new functions can easily be added in main() at it's proper place,
if necessary.
Input Parameters and Ranges:
None.
Called By:
None.
*************************************************************************/
#include <stdlib.h>
#include <math.h>


/* If the stack is small, then large arrays must not be kept as local
variables. Local variables are placed on stack for processing.
The following variables are kept out of main() for
monitoring from the 'watch' window. */
float
faData[1100],
faNomPksWav[2]={850.0,860.0},
faPks[4],
faPksWav[2],
faMicroStrn[2];
short
nStatus;
int
iaData[1100],
iaDMA3_DEST[275],
iaDMA4_DEST[275],
iBrgNum=2,
iaBrgRngs[4]={100,200,300,400},
iaBrgWdths[4]={8,9,8,9};
float fCoeff1 = 0.24256929,fCoeff2 = -4.176e-5,fIncept = 744.837472;
/* Calibration Coefficients for the CCD of SIE687 */
void main(void)
{
int i=0;
vInitC4x();
vInitUART();
for (;;){
nStatus = nAcqData(iaData,iaDMA3_DEST,iaDMA4_DEST);
/* nStatus = 0 , if successful*/
nStatus = nServUART(iaData);
/* sends integer data to UART if requested */
vFloatData(iaData+16,faData);
/* Type conversion, converts data from int to float */
/* Actual data starts 16 pixel later */
vFindPks(faData, iBrgNum, iaBrgRngs, iaBrgWdths,faPks);
for(i=0;i<2;i++){
faPksWav[i] = fIncept + faPks[i]*fCoeff1 +
faPks[i]*faPks[i]*fCoeff2;
faMicroStrn[i] = 1.2821e6*(faNomPksWav[i]-
faPksWav[i])/faNomPksWav[i];
}
}
}
*************************************************************************
***
* Function Prototype:
* vFindPks(float *faData, int iBrgNum, int *iaBrgRngs, int *iaBrgWdths,
* float *faPks)
```

```
*
* Author and Date Started: Alexander Carberry, MTE Kahn,, 8/25/99
*



* Description:
* The vFindPks() finds out all the Bragg peaks from the 1100 floating
point
* data values pointed by faData.
*
*
* Input Parameters and Ranges:
*
* int *faData:
* faData points to the float array where the 1100 acquired data set
* is saved.
*
* int iBrgNum:
* iBrgNum is the total number of Bragg peaks in the 1100 data set.
*
* int *iaBrgRngs:
* iaBrgRngs points to the location where the dynamic ranges of the
Bragg
* peaks are stored in terms of pixel indeces. The ranges must
* be stored in a sequence like: BG1_StPxl, BG1_EndPxl, BG2_StPxl,
* BG2_EndPxl, ...., where BG1 is the leftmost Bragg peak in the 1100
* data set. For example, the range values can be like: iaBrgRngs={50,
* 190,200,380,450,510,....}.
*
* int *iaBrgWdths:
* iaBrgWdths points to the location where the left and right widths of
* Bragg peaks are stored in terms of number of pixels. The widhts must
* be stored in a sequence like: BG1_L,BG1_R, BG2_L, BG2_R, ...., where
* BG1 is the leftmost Bragg peak in the 1100 data set. For example, the
* Bragg width values can be like: iaBrgWdths={8,12,6,9,7,11,....}.
*
*
* Returns:
* None
* Called By:
* main ()
*
*******************************************************************
*****
.def _vFindPks
_vFindPks:
;Save all the registers being used and modified
PUSH RC ;Save RC
PUSH IR0 ;Save IR0
PUSH IR1 ;Save IR1
PUSH AR0 ;Save AR0
PUSH R0 ;Save the lower 32 bits of R0
PUSHF R0 ;and the upper 32 bits
PUSH R1 ;Save the lower 32 bits of R1
PUSHF R1 ;and the upper 32 bits
PUSH R2 ;Save the lower 32 bits of R2
PUSHF R2 ;and the upper 32 bits
PUSH R3 ;Save the lower 32 bits of R3
```

```
PUSHF R3 ;and the upper 32 bits
PUSH R4 ;Save the lower 32 bits of R4
PUSHF R4 ;and the upper 32 bits
PUSH R5 ;Save the lower 32 bits of R5



PUSHF R5 ;and the upper 32 bits
PUSH R6 ;Save the lower 32 bits of R6
PUSHF R6 ;and the upper 32 bits
PUSH R7 ;Save the lower 32 bits of R7
PUSHF R7 ;and the upper 32 bits
PUSH R8 ;Save the lower 32 bits of R8
PUSHF R8 ;and the upper 32 bits
PUSH R9 ;Save the lower 32 bits of R9
PUSHF R9 ;and the upper 32 bits
LDI SP,AR0
LDI *-AR0(25),AR6 ;AR6=faData[], (24 PUSHes + 1 = 25)
LDI *-AR0(26),R6 ;R6=iBrgNum, (24 PUSHes + 2 = 26)
LDI *-AR0(27),AR5 ;AR5=iaBrgRngs[], (24 PUSHes + 3 = 27)
LDI *-AR0(28),AR4 ;AR4=iaBrgWdths[], (24 PUSHes + 4 = 28)
LDI *-AR0(29),AR3 ;AR3=faPks[], (24 PUSHes + 5 = 29)
;(AR6=faData[], is never changed)
BG_LOOP:
LDI *AR5++(1),IR0 ;IR0 = BGX_StPxl, (BGx_EndPxl>BGx_StPxl)
SUBI3 IR0,*AR5++(1),RC ;RC = BGX_EndPxl - BGX_StPxl
SUBI 1,RC
LDF *+AR6(IR0),R0 ;Init maximum value to the 1st element
ADDI 1h,IR0 ;Increment IR0
;The MAXM loop finds the int pixel # of the Bragg peaks
RPTB MAXM
CMPF *+AR6(IR0),R0 ;Compare by (R0 - *+AR6(IR0))
BGE MAXM
LDF *+AR6(IR0),R0 ;If greater, R0 = the new max value (float)
LDI IR0,R1 ;R1 = the pixel # having the max value (integer)
MAXM
ADDI 1h,IR0 ;Increment IR0 by 1
*
* The following instruction saves the integer pixel # having the max
value
* STF R1,*AR3++(1) ;save the pixel # having the max value (integer)
*
* for the following notaions k_ refers to index and y_ refers to value
LDI *AR4++(1),R0 ;R0 = BGX_L
SUBI3 R0,R1,IR0 ;IR0 = peak pixel # (R1) - BGX_L (R0) = k_left
LDI *AR4++(1),R0 ;R0 = BGX_R
ADDI3 R0,R1,IR1 ;IR1 = peak pixel # (R1) + BGX_L (R0) k_right
SUBI3 IR0,IR1,RC ;RC = IR1 - IR0 = Bragg range
LDF *+AR6(IR0),R7 ;R7 = y_left
SUBF3 R7,*+AR6(IR1),R8 ;R8 = y_right - y_left
FLOAT RC,R0
RCPF R0,R7 ;R7 = 1/R0,
MPYF R7,R0,R2
SUBRF 2.0,R2
MPYF R2,R7 ;End of 1st iteration (16 bit accuracy)
MPYF R7,R0,R2
SUBRF 2.0,R2
MPYF R2,R7 ;End of 2nd iteration (32-bit accuracy)
MPYF R7,R8 ;R8 = R8*R7 = slope
```

```
LDF 0.0,R3 ;R3 holds the sum of the area (=fsum)
LDF 0.0,R4 ;R4 holds the sum of the moments (=fCentroid)
LDI IR0,R2 ;R2 = k_left
;The CNTRD loop finds the centroid pixel # in floating point value
RPTB CNTRD
SUBI3 R2,IR0,R9 ;R9=IR0-R2=k-k_left; IR0=k;
FLOAT R9,R9
MPYF R8,R9 ;R9=R9*R8=slope*(k-k_left)
ADDF R7,R9 ;R9=R9+R7=y_corr
SUBF3 R9,*+AR6(IR0),R5 ;R5=y(k)-y_corr
ADDF R5,R3 ;R3=R3+R5 ;fSum=fSum+y(k)-y_corr
FLOAT IR0,R9 ;convert the pixel index to floating point
MPYF R9,R5 ;R5=R5*R2
ADDF R5,R4 ;R4=R4+R5 ;fCntrd=fCntrd+(y(k)-y_corr))*k)
CNTRD
ADDI 1h,IR0 ;Increment IR0 for next repeat
RCPF R3,R5 ;R5=1/R3,
MPYF R5,R3,R2
SUBRF 2.0,R2
MPYF R2,R5 ; End of 1st iteration (16 bit accuracy)
MPYF R5,R3,R2
SUBRF 2.0,R2
MPYF R2,R5 ; End of 2nd iteration (32-bit accuracy)
MPYF R5,R4 ;R4=R4*R5(fCentroid=fCentroid/fSum)
STF R4,*AR3++(1) ;save the float peak pixel in IEEE format
SUBI 1h,R6 ;Decrement R6 (R6 = R6 - 1)
BP BG_LOOP ;Branch if not zero and not negative to BG_LOOP
;Restore all the stacked registers
POPF R9 ;Restore the upper 32 bits of R8
POP R9 ;and the lower 32 bits
POPF R8 ;Restore the upper 32 bits of R8
POP R8 ;and the lower 32 bits
POPF R7 ;Restore the upper 32 bits of R7
POP R7 ;and the lower 32 bits
POPF R6 ;Restore the upper 32 bits of R6
POP R6 ;and the lower 32 bits
POPF R5 ;Restore the upper 32 bits of R5
POP R5 ;and the lower 32 bits
POPF R4 ;Restore the upper 32 bits of R4
POP R4 ;and the lower 32 bits
POPF R3 ;Restore the upper 32 bits of R3
POP R3 ;and the lower 32 bits
POPF R2 ;Restore the upper 32 bits of R2
POP R2 ;and the lower 32 bits
POPF R1 ;Restore the upper 32 bits of R1
POP R1 ;and the lower 32 bits
POPF R0 ;Restore the upper 32 bits of R0
POP R0 ;and the lower 32 bits
POP AR0 ;Restore AR0
POP IR1 ;Restore IR1
POP IR0 ;Restore IR0
POP RC ;Restore RC
RETS
```

5.2 Memory Allocation for the Real-Time Wavelength Modulated Optical Fiber Sensor System

```
/*************************************************************************
*******
Program File: afss.cmd
Programmer: Alexander Carberry and MTE Khan
Date: 2/10/2001
Description: This .cmd file declares, in the MEMORY part, all the valid
addresses of the memory spaces available for the C4x system. In the
SECTIONS
part, it instructs the loader where to load the different named or
default
sections of the program.
*************************************************************************
**/
MEMORY
{
ON_CHIP: org = 002FF800h, len = 00000800h
RS232: org = 00300000h, len = 00000008h
SRAM: org = 20000000h, len = 00080000h
RST_VEC: org = 80000000h, len = 00000001h
NVRAM: org = 80000100h, len = 0001E000h
}
SECTIONS
{
.text load = SRAM
.bss: load = SRAM
.axl_cos load = SRAM /* for TARTAN library functions */
.axl_glb load = SRAM /* for TARTAN library functions */
.stack load = ON_CHIP
}
```

Appendix 6

The Matlab Codes for the Simulation and the Signal Processing

6.1 Matlab Code to Simulate the Signal Response of the Wavelength Modulated EFPI Sensor System

```
%%%%%%%%%%%%%%%%%%%%%%%%%%%%%%%%%%%%%%%%%%%%%%%%%%%%%%%%%%%%%%%%%%%%%%%%%%%%%%%%
% Program File: FaPer.m
% Programmer: MTE KAHN
% Date: 8/20/2001
% Purpose: To simulate the signal response of the wavelength
% modulated EFPI sensor system,
% The responsivity of the CCD diode elements are assumed independent
% of wavelengths.
%%%%%%%%%%%%%%%%%%%%%%%%%%%%%%%%%%%%%%%%%%%%%%%%%%%%%%%%%%%%%%%%%%%%%%%%%%%%%%%%
clear all;
lam = 745:(960-745)/1099:960;
% range of the SLED optical source in nm, and the CCD array length
pk = 500; % peak amplitude value of the Gaussian SLED source
sigma = 12; % spread (std. deviation) of the Gaussian SLED source
mu = 858; % mean of the source in nm
fs = pk*exp((-(lam-mu).^2)/(2*sigma^2)); % amplitude value of the
source
rpr = 0.2; % Fresnel's ampl. reflection coeff. at the reference
interface
tpr = 1.2; % Fresnel's ampl. transmission coeff. at the reference
interface
rps = 0.3; % Fresnel's amplitude reflection coeff. at the sensing
interface
phi1 = 0; % reflection phase shift at the reference interface
phi2 = pi; % reflection phase shift at the sensing interface
a = 4.0; % fiber core radius in um
NA = 0.1; % fiber numerical aperture
g = 50 ; % gap in um
fa_g = rps*((a/(a+g*tan(asin(NA))))^2);
delta = ( ((4*pi*g*1e-6)./(lam*1e-9)) -phi2 + phi1 );
[x,y] = pol2cart(delta,tpr*fa_g);
ampl = x + j*y + rpr;
v = (fs.^2) .* abs(ampl).^2;
v = v + 50*randn(size(v));
plot(lam,v);
grid;
```

6.2 Matlab Code for the FFT Method of the Wavelength Modulated EFPI Sensor System, to Find the EFPI Gap Length *g*

```
%%%%%%%%%%%%%%%%%%%%%%%%%%%%%%%%%%%%%%%%%%%%%%%%%%%%%%%%%%%%%%%%%%%%%%%%%%%%
% Program File: rfft.m
% Programmer: MTE Kahn
% Date: 01/15/2001
% Purpose: To find the EFPI gap length g, for an acquired set of
% data, using the FFT method.
%%%%%%%%%%%%%%%%%%%%%%%%%%%%%%%%%%%%%%%%%%%%%%%%%%%%%%%%%%%%%%%%%%%%%%%%%%%%
clear all;
% Curve fitting coefficients for the index of the maximum FFT
% magnitudes, for the CCD spectrometer of SIE687.
fCurvFtCoeff0 = -2.354;
fCurvFtCoeff1 = 1.8196;
fCurvFtCoeff2 = -5.0963e-6;
load c:\mystuff\dtechstuff\data\sie687b\g80\g80a.dat;
x = g80a(17:1040); % The 1st active element starts at index 17
[b,a] = butter(3,0.03,'high');
y = filter(b,a,x);
fFFTMag = abs(fft(y));
fFFTMagMax = max(fFFTMag);
iIndexOfMaxA = find(fFFTMag == fFFTMagMax); % There are two maximum
values
iIndexOfMax = iIndexOfMaxA(1) % The 1st index is used
fNum = log(fFFTMag(iIndexOfMax-1)/fFFTMag(iIndexOfMax)) ...
- log(fFFTMag(iIndexOfMax+1)/fFFTMag(iIndexOfMax));
fDen = 2*log(fFFTMag(iIndexOfMax-1)/fFFTMag(iIndexOfMax)) ...
+ 2*log(fFFTMag(iIndexOfMax+1)/fFFTMag(iIndexOfMax));
fIndexOfMax = iIndexOfMax + fNum/fDen % Gaussian interpolation
g = fCurvFtCoeff0 + fCurvFtCoeff1*fIndexOfMax ...
+ fCurvFtCoeff2*fIndexOfMax*fIndexOfMax
plot(fFFTMag);
grid;
```

6.3 Matlab Code for the Discrete Gap Transformation on the Data of the Wavelength Modulated EFPI Sensor System, to Find the EFPI Gap Length *g*

```
%%%%%%%%%%%%%%%%%%%%%%%%%%%%%%%%%%%%%%%%%%%%%%%%%%%%%%%%%%%%%%%%%%%%%%%%%%%%%%%
% Program File: dgt.m
% Programmer: MTE Kahn,
% Date started: 01/15/2001
% Purpose: To find the EFPI gap length g, for an acquired set of
% data, using the Discrete Gap Transform (DGT) method.
%%%%%%%%%%%%%%%%%%%%%%%%%%%%%%%%%%%%%%%%%%%%%%%%%%%%%%%%%%%%%%%%%%%%%%%%%%%%%%%
clear all;
% Calibration coefficients to convert pixel indices to wavelenghts
% for the CCD spectrometer of SIE687. (provided by Ocean Optics Inc.)
fCoeff0 = 744.837472;
fCoeff1 = 0.24256929;
fCoeff2 = -4.176e-5;
iPixOffset = 16; % iPixOffset is the index of the first active element
% of the 1100 element CCD linear array spectrometer.
i = [1:1024];
iPix = i + iPixOffset;
fLam = fCoeff0 + fCoeff1*iPix + fCoeff2*(iPix.*iPix); %fLam in nm
load c:\mystuff\dtechstuff\data\sie687b\g50\g50a.dat;
fData = g50a(17:1040); % Only the data of the active elements are used
fDataMax = max(fData);
fData = fData/fDataMax;
n = 0;
for fGap = 30:0.005:80, % DGT transformation is done in this loop
fParam = ((4000.0 * pi * fGap) ./ fLam); % fGap in um
fReal = fData' .* cos(fParam);
fImag = fData' .* sin(fParam);
fSumReal = sum(fReal);
fSumImag = sum(fImag);
n = n+1;
fDGTMag(n) = (fSumReal*fSumReal + fSumImag*fSumImag);
% Square root on fDGTMag(n) is not necessary, as we need only
% to find the index of the maximum value, not the value itself.
end
fDGTMagMax = max(fDGTMag);
iIndexOfDGTMagMax = find(fDGTMag == fDGTMagMax);
g = 30 + (iIndexOfDGTMagMax-1)*0.005
ga = [30:0.005:80];
plot(ga,fDGTMag);
grid;
```

Appendix 7

Algorithm to implement non iterative solution to Helmholtz equation

```
for j = 2:n, % Look for fixed y(j)
A = sparse(m-1,m-1); b=zeros(m-1,1);
for i=2:m,
b(i-1) = (u1(i,j-1) -2*u1(i,j) + u1(i,j+1))/h1 + ...
f(t2,x(i),y(j)) + 2*u1(i,j)/dt;
if i == 2
b(i-1) = b(i-1) + uexact(t2,x(i-1),y(j))/h1;
A(i-1,i) = -1/h1;
else
if i==m
b(i-1) = b(i-1) + uexact(t2,x(i+1),y(j))/h1;
A(i-1,i-2) = -1/h1;
else
A(i-1,i) = -1/h1;
A(i-1,i-2) = -1/h1;
end
end
A(i-1,i-1) = 2/dt + 2/h1;
end
ut = A\b; % Solve the diagonal matrix.
%---------- loop in y -direction ----------
for i = 2:m,
A = sparse(m-1,m-1); b=zeros(m-1,1);
for j=2:n,
b(j-1) = (u2(i-1,j) -2*u2(i,j) + u2(i+1,j))/h1 + ...
f(t2,x(i),y(j)) + 2*u2(i,j)/dt;
if j == 2
b(j-1) = b(j-1) + uexact(t1,x(i),y(j-1))/h1;
A(j-1,j) = -1/h1;
else
if j==n
b(j-1) = b(j-1) + uexact(t1,x(i),y(j+1))/h1;
A(j-1,j-2) = -1/h1;
else
A(j-1,j) = -1/h1;
A(j-1,j-2) = -1/h1;
end
end
A(j-1,j-1) = 2/dt + 2/h1; % Solve the system
end
ut = A\b;
```